TANDEM TIME-OF-FLIGHT MASS SPECTROMETRY INCORPORATING QUADRATIC-FIELD TECHNOLOGY.

Benjamin Thomas

Submitted for the qualification of Doctor of Philosophy

University of Warwick

Department of Chemistry

September 2000

Table of Contents.

List of Figures.

Acknowledgements.

I would like to express my gratitude to a number of people. I would like to thank my academic supervisor Professor Peter Derrick for the opportunity to work on this research project and providing invaluable guidance. I would like to thank Alex Colburn for his valuable help and support in completing this project. I would like to specially thank Dr. Anastasios Giannakopulos for his continual involvement and support in this project. Without him this project would not have been possible. I would like to thank Dr. Alexander Makarov and Dr. David Reynolds for initial design work on the project. I would like to acknowledge the work of Andrew Bottrill, who operated the EB-TOF instrument.

I would like to express my gratitude to Sajid Bashir; Yi-Bing Zhang; Phillip Green; Liam McDonald; Mark Barrow; Dr. Helen Cooper; Dr. Elaine Scrivener; Dr. Ulla Andersen; Dr. Daniel Laffitte; Dr. Steve Thompson; Dr. Anne-Mette Hoberg; Dr. Mike Belov; Dr. Paul Myatt; Dr. Thomas Drewello; Dr. James Wallace; Dr. Julie Varney and Dr. Xidong Feng for their friendship, support and aid throughout this undertaking.

I would like to thank the members of the mechanical and electronics workshop for their rapid response to the various problems that arose throughout the project.

I would like to thank the EPSRC for providing me with a maintenance grant and funding the construction of the instrument.

Declaration.

I hereby declare that this thesis is my own work and that, to the best of my knowledge and belief, it contains no material previously published or written by another person, nor material which to a substantial extent has been accepted for the award of any other degree or diploma of a university or any other institute of higher learning, except where due acknowledgement is made in the text.

Benjamin Thomas

Abbreviations.

θ angle between the mirror axis and the ion optical axis

δ velocity spread

a acceleration/ quadratic-field ion mirror constant

amu atomic mass units.

C quadratic-field ion mirror constant.

CAD Collisionally activated decomposition.

CCD charge coupled device.

CID collision-induced dissociation

D diameter of the beam emerging from the laser.

d length of acceleration region in two-stage Wiley/McLaren ion source.

D length of field-free drift region/ maximum distortion of baseplate.

D_1 vertical displacement of front of first ion mirror

D_2 vertical displacement of front of quadratic-field ion mirror

Da Dalton

DC direct current

DE delayed extraction

DHB 2,5-dihydroxybenzoic acid

D_{sf} distance from counter electrode to space-focus plane

D_x horizontal width of the final detector

D_y is the vertical height of the final detector

e charge on an electron

E electric field strength

EB-TOF magnetic sector/time-of-flight tandem mass spectrometer

E_d electric field strength in acceleration region of two-stage Wiley/McLaren ion source

E_s electric field strength in ionisation region of two-stage Wiley/McLaren ion source

ESI electrospray ionisation

eV electron volts

F focal length of the lens

F force

FAB fast atom bombardment

FD field desorption

FTICR Fourier transform/ion cyclotron resonance mass spectrometer

FWHM full-width half-maximum

GC gas chromatograph

h length of the collision-cell

i relative sensitivity of detector to different mass-to-charge ratio fragments

ICT impulsive collision theory

k quadratic-field ion mirror constant

K term describing kinetic energy spread

L penetration depth of the ion inside the quadratic-field ion mirror

L total length of field-free regions in reflectron time-of-flight spectrometer

L_1 length of first field-free region in reflectron mass spectrometer

L_2 length of second field-free region in reflectron mass spectrometer

L_d distance from the time focus of MS-1 to the entrance to the quadratic-field ion mirror

l_d length of the of the detector assembly

l_{det} width of the detector

LDI laser desorption/ionisation

LEF linear electric field

L_{ff} length of field-free region between MS-1 and MS-2

L-SIMS liquid secondary ion mass spectrometry

m mass

M mass of ion

m/z mass-to-charge ratio

$m/\Delta m$ definition of mass resolution

m_a mass of the atom or group of atoms involved in the collision

MALDI matrix-assisted laser desorption/ionisation

MCP micro-channel plate

m_{frag} mass of fragment ion

m_g mass of the collision gas

m_{parent} mass of precursor ion

MS mass spectrometry

MS-1 first mass spectrometer of a tandem mass spectrometer

MS-2 second mass spectrometer of a tandem mass spectrometer

n_{elec} electrode number

n_{total} total number of field-sustaining electrodes

OAR open area ratio

PD plasma desorption

PD plasma desorption

PE prompt extraction

PEEK polyetheretherketone

PEG polyethyleneglycol

PID photo-induced dissociation

PSD post source decay

PTFE polytetrafluoroethylene

PVC polyvinylchloride

q charge

QET quasi-equilibrium theory

QIT/TOF quadrupole ion trap/time-of-flight mass spectrometer

RRKM Rice-Ramsperger-Kassel-Marcus

s distance

s_a distance from point of ion production to exit slit of ion source

SID surface-induced dissociation

SIMS secondary ion mass spectrometry

SWL safe working load

s_x distance between the entry and exit point at front of ion mirror

t time

t_0 time at which ion was created

t_{acc} time spent in acceleration region of a simple linear time-of-flight spectrometer

t_D time taken to traverse a field-free drift region

t_B time-of-flight through deceleration region of two-stage ion mirror

TDC time-to-digital converter

T_{grid} optical transmission of grid

TI thermospray ionisation

t_L time taken to traverse field-free regions of reflectron mass spectrometer

t_m time spent inside single-stage ion mirror

t_{MS-1} time-of-flight measured to a detector located in the second field-free region

$T_{observed}$ recorded time-of-flight to the collision-cell of the TOF-TOF spectrometer

TOF time-of-flight

TOF-TOF tandem time-of-flight mass spectrometer

t_R time spent in reflecting region of two-stage ion mirror

T_{source} time spent in ion source of the TOF-TOF spectrometer

t_{ta} turnaround time

t_{total} total measured flight time through the TOF-TOF spectrometer

U kinetic energy

U potential inside ion mirror

u velocity

U_0 initial energy of an ion

u_0 initial velocity

u_1 velocity spread associated with kinetic energy release during unimolecular decay

u_D drift velocity

U_D kinetic energy in drift region

U_{frag} kinetic energy of fragment ion

UHV ultra-high vacuum

U_{parent} kinetic energy of precursor ion

U_{tot} total kinetic energy

UV ultraviolet

u_z velocity of ion with δ velocity spread

V_{acc} accelerating voltage

V_{accel} accelerating voltage

V_{elec} voltage applied to a particular field-sustaining electrode

V_{mirror} mirror reflecting voltage

V_{mirror} voltage applied to the rear electrode of the ion mirror

w_0 Gaussian beam radius

x_0 source half-width

y_0 source half-height

z number of fundamental charges

zw kinetic energy release associated with unimolecular decay

α angle of the detector with respect to the ion beam or time-focus plane.

α inclination angle of first ion mirror due to distortion of baseplate

α_0 horizontal inclination angle

α-CHC α-cyano-4-hydroxy-cinnamic acid

β inclination angle of quadratic-field ion mirror due to distortion of baseplate

β_0 vertical inclination angle

γ relative mass deviation

δ relative energy deviation

ΔL difference in effective path-length

Δm mass uncertainty/peak width

Δs spatial extent of ionisation volume

ΔU kinetic energy spread

ΔU kinetic energy spread arising from ionisation volume

Δu_x radial velocity change after CID

Δu_z velocity change after CID

Δx maximum radial velocity spread

Δ_{xI} radial velocity spread resulting from kinetic energy release

Δz maximum axial velocity spread

Δ_{zI} axial velocity spread resulting from kinetic energy release

θ bias angle of the pores

λ laser wavelength

φ impact angle

ω frequency of oscillation in parabolic well

Abstract

The study involved the design, construction, optimisation and utilisation of a novel tandem time-of-flight (TOF-TOF) instrument. The instrument was designed to use a laser ion source capable of laser desorption or matrix-assisted laser desorption/ionisation. The instrument used a twin ion mirror geometry in which the first ion mirror was a single-stage ion mirror, while the second ion mirror was a quadratic-field ion mirror. The instrument was designed for high-energy (>10keV) collision-induced dissociation (CID).

The initial design criteria of a tandem time-of-flight spectrometer are discussed. The design and construction of the vacuum chamber and pumping system are discussed. The design and construction of the laser ion source are covered in detail. Computer simulations of typical ion trajectories were calculated using the SIMION program. The design and construction of the steering optics, single-stage ion mirror and pulsed mass gate are discussed. Computer simulations of ion trajectories were used to characterise the ion optical properties of the system. Experiments to characterise the energy focusing properties and transmission of the single-stage ion mirror were conducted. The mass resolving power of the single-stage ion mirror were characterised. The single-stage ion mirror achieved a resolution of 2000 full-width half-maximum (FWHM).

The design and construction of the differentially pumped collision-cell and the quadratic-field ion mirror are outlined. Experiments to demonstrate the transmission of the collision-cell and quadratic-field ion mirror are discussed. Experiments to characterise the energy focusing properties of the quadratic-field ion mirror were conducted.

The full instrument achieved precursor mass resolving powers of approximately 7000 (FWHM) for laser desorbed species and 3500 (FWHM) for MALDI generated peptide species. Initial CID results are presented. The study thoroughly discusses the problems with the current instrument configuration and goes on to propose solutions to the problems encountered.

CHAPTER ONE.

INTRODUCTION.

1.01 A Historical Overview of Time-of-Flight Mass Spectrometry.

The " Velocitron" was reported by Cameron and Eggers [1] in 1948, this was later to become known as the time-of-flight (TOF) mass spectrometer. The "Velocitron" had a flight path of 10m, an accelerating potential of 480V and used a pair of pulsed deflection plates located after the ion source to generate discrete ion packets. This early attempt at TOF mass spectrometry achieved a mass resolving power of approximately 2. The second instrument, reported by Wolff and Stevens [2], used a 1m flight path, a 300V extraction voltage and a pulsed electron beam to generate ion packets. The instrument achieved a mass resolving power of 20. Katzenstein and Friedland [3] constructed the third time-of-flight mass spectrometer. The instrument had a 1m flight path and achieved a mass resolution of approximately100.

In 1955 Wiley and McLaren [4] published their seminal paper regarding space focusing and time-lag energy focusing. The techniques described by Wiley and McLaren [4] resulted in significant improvements in mass resolution. Wiley and McLaren [4] reported mass resolving powers of 300 for an instrument with a flight path of just 0.4m. In 1957 the Bendix Corporation, later CVC Products (Rochester, NY), made the time-of-flight instrument commercially available. The commercial instruments incorporated time-lag focusing, 1m flight paths, 2800V accelerating

voltages and were capable of generating 10,000 spectra per second. Later instruments were capable of mass resolving powers of 600. The pulsed nature of the ion source, along with the instrument's ability to acquire a large number of spectra per second, resulted in the instrument being widely adopted by laboratories as a means of monitoring fast reactions.

In 1959 Gohlke [5] reported the first attempt at gas chromatograph/mass spectrometry (GC/MS), using a time-of-flight mass spectrometer. In 1963 McFadden *et al* [6] reported the use of a capillary GC/MS, using a fast-scanning time-of-flight mass spectrometer.

At this time, it appeared that the time-of-flight mass spectrometer had a strong commercial future. This was, however, to prove a false dawn.

In the late 1960's the quadrupole mass spectrometer became commercially available at reasonable prices. The quadrupole mass spectrometer quickly became widespread and popular. The quadrupole mass spectrometer had many favourable features, including simplicity, compactness, fast-scanning ability, high resolution and low-cost. The availability of computerised data systems, suitable for GC/quadrupole mass spectrometry, also contributed to their popularity. The speed, availability and cost of electronics suitable for TOF mass spectrometry, was to prove a hindrance to the development of TOF mass spectrometry until the early 1990's. The proliferation of the quadrupole mass analyser resulted in a reduction in interest in TOF mass spectrometry.

During the 1960's research into laser desorption [7] and pulsed ion and neutral bombardment of organic solids began [8]. Within fifteen years, the laser microprobe TOF mass spectrometer was commercially available,

through companies such as Leybold-Heraeus GmbH (LAMMA) and Cambridge Mass Spectrometry Ltd. (LIMA).

During the late 1960's and early 1970's, a major breakthrough in TOF mass spectrometry instrumentation occurred. Mamyrin and co-workers [9][10][11][12][13] designed a new method of correcting for kinetic energy spread. The new device was referred to as an ion mirror or reflectron mirror. At about the same time Poschenrieder [14] was improving the mass resolution of TOF spectrometers by using electrostatic analysers as a method of achieving isochronous time focusing and space focusing.

In 1974 Macfarlane and co-workers [15] found that the interaction between Cf-252 fission fragments and biological samples could be used to desorb and ionise large analyte molecules. The technique became known as plasma desorption (PD). The pulsed nature of the method, along with its ability to generate high-mass ions, meant that TOF mass spectrometry was the ideal means of analysing the ions produced. The discovery lead to resurgence in interest in TOF mass spectrometry. In 1978 Kistemaker and co-workers [16] reported the laser desorption of biomolecules. During the 1980's interest in pulsed ionisation techniques coupled to TOF mass spectrometers increased, as the analysis of biomolecules became increasingly important.

In 1988 matrix-assisted laser desorption/ionisation (MALDI) was developed from the older technique of laser desorption/ionisation (LDI). The MALDI technique was first introduced by Tanaka *et al* [17] and by Karas and Hillenkamp [18]. The method utilised by Tanaka *et al* [17] used a liquid matrix containing fine metal particles.

The technique adopted by Karas and Hillenkamp [18] used a strongly absorbing, organic solid as the matrix. The method used by Karas and Hillenkamp was adopted as the standard MALDI technique because of its high sensitivity. The MALDI technique dramatically increased the amount of research in the field of TOF mass spectrometry. In the early 1990's the first commercial MALDI TOF instruments became available. They are now commonly used in many chemical and biochemical laboratories for the analysis of high-mass synthetic polymers and biopolymers.

1.02 Linear Time-of-Flight Mass Spectrometers.

Time-of-flight mass spectrometry is based on a simple mass separation principle. Ions are generated in an ion source, from where they are extracted into the time-of-flight mass spectrometer by means of an electrostatic field. The ions then traverse a field-free region, before registering at an ion detector located at the end of the flight-tube. The velocities, and hence flight times, of the ions through the instrument are related to their mass-to-charge ratio. By measuring the output of the detector versus time it is possible to build up a histogram of ion intensities versus time-of-flight. Knowledge of the relationship between time-of-flight and mass-to-charge ratio allows a mass spectrum to be generated.

Basic Newtonian mechanics can be used to determine the behaviour of non-relativistic ions through a time-of-flight instrument. Consider an ion generated in a homogenous electrostatic field. Figure 1 shows a schematic diagram of a linear time-of-flight mass spectrometer. The important geometric properties of the instrument are defined.

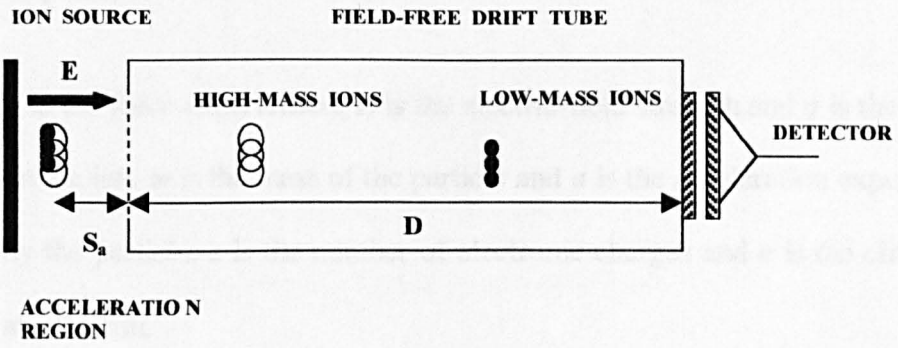

Fig. 1: Schematic diagram of a linear time-of-flight mass spectrometer with single-stage ion source. D is the length of the field-free drift region, E is the electric-field strength in the acceleration region and s_a is the distance from the point of ion production to the counter-electrode.

The ion in the source region experiences a force equal to:

$$F = Eq \tag{1.01}$$

$$F = ma \tag{1.02}$$

Where:

$$q = ze \tag{1.03}$$

F is the force experienced, E is the electric-field strength and q is the charge on the ion. m is the mass of the particle and a is the acceleration experienced by the particle. z is the number of electronic charges and e is the charge on an electron.

The acceleration of the ion can be expressed as:

$$a = \frac{du}{dt} \tag{1.04}$$

$$a = \frac{Eq}{m} \tag{1.05}$$

Acceleration is the rate of change of velocity. u is the velocity and t is the time.

The velocity of an ion can be expressed as:

$$u = \int \frac{Eq}{m} dt \tag{1.06}$$

$$u = u_0 + \left(\frac{Eq}{m}\right) \cdot t \tag{1.07}$$

u is the velocity of the ion after acceleration, u_0 is the initial velocity and t is the time spent in acceleration.

Time spent in acceleration can be expressed as:

$$t = \frac{u - u_0}{E}\left(\frac{m}{q}\right) \quad 1.08$$

The position of the ion:

$$s = \int u dt \quad 1.09$$

$$s = s_0 + u_0 t + \frac{1}{2}\left(\frac{Eq}{m}\right)t^2 \quad 1.10$$

s is the position of the ion and s_0 is the initial position of the ion.

The energy of the ion after acceleration can be expressed as:

$$qV = qEs_a \quad 1.11$$

V is the voltage applied to the accelerating electrode and s_a is the distance over which the ion is accelerated. The kinetic energy can be expressed as:

$$qEs_a = \frac{1}{2}mu_D^2 \quad 1.12$$

u_D is the drift velocity of the ion in the field-free region. The drift velocity of the ion can be expressed as:

$$u_D = \sqrt{\frac{2qEs_a}{m}} \quad 1.13$$

The time taken to traverse the field-free drift region can be expressed as:

$$t_D = \frac{D}{u_D} \quad 1.14$$

$$t_D = \frac{D}{\sqrt{2qEs_a/m}} \qquad 1.15$$

D is the length of the field-free drift region and t_D is the time taken to traverse the drift region.

For an ion formed at the surface of the repeller electrode:

$$t_D = \frac{D}{\sqrt{2qV/m}} \qquad 1.16$$

The total time-of-flight is the sum of the time spent in all regions plus the time at which the ion was created:

$$t_{TOF} = t_0 + t_{acc} + t_D \qquad 1.17$$

t_{TOF} is the total time-of-flight, t_0 is the time at which the ion is created, t_{acc} is the time spent in the acceleration region and t_D is the time spent in the drift region.

1.03 The Wiley and McLaren Time-of-Flight Mass Spectrometer.

In the late 1950's the Bendix Corporation produced the first commercial time-of-flight instrument. The instrument, designed by Wiley and McLaren [4], incorporated several revolutionary concepts.

The operating principles of the instrument are widely used to this day.

The instrument used an electron impact ion source followed by 0.4 m flight-tube. Figure 2 shows a simple schematic diagram of the instrument.

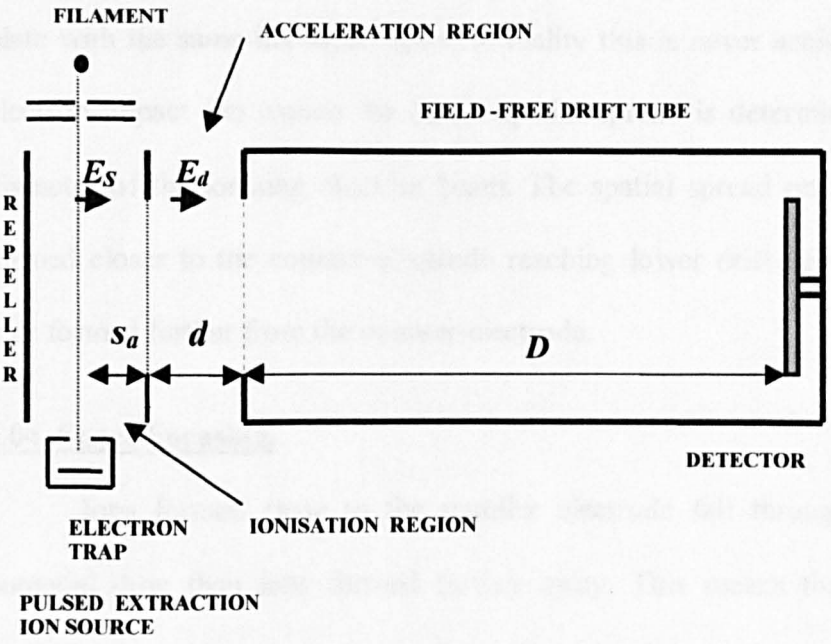

Fig. 2: Schematic diagram of the Wiley and McLaren time-of-flight mass spectrometer with pulsed ion source. D is the length of the field-free region, d is the length of the acceleration region and s_a is the distance from the point of ion production to the counter-electrode. E_s and E_d are the field strengths in the respective regions

The resolution of time-of-flight mass spectrometers is limited by a number of factors. Two of the most significant are the initial velocity distribution of the ions and the initial spatial spread. Ideally all ions would be formed at an equipotential plane, parallel to the surface of the repeller plate with the same initial energies. In reality this is never achieved. In an electron impact ion source the initial spatial spread is determined by the diameter of the ionising electron beam. The spatial spread results in ions formed closer to the counter-electrode reaching lower drift velocities than ions formed further from the counter-electrode.

1.04 Space Focusing.

Ions formed close to the repeller electrode fall through a larger potential drop than ions formed further away. This means that the ions formed close to the repeller electrode reach higher drift velocities than those formed further away. Downstream of the ion source, faster ions catch-up and overtake slower ions which formed ahead of them. This point is the point at which time compression is maximised. It was termed the "space-focus plane" by Wiley and McLaren [4].

A single-stage ion source (see figure 1) consists of a repeller electrode, to which an extraction voltage is applied, and a counter-electrode, which is maintained at the potential of the field-free region. The position of the space-focus plane can be expressed as:

$$D_{sf} = 2s_a \qquad 1.18$$

D_{sf} is the distance from the counter-electrode to the space-focus plane and s_a is the distance from the point of ion production to the counter-electrode. s_a is

a variable and therefore the distance D_{sf} is not a plane. The relationship holds only when the zone of ionisation is thin. The position of the space-focus plane is determined by the geometry of the single-stage ion source.

It is possible to construct a position versus time plot to show the principle of space focusing. Figure 3 shows the space-time trajectories of ions created in the ion source of the tandem time-of-flight (TOF-TOF) spectrometer described in subsequent chapters.

A number of basic assumptions were made when the space-time calculations were performed:

1) The electric field in the acceleration region was homogenous.
2) The source was 1-dimensional.

The space-focus plane represents the point at which time-spread is minimised. It is, therefore, the ideal location to position a detector in order to achieve maximum resolution. For a single-stage ion source the space-focus plane is typically located a few centimetres from the ion source. The time dispersion is insufficient to make it practical to position a detector here.

The Wiley and McLaren instrument introduced the concept of two-stage ion sources. Two-stage ion sources consist of an ionisation region, defined by the repeller plate and counter-electrode, followed by an acceleration region, defined by the counter-electrode and an electrode maintained at the voltage of the field-free region. Figure 2 shows a schematic diagram of Wiley and McLaren TOF spectrometer. The two-stage ion source allowed the position of the space-focus plane to be moved further down the flight tube.

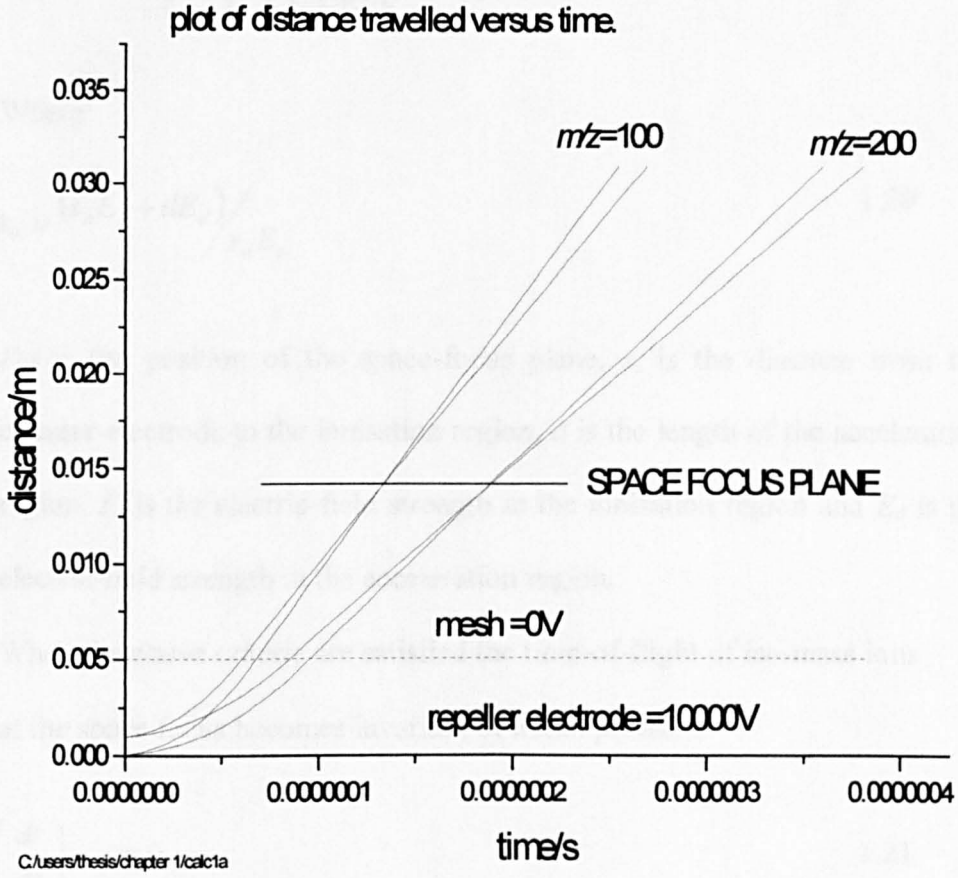

Fig. 3: Space-time trajectory illustrating space focusing. Calculated for ions of mass-to-charge ratio 100 and 200, created at the surface of the repeller plate and 1mm above the repeller plate. The ions possessed no initial velocity. The repeller plate was maintained at 10,000V and the counter-electrode at 0V. The separation between the two plates was 5mm. The space-focus plane was located 14mm from the repeller plate.

The position of the space-focus plane can be expressed as:

$$D_{sf} = 2s_a k_0^{3/2}\left(1 - \frac{1}{k_0 + k_0^{1/2}}\frac{d}{s_a}\right) \qquad 1.19$$

Where:

$$k_0 = \left(s_a E_s + dE_d\right)/s_a E_s \qquad 1.20$$

D_{sf} is the position of the space-focus plane, s_a is the distance from the counter-electrode to the ionisation region, d is the length of the acceleration region, E_s is the electric-field strength in the ionisation region and E_d is the electric-field strength in the acceleration region.

When the above criteria are satisfied the time-of-flight of iso-mass ions at the space focus becomes invariant of initial position:

$$\left(\frac{dt}{ds}\right)_{0,s_a} = 0 \qquad 1.21$$

The position of the space-focus plane can be controlled by varying the E_d/E_s ratio. Figure 4 shows a plot of the position of the space focus versus the ratio E_d/E_s. Figure 4 also shows a plot of the position of space-focus plane versus the counter-electrode voltage. The calculation was performed for the ion source of the TOF-TOF spectrometer. The accelerating voltage was +10kV and the source electric field was assumed to be homogenous.

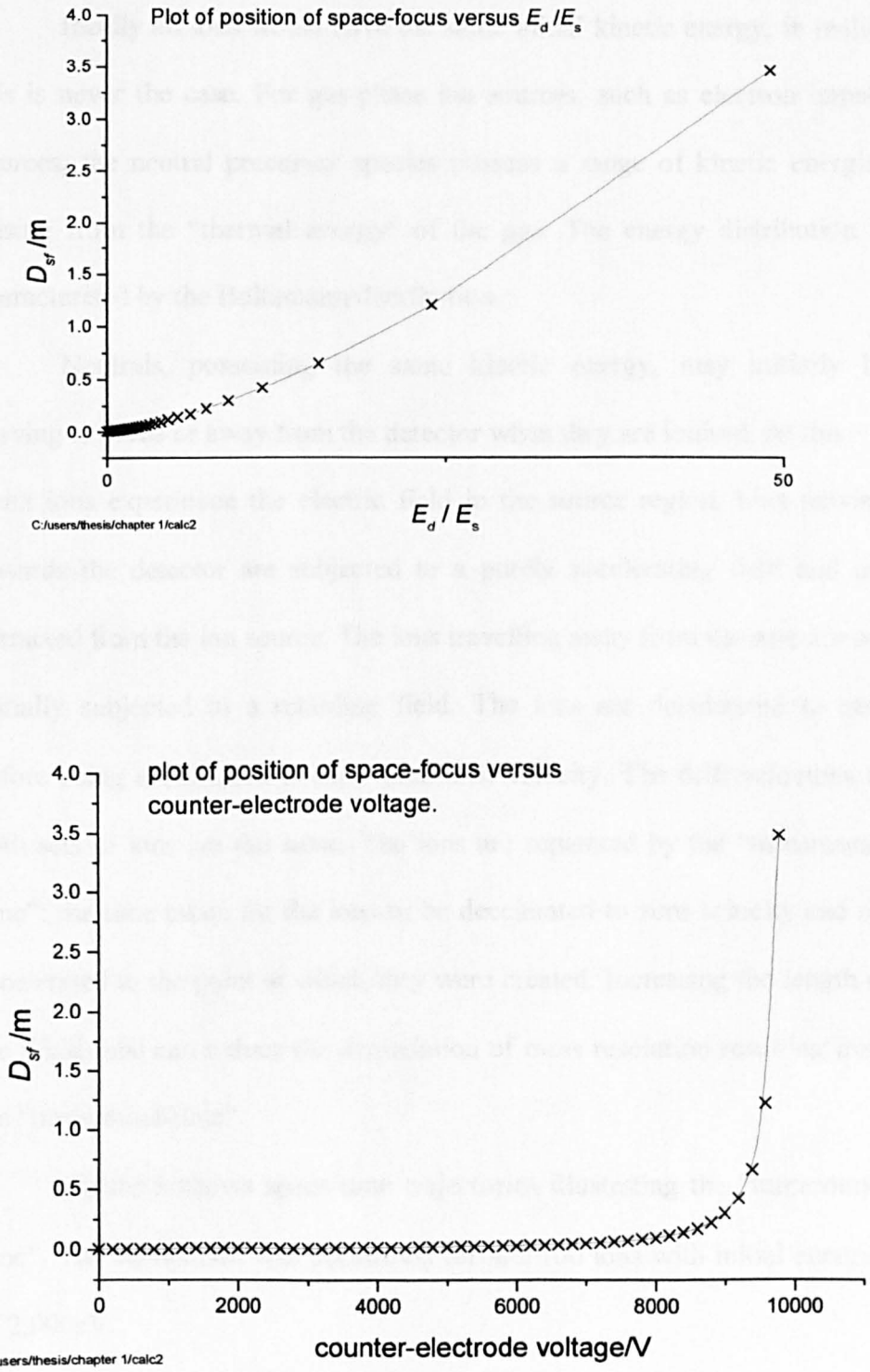

Fig. 4: (TOP) Plot of position of space focus, D_{sf}, versus E_d/E_s. (BOTTOM) Plot of position of space focus, D_{sf}, versus counter-electrode voltage, for the ion source of the TOF-TOF spectrometer.

1.05 Ions Formed in the Gas-Phase and the Turnaround Aberration.

Ideally all ions would have the same initial kinetic energy, in reality this is never the case. For gas-phase ion sources, such as electron impact sources, the neutral precursor species possess a range of kinetic energies arising from the "thermal energy" of the gas. The energy distribution is characterised by the Boltzmann distribution.

Neutrals, possessing the same kinetic energy, may initially be moving towards or away from the detector when they are ionised. At this point ions experience the electric field in the source region. Ions moving towards the detector are subjected to a purely accelerating field and are extracted from the ion source. The ions travelling away from the detector are initially subjected to a retarding field. The ions are decelerated to zero before being accelerated to their final drift velocity. The drift velocities of both sets of ions are the same. The ions are separated by the "turnaround-time"; the time taken for the ions to be decelerated to zero velocity and re-accelerated to the point at which they were created. Increasing the length of the flight tube can reduce the degradation of mass resolution resulting from the "turnaround-time".

Figure 5 shows space-time trajectories illustrating the "turnaround-time". The calculation was performed for *m/z* 100 ions with initial energies of 2,000eV.

Consider ions created at the same time, at the same distance from the detector. The time spent in acceleration can be expressed as:

$$t_{acc} = \frac{u - u_0}{E}\left(\frac{m}{q}\right) \qquad 1.22$$

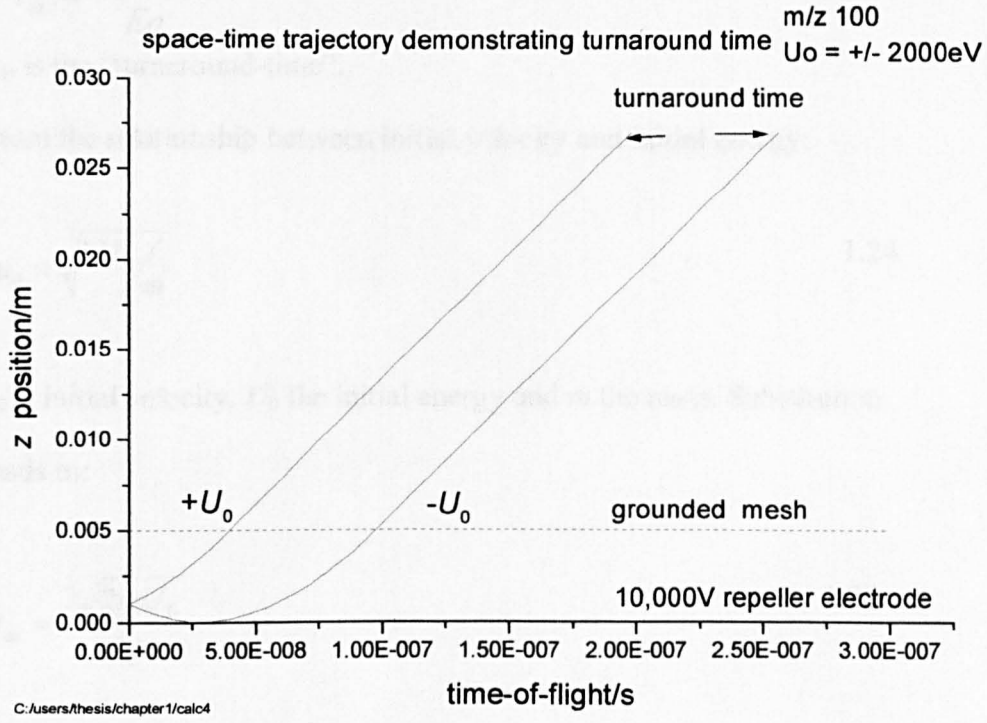

Fig. 5: Space-time trajectories illustrating the principle of the "turnaround time".

For ions with initial velocities directed away from the detector; $u_0=-u_0$. The "turnaround-time" can be expressed as:

$$t_{ta} = \frac{2|u_0|m}{Eq} \qquad 1.23$$

t_{ta} is the "turnaround-time".

From the relationship between initial velocity and initial energy:

$$u_0 = \sqrt{2U_0/m} \qquad 1.24$$

u_0 is initial velocity, U_0 the initial energy and m the mass. Substitution leads to:

$$t_{ta} = \frac{2\sqrt{2mU_0}}{Eq} \qquad 1.25$$

Ions travelling at the same speed, but in opposite directions, reach the same drift velocity after acceleration. The ions are separated at the detector by the "turnaround-time".

The "turnaround-time" can be minimised by increasing the length of the field-free region, as this increases the total flight time relative to the "turnaround-time". It can also be seen that increasing the electric-field strength in the extraction region reduces the "turnaround-time". The electric-field strength may be increased by using larger accelerating potentials or by decreasing the separation between the repeller plate and the counter-electrode.

The time taken for an ion to travel from its initial position s_0 to s can be obtained from the quadratic expression:

$$s = s_0 + u_0 t + \frac{1}{2}\left(\frac{Eq}{m}\right)\cdot t^2 \qquad 1.26$$

Taking the roots of the quadratic expression and substituting initial velocity u_0 with:

$$u_0 = \sqrt{2U_0/m} \qquad 1.27$$

The following expression is obtained:

$$t = \frac{-\sqrt{2mU_0}}{Eq} \pm \frac{\sqrt{2m[U_0 + Eqs]}}{Eq} \qquad 1.28$$

The time spent in acceleration can be expressed as:

$$t_{acc} = \frac{\sqrt{2m[U_0 + qEs]}}{Eq} \pm \frac{\sqrt{2mU_0}}{Eq} \qquad 1.29$$

The second term describes the "turnaround-time". The time-of-flight of an ion can be calculated with knowledge of the time spent in the field-free drift region. The energy of an ion in the drift region, U_D, can be expressed as:

$$U_D = U_0 + qEs_a \qquad 1.30$$

The drift velocity can therefore be expressed as:

$$u_D = \sqrt{\frac{2(U_0 + qEs_a)}{m}} \qquad 1.31$$

The time spent in the drift region can be expressed as:

$$t_D = \frac{D}{2}\sqrt{\frac{2m}{(U_0 + qEs_a)}} \qquad 1.32$$

The total time-of-flight is the sum of the times spent in the acceleration and drift regions:

$$t_{TOF} = \frac{(2m)^{1/2}\left[(U_0 + qEs_a)^{1/2} \pm U_0^{1/2}\right]}{qE} + \frac{(2m)^{1/2} D}{2(U_0 + qEs_a)^{1/2}} \qquad 1.33$$

The contribution of the "turnaround-time" to the degradation of mass resolving power in MALDI and LDI ion sources is not understood. Desorbed neutrals and ions, formed by MALDI, exhibit initial velocities biased towards the detector and cannot be considered to possess truly random initial velocity distributions, as would be found in a free gas.

1.06 Ions Formed at Surfaces.

Ions formed at a flat surface travel the same distance to the detector and experience the same accelerating potential. If V is the potential difference applied across the acceleration region, then the energy of the ion in the drift region can be expressed as:

$$U_D = U_0 + qV \qquad 1.34$$

The first term, U_0, is the initial kinetic energy. The second term is the energy gained from the accelerating field.

The drift time can be expressed as:

$$t_D = \frac{D}{2}\sqrt{\frac{2m}{(U_0 + qV)}} \qquad 1.35$$

The length of the field-free region, D, is much larger than the length of the acceleration region, s_a. The time spent in the field-free region, t_D, is therefore much larger than the time spent in acceleration, t_{acc}. Time spread, arising from ions possessing different initial kinetic energies, can be considered to be predominantly due to differences in time spent in the drift regions:

$D >> s_a$

$t_D >> t_{acc}$

$\Delta t_D >> \Delta t_{acc}$

Assuming that the total time-of-flight is approximately equal to:

$$t_{TOF} \approx t_D = \frac{D}{2}\sqrt{\frac{2m}{(U_0 + qV)}} \qquad 1.36$$

Differentiating with respect to U_0 and multiplying by dU_0 gives:

$$dt = \frac{\frac{D}{2}\sqrt{\frac{m}{2}}}{(U_0 + qV)\sqrt{U_0 + qV}} dU_0 \qquad 1.37$$

Dividing by equation 1.36 and multiplying by 2:

$$\frac{2dt}{t} = \frac{dm}{m} = \frac{dU_0}{U_o + qV} \qquad 1.38$$

The mass resolving power can be expressed as:

$$\frac{m}{\Delta m} = \frac{U_0 + qV}{\Delta U_0} \qquad 1.39$$

As $qV >> \Delta U_0$, this can be simplified to:

$$\frac{m}{\Delta m} \approx \frac{qV}{\Delta U_0} \qquad 1.40$$

The model for ions formed at surfaces, applies most readily to desorption of pre-formed ions from solids.

1.07 Time-Lag Energy Focusing.

Time-lag energy focusing, or delayed-extraction as it is now more commonly known as, was first introduced by Wiley and McLaren [4]. The technique improved the mass resolution by compensating for the initial velocity distribution of the ions.

A pulsed ionisation event generates an ion packet. During the period of ionisation the source region contains no accelerating field. The ions drift with velocities that are dependent upon their initial energies. The position of the ions at any given time is related to their initial velocity. After a time delay an extraction pulse is applied to the source. Ions that have migrated towards the detector acquire less kinetic energy than those that have migrated away from the detector. Ions extracted from positions close to the repeller catch-up and overtake ions possessing less kinetic energy. This point is the time focus, and at this point time spread is minimised and mass resolution

maximised. Figure 6 shows space-time trajectories for *m/z* 100 ions formed at the surface of the sample probe with no initial velocity and a positive initial velocity. Note how ions with positive initial velocities drift away from the repeller plate during the delay time, before being extracted.

For a single-stage ion source, the time focus is located at a distance $D=2s_a$. By setting $U_0 = 0$ and differentiating equation 1.33 with respect to s_a, the following expression can be derived:

$$\frac{dt}{ds_a}(U_0 = 0) = \sqrt{\frac{m}{2qEs_a}} \times \left(1 - \frac{D}{2s_a}\right) \qquad 1.41$$

The function reaches a minimum when $D=2s_a$. The time focus is located at a distance of $2s_a$ from the counter-electrode. The short flight distance does not provide sufficient time dispersion to allow for high resolution. Time-lag energy focusing ion sources are therefore two-stage sources, which allow the position of the time focus to be moved down the field-free region, towards the detector. By controlling the delay and the ratio E_d/E_s, the position of the time focus can be made coincident with the detector.

An ion source cannot be configured to simultaneously compensate for initial position (space focusing) and initial energy (time-lag focusing). The technique resulting in the largest gain in mass resolving power is therefore used. This varies between different instruments and ionisation techniques. Ions desorbed from surfaces do

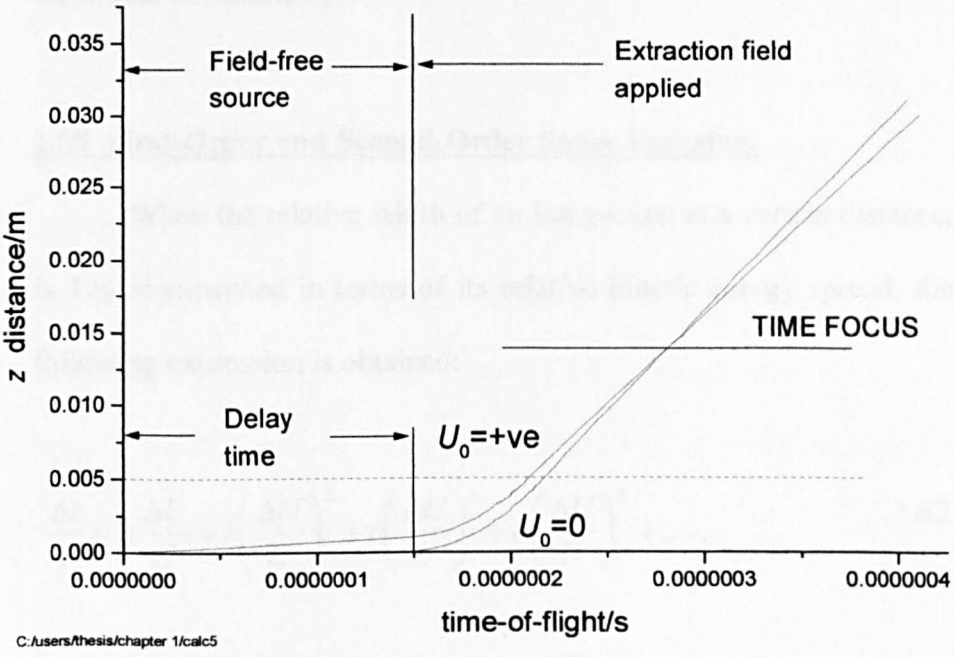

Fig. 6: Space-time trajectories showing the principle of time-lag focusing.

not possess large initial spatial spreads. The resolution of ions formed at surfaces has been shown to be largely dependent upon the initial energy spread of the ion packet. Time-lag focusing may therefore provide the most significant improvement in resolution. For sources with large ionisation volumes, space focusing may provide greater resolution enhancement.

1.08 First-Order and Second-Order Space Focusing.

When the relative width of an ion packet, at a certain distance, is Taylor-expanded in terms of its relative kinetic energy spread, the following expression is obtained:

$$\frac{\Delta t}{t} = a\frac{\Delta U}{U} + b\left(\frac{\Delta U}{U}\right)^2 + c\left(\frac{\Delta U}{U}\right)^3 + d\left(\frac{\Delta U}{U}\right)^4 + \ldots\ldots \qquad 1.42$$

Δt is the peak width, t is the time-of-flight and a, b, c and d are coefficients. U is the drift energy and ΔU is the energy spread.

For a single-stage ion source the coefficient of the linear term reduces to zero at the time focus, *i.e.* a=0. Wiley and McLaren [4] introduced the two-stage ion source. The two-stage ion source allowed the position of the first-order space focus to be moved. Weinkauf *et al* [19] showed that appropriate selection of ion source geometry and voltages allowed second-order space focusing.

The conditions for second-order space focusing are:

$$s_a = \frac{D_{sf} - 2d}{2\cdot(d + D_{sf})}\left(D_{sf}\left(\frac{D_{sf} - 2d}{3D_{sf}}\right)^{3/2} + d\right) \qquad 1.43$$

$$V_2 = V_1 \frac{2(d + D_{sf})}{3D_{sf}} \qquad 1.44$$

D_{sf} is the position of the second-order space focus, d is the width of the acceleration region and s_a is the distance from the point of ion production to the counter-electrode. V_1 is the potential at which the ion was created and V_2 is the potential difference across the acceleration region. The position of the second-order space focus cannot be moved. Second-order space focusing results in additional time compression at the detector, allowing higher resolution to be obtained. Weinkauf and co-workers [20] constructed a second-order space focusing instrument with a drift length of 13cm. Weinkauf and co-workers reported achieving a resolution in excess of 800 for xylene.

1.09 Mass Resolving Power

The mass resolving power of a mass spectrometer determines the maximum mass at which the instrument can resolve one mass unit. The mass resolution has important implications on the accuracy with which the mass of any species can be determined and assigned.

Mass resolution is defined as $m/\Delta m$, where m is the mass of the species and Δm is the mass uncertainty or peak width. In time-of-flight mass spectrometry the peak width is measured at 50% signal intensity, or full-width half-maximum (FWHM). In sector instruments it is common to find resolution determined using peak widths measured at 10% signal height.

It is useful, in time-of-flight mass spectrometry, to define resolution in the time domain:

$$m \propto t^2$$
$$m = Ct^2$$
$$dm/dt = 2Ct$$
$$dm/m = 2dt/t$$

Therefore:

$$\frac{m}{\Delta m} = \frac{t}{2\Delta t} \qquad 1.45$$

This is one of the most important relationships in time-of-flight mass spectrometry.

1.10 The Ion Reflectron in Time-of-Flight Mass Spectrometry.

A major advance in time-of-flight mass spectrometry occurred with the introduction of the ion mirror, also termed the reflectron. Alikhanov [21] introduced a single-stage ion mirror, capable of first-order correction of initial energy. In 1966 Mamyrin [9] patented the two-stage ion mirror, capable of second-order correction with respect to initial energy.

The reflectron is a simple device, used to enhance mass resolution. At its simplest, the reflectron consists of a single, linear, homogenous electric field. Iso-mass ions possessing large kinetic energies spend less time in the field-free region than those ions possessing less kinetic energy. The resultant time spread degrades

mass resolution. In a reflectron instrument, high-energy ions penetrate the retarding electric field more deeply than low-energy ions. By correctly selecting the electric-field strength inside the ion mirror, the time-of-flight of the high-energy and low-energy ions can be made the same.

1.11 Single-Stage Ion Mirrors.

The simplest form of ion mirror is the single-stage ion mirror. The single-stage reflectron consists of a homogenous electric field that has a constant electric-field strength throughout the ion mirror. The electric field can be generated between two pieces of flat mesh. A solid electrode can be used to replace the rear mesh. It is common practice however to use mesh, as this allows a detector to be positioned behind the reflectron. This allows the instrument to be used as a linear TOF instrument. Applying a suitable voltage to the rear electrode, while the front electrode is grounded, generates a retarding field inside the mirror. In order to form a homogenous field between the two grids, field-sustaining electrodes are positioned along the length of the mirror. The ring-like electrodes are usually equidistantly spaced, and connected to the high-voltage supply by a chain of equal resistance resistors. Figure 7 shows a schematic representation of a single-stage ion mirror with a mono-energetic ion trajectory. The constant electric field, *E*,

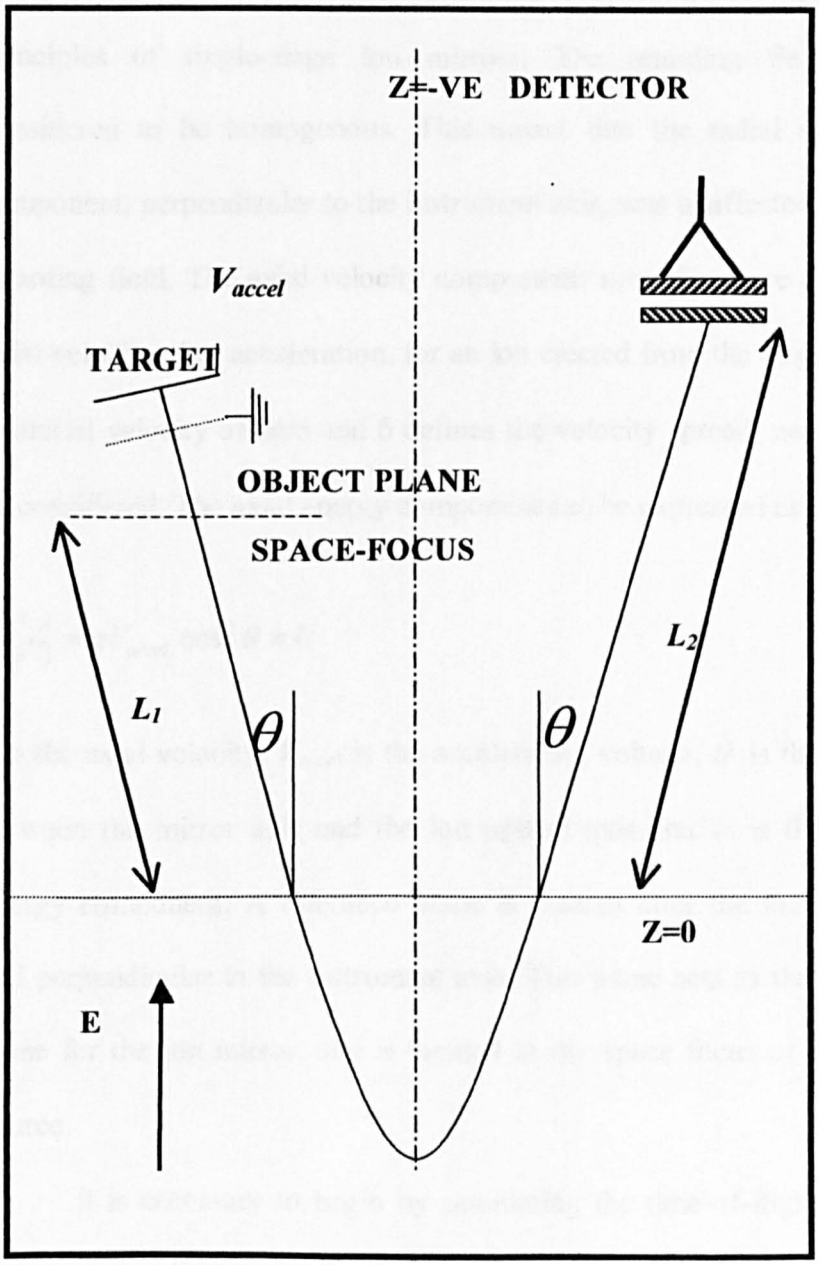

Fig. 7: Schematic diagram showing a single-stage ion mirror.

defines the instrument axis, denoted as the z-axis. The instrument consists of a two field-free regions: $z < 0$, $E_z = 0$ and the ion mirror: $z > 0$, $E_z = E$. Standing and co-workers [22] have described the operating principles of single-stage ion mirrors. The retarding field was considered to be homogenous. This meant that the radial velocity component, perpendicular to the instrument axis, was unaffected by the retarding field. The axial velocity component: $u_z = u + \delta$, where u is the axial velocity after acceleration, for an ion ejected from the target with an initial velocity of zero and δ defines the velocity spread, need only be considered. The axial energy component can be expressed as:

$$mu^2/2 = qV_{accel.} \cos^2 \theta = U \qquad 1.46$$

u is the axial velocity, V_{accel} is the accelerating voltage, θ is the angle between the mirror axis and the ion optical axis and U is the axial energy component. A reference plane is located after the ion source and perpendicular to the instrument axis. This plane acts as the object plane for the ion mirror, and is located at the space focus of the ion source.

It is necessary to begin by calculating the time-of-flight of an ion with zero initial velocity (*i.e.* $\delta=0$), from the object plane to the detector. The time taken for the ion to travel between the point of ion production to the object plane is neglected, as the time spent in the

source region is negligible compared to the time spent in the field-free regions and the ion mirror. The distance from the object plane to the front of the mirror is L_1, and the distance from the front of the reflectron to the detector is L_2. The total length of the field-free regions is: $L=L_1+L_2$. The reflectron does not alter the magnitude of the axial velocity after the mirror. It does, however, reverse the direction. The time spent in the field-free regions can be expressed as: $t_L=L/u$. The time spent in the mirror can be expressed as: $t_m=2u/a$. Acceleration: $a=qE/m$. E is the electric-field strength of the retarding field.

The total time-of-flight though the field-free regions and the ion mirror can be expressed as:

$$t = t_m + t_L = \frac{2m}{qE}u + \frac{L}{u} \qquad 1.47$$

Consider variations in u. Time-of-flight reaches a minimum when dt/du = 0. This occurs when:

$$\frac{2mu}{qE} = \frac{L}{u} \qquad 1.48$$

Quite simply, the time spent inside the ion mirror equals the time spent in the field-free regions: $t_m=t_L=L/u$.

The field strength of the retarding field must be:

$$E = \frac{2mu^2}{qL} = \frac{4U}{qL} \qquad 1.49$$

The time-of-flight through the entire instrument, under the above conditions, can be expressed as:

$$t = \frac{2L}{u} = \left(\frac{2L}{\sqrt{2U}}\right)\sqrt{m} \qquad 1.50$$

The time-of-flight through the reflectron mirror remains proportional to $\sqrt{m}$. Spectra can be calibrated using the procedure used for linear TOF spectrometers.

The penetration depth, l, of the ion inside the ion mirror can be expressed as:

$$U = lqE = \frac{l4U}{L} \qquad 1.51$$

The penetration depth: $l=L/4$.

The effective flight path through the ion mirror is twice the penetration depth: 2 x $L/4$ = $L/2$. The minimum physical length of the ion mirror is $1/4^{th}$ the length of the field-free regions, L.

The physical length of the ion mirror is greater than the penetration depth, l, in order to ensure that ions do not pass close to the rear electrode of the ion mirror. Short-range fringing fields, close to the rear electrode, result in temporal scattering and degradation of mass resolution.

Consider ions that possess an initial velocity other than zero.

The following expression can be derived for the total time-of-flight:

$$t = t_m + t_L = \frac{2m}{qE}(u+\delta) + \frac{L}{u+\delta} \qquad 1.52$$

Expanding the second term as a function of δ:

$$t = \frac{2m}{qE}(u+\delta) + \frac{L}{u} - \delta\frac{L}{u^2} + \delta^2\frac{L}{u^3} - \delta^3\frac{L}{u^4} + \ldots \qquad 1.53$$

$$t = \left[\frac{2mu}{qE} + \frac{L}{u}\right] + \frac{\delta}{u}\left[\frac{2mu}{qE} - \frac{L}{u}\right] + \left(\frac{\delta}{u}\right)^2\frac{L}{u} - \left(\frac{\delta}{u}\right)^3\frac{L}{u} + \ldots \qquad 1.54$$

The linear term vanishes when the following criteria are fulfilled:

$$\frac{2mu}{qE} = \frac{L}{u} \qquad 1.55$$

$$E = \frac{2mu^2}{qL} = \frac{4U}{qL} \qquad 1.56$$

Under these conditions the time-of-flight is independent of the velocity to the first-order, *i.e.* $dt/du = 0$. First-order time focusing is achieved at the detector plane. The time-of-flight can be expressed as:

$$t = \frac{L}{u}\left[2 + \left(\frac{\delta}{u}\right)^2 - \left(\frac{\delta}{u}\right)^3 + \ldots\right] \qquad 1.57$$

1.12 The Two-Stage Ion Mirror in Time-of-Flight Mass Spectrometry.

The two-stage ion mirror was originally conceived by Mamyrin and co-workers [9][10][11][12][13]. Single-stage ion mirrors are capable of first-order time focusing. The two-stage reflectron is capable of second-order time focusing. Instruments based on two-stage ion mirrors are more compact and achieve higher mass resolving

powers than single-stage reflectrons. Their high mass-resolution, high transmission and ability analyse metastable fragment species has resulted in them becoming the most commercially widespread ion mirror.

The two-stage ion mirror is mechanically more complex than its single-stage analogue. The mirror consists of two separate electric field regions, defined by grids. The first and strongest electrostatic field forms the deceleration region. The second region forms the reflecting field. Figure 8 shows a schematic diagram of a two-stage reflectron, time-of-flight mass spectrometer.

Mamyrin and co-workers [10] derived expressions describing the behaviour two-stage ion mirrors.

Assuming the extraction potential of the source to be $U=KU_0$, where U_0 corresponds to the mean ion energy and K is a term close to unity.

The total time-of-flight is the sum of the time spent in each region:

$$t = t_L + t_B + t_R \qquad 1.58$$

t is the total flight time, t_L is the time spent in the field-free regions, t_B is the time spent in the deceleration region and t_R is the time spent in the reflecting region.

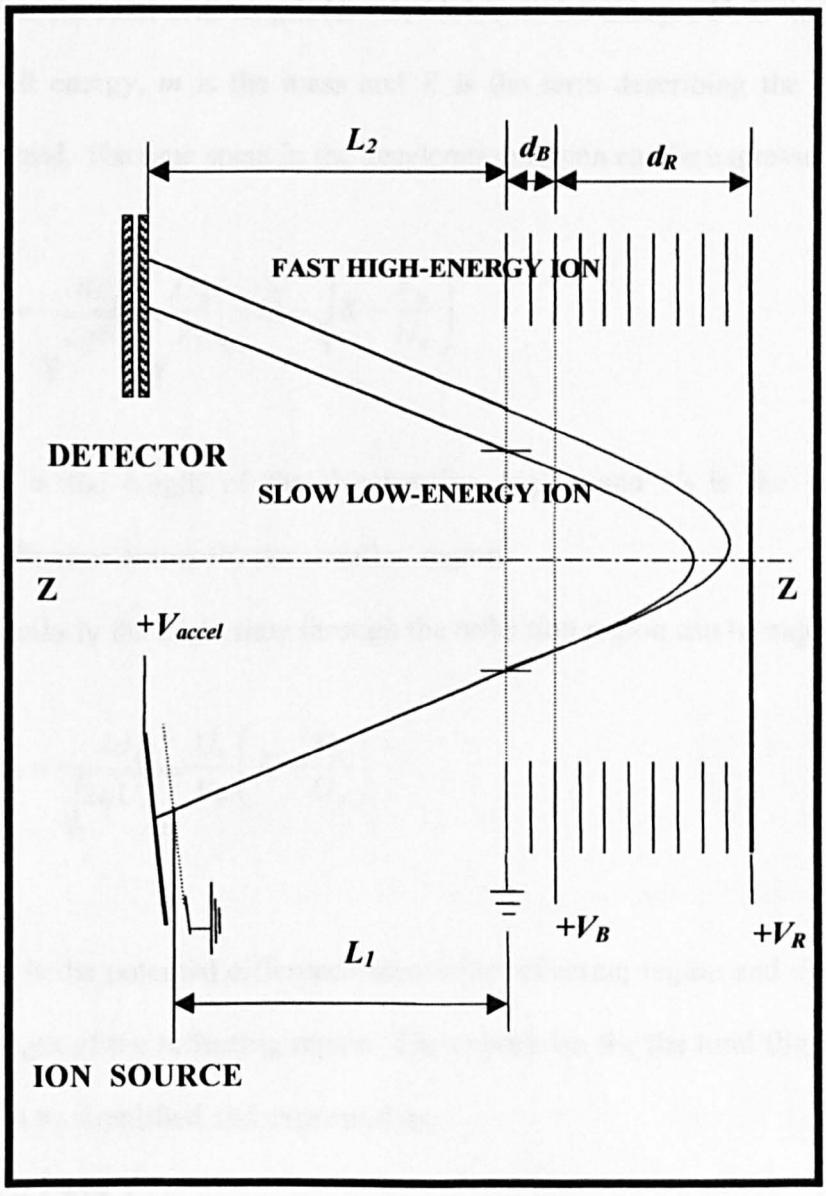

Fig. 8: Schematic diagram of a two-stage ion mirror.

The time spent in the drift region can be expressed as:

$$t_L = \frac{L}{\sqrt{2qU_0/m}} \frac{1}{\sqrt{K}} \quad 1.59$$

L is the total drift length ($L = L_1 + L_2$), q is the charge, U_0 is the mean drift energy, m is the mass and K is the term describing the energy spread. The time spent in the deceleration region can be expressed as:

$$t_B = \frac{4d_B}{\sqrt{2qU_0/m}} \frac{U_0}{V_B} \left(\sqrt{K} - \sqrt{K - \frac{V_B}{U_0}} \right) \quad 1.60$$

d_B is the length of the deceleration region and V_B is the voltage difference across the deceleration region.

Similarly the flight time through the reflection region can be expressed as:

$$t_R = \frac{4d_R}{\sqrt{2qU_0/m}} \frac{U_0}{V_R} \left(K - \frac{V_B}{U_0} \right) \quad 1.61$$

V_R is the potential difference across the reflecting region and d_R is the length of the reflecting region. The expression for the total flight time can be simplified and expressed as:

$$t = CF(K) \quad 1.62$$

Where:

$$F(K) = \frac{A_1}{\sqrt{K}} + nA_1 \left(\sqrt{K} - \sqrt{K - p} \right) + \sqrt{K - p} \quad 1.63$$

$$C = \frac{4d_B}{\sqrt{2qU_0/m}} \frac{U_0}{V_R} \quad 1.64$$

$$A_1 = \frac{L}{4d_R}\frac{V_R}{U_0} \qquad n = \frac{4d_B}{L}\frac{U_0}{V_B} \qquad p = \frac{V_B}{U_0} \tag{1.65}$$

The total flight time, t, is function of four instrument parameters:

$$t = t\left(\frac{d_B}{L};\frac{d_R}{L};\frac{V_R}{U_0};\frac{V_B}{U_0}\right) \tag{1.66}$$

To achieve second-order time focusing the following criteria must be fulfilled. The flight time must be independent of energy:

$$\left(\frac{dt}{dU}\right)_{U=U_0} = 0 \qquad \left(\frac{d^2t}{dU^2}\right)_{U=U_0} = 0 \tag{1.67}$$

The two-stage ion mirror is the most commonly used energy compensation device. The majority of commercial instrumentation companies use two-stage ion mirrors.

The first instrument was constructed by Mamyrin and co-workers [11]. The instrument had an effective drift length of 1.6 m and used an electron impact ion source with an extraction voltage of 300 V. The instrument attained mass resolving powers (FWHM) of 2400-3500. The two-stage ion mirror has been developed and improved over recent years. Yang and Reilly [23] have reported achieving a mass resolution of 11,000 for ions produced by UV laser desorption. The mass resolving power was in part due to a novel source configuration,

which used a total internal reflection prism to minimise ionisation volume. Bergmann *et al* [24][25][26] reported achieving a mass resolving power of 35,000 for cesium atoms (6 m drift length). Schlag and co-workers [27] have reported achieving a mass resolving power of 6,500 for angiotensin (*m/z* 1295). The high resolution was partially due to the ionisation method: the analyte was laser desorbed into a molecular beam, before being ionised by a second laser. The supersonic beam resulted in cooling of the translational degrees of freedom thus minimising energy spread. Della-Negra and Le Beyec [28] constructed a coaxial two-stage instrument using a ^{252}Cf plasma desorption ion source. The authors reported achieving mass resolving powers of 4,500 for Cs^+, and 5,000 for nigericine (*m/z* 769).

1.13 Gridless Ion Mirrors and Spatially Focussing Ion Mirrors.

Spatially focusing ion mirrors currently represent the maximum obtainable performance in terms of sensitivity. The gridless ion mirror, as its name suggests, has no field defining grids. There are several problems with meshed electrodes:

1) Reduced ion transmission due to ions colliding with grid wires.
2) Reduced ion transmission because of grid micro-optics/micro-lensing.
3) Reduced mass resolving power.

The field-sustaining electrodes of grid-free ion mirrors are used to shape the electrostatic field. The field generated by grid-free ion mirrors is inhomogenous, and therefore the behaviour of the ions can

no longer be described using simple mathematics. The electric field and time-of-flight of the ion must be modelled using suitable ray-tracing software.

Wollnik and co-workers [29] have designed and constructed a gridless ion mirror capable of simultaneous temporal and spatial focusing. The reflectron possessed cylindrical symmetry. Conical shaped, field-sustaining electrodes formed a spatially focusing electrostatic field at the entrance to the ion mirror. The instrument achieved mass resolving powers of 3,500 for xenon isotopes. Wollnik and co-workers [30] have described similar gridless ion mirrors capable of mass-resolving powers of 15,000-28,000.

1.14 Tandem Time-of-Flight Mass Spectrometers and Multiple Reflection Instruments.

Tandem time-of-flight spectrometers and multiple reflection time-of-flight instruments are uncommon. Tandem instruments are designed to select a precursor ion, fragment it and analyse the fragments. The process can give invaluable structural information about the precursor species. The only widely available, commercial time-of-flight instruments capable of fragment analysis are those configured for metastable/post-source decay (PSD). Multiple reflection instruments and tandem geometry instruments, remain the domain of the specialised research laboratory. Multiple reflection instruments are used for two reasons:

1) They increase the length of the field-free regions without significantly increasing the dimensions of the vacuum chamber. The longer flight path results in increased time dispersion and mass resolving power.
2) Twin reflection instruments are suitable for high-energy collision-induced dissociation and photo-induced dissociation.

Su [31] has described the construction of a parallel plate time-of-flight analyser. The instrument consisted of two gridded, two-stage ion mirrors. Figure 9 shows a schematic diagram of the instrument constructed by Su. The instrument used an electron impact ion source and achieved mass resolving powers of 3,500 for rubidium cations. Su reported that the maximum number of reflections before signal was undetectable was 4.

Piyadasa *et al* [32] have described the construction of a twin ion mirror instrument, in which the mirrors faced each other in a coaxial configuration. Figure 10 shows a schematic diagram of the instrument described by Piyadasa *et al.* The ion source was located behind one ion mirror, while the detector was positioned behind the other. In order to allow the ions to enter the time-of-flight spectrometer the mirrors were pulsed. The first ion mirror was grounded, and then switched to high-voltage in order to allow the ions into the spectrometer. The ions were then allowed to traverse backwards and forwards between both ion mirrors, before the second mirror was grounded in order to allow the ions to be detected. The technique resulted in a limited mass range being observable and complex mass

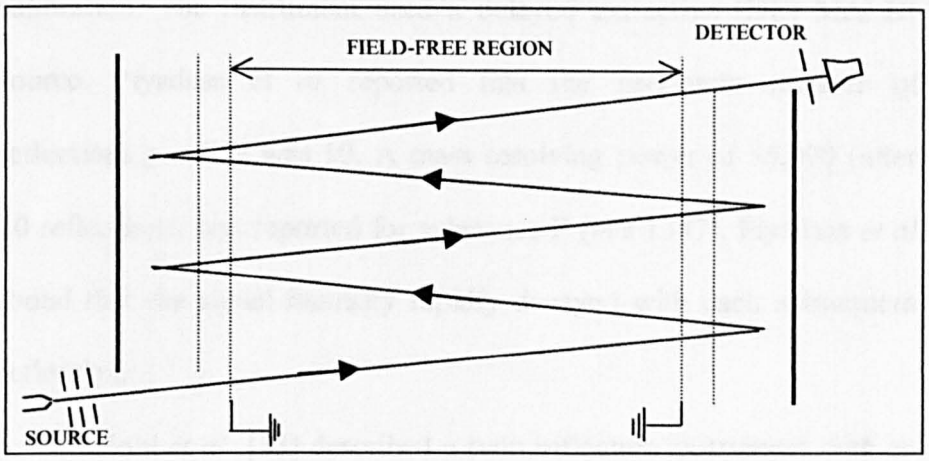

Fig. 9: Schematic diagram of the parallel plate time-of-flight instrument designed by Su [31].

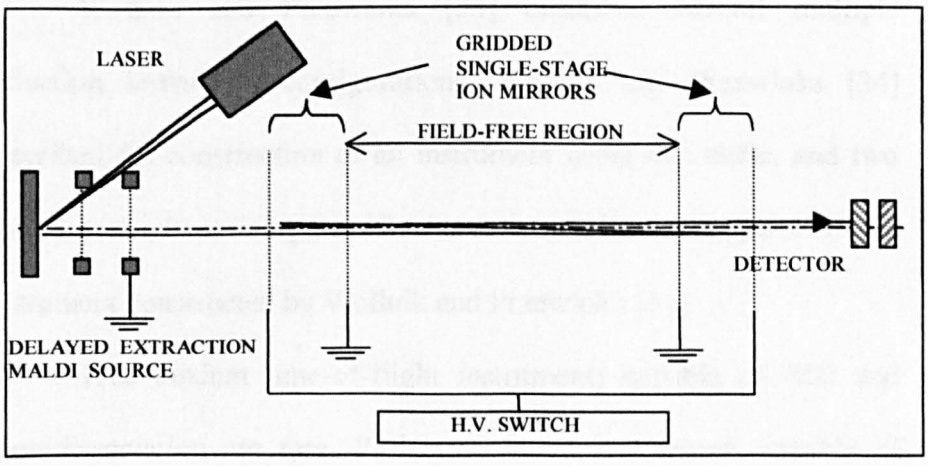

Fig. 10: Schematic diagram of the twin coaxial ion mirror time-of-flight spectrometer designed by Piyadasa *et al* [32].

calibration. The instrument used a delayed extraction (DE) MALDI source. Piyadasa *et al* reported that the maximum number of reflections possible was 10. A mass resolving power of 55,000 (after 10 reflections) was reported for substance P (*m/z* 1347). Piyadasa *et al* found that the signal intensity rapidly decayed with each subsequent reflection.

Hohl *et al* [33] described a twin reflectron instrument with an electron impact ion source, for use in spacecraft. The instrument achieved three reflections through use of an inhomogenous, two-stage, grid-free ion mirror and a specially designed "hardmirror".

Figure 11 shows a schematic diagram outlining the operating principles of the instrument.

Wollnik and Przewloka [34] described several multiple reflection instrument configurations. Wollnik and Przewloka [34] described the construction of an instrument using one static, and two pulsed ion mirrors. Figure 12 shows a schematic diagram of the instrument constructed by Wollnik and Przewloka [34].

True tandem time-of-flight instruments capable of CID and photodissociation are rare. Reflectron based instruments capable of analysing metastable/PSD fragments are commonly used [35][36][37]. PSD instruments, although not true tandem instruments are the simplest forms of time-of-flight spectrometer capable of analysing fragment species. Typical PSD instruments are configured as follows:

1) MALDI ion source.

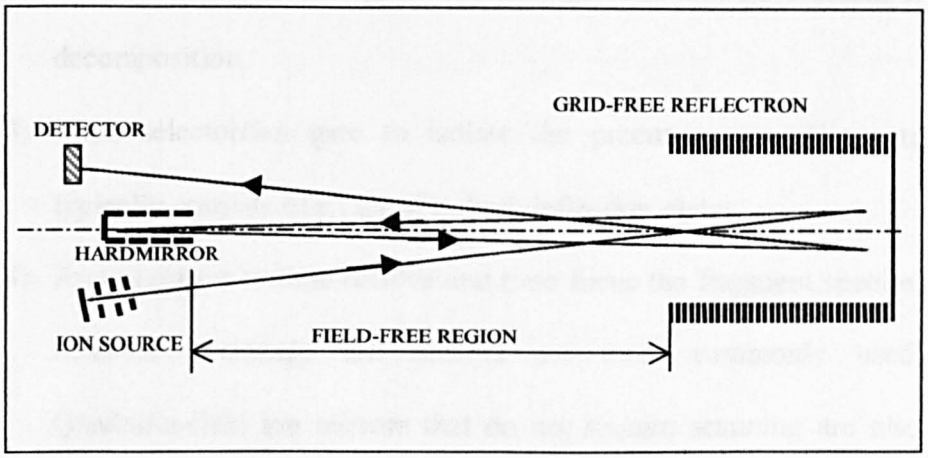

Fig. 11: Schematic diagram showing the principle of operation of the multiple reflection time-of-flight spectrometer designed by Hohl *et al* [33].

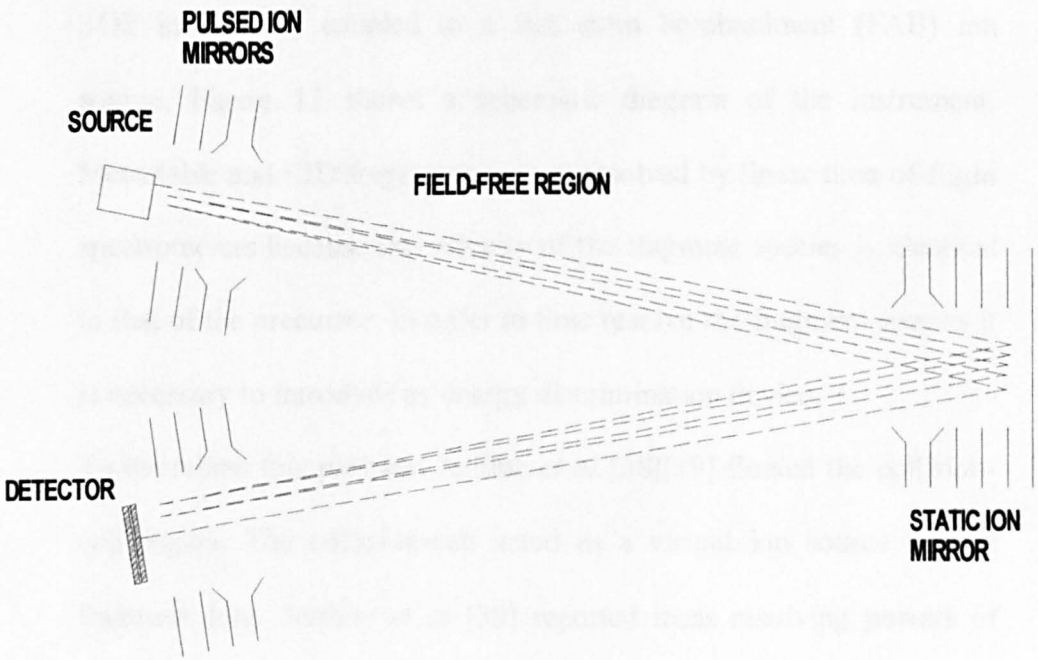

Fig. 12: Schematic diagram showing the principle of operation of the multiple reflection time-of-flight spectrometer designed by Wollnik and Przewloka [34].

2) Short field-free drift region in which species undergo metastable decomposition.
3) Mass selector/ion gate to isolate the precursor ion. The gate typically consists of a pair of pulsed deflection plates.
4) An ion mirror to time resolve and time focus the fragment species. Scanned two-stage ion mirrors are most commonly used. Quadratic-field ion mirrors that do not require scanning are also used, but are less common.

The simple addition of a gate to most reflectron instruments means that they can be used for metastable fragment analysis.

Jardine *et al* [38][39] have described a linear TOF/CID/linear TOF instrument, coupled to a fast atom bombardment (FAB) ion source. Figure 13 shows a schematic diagram of the instrument. Metastable and CID fragments are not resolved by linear time-of-flight spectrometers because the velocity of the fragment species is identical to that of the precursor. In order to time resolve the fragment species it is necessary to introduce an energy discrimination device.

To overcome this problem Jardine *et al* [38][39] floated the collision-cell region. The collision-cell acted as a virtual ion source for the fragment ions. Jardine *et al* [38] reported mass resolving powers of 100-300 (FWHM) for precursor ions and a mass resolving power of 14 for fragment species.

Cooks and co-workers [40] described a linear TOF/surface-induced dissociation (SID)/linear TOF instrument. The first linear TOF spectrometer time separated and selected the precursor ion. The second

linear TOF instrument time resolved the fragment species. The instrument used the same operating principles as those used by Jardine *et al* [38]. The SID region was floated and acted as a virtual ion source for the fragment species. Figure 14 shows a diagram of the instrument constructed by Cooks and co-workers [40].

Williams *et al* [41] have described the construction of a SID tandem time-of-flight instrument using a modified ion mirror. The mirror did not operate as an energy compensation device. Instead, the reflectron was adapted to form a deceleration/re-acceleration stage, providing time separation of the fragment species. The authors reported a fragment mass resolution of 65. Figure 15 shows a schematic diagram of the instrument built by Williams *et al* [41].

Photodissociation experiments using time-of-flight spectrometers of various configurations are not uncommon. Several groups have described the construction and use of linear time-of-flight/photodissociation/linear time-of-flight spectrometers. Brucat *et al* [42] have described the construction of a linear time-of-flight spectrometer coupled to a pulsed orthogonal time-of-flight spectrometer. Figure 16 shows a schematic diagram of the instrument constructed by Brucat *et al.* The instrument used a cluster ion source.

Bloomfield *et al* [43][44] have constructed a linear TOF/photodissociation/linear TOF instrument. Figure 17 shows a schematic diagram of the photodissociation spectrometer built by Bloomfield *et al.* The instrument used a floated photodissociation region to provide temporal separation of the fragment species.

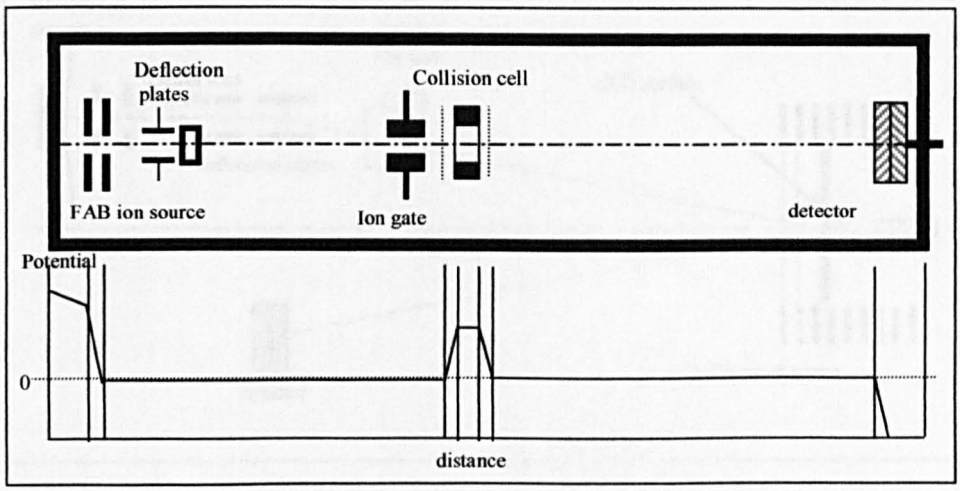

Fig 13: Schematic diagram of the linear TOF/CID/linear TOF instrument constructed by Jardine *et al* [38].

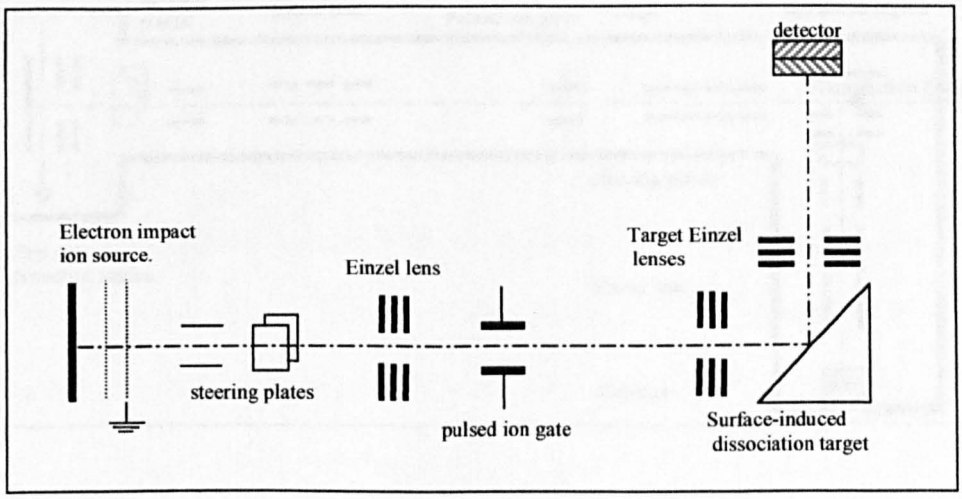

Fig. 14: Schematic diagram of the linear TOF/SID/linear TOF instrument constructed by Cooks and co-workers [40].

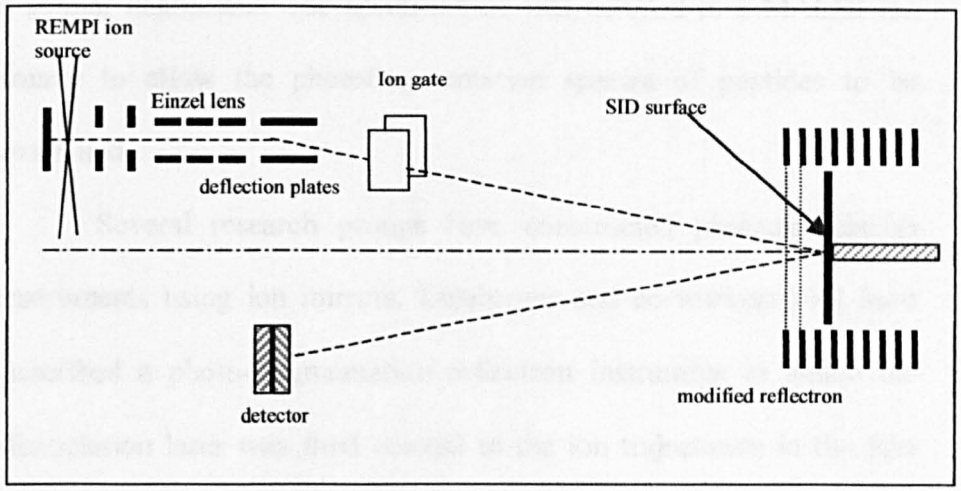

Fig. 15: Schematic diagram of the SID instrument constructed by Williams *et al* [41].

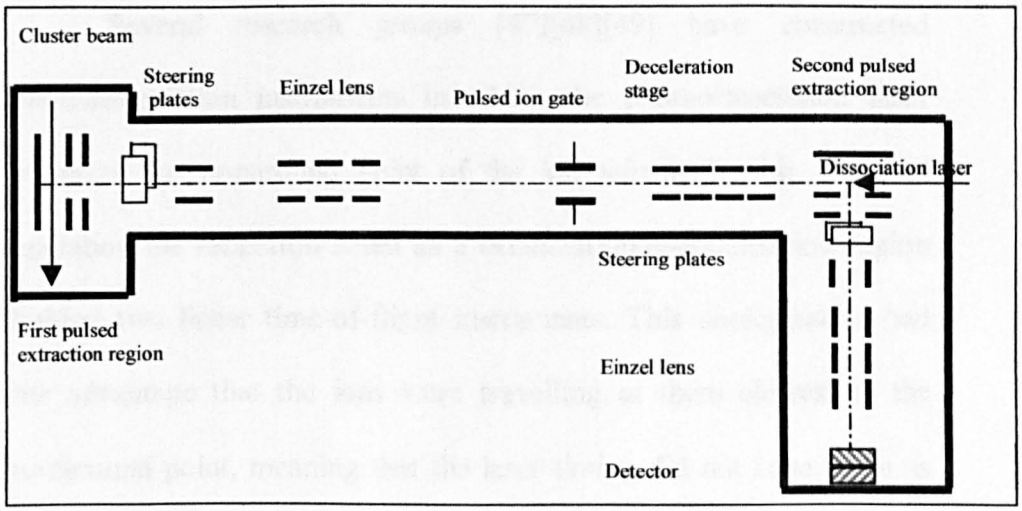

Fig.16: Schematic diagram of the linear TOF /photodissociation/ orthogonal TOF instrument designed by Brucat *et al* [42].

Russell and co-workers [45] have described the construction of a similar instrument. The spectrometer was coupled to a MALDI ion source to allow the photofragmentation spectra of peptides to be examined.

Several research groups have constructed photodissociation instruments using ion mirrors. Lineberger and co-workers [46] have described a photo-fragmentation reflectron instrument in which the dissociation laser was fired coaxial to the ion trajectories in the first field-free region. This effectively meant that there was no mass separation prior to photodissociation. The ion mirror mass separated the fragment ions from the parent ions. Figure 18 shows a schematic diagram of the instrument configuration. The authors reported achieving mass resolving powers of less than 50.

Several research groups [47][48][49] have constructed photodissociation instruments in which the photodissociation laser traverses the turnaround point of the ion mirror. In this mode of operation the reflectron acted as a deceleration/re-acceleration region linking two linear time-of-flight instruments. This configuration had the advantage that the ions were travelling at there slowest at the turnaround point, meaning that the laser timing did not have to be as precise. Singal and co-workers [49] reported achieving fragment ion mass resolutions of 60. Figure 19 shows a schematic diagram of this instrument configuration.

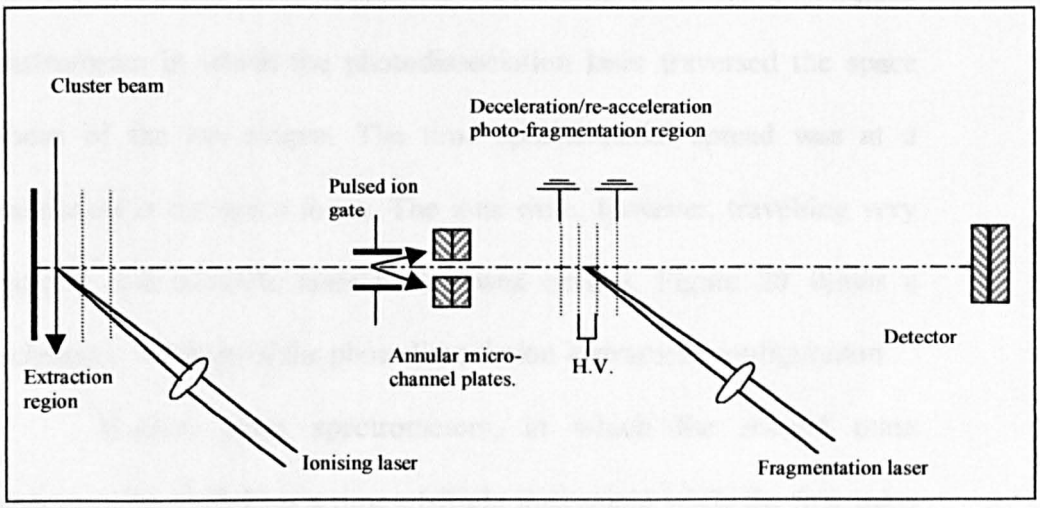

Fig. 17: Schematic diagram of the linear TOF/photodissociation/linear TOF instrument constructed by Bloomfield *et al.*

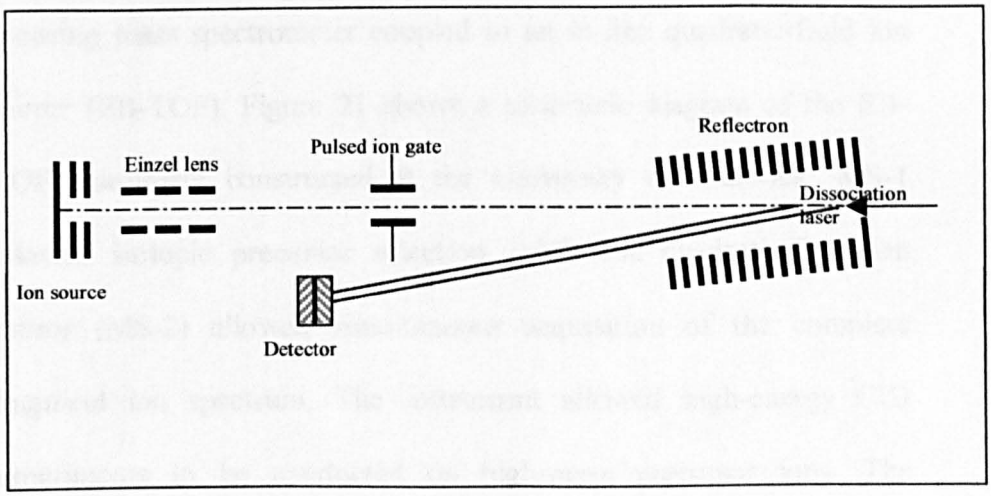

Fig. 18: Schematic diagram of the photodissociation instrument constructed by Lineberger and co-workers.

Weinkauf *et al* [50] and Alexander *et al* [51] designed instruments in which the photodissociation laser traversed the space focus of the ion source. The time spread/spatial spread was at a minimum at the space focus. The ions were, however, travelling very quickly and accurate laser timing was critical. Figure 20 shows a schematic diagram of the photodissociation instrument configuration.

Tandem mass spectrometers, in which the second mass spectrometer (MS-2) is a time-of-flight instrument while the first mass analyser (MS-1) uses a different mass separation principle, are becoming more common. Included among these are magnetic sector instruments coupled to time-of-flight analysers. Derrick and co-workers [52] have constructed an instrument consisting of a double-focusing mass spectrometer coupled to an in-line quadratic-field ion mirror (EB-TOF). Figure 21 shows a schematic diagram of the EB-TOF instrument constructed at the University of Warwick. MS-1 allowed isotopic precursor selection, while the quadratic-field ion mirror (MS-2) allowed simultaneous acquisition of the complete fragment ion spectrum. The instrument allowed high-energy CID experiments to be conducted on high-mass precursor ions. The instrument built by Russell and co-workers [53] used the same instrument geometry as that used by Derrick and co-workers [52]. The time-of-flight analyser was, however, a single-stage ion mirror. The instrument constructed by JEOL (JEOL USA Inc.) [54][55] was similar, but used a reverse geometry (magnetic sector/electrostatic sector) spectrometer coupled to a coaxial, curved-field ion mirror.

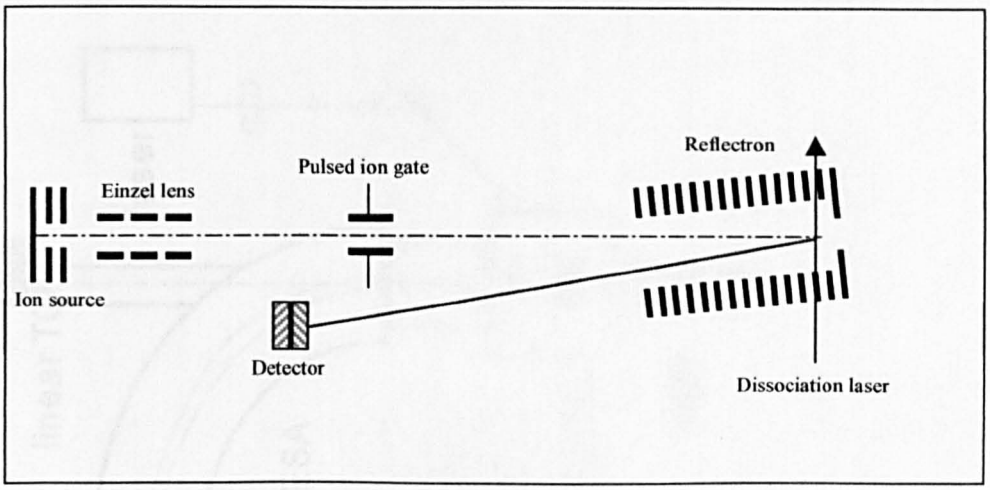

Fig. 19: Schematic diagram of a photodissociation instrument in which the laser traverses the turnaround point.

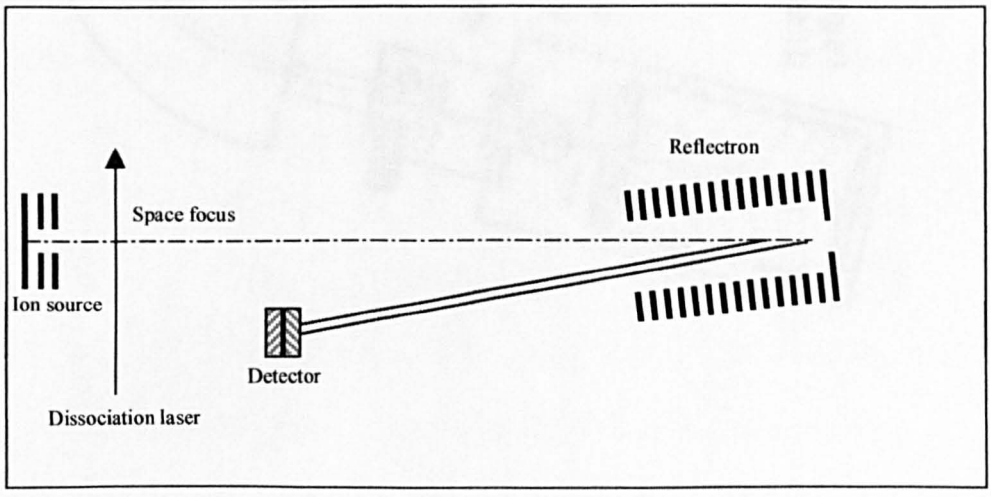

Fig. 20: Schematic diagram showing the instrument configuration used Alexander *et al* [51] and Weinkauf *et al* [50].

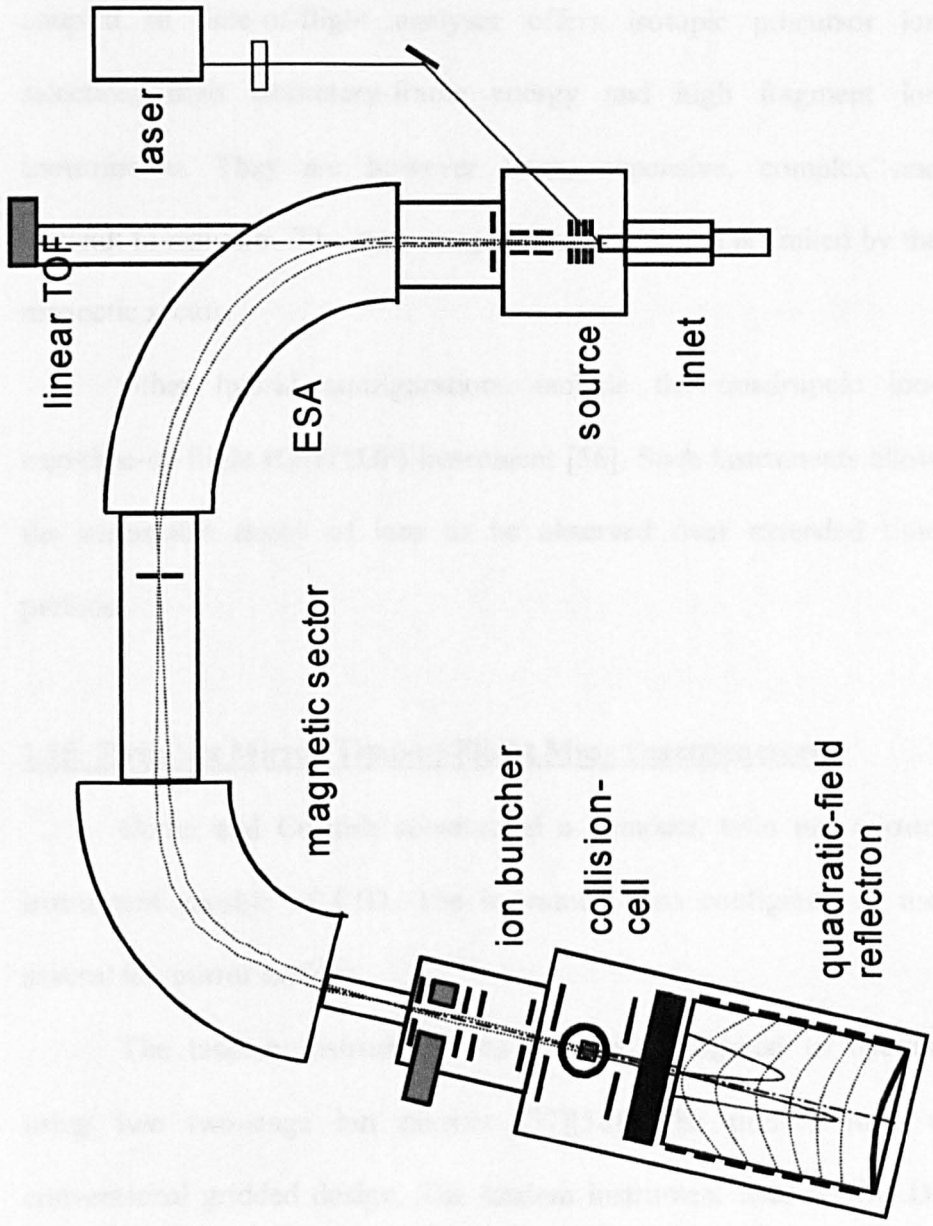

Fig. 21 Schematic diagram of the EB-TOF instrument constructed by Derrick and co-workers [52].

The hybrid configuration of double-focusing mass spectrometer coupled to time-of-flight analyser offers isotopic precursor ion selection, high laboratory-frame energy and high fragment ion transmission. They are however large, expensive, complex and difficult to maintain. The mass range of the instrument is limited by the magnetic sector.

Other hybrid configurations include the quadrupole ion-trap/time-of-flight (QIT/TOF) instrument [56]. Such instruments allow the metastable decay of ions to be observed over extended time periods.

1.15 Twin Ion Mirror Time-of-Flight Mass Spectrometers.

Cotter and Cornish constructed a compact, twin ion mirror, instrument capable of CID. The instrument was configured to use several ion mirror designs.

The tandem instrument was initially configured to operate using two two-stage ion mirrors [57][58]. The mirrors used a conventional gridded design. The tandem instrument used a MALDI ion source with a 600 ps pulse-width nitrogen laser. The laser beam was incident on the probe tip at an angle of 6°. The source was a standard single-stage design using conventional Einzel lenses and steering electrodes.

The instrument was housed in a compact, aluminium coffin vacuum chamber: 32 inch (length) x 8.4 inch (width) x 6 inch (depth).

The instrument used an accelerating voltage of 4 kV. The mirror axes were tilted at 3° with respect to the ion optical axis. The data acquisition system used 1 Gsample/s transient recorder/digital oscilloscope with a bandwidth of 500MHz. The collision region used a pulsed valve to introduce collision gas. Ion selection was achieved through use of a pair of pulsed deflection plates. The tandem two-stage ion mirror spectrometer was reported to achieve mass resolving powers of 800-1500 for low molecular-weight matrix and laser dye species. Cotter and Cornish reported mass resolving powers of 1600 (dermenkephalin: MW 954), 2300 (enkephalin: MW 573) and 1700 (proenkephalin MW 899) for low molecular-weight analyte species. Initial CID results [59] with rhodamine (m/z=429) showed that the fragment ion resolution was poor, though no explicit value was quoted. Less than 50% of the fragment mass range was detectable.

Cotter and Cornish [60] commented that the sensitivity of the tandem instrument to metastable species, such as peptides, was low. Cotter and Cornish believed the problem to be caused by the ion mirrors. Cotter and Cornish [60] subsequently re-designed the mirror configuration and replaced both mirrors with conventional gridded, single-stage reflectron mirrors. Cotter and Cornish [60] reported mass resolving powers of 9,000-11,000 for parent ion species gramicidin S and rhodamine 6G. Fragment resolution of up to 1000 was reported for rhodamine 6G. The mass calibration of the fragment spectrum for single-stage ion mirrors was shown to be a simple linear function. The disadvantage of using a single-stage ion mirror, was that it was

incapable of simultaneously time focusing the entire fragment mass spectrum at the detector plane. The mass resolving power therefore decreased with decreasing fragment mass.

To solve this problem, Cotter and Cornish replaced the second mirror with a curved-field reflectron [61][62][63]. The curved-field reflectron was capable of simultaneously time focusing 90 % [64] of the fragment mass range, thereby reducing the need to scan the mirror voltage. Cotter and Cornish [61] reported achieving fragment mass resolving powers of 1000 across the majority of the fragment mass range.

Cotter and co-workers [65] have published CID spectra obtained for C_{60} using a single-stage/curved-field ion mirror, tandem time-of-flight spectrometer. These results can be compared with the CID results obtained from the TOF-TOF instrument outlined in subsequent chapters. Cotter and co-workers reported mass resolving powers of 2000 (FWHM), for $C_{60}^{+\cdot}$ generated by MALDI (matrix-assisted laser desorption/ionisation). This compared with resolving powers of 6000-7000 (FWHM) for ions generated using LDI (laser desorption/ionisation) on the TOF-TOF spectrometer constructed at the University of Warwick. Visual inspection of the spectra published by Cotter and co-workers showed that the signal-to-noise ratio was considerably better than that achieved on the TOF-TOF spectrometer constructed at the University of Warwick. A comparison of the CID results, using argon as the collision gas, showed:

1) The spectra were qualitatively similar.

2) The detectable fragment mass range of the TOF-TOF instrument at the University of Warwick was slightly superior to that of the Cotter/Cornish TOF-TOF spectrometer. Low-mass fragments ($m/z<C_9^{+\cdot}$) were detectable on the TOF-TOF instrument at the University of Warwick.

3) The fragment sensitivity of the instrument constructed by Cotter and Cornish was superior. The authors reported that a CID spectrum could be obtained by averaging 100-200 individual spectra. To acquire a reasonable quality CID spectrum using the TOF-TOF spectrometer constructed at the University of Warwick required ion-counting for 45-60 minutes, at a laser firing frequency of 2-3 Hz (5,400-10,800 individual spectra). The characteristics of the two TOF-TOF instruments are summarised below:

Property	Cornish/Cotter TOF-TOF.	TOF-TOF at the University of Warwick
Ion source	Single-stage MALDI source	Single-stage MALDI source
Laser type	600 ps pulse-width nitrogen laser	4 ns pulse-width nitrogen laser
Data acquisition system	1 Gsample/s transient recorder/digital oscilloscope (500 MHz bandwidth)	1 Gsample/s transient recorder/digital oscilloscope (500 MHz bandwidth)
Mirror configuration	Twin two-stage ion mirrors. Twin single-stage ion mirrors. Single-stage ion mirror and curved-field ion mirror.	Single-stage ion mirror and quadratic-field ion mirror.
Accelerating voltage	+4 kV	+10-15 kV
Detectors	3 chevron micro-channel plate detectors.	3 chevron micro-channel plate detectors.
Post-acceleration	-5 kV	-1.8 kV

Collision region	Pulsed valve	Differentially pumped region with apertures.
Mirror construction	68 field-sustaining electrodes used in both the single-stage and curved-field ion mirror.	17 field-sustaining electrodes used in the single-stage ion mirror and 28 in the quadratic ion mirror.

Table 1.1

Beussman *et al* [66] have described the construction of a tandem reflectron instrument designed for photo-induced dissociation (PID). The instrument was similar to that described by Cotter and Cornish. The source consisted of a gas chromatograph (GC) coupled to a pulsed extraction electron impact ion source. Beussman *et al* used a grid-free, spatially focusing ion mirror for the first reflectron. The dissociation laser interacted with the ions at the temporal focus of the first ion mirror. An acceleration region, located after the PID region, facilitated mass dispersion of the product ions. The second ion mirror was an unconventional gridded, two-stage ion mirror capable of simultaneously time focusing a broad energy range [67]. Beussman *et al* [61] reported achieving fragment mass resolving powers of up to 300.

1.16 Laser Ion Sources.

The wider utilisation of mass spectrometry as an analytical tool is dependent upon advances in instrumentation and ionisation techniques. Each new method of producing gaseous ions results in new classes of chemical compounds being analysed by mass spectrometry. A significant problem with early ionisation techniques, such as electron impact and chemical ionisation, was their inability to form

ions from non-volatile, labile, high-mass analytes. The advent of new ionisation techniques has meant that new classes of high molecular-weight compounds can be analysed by mass spectrometry. Amongst these techniques are thermospray ionisation (TI)[68], field desorption (FD)[69], secondary ion mass spectrometry (SIMS)[70][71], plasma desorption (PD)[72], fast atom bombardment (FAB)[73], electrospray ionisation (ESI)[74], laser desorption (LD)[75] and matrix-assisted laser desorption/ionisation (MALDI)[17][18].

1.17 Laser Desorption and Laser Ionisation Mass Spectrometry

Mayman constructed the first chromium-doped ruby laser in 1960. The first application of laser radiation for ion generation took place in 1963 [76]. Laser assisted methods of evaporation and ionisation become commercially widespread with the availability of the LAMMA (Leybold-Heraeus GmbH) and LIMA (Cambridge Mass Spectrometry Ltd.) instruments. The pulsed nature of laser ion sources meant they were ideally suited to time-of-flight spectrometers.

The introduction of matrix-assisted laser desorption/ionisation (MALDI) by Karas and Hillenkamp [18] and Tanaka *et al* [17] dramatically increased the commercial and research interest in pulsed laser ion sources coupled to time-of-flight instruments. Along with electrospray ionisation, MALDI is the now amongst the most important ionisation techniques for the study of high-mass, non-volatile compounds. The MALDI technique has been applied to a wide range of

analyte species, including proteins, peptides, synthetic polymers and fullerenes.

The MALDI technique encompasses a wide range of sample preparation protocols, laser wavelengths, pulse energies and pulse duration. The MALDI ionisation mechanism is unlikely to be one, single mechanism. The MALDI mechanism was for many years poorly understood, and it is only in recent years that a large number of experiments have been conducted to determine the properties of MALDI generated ions and the mechanism by which they are produced. Even now practitioners lack a complete understanding of the MALDI process. The ionisation mechanism remains less well understood than the desorption/ablation mechanism. It is possible to summarise the general conditions for UV MALDI:

1) An organic matrix species that absorbs strongly at the laser frequency is used to absorb laser radiation. The matrix is typically a benzoic acid or cinnamic acid derivative. The matrix is co-crystallised with the analyte species. The matrix is usually in excess, typically 1000:1, matrix:analyte.
2) The most commonly used laser system is the nitrogen laser (337nm), with a pulse-width of several hundred picoseconds to twenty nanoseconds. Harmonics of Nd:YAG lasers are used in research laboratories with specialist equipment (Nd:YAG x 3 =355 nm and Nd:YAG x 4 = 266 nm).

Zenobi and Knochenmuss [77] have published a thorough review of the subject field and discussed the evidence for the postulated mechanisms.

1.18 Collision-Induced Dissociation

Collision-induced dissociation (CID), also referred to as collision-activated decomposition (CAD), has proved an invaluable tool for the structural elucidation of a large range of chemical compounds.

CID of polyatomic ions is believed to involve a two step process [78][79]. The first step involves the activation of the AB^+ analyte ion through collision with the neutral collision gas G. The second step involves the unimolecular dissociation of the analyte.

$$AB^+ + G \longrightarrow (AB^+)^* + G^*$$

$$(AB^+)^* \xrightarrow{K(E),\ P(E)} A^+ + B$$

The rate of the dissociation step is determined by the unimolecular rate constant, *k(E)*, and the internal energy distribution, *P(E)*. The collision interaction time is short in comparison with the dissociation-time. During this time delay the internal energy acquired during the collision is redistributed among the internal degrees of freedom of the ion. The energy of the collision and the extent of subsequent redistribution of internal energy prior to fragmentation are key to understanding the CID of polyatomic species.

Durup [80] classified the possible collisional energy transfer processes as follows:

(1) Electronic excitation (vertical transition), predominant at high energy.

(2) Elastic scattering off one single atom of the ion.

(3) Internal energy transfer in a long-lived ion-molecule complex, probable only at low energies

(4) Perturbation to an excited species which leads to a transition to a repulsive electronic state resulting in dissociation.

Bricker and Russell [81] examined the collision-induced dissociation of chlorophyll α ion using different noble gases. They noted that the translational energy loss of the ions decreased through He to Kr. They correlated this effect with the ionisation energy of the collision gas and suggested that the excitation of the target gas played an important role. Sheil and Derrick [82] subsequently showed that the correlation was not valid for all collision gases. Uggerud and Derrick [83] developed the impulsive collision theory (ICT) for use in mass spectrometry. ICT recognised the importance of the mass of the collision gas. ICT assumed that energy and momentum transfer took place between the target gas atom and a single atom within the ion. The atoms involved in the collision were considered to be hard spheres, i.e. uncompressible.

The maximum energy available for transfer to the internal degrees of freedom can be expressed as:

$$E_{cm} = \frac{m_g}{m_g + m_{ion}} E \qquad 1.68$$

E_{cm} is the centre-of-mass collision energy, m_g is the mass of the target gas, m_{ion} is the mass of the ion and E is the laboratory-frame kinetic energy. ICT relates the scattering angle to the impact angle. Figure 22

shows a diagram illustrating the impact angle. The scattering angle can be expressed as:

$$\tan\theta = \frac{2m_a m_g \cos\varphi \sin\varphi}{2m_a m_g \cos^2\varphi - m_{ion}\left(m_a - m_g\right)} \qquad 1.69$$

θ is the scattering angle, φ is the collision angle, m_a is the mass of the atom involved in the collision and m_g is the mass of the collision gas. m_{ion} is the mass of the ion. The maximum internal energy acquired by the ion during collision can be expressed as:

$$Q_{max} = 4\frac{m_a m_g}{\left(m_g + m_a\right)^2}\frac{m_g}{m_{ion}}\frac{m_{ion} - m_a}{m_{ion}}E \qquad 1.70$$

Q_{max} is the maximum possible internal energy acquired.

For high-mass ions the average internal energy, $\langle Q \rangle$, acquired can be expressed as:

$$\langle Q \rangle \approx 2\frac{m_a m_g}{\left(m_g + m_a\right)^2}E_{cm} \qquad 1.71$$

The equation predicts a proportional relationship between the centre-of-mass collision energy and average internal energy acquired during collision. To induce significant amounts of fragmentation, it is therefore necessary to use high centre-of-mass collision energies for high-mass analytes. This can be achieved by using large accelerating voltages or heavy target gases. The theory also predicts that heavier collision gases result in increased scattering. This has important implications for the sensitivity, to fragment ions, of instruments when

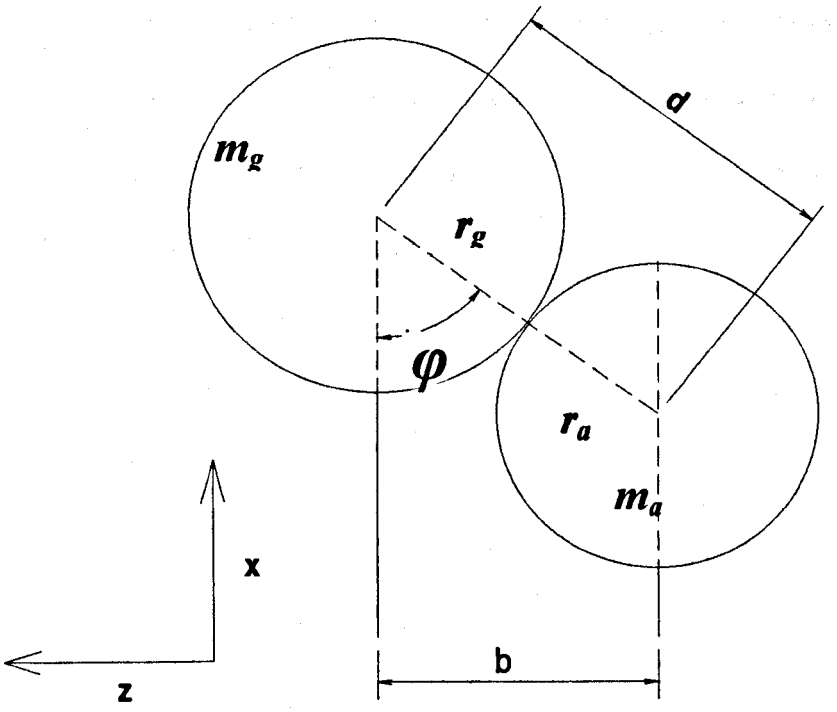

$$\mathbf{Sin}\varphi = \mathbf{b}/(r_g + r_a) = \mathbf{b}/\mathbf{d}$$

Fig. 22 Diagram showing impact angle, φ. z-axis is the ion optical axis and x-axis is the radial axis.

heavy target gases are used. This is especially true when the final mass analyser is a quadratic-field ion mirror. The defocusing nature of the electrostatic field in the ion mirror means that it is highly sensitive towards the angular deflection of the ion beam.

The statistical quasi-equilibrium theory (QET) [84] and Rice-Rampsperger-Kassel-Marcus (RRKM) theory [85][86][87][88] have described the unimolecular dissociation of collisionally activated ions. The model assumes that the molecule is a system of loosely coupled oscillators that allows energy to flow between the internal modes.

Internal energy is therefore randomised throughout the molecule ion. There is a finite probability that sufficient energy will be localised in a bond to break it, resulting in fragmentation of the molecule ion. The more internal energy present within the molecule-ion the greater the probability of the molecule-ion dissociating.

1.19 References.

[1] A. E. Cameron and D. F. Eggers, Jr., Rev. Sci. Instrum., 19 (1948) 605.

[2] M. M. Wolff and W. E. Stephens, Rev. Sci. Instrum., 24 (1953) 616.

[3] H. S. Katzenstein and S. S. Friedland, Rev. Sci. Instrum., 26 (1955) 324.

[4] W. C. Wiley and I. H. McLaren, Rev. Sci. Instrum., 26 (1955) 1150

[5] R. S. Gohlke, Anal. Chem., 31 (1959) 535.

[6] W. H. McFadden, R. Teranishi, D. R. Black, J. C. Day, J. Food Sci., 28 (1963) 316.

[7] B. E. Knox and F. J. Vastola, Chem. Eng. News, 44, No 44, 48 (1966);

[8] D. W. Thomas in D. Price and J. E. Williams (Eds.), "Time-of-Flight Mass Spectrometry", Pergamon Press, Oxford, pp. 171-210 (1969).

[9] B. A. Mamyrin, Russian Patent No. 198,034 (1966).

[10] V.I. Karataev, B. A. Mamyrin and D. V. Shmikk, Sov. Phys. – Tech. Phys., 16 (1972) 1177. English translation of a report that appeared in 1971.

[11] B. A. Mamyrin, V. I. Karataev, D. V. Shmikk and V. A. Zagulin, Sov. Phys.-JETP, 37 (1973) 45.

[12] M. A. Ivanov, B. N. Kozlov, B. A. Mamyrin, D. V. Shmikk and V. G. Shchebelin, J. Tech. Phys., 62 (1983) 2039.

[13] B. A. Mamyrin, Int. J. Mass Spectrom. Ion Processes, 131 (1994) 1.

[14] W. P. Poschenrieder, Int. J. Mass Spectrom. Ion Phys., 9 (1972) 357.

[15] D. F. Togerson, R. P. Skowronski and R. D. Macfarlane, Biochem. Biophys. Res. Commun., 60 (1974) 616.

[16] M. A. Posthumus, P. G. Kistemaker, H. L. C. Meuzelaar and M. C. Ten Noever de Brauw, Anal. Chem., 50 (1978) 985.

[17] K. Tanaka, H. Waki, Y. Ido, S. Akita, Y. Yosida, T. Yoshida, Rapid Commun. Mass Spectrom., 2, (1988)151

[18] M. Karas and F. Hillenkamp, Anal. Chem., 60 (1988) 2299.

[19] R. Weinkauf, K. Walter, C. Weickhardt, U. Boesl and E. W. Schlag, Z. Naturforsch., A, 44 (1989)1219.

[20] U. Boesl, R. Weinkauf, C. Weickhardt and E. W. Schlag, Int. J. Mass Spectrom. Ion Proc., 131 (1994) 87.

[21] S. G. Alikhanov, Sov. Phys. -JETP, 4 (1957) 452.

[22] X. Tang, R. Beavis, W. Ens, B. Lafortune, B. Schueler and K. G. Standing, Int. J. Mass Spectrom. Ion Processes, 85 (1988) 43.

[23] M. Yang and J. P. Reilly, Int. J. Mass Spectrom. Ion Processes, 75 (1987) 209.

[24] T. Bergmann, T. P. Martin and H. Schaber, Rev. Sci. Instrum., 61 (1990) 2592.

[25] T. Bergmann, T. P. Martin and H. Schaber, Rev. Sci. Instrum., 60 (1989) 347.

[26] T. Bergmann, T. P. Martin and H. Schaber, Rev. Sci. Instrum., 60 (1989) 792.

[27] U. Boesl, J. Grotemeyer, K. Walter and E. W. Schlag, Anal. Instrum., 16 (1987) 151.

[28] S. Della-Negra and Y. Le Beyec, Int. J. Mass Spectrom. Ion Processes, 61 (1984) 21.

[29] R. Kutscher, R. Grix. G. Li and H. Wollnik, Int. J. Mass Spectrom. and Ion Processes, 103 (1991) 117.

[30] R. Grix, R. Kutscher, G. Li, U. Gruner and H. Wollnik. Rapid Commun. Mass Spectrom., 2 (1988) 83.

[31] Ching-Shen Su, Int. J. Mass Spectrom. Ion Processes, 88 (1988) 21.

[32] C. K. G. Piyadasa, P. Hakansson and T. R. Ariyaratne, Rapid. Commun. Mass Spectrom., 13 (1999) 620.

[33] M. Hohl, P. Wurz, S. Scherer, K. Altwegg and H. Balsiger, Int. J. Mass Spectrom., 188 (1999) 189.

[34] H. Wollnik and M. Przewloka, Int. J. Mass Spectrom. Ion Processes, 96 (1990) 267.

[35] B. Spengler, D. Kirsch and R. Kaufmann, J. Phys. Chem., 96 (1992) 9678.

[36] R. Kaufmann, D. Kirsch and B. Spengler, Int. J. Mass Spectrom., Ion Processes, 131 (1994) 355

[37] R. Kaufmann, B. Spengler, and F. Lutzenkirchen, Rapid Commun. Mass Spectrom., 7 (1993) 902.

[38] D. R, Jardine, J. Morgan, D. S. Alderdice and P. J. Derrick, Org. Mass Spectrom., 27 (1992) 1077.

[39] D. R. Jardine, D. S. Alderdice and P. J. Derrick, Org. Mass Spectrom. 26, (1991), 915.

[40] K. Schey, R. G. Cooks, R. Grix and W. Wollnik, Int. J. Mass Spectrom. and Ion Processes, 77 (1987) 49.

[41] E. R. Williams, L. Fang, R. N. Zare, Int. J. Mass Spectrom. Ion Processes, 123 (1993) 233.

[42] P.J. Brucat, L.-S. Zheng, C. L. Pettiette, S. Yang and R. E. Smalley, J. Chem. Phys., 84 (1986) 3078.

[43] L. A. Bloomfield, R. R. Freeman and W. L. Brown, Phys. Rev. Letts., 54 (1985) 2246.

[44] L. A. Bloomfield, M. E. Geusic, R. R. Freeman and W. L. Brown, Chem. Phys. Letts., 121, (1985) 33.

[45] M. E. Gimon-Kinsell, G. R. Kinsell, R. D. Edmondson and D. H. Russell, J. Am Soc. Mass Spectrom., 6 (1995) 578.

[46] M. A. Johnson, M. L. Alexander and W. C. Lineberger, Chem. Phys. Lett. 112 (1984) 285.

[47] K. LaiHing, P. Y. Cheng, T. G. Taylor, K. F. Willey, M. Peschke and M. A. DuncanAnal. Chem., 61 (1989) 1460.

[48] D. S. Cornett, M. Peschke, K. LaiHing, P. Y. Cheng, K. F. Willey and M. A. Duncan, Rev. Sci. Instrum., 63 (1992) 2177.

[49] W. J. Jia, K. W. D. Ledingham, C. T. J. Scott, C. Kosmidis and R. P. Singhal, Rapid Commun. Mass Spectrom., 9 (1995) 761.

[50] R. Weinkauf, K. Walter, C. Weickhardt, U. Boesl, E. W. Schlag, Z. Naturforsch., A, 44 (1989) 1219.

[51] M. L. Alexander, N. E. Levinger, M. A. Johnson, D. Ray and W. C. Lineberger, J. Chem Phys. 88, (1988) 6200.

[52] U. N. Anderson, A. W. Colburn, A. M. Makarov, E. N. Raptakis, D. J. Reynolds, P.J. Derrick and S. C. Davis, A. D. Hoffman and S. Thomson, Rev. Sci. Instrum., 69 (1998) 1650.

[53] Time-of-flight mass spectrometry, ACS symposium series, American Chemical Society,1994, Tandem Time-of-Flight Mass Spectrometry: A Magnetic Sector-Reflectron Time-of-Flight Mass Spectrometer. F. H. Strobel and D. H. Russell, pp-73

[54] C. Martin, G. Samuelson, J. Finch, V. Wysocki, A. Somogyi, Proc. 46th ASMS Conf. On Mass Spectrometry and Allied Topics, Orlando, FL, May 31-june 4, 1998, pp.1252.

[55] E. N. Nikolaev, A. Somogyi, C. Gu., L. Breci, V. H. Wysocki, J. W. Finch, C. D. Martin and G. L. Samuelson, Proc. 46th ASMS Conf. On Mass Spectrometry and Allied Topics, Orlando, FL, May 31-june 4, 1998, pp 41.

[56] V. L. Doroshenko and R. J. Cotter, J. Mass Spectrom., 3 (1998) 305.

[57] T. J. Cornish and R. J. Cotter, Rapid Commun. Mass Spectrom., 6 (1992) 242.

[58] R. J. Cotter and T. J. Cornish, (1993) US Patent No. 5,202,563.

[59] T. J. Cornish and R. J. Cotter, Anal. Chem. 65 (1993) 1043.

[60] T. J. Cornish and R. J. Cotter, Org. Mass Spectrom. 28 (1993) 1129.

[61] T. J. Cornish and R. J. Cotter, Rapid Commun. Mass Spectrom., 7 (1993) 1037.

[62] T.J. Cornish and R. J. Cotter, Rapid Commun. Mass Spectrom., 8 (1994) 781

[63] T.J. Cornish and R. J. Cotter, (1995) US Patent No: 5,464,985.

[64] M. M. Cordero, T. J. Cornish, R. J. Cotter and I. A. lys, Rapid. Commun. Mass Spectrom., 9 (1995) 1356.

[65] M. M. Cordero, T. J. Cornish and R. J. Cotter, J. Am. Soc. Mass Spectrom. 7 (1996) 590.

[66] D. J. Beussman, P. R. Vlasak, R. D. Mclane, M. A. Steerlin and C. G. Enke, Anal. Chem. 67 (1995) 3952.

[67] P. R. Vlasak, D. J. Beussman, Q. Ji and C. G. Enke, J. Am. Soc. Mass Spectrom. 7 (1996) 1002.

[68] M. L. Vestal, Int. J. Mass Spectrom. Ion Phys., 46 (1983) 193.

[69] H. D. Beckey, Field Ionization and Field Desorption Mass Spectrometry, Pergamon Press, Oxford, 1978.

[70] A. Benninghoven, D. Jaspers and W. Sichtermann, Appl. Phys., 11 (1976) 35.

[71] H. Grade and R. G. Cooks, J. Am. Chem. Soc. 100 (1978) 5615.

[72] R. D. Macfarlane, Anal. Chem. 55 (1983) 1247.

[73] M. Barber, R. S. Bordoli, G. J. Elliott, R. D. Sedgwick and A. N. Tyler, J. Chem. Soc. Chem. Commun., 7 (1981) 325.

[74] J. Fenn, M. Mann, C. K Meng and S. F. Wong, Mass Spectrom. Rev., 9 (1990) 37.

[75] M. A. Postumus, P. G. Kistemaker, H. L. C. Meuzelaar and M. C. Ten Noever de Brauw, Anal. Chem., 50 (1978) 985

[76] R. E. Honig, Sppl. Phys. Lett., 3 (1963) 8.

[77] R. Zenobi and R. Knochenmuss, Mass Spectrom. Rev. 17 (1998) 337.

[78] R. G. Cooks in Collision Spectroscopy, R. G. Cooks, Plenum Press: New York (1978), Chapter 7.

[79] K. Levsen and H. Schwarz, Mass Spectrom. Rev., 2 (1983) 77.

[80] J. Durup in "Recent Developments in Mass Spectrometry", K. Ogata, T. Hayakawa (Eds.), University Park Press, Baltimore (1970) pp 921.

[81] J. Bricker and D. H. Russell, J. Am. Chem Soc., 108 (1986) 6174.

[82] M. Sheil and P. J. Derrick, Org. Mass Spectrom., 23 (1988) 429.

[83] E. Uggerud and P. J. Derrick, J. Phys. Chem., 95 (1991) 1430.

[84] H. M. Rosenstock, M. B. Wallenstein, A. L. Wahrhaftig and H. Ehring, Proc. Natl. Acad. Sci. USA, 59 (1952) 667.

[85] R. A. Marcus and O. K. Rice J. Phys. Colloid Chem., 55 (1951) 894.

[86] O. K. Rice and H. C. Ramsperger, J. Am. Chem. Soc., 49 (1927) 1616.

[87] L. S. Kassel, J. Phys. Chem., 32 (1928) 225.

[88] R. A. Marcus, J. Chem, Phys., 20 (1952) 359.

CHAPTER TWO.

Quadratic, Parabolic, Curved and Non-Linear Ion Mirrors.

2.01 Quadratic-Field Ion Mirrors.

The potential distribution along the ion optical axis, z, in an ideal quadratic-field ion mirror can be expressed as:

$$U(z)=\frac{k}{2}(z-a)^2+C \qquad 2.01$$

This is commonly expressed in the form:

$$U(z)=\tfrac{1}{2}kz^2 \qquad 2.02$$

U is the potential along the z-axis (ion optical axis), z is the position and k, a and C are constants. The constant k is analogous to the force constant in the equation describing the simple harmonic motion of a pendulum. The constant k effectively defines the strength of the retarding force acting on the particle. Larger k values result in deeper parabolic potential wells with gradients that increase more rapidly. a defines the position on the z-axis of the potential minimum. C defines the height of the potential minimum. C is typically zero for most ion mirrors. Figure 23 shows a plot of an ideal parabolic well. The equation of motion along the z-axis can be expressed as:

$$\frac{d^2z}{dt^2}=-\frac{q}{m}k(z-a) \qquad 2.03$$

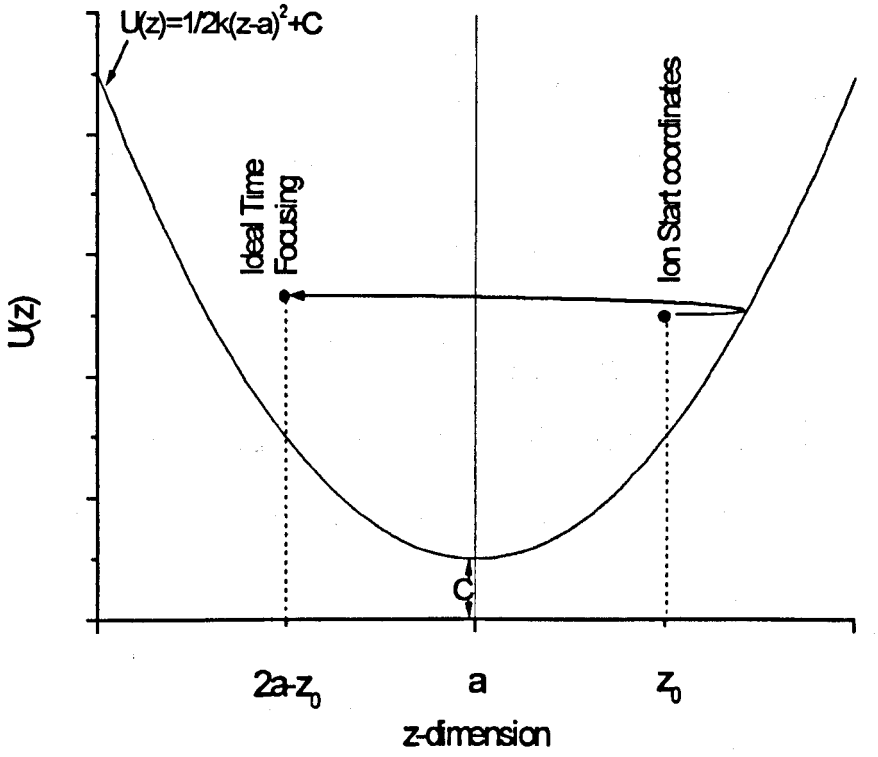

Fig. 23: Plot showing the ideal quadratic potential along the z-axis (ion optical axis). Where z_0 is the initial co-ordinate of the ion in the potential well and $2a$-z_0 is the co-ordinate of ideal time-focusing.

q is the specific charge on the ion ($q=ze$, where z is the number of charges on the ion and e is the charge on an electron.) and m is the mass of the ion.

For any real-world case $q/m>0$ and $k>0$. Making these assumptions equation 2.03 can be solved:

$$z(t) = a + (z_0 - a)\cos\omega t + \left(2\frac{V_{acc}}{k}\right)^{1/2}\sin\omega t \qquad 2.04$$

z_0 is the starting co-ordinate of the ion and V_{acc} is the accelerating potential experienced by the ion. ω, frequency of oscillation in the parabolic well, can be expressed as:

$$\omega = \left(\frac{q}{m}k\right)^{1/2} \qquad 2.05$$

From equation 2.04, after integer number of half periods:

$$T_n = \left(\frac{\pi}{\omega}\right)n \qquad n = 1,2,3..... \qquad 2.06$$

After each reflection the z co-ordinate becomes:

$$z(T_n) = a + (z_0 - a)(-1)^n \qquad 2.07$$

It can be seen that reflection, *i.e.* time-of-flight through the ion mirror, is independent of the energy, qV_{acc}, of the ion. Thus by extension the time-of-flight of the ion must be independent of the initial velocities of the ions. So far, a simple 1-dimensional model of the oscillation of a particle in a 1-dimensional potential well has been outlined. For a real 3-dimensional electrostatic field, it is necessary that the Laplace equation be satisfied without changing the fundamental nature of the potential well expressed by equations 2.01 and 2.02.

Gall *et al* [1] have shown that the above criteria are fulfilled for a 3-dimensional electrostatic field of the following form:

$$U(x,y,z)=\frac{k}{2}(z-a)^2+W(x,y) \qquad 2.08$$

Where:

$$\frac{\partial^2 W}{\partial x^2}+\frac{\partial^2 W}{\partial y^2}=-k \qquad 2.09$$

For this 3-dimensional electrostatic field the period of oscillation, T_n, remains independent of the initial ion conditions such as initial energy, initial angular spread and initial co-ordinate spread. The flight time in the field is dependent only upon the mass-to-charge ratio of the ion. The quadratic-field ion mirror is often referred to as the "ideal ion mirror" capable of ideal time focusing *i.e.* in terms of classical charged particle optics the mirror is capable of infinite order time-of-flight focusing with respect to kinetic energy (*i.e.* first-order, second-order, third-order etc).

Makarov [2] considered a wide range of fields capable of achieving ideal time focusing. The practically useful fields are defined below.

Axially symmetric, hyperbolic potential:

$$U(r,z)=\frac{k}{2}(z-a)^2-\frac{k}{4}r^2+C \qquad 2.10$$

r and z are cylindrical co-ordinates while a, k and C are constants outlined previously.

Planar symmetric, hyperbolic potential:

$$U(x,y,z)=\frac{k}{2}(z-a)^2-\frac{k}{2}(x-b)^2+d\cdot y+C \qquad 2.11$$

b and d are constants (usually b=d=0).

Axially symmetric, hyperlogarithmic potential:

$$U(r,z)=\frac{k}{2}(z-a)^2-\frac{k}{4}r^2+b\cdot\ln\left(\frac{r}{d}\right)+C \qquad 2.12$$

b>0 and d>0 are constants. All three fields are necessarily incarnations of the basic field described by equation 2.08.

The obvious drawback of the axially symmetric hyperbolic potential and the planar hyperbolic potential is their rapidly changing electric-field strength in the radial (r) and transverse (x) field direction. This property means that the quadratic-field ion mirror is spatially defocusing in nature, resulting in lower ion transmission than single-stage or two-stage ion mirrors. The spatially defocusing nature does mean that quadratic-field ion mirrors are best suited to coaxial instruments in which the mirror and ion optical axes are coincident.

Single-stage and two-stage ion mirrors compensate for differences in time spent in the field-free regions by adding a suitable trajectory detour for ions with different kinetic energies. The quadratic-field ion mirror cannot compensate for differences in time spent in field-free regions. The addition of such regions severely limits the maximum obtainable resolution. Yoshida [3] discussed how, for any field-free region with a length greater than zero, the quadratic-field ion mirror looses its ideal time focusing characteristics. Indeed a quadratic-field ion mirror achieves only first-order time focusing. For first-order time focusing to occur the a term in equation 1 must be correctly selected. For real instruments, in which different regions of the spectrometer need to be separated, it is impossible not to include field-

free regions. Inclusion of a field-free region means that quadratic-field ion mirrors lose their ideal time focusing properties. Well-designed gridless, two-stage ion mirrors [4][5][6] capable of spatial focusing and second-order time focusing may achieve higher transmission and resolution than comparable quadratic-field ion mirrors because of the consequences of field-free regions.

The significant potential advantage of the quadratic-field ion mirror arises in tandem mass spectrometry, because of the ability to time focus the entire fragment energy-range at the detector plane without scanning the ion mirror reflecting voltage. The problem with the two-stage reflectron is that it can only time focus a small portion of the fragment ion spectrum at the detector plane. To acquire the entire fragment spectrum with a suitably high resolution it is typically necessary to scan the mirror voltage through many steps (10 would not be unusual)[7].

2.02 History of Quadratic, Parabolic, Curved and Non-Linear Ion Mirrors.

Carrico and co-workers [8][9][10][11] conducted extensive work on quadratic-field ion mirrors in the 1970's. Carrico and co-workers work differs in one significant respect from most subsequent work in that it used reflector designs in which a direct current (DC) component and an oscillatory current component were applied to the ion mirror. The static component formed a quadratic-field ion mirror and provided time focusing. The oscillatory electric field component

provided the mass separation behaviour of the system. The time-of-flight of an ion with a particular mass-to-charge ratio was related to the frequency of the oscillatory field. Carrico and co-workers proposed most of the possible instrument configurations for generating quadratic-potential reflecting fields. These have subsequently been developed by groups interested in the behaviour of ions in purely static electric fields. Research into oscillatory electric field time-of-flight has remained largely under-developed since the 1970's.

Research into static quadratic-field ion mirrors was reported in 1986 by Yoshida [3] and Rockwood [12]. Figure 24 shows a schematic diagram of the quadratic-field ion mirror described by Yoshida [3]. Yoshida [3] and Rockwood [12] both used ion mirrors consisting of multiple, discrete, ring-like field-sustaining electrodes connected by a resistor chain. The values of the resistors were chosen so that the voltage on the ion mirror electrodes approximated that of the quadratic potential. Electrostatic field-sag meant that the electric field along the central mirror axis of the ion mirror did not follow the ideal quadratic potential. It was possible to minimise the deviation from the ideal by making the length of the ion mirror large in comparison with the diameter and by using a large number of electrodes. Figure 25 shows the results of a SIMION [13] calculation performed on the axially symmetric quadratic-field ion mirror described by Yoshida [3]. The reflectron consisted of 100 field-sustaining electrodes of thickness 1mm spaced at 10mm intervals. The

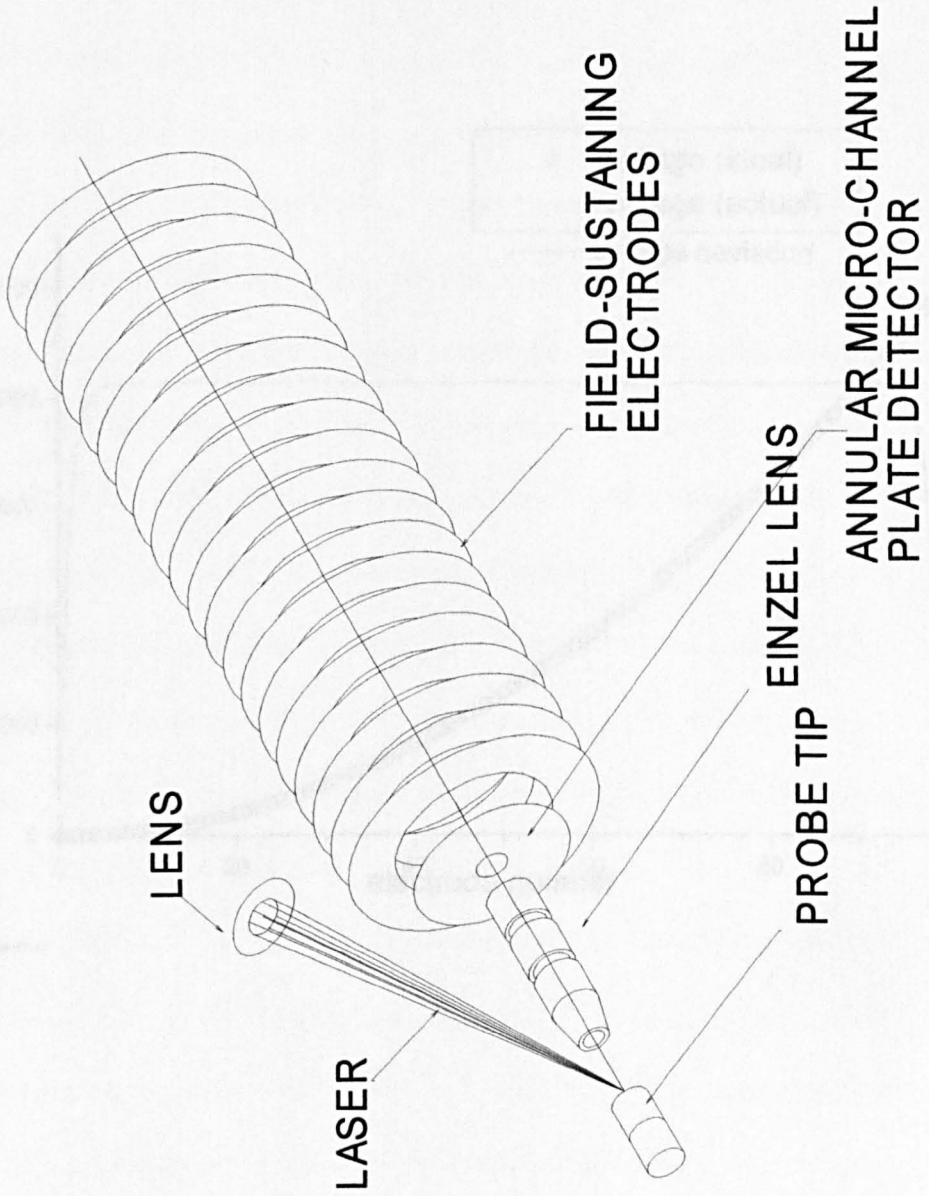

Fig. 24: Schematic diagram of the quadratic-field ion mirror described by Yoshida [3].

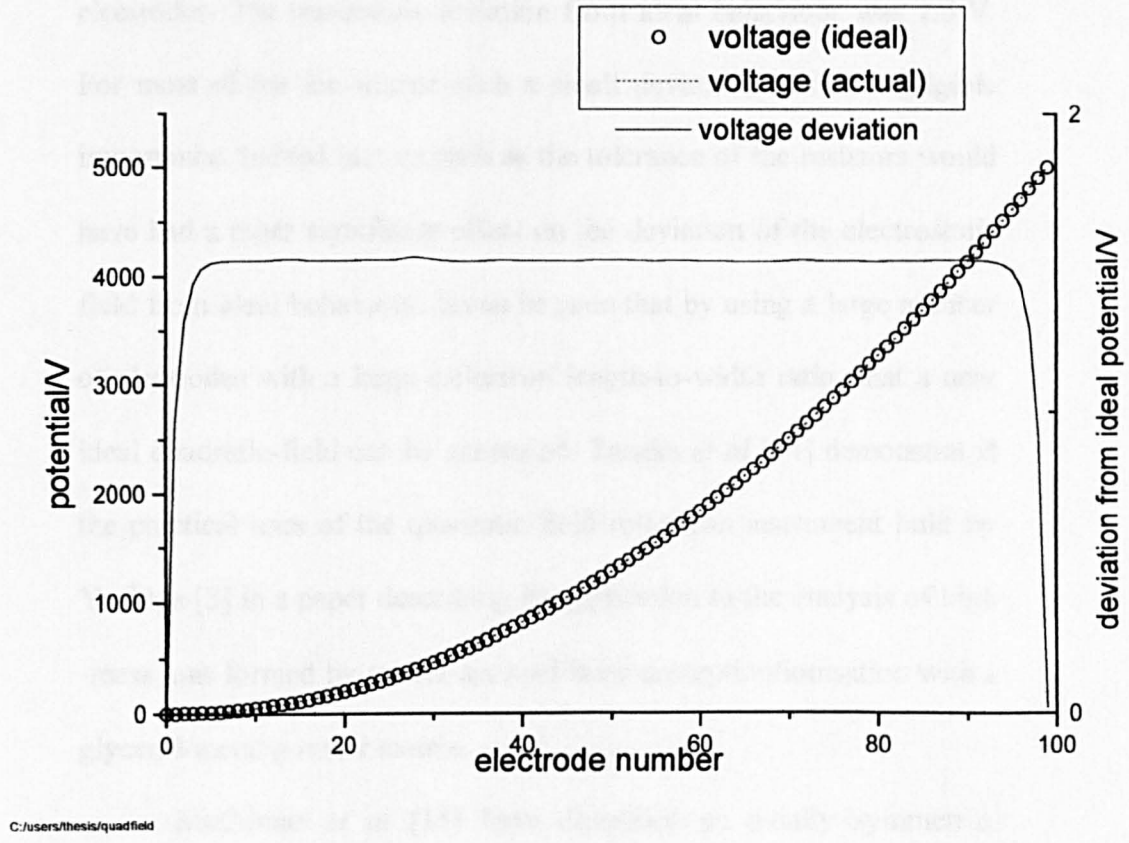

Fig. 25: Plot of ideal axial quadratic potential versus calculated theoretical quadratic potential for 100 electrode ion mirror described by Yoshida [3]. Deviation from ideal potential also shown.

ring-like electrodes were 80 mm outer diameter by 40 mm inner diameter. The results show the electric field generated along the central mirror axis when an ideal quadratic potential was applied to the electrodes. The maximum deviation from ideal behaviour was 1.5 V. For most of the ion mirror such a small deviation was of negligible importance. Indeed factors such as the tolerance of the resistors would have had a more significant effect on the deviation of the electrostatic field from ideal behaviour. It can be seen that by using a large number of electrodes with a large reflectron length-to-width ratio, that a near ideal quadratic-field can be generated. Tanaka *et al* [14] demonstrated the practical uses of the quadratic-field reflectron instrument built by Yoshida [3] in a paper describing its application to the analysis of high -mass ions formed by matrix-assisted laser desorption/ionisation with a glycerol/metal powder matrix.

McComas *et al* [15] have described an axially symmetric, linear electric field (LEF) instrument, in which the electric-field strength was proportional to the penetration depth of the ion. The device consisted of resistively coupled electrodes that sustained the desired potential along the mirror axis. Doroshenko and Cotter [16] have described an instrument consisting of a quadrupole ion trap coupled to a coaxial parabolic ion mirror of axial symmetry similar to the design of Yoshida [3].

At the University of Warwick an axially symmetric, hyperbolic electric field has been approximated by use of appropriately shaped electrodes [17]. The instrument used a hyperbolic shaped

monopole electrode and cone electrode to generate the desired quadratic-field. Carrico and co-workers [9][11] described a similar configuration for generating a quadratic-field for use in oscillatory electric field time-of-flight. Figure 26 shows a schematic diagram of the quadratic-field monopole time-of-flight spectrometer constructed at the University of Warwick [17]. Figure 26 also shows a diagram of the oscillatory electric field time-of-flight spectrometer proposed by Carrico and co-workers [9][11].

Several groups have used planar hyperbolic fields. Gloeckler and co-workers [18][19] have described the construction of an instrument using shaped electrodes to generate the desired field along the ion optical axis. The instrument used a floated hyperbolic shaped electrode and a grounded "V" shaped electrode to generate the quadratic potential. The "VMASS" instrument was designed for use onboard the SOHO, ACE and GGS/WIND spacecraft to facilitate the analysis of the solar wind. The compact design and high resolution meant that the instrument was ideally suited for space exploration. It was possible to approximate the quadratic-field by replacing the hyperbolic electrode with a circular rod. This allowed for simplified construction and machining. Carrico and co-workers [9][11] described an instrument using a circular rod electrode. Davis and Evans [20][21] have patented a similar system consisting of a cylindrical electrode and "V" shaped electrode for use as a mass analyser. Figure 27 shows

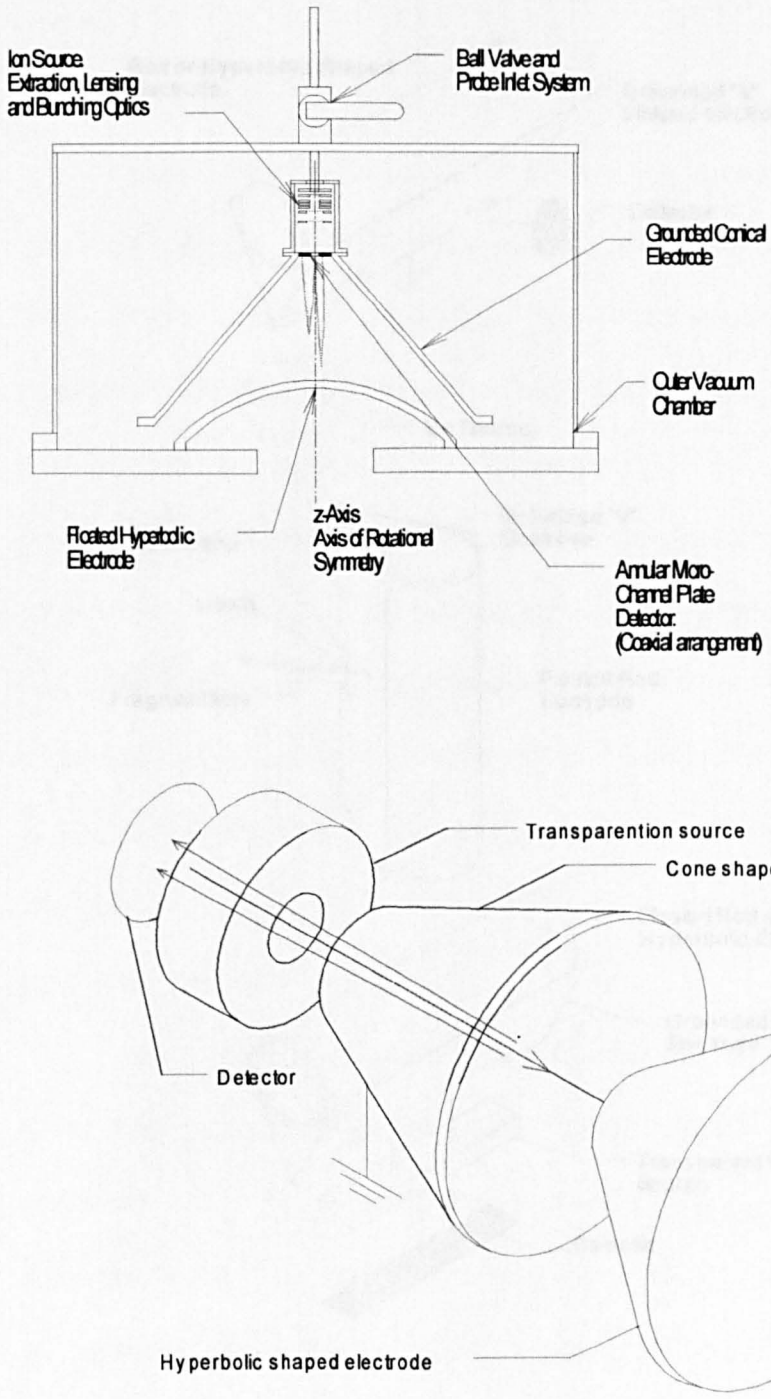

Fig. 26: (TOP) Schematic diagram of the monopole quadratic-field ion mirror constructed at the University of Warwick [17]. (BOTTOM) Oscillatory electric field time-of-flight mass spectrometer proposed by Carrico and co-workers [9][11].

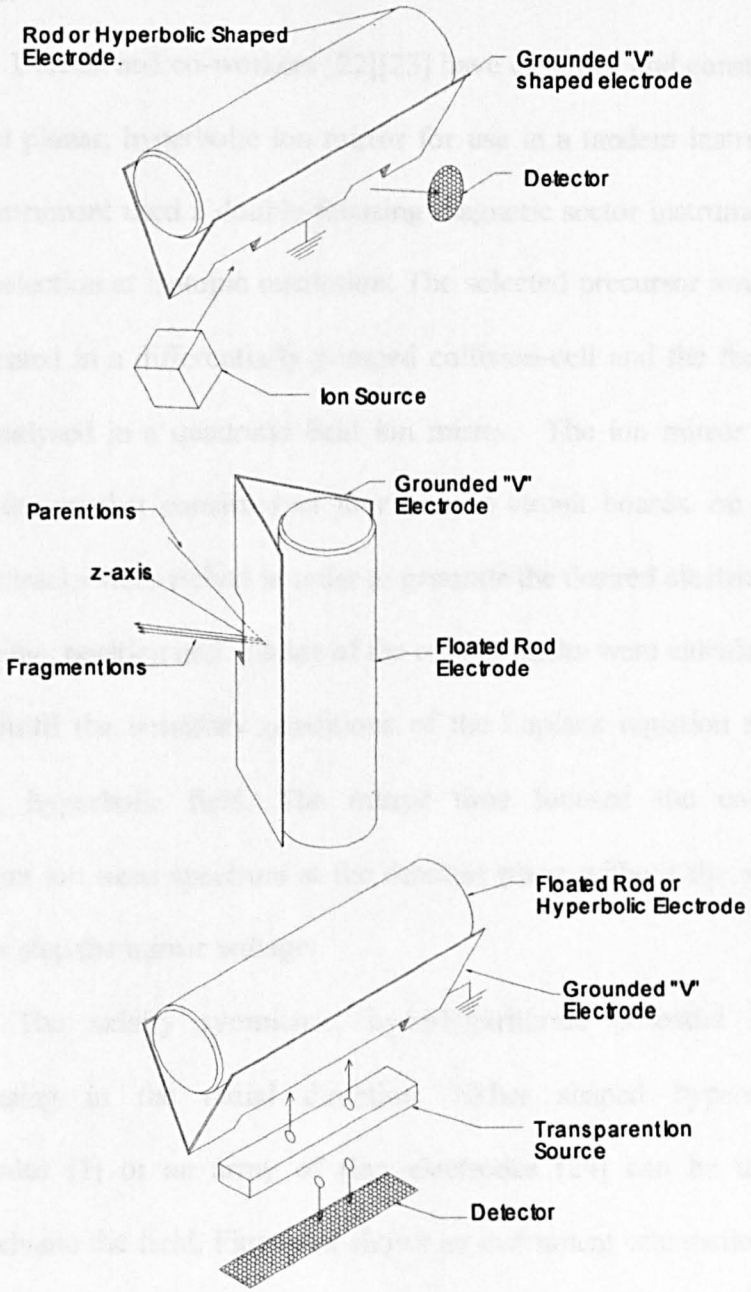

Fig. 27: Instrument schematics of various planar hyperbolic field instruments. (TOP) Gloeckler and co-workers [18] and Carrico and co-workers [9][11] design; (MIDDLE) Davis and Evans [20]; (BOTTOM) Carrico and co-workers [9][11] proposed design, incorporating a transparent ion source.

schematic diagrams of various planar hyperbolic quadratic-field ion mirrors.

Derrick and co-workers [22][23] have designed and constructed a novel planar, hyperbolic ion mirror for use in a tandem instrument. The instrument used a double-focusing magnetic sector instrument for mass selection at isotopic resolution. The selected precursor ions were fragmented in a differentially pumped collision-cell and the fragment ions analysed in a quadratic-field ion mirror. The ion mirror was a novel design that consisted of four printed circuit boards, on which copper tracks were etched in order to generate the desired electric field. The shape, position and voltage of the copper tracks were calculated so as to fulfil the boundary conditions of the Laplace equation for the planar, hyperbolic field. The mirror time focused the complete fragment ion mass spectrum at the detector plane without the need to scan or step the mirror voltage.

The axially symmetric, hyperlogarithmic potential is not defocusing in the radial direction. Either shaped hyperconical electrodes [1] or an array of ring electrodes [24] can be used to approximate the field. Figure 28 shows an instrument schematic of the spectrometer developed by Ivanov *et al* [24]. The device used a multitude of ring-like electrodes to generate the quadratic-field. The central set of electrodes acted to constrain the trajectory of the ions thus preventing defocusing of the ion beam. Appropriately shaped solid inner and outer electrodes can be used to replace the multitude of ring electrodes [1].

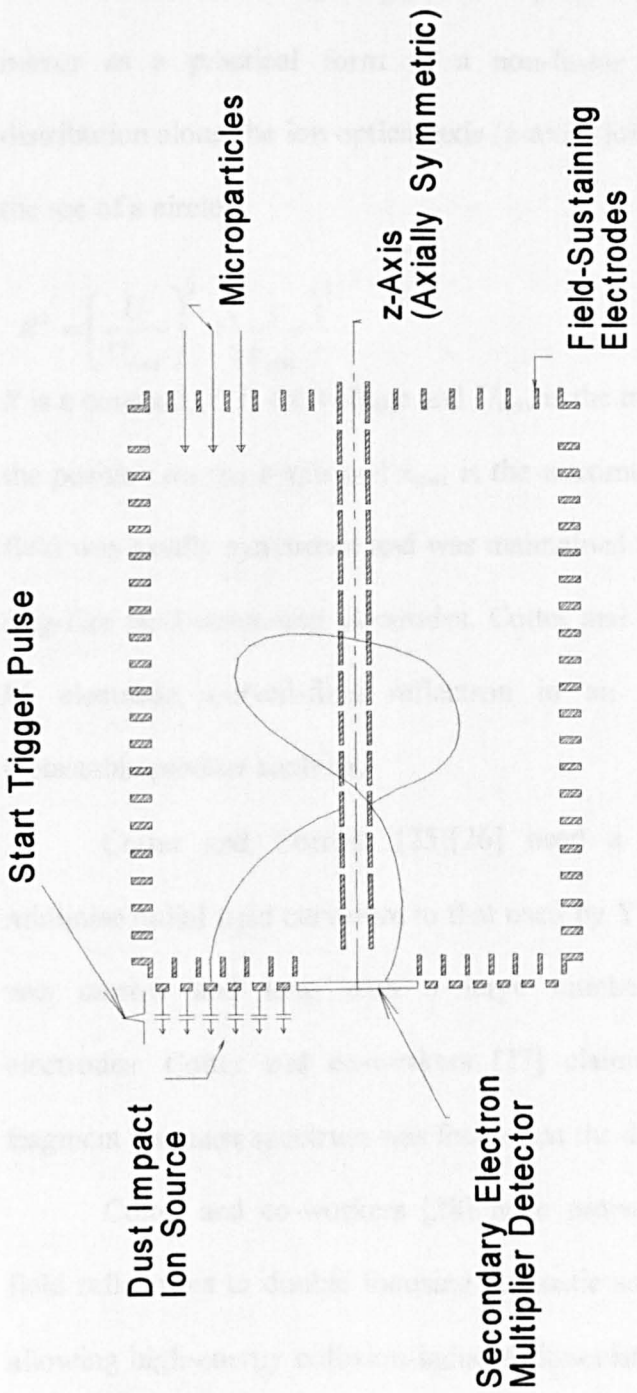

Fig. 28: Schematic diagram of the axially symmetric, hyperlogarithmic quadratic-field instrument built by Ivanov *et al* [24].

Cotter and Cornish [25] have proposed a curved-field ion mirror as a practical form of a non-linear field. The potential distribution along the ion optical axis (z-axis) followed the equation of the arc of a circle:

$$R^2 = \left(\frac{U}{U_{max}}\right)^2 + \left(\frac{z}{z_{max}}\right)^2 \qquad 2.13$$

R is a constant, U is the voltage and U_{max} is the maximum voltage. z is the position on the z-axis and z_{max} is the maximum displacement. The field was axially symmetric and was maintained by resistively coupled ring-like field-sustaining electrodes. Cotter and Cornish [26] used an 86 electrode, curved-field reflectron in an instrument used for metastable product analysis.

Cotter and Cornish [25][26] used a similar approach to minimise radial field curvature to that used by Yoshida. The reflectron was narrow and long with a large number of field-sustaining electrodes. Cotter and co-workers [27] claimed that 90 % of the fragment ion mass spectrum was focused at the detector plane.

Cotter and co-workers [28] have proposed coupling curved-field reflectrons to double focusing magnetic sector instruments, thus allowing high-energy collision-induced dissociation experiments to be conducted. Martin and co-workers [29][30] subsequently developed the instrument.

Cotter and co-workers [31][32][33] have designed and built a twin reflectron instrument capable of collision-induced dissociation. The first, single-stage, ion mirror time focused the ion packet at the

collision-cell where fragmentation occurred. The fragment species were time resolved and time focused by a curved-field ion mirror.

Cotter and Cornish [34][35] have described the construction of an "end cap reflectron". The device used a grounded cylinder with floated back electrode to generate a non-linear electric field that acted as a reflectron. Moving the back-plate backwards and forwards controlled the time focusing properties of the reflecting field. Cotter and Cornish claimed that the reflectron was capable of high-order kinetic energy correction and demonstrated a resolution of 200 for bradykinin ions generated by matrix-assisted laser desorption/ionisation. The instrument was compact, being approximately 100 mm long by 50 mm diameter. The addition of vacuum chamber, laser system and data acquisition system meant that the complete spectrometer was considerably larger. Figure 29 shows a schematic diagram of the miniaturised non-linear ion mirror constructed by Cotter and Cornish [34][35]. Figure 29 also shows a SIMION model of the potential energy surface generated inside the ion mirror.

Several groups have described the use of quadratic-field accelerating regions. Crane and Mills [36] were the first workers to describe such an arrangement. Their instrument used a pulsed quadratic- field formed by a closed cylinder arrangement to bunch a positron beam at the detector plane. Hulett *et al* [37] have described a similar quadratic-field acceleration/bunching spectrometer for the analysis of small ionic species.

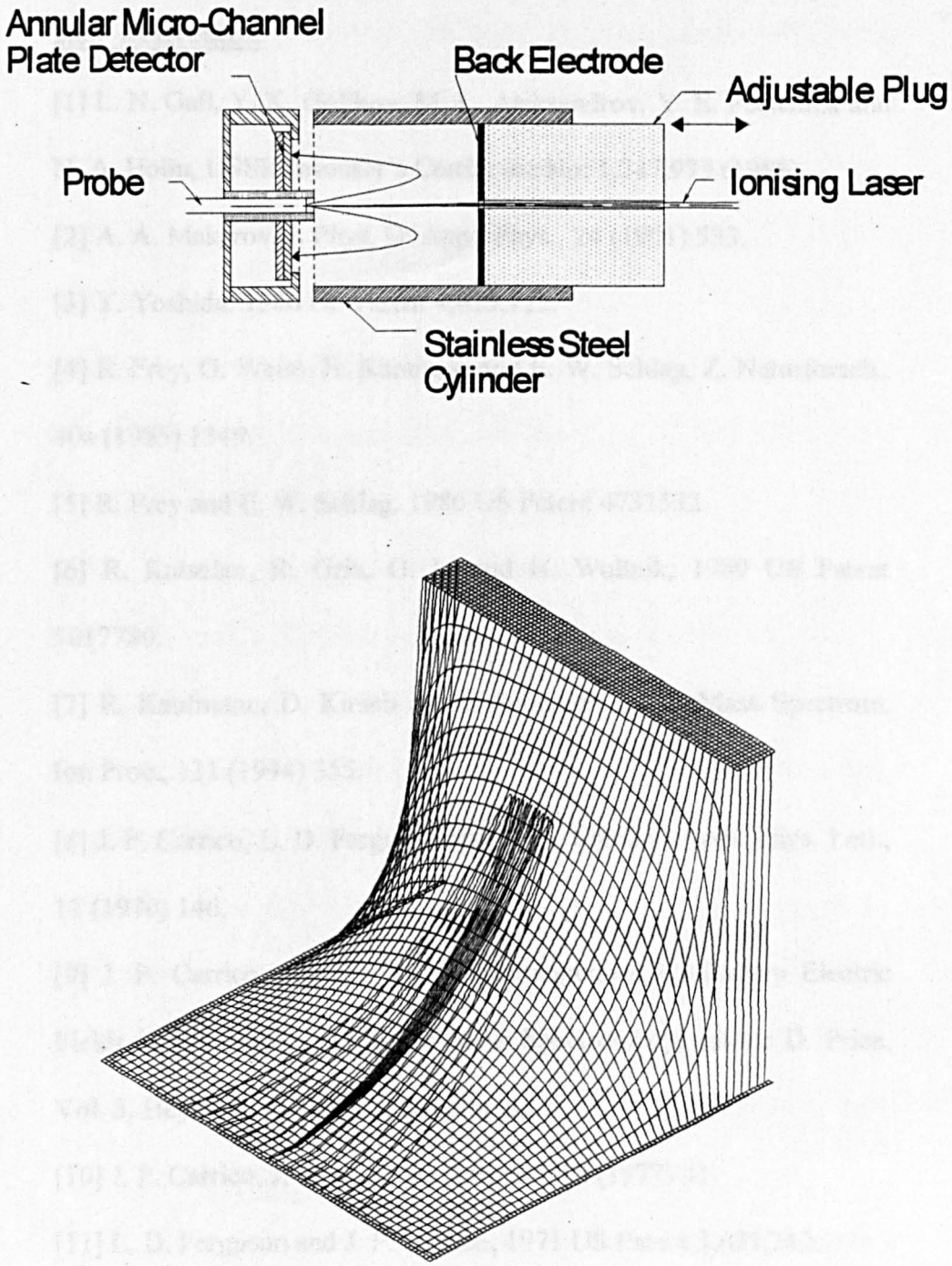

Fig. 29: (TOP) Schematic diagram of the miniaturised non-linear ion mirror constructed by Cotter and co-workers [34][35]. (BOTTOM) SIMION model of the potential energy surface inside the ion mirror.

2.03 References.

[1] L. N. Gall, Y. K. Golikov, M. L. Aleksandrov, Y. E. Pechalina and N. A. Holin, USSR Inventor's Certificate No: 1,247,973 (1986).

[2] A. A. Makarov, J. Phys. D: Appl. Phys., 24 (1991) 533.

[3] Y. Yoshida, 1986 US Patent 4,625,112.

[4] R. Frey, G. Weiss, H. Kaminski and E. W. Schlag, Z. Naturforsch., 40a (1985) 1349.

[5] R. Frey and E. W. Schlag, 1986 US Patent 4731532.

[6] R. Kutscher, R. Grix, G. Li and H. Wollnik, 1989 US Patent 5017780.

[7] R. Kaufmann, D. Kirsch and B Spengler, Int. J. Mass Spectrom. Ion Proc., 131 (1994) 355.

[8] J. P. Carrico, L. D. Ferguson and R. K. Mueller, Appl. Phys. Lett., 17 (1970) 146.

[9] J. P. Carrico, Application of Inhomogenous Oscillatory Electric Fields in Ion Physics, Dynamic Mass Spectrometry, Editor D. Price, Vol. 3, Heyden and Son Ltd, London, pp.1.

[10] J. P. Carrico, J. Phys. E: Sci. Instrum.,10 (1977) 31.

[11] L. D. Ferguson and J. P. Carrico, 1971 US Patent 3,621,242.

[12] A. L. Rockwood Proc. 34th ASMS Conf. On Mass Spectrometry and Allied Topics, Cincinnati, OH, 1986, pp.173.

[13] SIMION 3D, version 6, D. A. Dahl, Idaho National Engineering Laboratory (1995).

[14] K. Tanaka, H. Waki, Y. Ido, S. Akita, Y. Yoshida and T. Yoshida, Rapid Commun. Mass Spectrom., 2 (1988) 151.

[15] D. J. McComas and J. E. Nordholt, Rev. Sci. Instrum., 61 (1990) 3095.

[16] V. M. Doroshenko and R. J. Cotter, J. Mass Spectrom., 33 (1998) 305.

[17] Work unpublished.

[18] D. C. Hamilton, G. Gloeckler, F. M. Ipavich, R. A. Lundgrer, R. B. Sheldon and D. Hovestadt, Rev. Sci. Instrum. 61 (1990) 3104.

[19] G. Gloeckler, Rev. Sci. Instrum., 61 (1990) 3613.

[20] S. C. Davis, 1991 US Patent 5,077,472.

[21] S. C. Davis and S. Evans, 1993 US Patent 5,180,914.

[22] U. N. Anderson, A. W. Colburn, A. A. Makarov, E. N. Raptakis, D. J. Reynolds, P. J. Derrick, S. C. Davis, A. D. Hoffman and S. Thomson, Rev. Sci. Instrum., 69 (1998)1650.

[23] A. A. Makarov, E. N. Raptakis and P. J. Derrick, Int. J. Mass Spectrom. and Ion Processes, 146/147 (1995) 165.

[24] V. P. Ivanov, A. A. Makarov and A. A. Sysoev, Proc. 4th Int. Seminar on the Manufacturing of Scientific Space Instruments, Frunze, 1990, IKI AN, Moscow, 1990, vol. 2, p 65.

[25] R. J. Cotter in Time-of-Flight Mass Spectrometry Instrumentation and Applications in Biological Research, ACS symposium Series 1997, Ed R. J. Cotter, pp 194.

[26] T. J. Cornish and R. J. Cotter, Rapid Commun. Mass Spectrom., 8 (1994) 781.

[27] M. M. Cordero, T. J. Cornish, R. J. Cotter and I. A. Lys, Rapid Commun. Mass Spectrom., 9 (1995) 1356.

[28] R. J. Cotter, T. J. Cornish and B. Musselmann, Rapid Commun. Mass Spectrom., 8 (1994) 339.

[29] C. Martin, G. Samuelson, J. Finch, V. Wysocki and A. Somogyi, Proc. 46th ASMS Conf. On Mass Spectrometry and Allied Topics, Orlando, FL, May 31-June 5, 1998, pp. 1252.

[30] E. N. Nikolaev, A. Somogyi, C. Gu, L. Breci, V. H. Wysocki, J. W. Finch, C. D. Martin and G. L. Samuelson, Proc. 46th ASMS Conf. On Mass Spectrometry and Allied Topics, Orlando, FL, May 31-June 5, 1998, pp 41.

[31] T. J. Cornish and R. J. Cotter, 1995 US Patent 5,464,985.

[32] T. J. Cornish and R. J. Cotter, Rapid Commun. Mass Spectrom., 7 (1993) 1037.

[33] M. M. Cordero, T. J. Cornish and R. J. Cotter, J. Am. Soc. Mass Spectrom., 1996 (1996) 590.

[34] T. J. Cornish and R. J. Cotter, Anal. Chem., 69 (1997) 4615.

[35] R. J. Cotter and T. J. Cornish, 1996 US Patent 5,814,313.

[36] W. S. Crane and A. P. Mills, Rev. Sci. Instrum. 56 (1985) 1723.

[37] L. D. Hulett, D. L. Donohue and T. A. Lewis, Rev. Sci. Instrum., 62 (1991) 2131.

CHAPTER THREE.

Overview of Instrument and Vacuum System.

3.01 Instrument Overview.

The tandem time-of-flight/time-of-flight (TOF-TOF) mass spectrometer was originally conceived as taking one of two possible instrument configurations. The first configuration consisted of a series of electrostatic sectors configured so as to achieve iso-chronous time focusing. The second was a twin reflectron instrument with an intermediate time focus.

Poschenrieder [1] and Bakker [2][3] proposed the use of electric-sector fields in time-of-flight mass spectrometry, as a means of achieving iso-chronous time focusing. The principles of multiple iso-chronous time focusing were established by Poschenrieder [1][4]. Multiple iso-chronous time focusing, referred to as triple iso-chronous time focusing by Matsuda and co-workers [5][6], describes the ability of a spectrometer to correct for the initial angle, initial energy and initial position of the ions. Triple space focusing, as referred to by Matsuda and co-workers [5][6], describes the ability of a spectrometer to achieve a spatial focus irrespective of the ions initial angle (in the vertical or horizontal) and energy.

The proposed electrostatic sector time-of-flight instrument was similar to that proposed by Matsuda and co-workers [5]. Matsuda and co-workers [6] constructed a time-of-flight spectrometer incorporating four, 269° toroidal electric fields in a "cloverleaf" arrangement. Figure

30 shows a schematic diagram of the "cloverleaf" configuration constructed by Matsuda and co-workers [6]. The instrument constructed by Matsuda and co-workers [6] achieved simultaneous triple iso-chronous time focusing and triple space focusing. The "cloverleaf" arrangement of the electric sectors meant that the entire spectrometer was enclosed within a compact vacuum chamber, with a diameter of only 0.4 m. The effective pulse-width (FWHM) of the ion source was 15 ns. The peak width at the detector was 18 ns. The instrument was reported to achieve ion transmission of 90 % and a mass resolving power of 730.

Flight time deviations, *i.e.* packet width at the detector plane, can be expressed as a power series expansion [6]:

$$t = T_x x_0 + T_a \alpha_0 + T_\gamma \gamma + T_\delta \delta + T_{xx} x_0^2 + T_{x\alpha} x_0 \alpha_0 + T_{x\delta} x_0 \delta + T_{\alpha\alpha} \alpha_0^2 + T_{\alpha\delta} \alpha_0 \delta + T_{\delta\delta} \delta^2 + T_{yy} y_0^2 + T_{y\beta} y_0 \beta_0 + T_{\beta\beta} \beta_0^2 + \ldots\ldots \quad 3.01$$

t is the time deviation, x_0 and y_0 are the source slit half-width and half-height respectively, α_0 and β_0 are the horizontal and vertical inclination angles respectively and γ and δ are the relative mass and energy deviations respectively. T_γ is the mass dispersion coefficient, while T_x, T_α, T_δ are the aberration coefficients with respect to initial position, angle and energy. For first-order triple iso-chronous time focusing to be achieved the flight time must be independent of position, angle and energy i.e. T_x=0, T_α=0 and T_δ=0. To achieve high resolution, high-order terms must be minimised.

In order to achieve high transmission, triple space focusing must be accomplished. In a similar manner to that used to describe the flight time deviation, the position of a particle at the detector plane can be expressed as:

$$x = X_x x_o + X_\alpha \alpha_0 + X_\delta \delta + \ldots\ldots \quad 3.02$$

$$y = Y_y y_0 + Y_\beta \beta_0 + Y_\delta \delta + \ldots\ldots \quad 3.03$$

x and y are the width and height of the ion at the detector plane respectively. X_x, X_α, X_δ, Y_y, Y_β and Y_δ are the aberration coefficients. Higher order terms have been neglected. To achieve triple space focusing X_α=0, X_δ=0 and Y_β=0. By introducing symmetry into the arrangement of the electric sectors certain aberration coefficients can be reduced to zero. Doubly symmetric systems, consisting of four electric fields, result in the X_α, X_δ, T_x and T_α coefficients being eliminated. In order to achieve high resolution the second-order aberration coefficients must be minimised.

Matsuda and co-workers [5] first discussed the proposed TOF-TOF spectrometer configuration. The "zig-zag" arrangement of four electrostatic sectors resembled a snake. This resulted in the TOF-TOF spectrometer being named "Nessie". Figure 31 shows a schematic diagram of the proposed snake configuration time-of-flight mass spectrometer.

The second proposed time-of-flight spectrometer design utilised two ion mirrors. The purpose of the first ion mirror was to form a time focus at a collision-cell. The second ion mirror was to

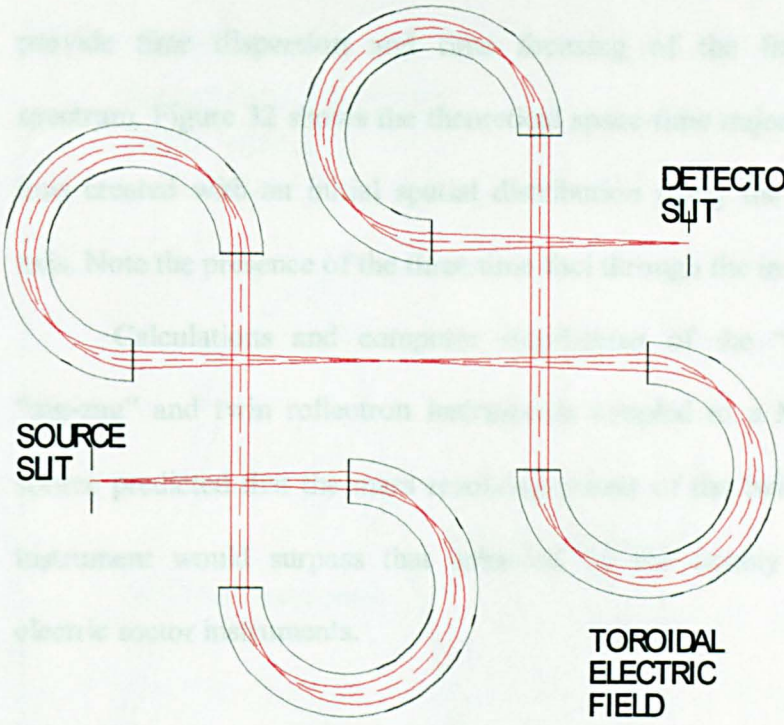

Fig. 30: Schematic diagram of the "cloverleaf" electric sector time-of-flight spectrometer constructed by Matsuda and co-workers [6]. The spectrometer achieved triple iso-chronous and triple space focusing.

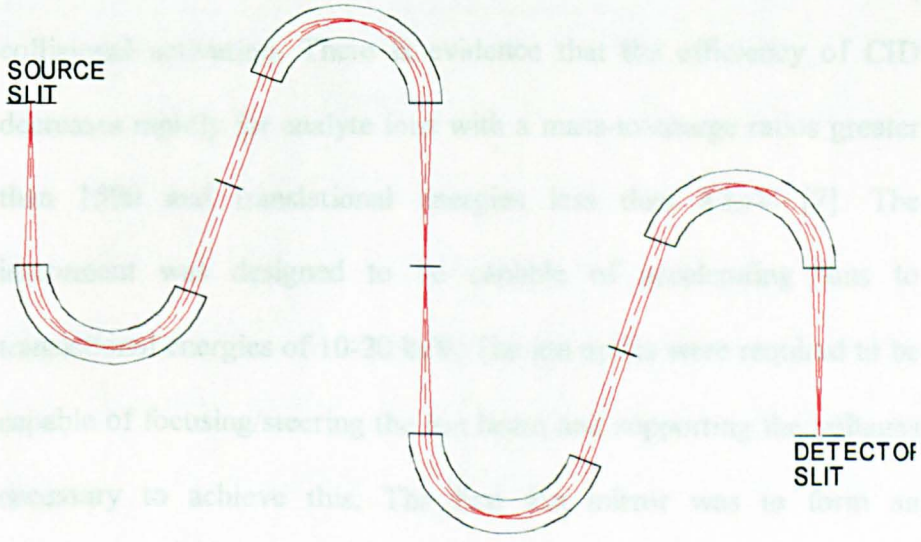

Fig. 31: Schematic diagram of the proposed "zig-zag" configuration electric sector time-of-flight spectrometer.

provide time dispersion and time focusing of the fragment ion spectrum. Figure 32 shows the theoretical space-time trajectory of two ions created with an initial spatial distribution along the ion optical axis. Note the presence of the three time foci through the instrument.

Calculations and computer simulations of the "cloverleaf", "zig-zag" and twin reflectron instruments coupled to a MALDI ion source predicted that the mass resolving power of the twin reflectron instrument would surpass that achieved by the doubly symmetric electric sector instruments.

3.02 Twin Ion Mirror Instrument –Design constraints.

The instrument was to use an ultraviolet MALDI ion source capable of generating intact high-mass ions from proteins, peptides and synthetic polymers. The ions were to be accelerated to high kinetic energies to allow high-mass species to be efficiently dissociated by collisional activation. There is evidence that the efficiency of CID decreases rapidly for analyte ions with a mass-to-charge ratios greater than 1500 and translational energies less than 8 keV [7]. The instrument was designed to be capable of accelerating ions to translational energies of 10-20 keV. The ion optics were required to be capable of focusing/steering the ion beam and supporting the voltages necessary to achieve this. The first ion mirror was to form an intermediate time focus at the collision-cell, while maximising the transmission efficiency of the ion mirror and associated optics.

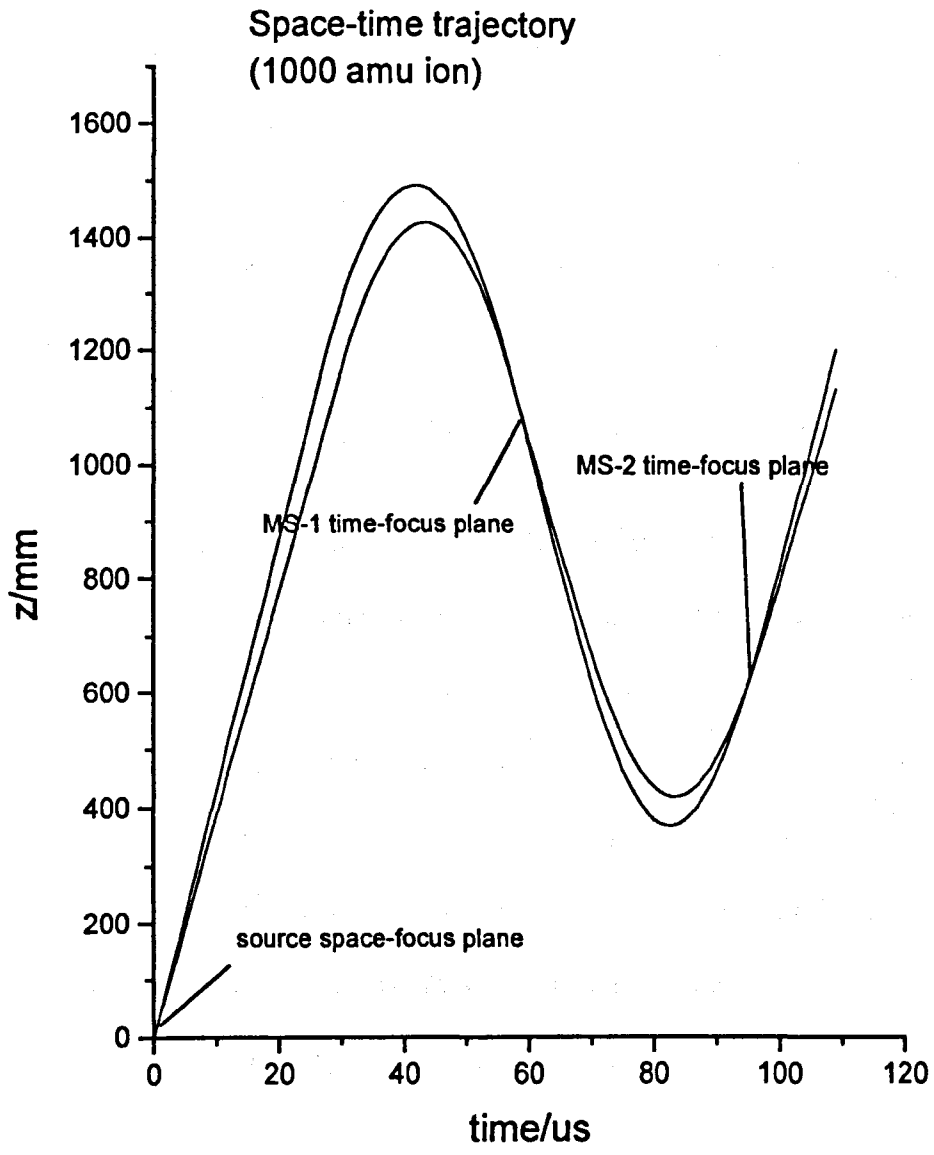

Fig. 32: Theoretical space-time trajectory showing the three time foci.

The second ion mirror needed to be capable of time dispersing and time focusing the fragment ions. The laws of conservation of momentum and energy meant that fragment species possessed the same velocity as the precursor species.

The kinetic energy of the fragment species can be expressed as:

$$U_{frag} = U_{parent}\left(m_{frag}/m_{parent}\right) \qquad 3.04$$

U_{frag} and U_{parent} are the kinetic energy of the fragment and precursor species respectively. m_{frag} and m_{parent} are the mass of the fragment and parent ion respectively. The kinetic energies possessed by fragment species may range from a few electron volts, for low-mass fragments, to several thousand electron volts for high-mass fragment species. In order to time separate the fragment species a retarding electric field or ion mirror must be introduced to discriminate between the different kinetic energy fragment species. Time separation of fragment species is relatively simple. The problem occurs when trying to simultaneously time focus the complete fragment mass range at the detector plane. The large range of kinetic energies possessed by fragment species mean that single-stage and two-stage ion mirrors must be scanned. This is time consuming, increases the complexity of mass calibration and reduces instrument sensitivity. The quadratic-field ion mirror designed by Yoshida [8] and the curved-field reflectron designed by Cotter and Cornish [9] allowed 90-100 % of the fragment mass range to be simultaneously time focused at the detector plane, thereby removing

the need to scan the mirror voltage. The second ion mirror (MS-2) was therefore chosen to be a quadratic-field ion mirror.

Because time-of-flight instruments use time dispersion to mass separate different mass ions it was necessary to include a method of selecting precursor ions. Pulsed electrostatic deflectors are commonly used to mass select precursor ions in time-of-flight spectrometers.

It was desirable to include a linear time-of-flight spectrometer to allow optimisation of sample preparation protocols and ion source parameters. The linear time-of-flight spectrometer was constructed by placing a detector behind the first ion mirror.

The instrument was required to achieve high parent and fragment ion transmissions. This allowed measurements to be made with a high degree of sensitivity. The design of the instrument was required to allow future additions and modifications to be made easily.

3.03 The Main Vacuum Chamber and Vacuum System.

The vacuum system consisted of three main vacuum regions. The ion source was mounted in its own separate vacuum chamber, which was bolted onto the main chamber. This allowed easy access to the ion source and ensured rapid evacuation times after sample introduction. The collision-cell was housed in a differentially pumped chamber inside the main chamber. This ensured that a suitable collision-cell pressure could be attained without reducing the vacuum within the main chamber. The main vacuum chamber housed all elements of the time-of-flight spectrometer other than the ion source.

This included the single-stage ion mirror, the collision-cell, the quadratic-field ion mirror, the detection system and all associated ion optics.

The main vacuum chamber was a simple box structure. This allowed ease of access to all components, as well as adequate space for future system modifications. The downside of using a box vacuum chamber was that the chamber was bulky and heavy. The use of a simple box structure allowed all ion optical components to be accurately located on the flat baseplate of the vacuum chamber. This did away with the need for complex alignment rails. Under vacuum conditions, external atmospheric pressure causes all chambers to distort. It was crucial that this distortion did not destroy the alignment of the ion optical elements. The most simplistic solution was to "over-engineer" the chamber, so as to minimise distortion. The mass of the chamber was required, however, to remain within manageable limits. The maximum safe working-load (SWL) of the laboratory gantry system was 500 kg.

The lid and baseplate of the chamber were the largest unsupported spans. Distortion was therefore likely to be most significant in these important regions. The addition of ribs to the baseplate and lid increased the rigidity of the chamber while minimising wall thickness and weight.

The chamber was constructed from 316L stainless steel because of its strength, corrosion resistance, magnetic properties, vacuum suitability and the developed nature of stainless steel welding

technology. The Department of Engineering at the University of Warwick conducted finite element analysis calculations on a wire-mesh model of the chamber, using the I-DEAS® software package. The maximum deflection of the baseplate was calculated to be 30 μm. The maximum distortion of the baseplate was subsequently measured using a precision dial gauge and found to be 40 μm. The source chamber and associated optics were mounted on the end wall of the main vacuum chamber. Distortion of this wall would have resulted in misalignment of the critically important ion source. It was therefore imperative that distortion of the end wall be kept to an absolute minimum. The end wall was 50 mm thick in order to provide sufficient support for the source chamber and minimise distortion. Finite element analysis predicted that the distortion along the top edge of the end wall would be less than 16 μm.

The baseplate of the chamber deflected inwards most at the centre of the baseplate, near the collision-cell. The baseplate did not distort significantly at the edges, where it joined the walls of the chamber. The front electrodes of both ion mirrors were located near to the centre of the baseplate, while the rear electrodes were positioned near the walls of the vacuum chamber. This resulted in the front ends of both ion mirrors being elevated relative to their rear electrodes and the ideal horizontal ion optical plane. Figure 33 shows the inclination of the ion mirrors with respect to the ion optical plane. The elevation of the ion mirrors relative to the ion optical plane was estimated from the geometry of the spectrometer. For a baseplate that distorted it was

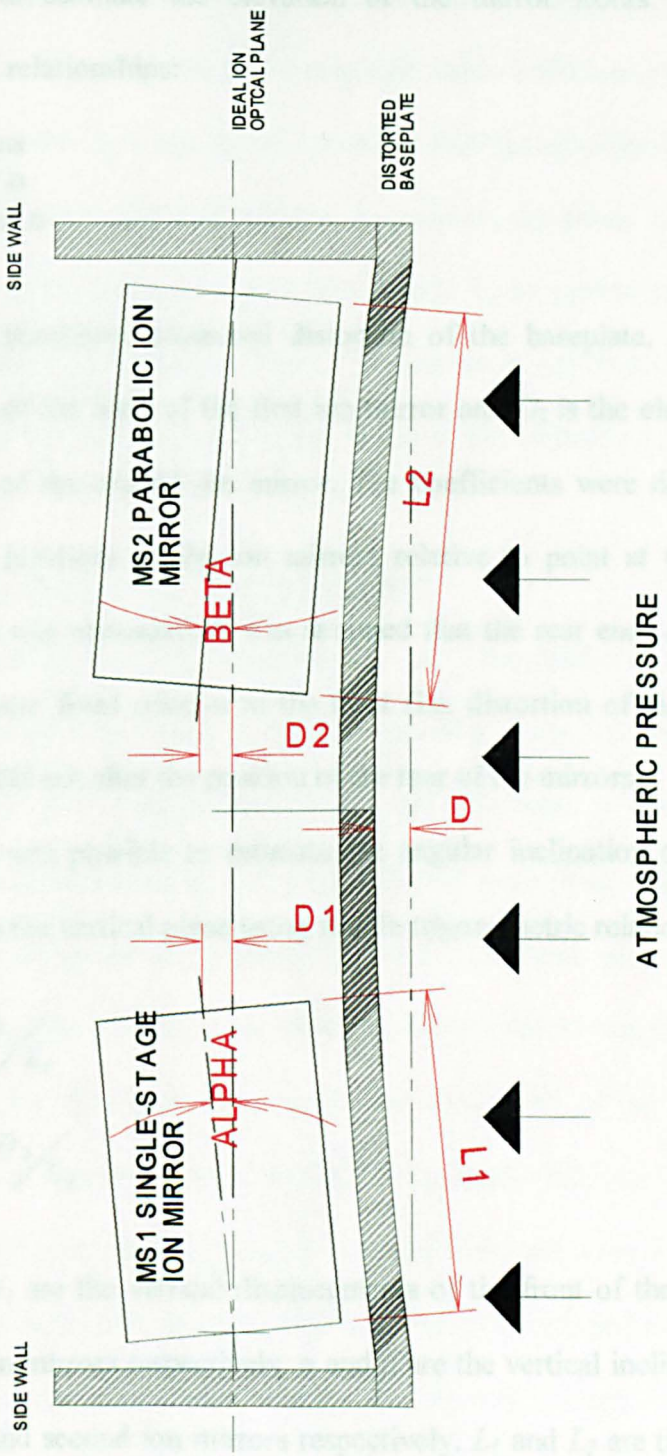

Fig. 33: Schematic diagram showing distortion of the baseplate and the elevation of the ion mirrors.

possible to estimate the elevation of the mirror fronts using the following relationships:

$$\begin{aligned} D &= 40\ \mu m \\ D_1 &= 0.7D \\ D_2 &= 0.85\ D \end{aligned} \qquad 3.05$$

D is the maximum measured distortion of the baseplate, D_1 is the elevation of the front of the first ion mirror and D_2 is the elevation of the front of the second ion mirror. The coefficients were determined from the positions of the ion mirrors relative to point at which the distortion was measured. It was assumed that the rear ends of the ion mirrors were fixed relative to the front (i.e. distortion of the vacuum chamber did not alter the position of the rear of the mirrors).

It was possible to estimate the angular inclination of the ion mirrors in the vertical plane using simple trigonometric relationships:

$$\tan \alpha = D_1 / L_1 \qquad 3.06$$

$$\tan \beta = D_2 / L_2 \qquad 3.07$$

D_1 and D_2 are the vertical displacements of the front of the first and second ion mirrors respectively. α and β are the vertical inclinations of the first and second ion mirrors respectively. L_1 and L_2 are the lengths of the first and second ion mirrors respectively. Using knowledge of the geometry of the mirrors, the length of the field-free regions and by assuming that the ion mirrors behaved in an ideal manner, the vertical displacement of the ion beam with respect to the ideal horizontal ion optical plane was calculated. Figure 34 shows a schematic

representation of the instrument with the vertical displacements of the ion beam at the exit to the first ion mirror, at the collision-cell/entrance to the quadratic-field ion mirror and at the final detector displayed. The calculated values assumed that the ion mirrors possessed no fringing fields or defocusing properties that would have further aggravated vertical beam inclination. Figure 35 shows a schematic diagram illustrating the influence of fringing fields on ion trajectories.

3.04 Manufacture of Vacuum Chamber.

The Department of Engineering at Cambridge University manufactured the main vacuum chamber. The chamber was constructed from 316L stainless steel. The side-walls of the chamber were constructed from 30 mm thick stainless steel plate, while the lid and baseplate were manufactured from 25 mm thick plate. The end wall supporting the source chamber was made from 50 mm thick plate. The chamber consisted of a simple box with a lid of the following dimensions: length=1.56 m, width=0.72 m, depth=0.35 m. During the stress-relief process the baseplate and lid distorted. One face of the plates was milled flat in order to ensure that the lid sealed and that the ion optical elements located accurately. There remained, however, a distinct curvature of the outer faces of the two plates. The walls of the chamber were bolted onto the baseplate of the chamber and then bolted to one another using M8 bolts to ensure that a rigid box was formed. The joints were welded to provide a vacuum tight metal-metal seal.

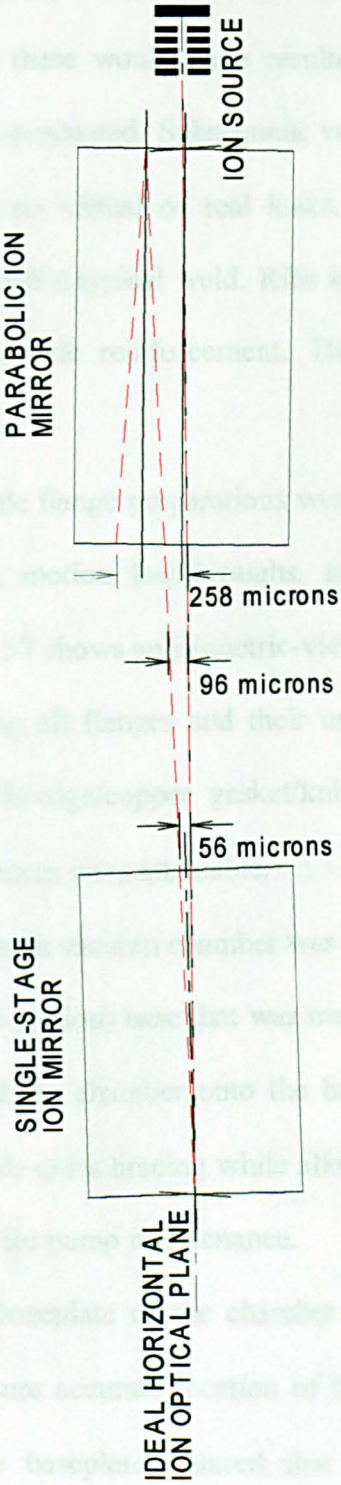

Fig. 34: Schematic diagram showing the vertical displacement of the ion beam with respect to the horizontal ion optical plane at the exit of MS-1, the collision-cell/entrance to MS-2 and at the final detector.

Care was taken to ensure that no vesicles were trapped in the weld structures, as these would have resulted in a virtual leak when the chamber was evacuated. Subsequent vacuum testing showed that the chamber had no virtual or real leaks. Figure 36 shows a sectional diagram through a typical weld. Ribs were welded onto the baseplate and lid to provide reinforcement. The ribs were 20 mm thick by 100 mm deep.

Suitable flange preparations were positioned to allow electrical feedthroughs, motion feedthroughs, pumps and access ports to be fitted. Figure 37 shows an isometric-view of the main vacuum chamber and lid, listing all flanges and their uses. The flanges used standard Conflat® knife-edge/copper gasket/knife-edge seals to ensure high-vacuum pressures were attainable.

The main vacuum chamber was mounted on a welded steel tube (square cross-section) base that was manufactured in-house. Four M12 bolts secured the chamber onto the base. The base was designed to ensure suitable cross bracing while allowing access to the underside of the chamber for pump maintenance.

The baseplate of the chamber was polished to a sub-micron finish to ensure accurate location of the ion optical elements. Dowel holes in the baseplate ensured that ion optical components were accurately positioned relative to each other and the ion source. The exterior faces of the chamber were bead-blasted to provide a clean finish. Calculations showed that the empty chamber weighed 500 kg.

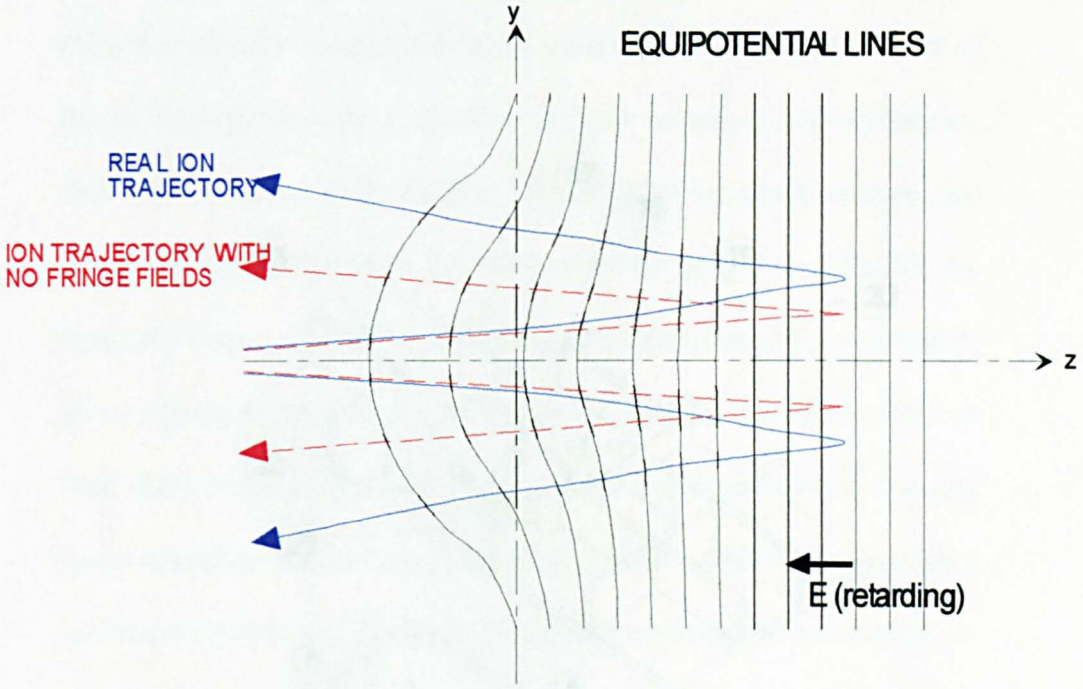

Fig. 35: Schematic diagram showing ion trajectories with and without fringing fields at the entrance to an ion mirror.

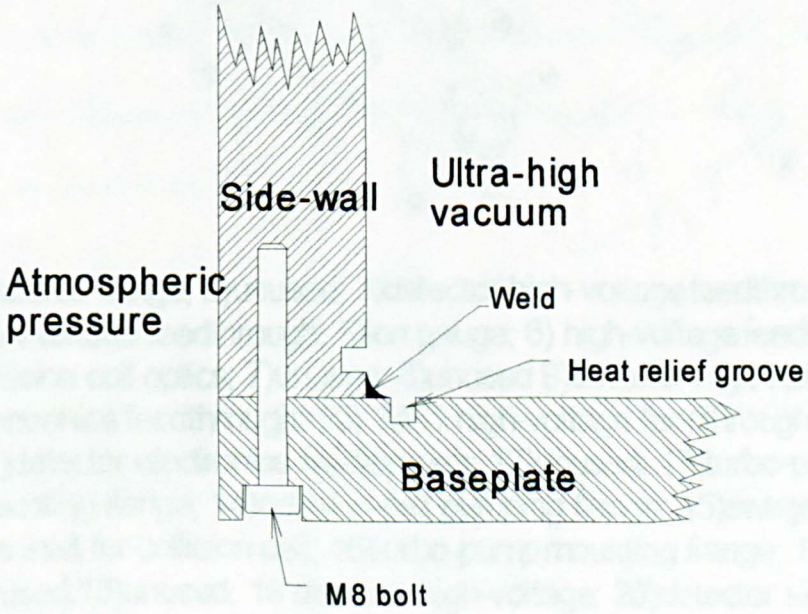

Fig. 36: Section through a typical weld, showing how the main vacuum chamber was constructed.

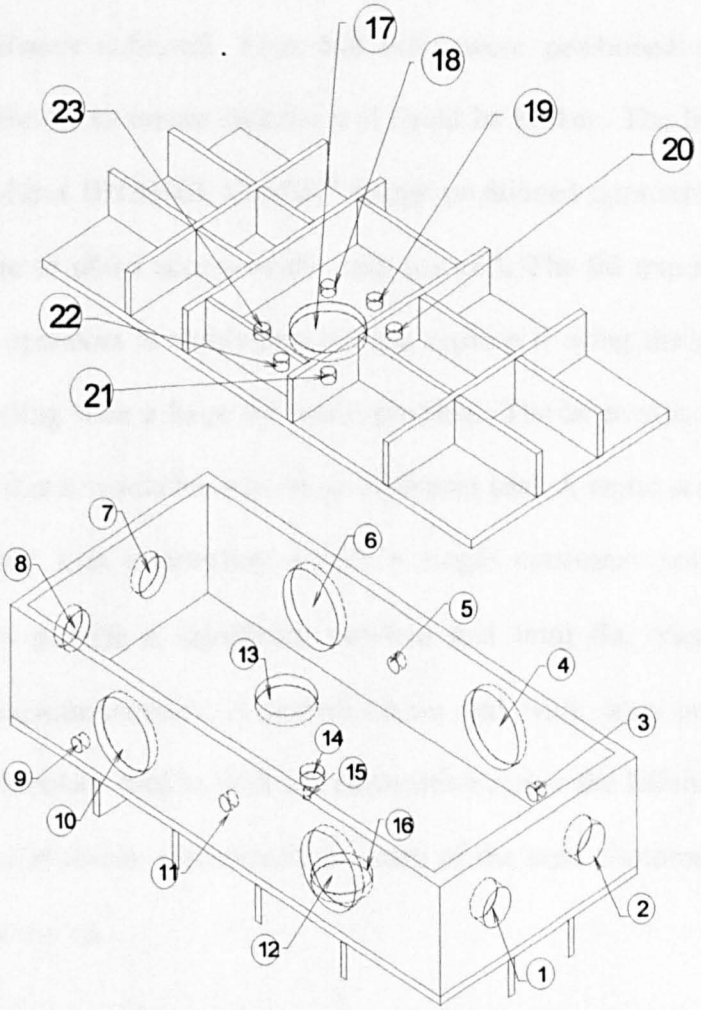

1)source flange; 2)unused; 3)detector high-voltage feedthrough;4) MS2 high-voltage feedthrough; 5)ion gauge; 6) high-voltage feedthrough collision cell optics; 7)unused; 8)unused 9)detector high-voltage and electronics feedthrough; 10) MS1 high-voltage feedthrough; 11)detector electronics feedthrough; 12)unused; 13)turbo-pump mounting flange; 14)collision-cell pumping flange; 15)swagelok fitting, gas inlet for collision cell; 16)turbo-pump mounting flange; 17) unused;18)unused; 19 detector high-voltage; 20)detector signal; 21) unused; 22) unused; 23) unused.

Fig. 37: Isometric view of the main vacuum chamber and lid.

The lid was manufactured from 25 mm thick 316L stainless steel. The lid was reinforced with ribs. The lids internal and external faces were bead-blasted to provide a clean finish. The sealing faces of the lid were polished to a sub-micron finish to ensure a good vacuum seal was always achieved. Four M8 bolts were positioned at the corners of the lid to ensure that the seal could be broken. The lid was designed with a DN200CF Conflat® flange positioned approximately in the centre to allow access to the collision-cell. The lid required at least three operators to safely remove and replace it using the gantry system. Sealing such a large lid was a problem. The large size of the seal meant that it would have to be an elastomer seal. A metal seal was impracticable. Gas permeation across a single elastomer seal was expected to provide a significant problem and limit the maximum attainable vacuum pressure. A dual elastomer seal, with rotary pumped void, was therefore used to limit gas permeation across the lid/chamber seal. Figure 38 shows a schematic diagram of the dual elastomer seal used to seal the lid.

3.05 Vacuum System.

The main chamber was pumped by two water-cooled 600 l/s turbomolecular pumps (Turbovac 600, Leybold Heraeus, Germany) mounted on two DN160CF Conflat® flanges located on the underside of the chamber. Leybold control units (TURBOTRONIK NT 20, Leybold Heraeus, Germany) powered the turbomolecular pumps. Fitting the pumps in the confined space under the vacuum chamber

proved exceptionally difficult. The turbomolecular pumps have, however, proved to be very reliable and have not had to be removed for maintenance. A tungsten filament ionisation gauge (AIG 17G, Caburn MDC, Sussex, U.K.) mounted on a DN40CF Conflat® flange monitored the pressure inside the main vacuum chamber. The ionisation gauge was connected to a PGC2 UHV Pressure Gauge Controller (Caburn MDC, Sussex, U.K.). The vacuum detection limit for the pressure monitoring system was $3x10^{-11}$ mbar.

A 25 m^3/h two-stage rotary pump (TRIVAC series, Leybold Heraeus, Germany) backed the two turbomolecular pumps and rough pumped the main chamber. A Pirani gauge (PG K16, Caburn MDC, Sussex, UK), coupled to the UHV Pressure Gauge Controller, monitored the pressure in the backing line. The fore-line vacuum flanges of the two turbomolecular pumps were connected to the rotary pump by DN40KF PVC flexible vacuum hose, downsized to DN25KF to fit the rotary pump. A standard valve was used to isolate the main vacuum chamber from the rotary pump. The high-vacuum region was protected from oil back-steaming from the rotary pump by the presence of a foreline coaxial trap (Caburn MDC, Sussex, U.K.).

An air-cooled 150 l/s turbomolecular pump (TURBOVAC 150, Leybold Heraeus, Germany) evacuated the differentially pumped collision-cell. The pump was mounted on an extension tube, which allowed the pump to hang bellow the rib structure on the underside of the chamber. The pump was air-cooled by an electrical fan mounted on the underside of the pump-body. A 12 m^3/h, two-stage rotary pump

(Edwards, UK) backed the turbomolecular pump. The turbomolecular pump's fore-line flange was connected to the rotary pump by a DN25KF stainless steel bellows pipe.

Two 55 l/s turbomolecular pumps (TURBOVAC 55, Leybold Heraeus, Germany), controlled by Leybold power supplies (TURBOTRONIK NT10, Leybold Heraeus, Germany), evacuated the source chamber. One pump was mounted directly on top of the source chamber and was connected by a 60 mm diameter pumping port sealed by a Viton® "o"-ring. The other pump was hung bellow the source chamber on a cross (Caburn MDC, Sussex, U.K.). An ion gauge (Edwards, U.K.) was used to monitor the pressure in the source region. A 10 m^3/h two-stage rotary pump (TRIVAC series, Leybold Heraeus, Germany) backed the two turbomolecular pumps. The fore-line flanges of the turbomolecular pumps were connected to the rotary pump by DN16KF stainless steel bellows tubing. The rotary pump was isolated from the source region by a high-vacuum valve. Oil back-streaming was prevented by the presence of bronze-wool element, coaxial foreline trap (Caburn MDC, Sussex, U.K.). A Pirani gauge (PG 17K, Caburn MDC, Sussex, U.K.) was used to monitor the pressure in the backing line. An 8 m^3/h two-stage rotary pump (Edwards, UK) was used to evacuate the sample inlet system. This ensured that the pressure inside the source chamber remained below acceptable limits when the probe was inserted. Brass compression fittings and 6 mm outer-diameter polythene tubing was used to make the connection

between the inlet system and the rotary pump. Figure 39 shows a schematic diagram of the complete vacuum system.

The void between the two elastomer seals of the lid was pumped by the 25 m^3/h two-stage rotary pump that backed the turbomolecular pumps evacuating the main chamber. The elastomer seals were made from Viton® cord, which was spliced and bonded with contact adhesive.

Great care was taken in the design of internal components to ensure that all voids pumped quickly and efficiently. Suitable air-bleed holes and adapted threads meant that voids were pumped quickly.

Before the chamber was pumped down for the first time it was thoroughly cleaned. This ensured that machining lubricants/coolants and particulate matter that might have damaged the turbomolecular pumps were removed. The following cleaning procedure was used to clean the internal faces of the chamber and all internal components.

1) Washed with a hot solution of detergent. Extreme care was taken to remove all metal turnings, fragments and particles.
2) Rinsed using hot water.
3) Rinsed using acetone.
4) Rinsed using methanol.
5) Rinsed with hexane
6) Rinsed with freon

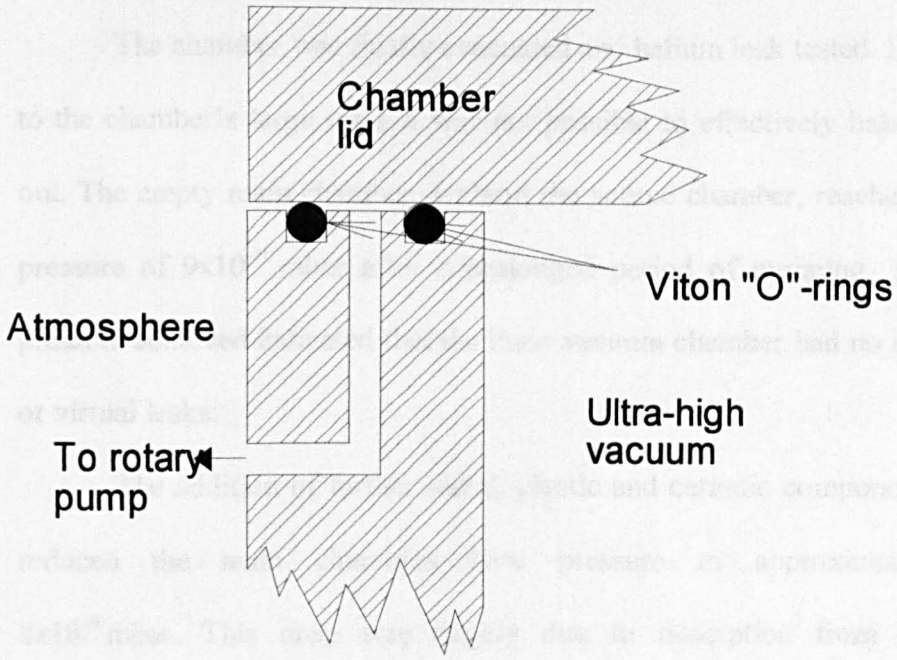

Fig. 38: Schematic diagram of the side wall and lid showing the dual "o"-ring elastomer seal.

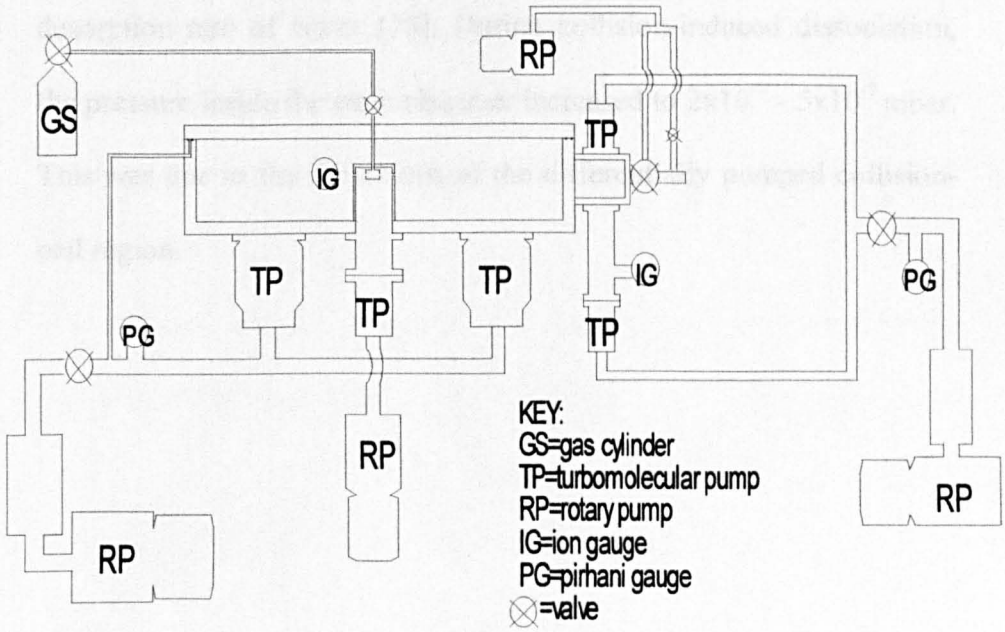

Fig. 39: Diagram showing the layout of the vacuum system.

The chamber was finally evacuated and helium leak tested. Due to the chamber's large mass it was not possible to effectively bake it out. The empty main chamber, without the source chamber, reached a pressure of $9x10^{-10}$ mbar after a prolonged period of pumping. The pressure achieved indicated that the main vacuum chamber had no real or virtual leaks.

The addition of further metal, plastic and ceramic components reduced the main chambers base pressure to approximately $8x10^{-9}$ mbar. This drop was largely due to desorption from the increased surface area and diffusion from the *in-vacuo* components. Although no residual gas analysis measurements were taken, it was likely that the base pressure of the chamber was limited by the surface desorption rate of water [10]. During collision-induced dissociation, the pressure inside the main chamber increased to $2x10^{-7}$ - $5x10^{-7}$ mbar. This was due to the limitations of the differentially pumped collision-cell region.

3.06 References.

[1] W. P. Poschenrieder, Int. J. Mass Spectrom. Ion Phys., 9 (1972) 357.

[2] J. M. B. Bakker Int. J. Mass Spectrom. Ion Phys.,6 (1971) 291.

[3] J. M. B. Bakker, Ph. D.Thesis, University of Warwick, 1969.

[4] W. P. Poschenrieder, Int. J. Mass Spectrom. Ion Phys. 6 (1971) 413.

[5] T. Sakurai, Y. Fujita, T. Matsuo, H. Matsuda, I. Katakuse, K. Miseki, Int. J. Mass Spectrom. Ion Processes, 66 (1985) 283.

[6] T. Sakurai, T. Matsuo and H. Matsuda, Int. J. Mass Spectrom. Ion Processes, 63 (1985) 273.

[7] G. M. Neumann, M. M. Sheil and P. J. Derrick, Z. Naturforsch., 39a (1984) 584.

[8] Y. Yoshida, 1986 US Patent No. 4,625,112.

[9] T. J. Cornish and R. J. Cotter, Rapid Commun. Mass Spectrom., 8 (1994) 781.

[10] A Users Guide to Vacuum Technology, J. F. O'Hanlon, Wiley and Sons, New York, 1989.

CHAPTER FOUR.

Laser Ion Source.

4.01 Factors Limiting Mass Resolution of Time-of-Flight Mass Spectrometry.

A number of factors lead to time spread at the detector plane. These factors limit the achievable mass resolution of a time-of-flight mass spectrometer. The type of ion source coupled to the time-of-flight spectrometer is an important factor in determining the mass resolution achieved. Mass resolving powers of 10,000-20,000 have been reported for non-MALDI ion sources coupled to time-of-flight spectrometers [1][2][3][4]. Such mass resolving powers have yet to be achieved using conventional MALDI TOF instruments. Indeed, mass resolving powers are typically limited to a few thousand [5][6][7]. The factors limiting achievable mass resolution are:

1) Initial energy distributions, resulting from different initial desorption velocities. Time-lag focusing and ion mirrors can partially compensate for these factors. Velocity distributions in gas-phase ion sources can lead to turnaround times. The effect can be minimised by use of strong extraction fields and long field-free regions.
2) Initial ionisation volume. The initial spatial distribution can result in the formation of kinetic energy deficits in the field-free region. Space focusing ion sources can be used to compensate for initial spatial spread.

3) Temporal spread of ion generation. Uncertainty in the time of ion generation arises from the pulse-width of the laser system or the rise-time of the pulsed extraction system. Using ultra-short pulse-width lasers and fast switching electronics can reduce these effects.
4) Post-acceleration regions. Post-acceleration regions in front of detectors can result in time broadening, because metastable fragment species have slightly shorter flight times through these regions than precursor ions.
5) Natural isotope distribution. The isotope distribution can reduce mass resolution, unless the instrument resolution is sufficiently high to resolve the isotopic peaks. This has important implications for mass calibration and mass accuracy. For proteins with masses in excess of 4,500 the binomial isotope distribution is symmetric.
6) Time broadening arising from the detection system and data system electronics. Temporal uncertainty associated with formation of secondary electrons and sample digitisation rates.
7) Space-charge effects. Ion-ion Coulombic repulsion in the source region can result in time spread. Ion-neutral collisions in desorption plume may result in kinetic energy spreads. Both factors can be minimised by careful control of the laser attenuation.
8) Ion optics and grids. Inhomogenous electric fields mean different portions of the ion beam experience different electric fields and thus have slightly different flight times. Correct choice of instrument parameters can minimise time spread associated with

grids and optics. Bergmann *et al* [8] derived theoretical treatments for the effects of grids.

4.02 Sources of Kinetic Energy Spread.

A standard practice when designing a MALDI ion source is to use a strong electric field in the extraction region. This is principally done to minimise three effects. Strong extraction fields minimise turnaround times. Ion mirrors cannot compensate for differences in time spent in the acceleration region. Therefore by making the extraction region short, with a large voltage difference applied across it, it is possible to minimise the degradation of resolution resulting from differences in time spent in the acceleration region. The MALDI process is commonly thought to involve a rapid solid-phase to gas-phase transition, followed by a jet expansion or pulsed hydrodynamic flow into the vacuum region [9][10][11][12][13]. The velocities of the desorbed species are largely independent of their mass. By maximising the acceleration voltage it is possible to minimise the effect of the initial desorption velocity, by making it a small fraction of the ion's total kinetic energy in the drift region.

Prompt ionisation or desorption of pre-formed ions would mean that ions possessed kinetic energies in the drift region derived from the extraction voltage, plus an excess kinetic energy arising from the desorption energy. The jet expansion model predicts that all ions, irrespective of mass, achieve approximately the same desorption velocity. High-mass ions possess larger desorption energies than low-

mass ions. These observations are broadly supported by field-free experiments, conducted by various groups [13][14][15][16][17][18][19][20][21], to determine the desorption velocities and energies of various species.

Experiments to determine the kinetic energy of ions, formed by MALDI in high-voltage ion sources, show that some ions possess an energy deficit in the field-free drift space. These experiments can be divided into two basic types. The simplest method is the retarding field method [22], in which a mesh with a retarding potential is placed in the path of the ion beam. By scanning the retarding voltage the kinetic energy distribution of the ions can be measured. There are several problems associated with this technique. Grid micro-optics and inhomogenous electric fields limit the accuracy with which the kinetic energy can be determined. Another major disadvantage of the technique is that it relies on measuring the signal intensity in order to determine the kinetic energy distribution. This can be especially problematic when the technique is applied to MALDI generated ions, because the shot-to-shot signal reproducibility of MALDI is poor.

The second method uses an electrostatic-sector analyser (ESA) [23][24][25] to measure the kinetic energy of the ions. The technique is more complex, but provides a greater degree of accuracy. Both techniques show that a large number of the ions produced in high-voltage MALDI ion sources possessed large kinetic energy deficits. This is to say that ions formed in MALDI ion sources possess translational energies less than the accelerating potential. Experiments

conducted by Standing and co-workers [26] indicated that the kinetic energy deficit was strongly influenced by the electric-field strength in the acceleration region. Stronger extraction fields resulted in larger energy deficits than weak extraction fields. Standing and co-workers [22] also noted that the energy deficit increased with increasing protein mass.

There are several factors that result in the formation of kinetic energy deficits. It is likely that a large proportion of the analyte ions are formed by gas-phase ionisation processes, such as protonation and cation attachment, in the desorption-plume [27][28][29]. Various research groups [30][31] have shown experimentally that gas-phase cationisation processes can result in ion formation. Ions formed in the gas-phase are further from the repeller plate when they experience the accelerating field than those formed promptly. The ions formed in the gas-phase acquire less kinetic energy than those formed at the surface of the probe.

The second process involves the ion's progress through the acceleration region being impeded by collisions with neutral species present in the desorption plume. The observation that delayed extraction reduces the amount of metastable fragmentation has been cited as evidence of this [20][32].

A further possible explanation for the formation of kinetic energy deficits is sample surface and repeller surface irregularities. Different regions of a crystalline sample protrude from the probe tip to different extents. This means that ions formed in "valley" regions,

close to the probe surface, acquire more kinetic energy than those formed from protruding crystals. This effect is dependent upon the dimensions of the crystals. In turn the dimensions of the crystals are dependent upon sample preparation considerations, such as solvent evaporation rate, temperature, humidity etc.

It is likely that the MALDI mechanism is a highly complex aggregate process, involving a large number of individual processes and interdependent effects. The mechanistic considerations are likely to be altered by different analyte/matrix combinations, sample preparation protocols etc.

It has been suggested that ions formed by MALDI can be generated by two separate but concomitant mechanisms: the so-called two-component mechanism [29]. Under this model ions can be promptly formed or pre-formed [33] at the probe surface and desorbed into the gas-phase, or desorbed as neutral species and ionised in the gas-phase.

4.03 Temporal Distributions.

The finite length of the ionisation event limits the maximum instrument resolution. For a MALDI ion source or laser desorption ion source the pulse-width of the ionising laser limits the time over which ions are formed. It has been shown that desorption continues for a considerable time after the laser pulse [34], but that the observed ions are generated promptly [35].

The laser systems used in MALDI typically have pulse-widths (FWHM) in the 100's of picoseconds to 10's of nanoseconds range. It has been found that the laser pulse-width has little influence on MALDI mass spectra [36][37][38]. This indicates that the energy density, or fluence (J/cm^2), determines the desorption/ionisation process, as opposed to the rate of energy flow or irradiance (W/cm^2).

The most commonly used laser system in MALDI instruments is the nitrogen laser, supplying photons at 337 nm (3.68 eV). The nitrogen laser's relatively low-cost, compact size and instant operation make it ideal.

4.04 Angular Distribution of Ions.

The initial angular distribution of the ions has important implications for the properties of the ion beam and the associated ion optics. An accurate understanding of the initial angular spread is an important aid to realistic ion optical modelling of any instrument. Several groups have studied the angular distribution of ions generated by MALDI. Ayala *et al* [39] determined the initial angular spread of poly-DL-alanine, using 2,5-dihydroxybenzoic acid matrix. A 355 nm, frequency tripled Nd:YAG laser, incident at an angle of 26° to the normal was used. The experiment determined the angular distribution of the neutral analyte molecules in a field-free region. The experiments showed that most of the ions possessed angular spreads of +80°/-80° in both the azimuthal and polar directions. Bökelmann and co-workers [15][28] conducted angular resolved time-of-flight experiments to

determine the angular distribution of MALDI generated ions. Their experiments showed that DHB monomer ions, generated from neat DHB prepared by the dried droplet method, were produced over an angular spread of +65°/-65° about the normal. Bökelmann and co-workers noted that the majority of ions were generated within a spread of +30°/-30° about the normal. Results for alkali metal ions showed that virtually all ions were produced within a spread of +65°/-65° and that the majority of ions were produced within +30°/-30°. Results for substance P, with DHB matrix (dried droplet sample preparation method), showed angular distributions of +75°/-75°.

Zhang *et al* [19] conducted a series of experiments to determine the axial and radial velocity components of ions formed by MALDI. Their results indicated that the majority of dynorphin 1-13 ions were produced with an angular spread of +33°/-33°, while α-cyano-4-hydroxycinnamic acid dimer ions were produced with an angular spread of +45°/-45°. The studies showed that the axial velocity component was considerably greater than the radial velocity component. These findings support the jet expansion model of MALDI ion formation.

Experiments have shown that the initial direction of travel of ions is biased towards the laser beam, and that species possess a cosine intensity/angle distribution [39][40][41][42]. Figure 40 shows a diagram showing this effect.

4.05 TOF-TOF Spectrometer Ion Source.

The purpose of the ion source was to generate and then focus/collimate the ions to provide an ion beam with suitable dimensions/properties to traverse the TOF-TOF spectrometer. The TOF-TOF spectrometer was designed to utilise a laser ionisation ion source capable of laser desorption/ionisation and MALDI. A standard nitrogen laser (VSL 337 ND, Laser Science Inc., Newton, MA, USA) with an output wavelength of 337 nm was used as the desorption/ionisation laser. The laser had a pulse-width of 4ns (FWHM) and supplied 40 μJ pulses. The laser system and accompanying optics were supported on an aluminium bench that was designed and built in-house. Four M8 bolts secured two brackets to the side of the main vacuum chamber, which in turn supported the bench. A grid network of M6 tapped holes in the bench allowed optical components to be positioned and clamped. A micrometer controlled variable attenuator (Newport, Irvine, CA, USA) was used to control the laser fluence. The attenuator was a rotating quartz-wedge type, using the principle of Fresnel reflection to induce attenuation. The laser beam was focused onto the probe assembly by an externally mounted, 500 mm focal length, biconvex lens (Comar, Cambridge, UK). The lens was mounted in a support clamp (Newport, Irvine, CA, USA) that allowed 1 cm lateral travel for precise positioning of the focal point. The laser beam was reflected into the source vacuum chamber by two UV protected, aluminised mirrors (Comar, Cambridge, UK) mounted on kinematic mirror supports (Newport, Irvine, CA, USA). A final in-vacuum aluminised mirror (Comar,

Cambridge, UK) reflected the laser beam onto the probe target at an angle of incidence of 45° with respect to the ion optical axis. Two iris diaphragms (Newport, Irvine, CA, USA) were positioned along the path of the laser beam and securely fastened. The trigger pulse for the time-of-flight clock was provided by a fast UV photodiode, triggered by a reflection. A black and white CCD camera was positioned so as to observe the region of ion production. This aided the alignment of the laser beam on the target.

The ion source was conceived as a continuous extraction ion source. The ion source was a gridless design [43] to maximise transmission. The presence of grids would have resulted in collisions between the ions and the grid wires, thus reducing transmission and inducing fragmentation. The source was modelled using SIMION version 6 [44].

The ion source had to be capable of accelerating ions to the high kinetic energies demanded by high-energy CID. The lensing system in the ion source needed to be capable of collimating a high-energy ion beam. The only control over the electric-field strength was the separation distance between the repeller plate and the counter-electrode. There were several important considerations when determining the electric-field strength. To minimise the effect of space-charge and turn-around time it was necessary to maximise the extraction field strength. This also minimised source residence time. A strong extraction field provided superior beam collimation.

There were, however, resolution degrading effects which were aggravated by the use of strong extraction fields. The energy deficits, produced when ions were formed by delayed gas-phase ionisation, were increased. High electric-field strengths also resulted in increased metastable decomposition of certain susceptible species. This occurred because ions were more rapidly accelerated through the neutral desorption plume, they therefore experienced more energetic collisions and hence acquired more internal energy.

The TOF-TOF spectrometer used a 5 mm acceleration gap, resulting in field strengths of between 20 kV/cm and 40 kV/cm. The TOF-TOF spectrometer's ion source was a strong electric-field ion source. For the sake of simplicity a single-stage ion source, capable of first-order space focusing, was used on the prototype instrument.
This meant that the position of the space focus was determined solely by the geometry of the extraction region:

$$D = 2s_a \qquad 4.01$$

D is the position of the space focus and s_a is approximately the separation of the repeller electrode and counter-electrode.
The space-focus plane was located approximately 15 mm from the repeller electrode. The design of the ion source needed to provide provision for future developments, such as the incorporation of two-stage extraction fields and pulsed-extraction techniques. The ion source was mounted in a separate chamber and the source optics were mounted in such a way that they could easily be removed and replaced.

After the extraction region the ion beam had to be focused and collimated by suitable electrostatic lens assemblies. Cylindrical symmetry Einzel lenses were used because of their simple construction and operation. The Einzel lenses were operated in an accelerating arrangement; *i.e.* negative potentials were applied to the central lens elements to minimise time aberrations. The geometry, spacings and potentials of the ion source were modelled using SIMION. In order to achieve meaningful simulations of the ion source region it was necessary to possess an understanding of the basic physics involved in the MALDI process and the physical properties of the ions.

4.06 Laser Spot Size.

The finite size of the laser spot on the probe defined the minimum radial area over which ions were created. Jet expansion, followed by delayed gas-phase ionisation, would have further increased the radial dimensions of the ionisation region. The beam waist diameter of a laser beam can be estimated using Gaussian beam optics:

$$2w_0 = \left(\frac{4\lambda}{\pi}\right)\left(\frac{F}{D}\right) \qquad 4.02$$

w_0 is the Gaussian beam radius, λ is the wavelength, F is the focal length of the lens and D is the diameter of the beam emerging from the laser. Performing this calculation for the nitrogen laser used on the TOF-TOF spectrometer provided a beam waist of 13 microns. The intensity was theoretically $1/e^2$ or 0.135 that of the axial intensity at that beam diameter. The intensity at 26 microns beam diameter was

theoretically 0.03 % of the axial intensity. The laser spot was subsequently measured by placing photosensitive paper on the probe tip and firing the laser at the target. The burn mark was then placed under a microscope equipped with a CCD camera and its dimensions measured. Figure 41 shows a typical CCD image of the burn mark. The spot was approximately elliptical in shape, with dimensions of: 170 microns wide by 100 microns high. For the purposes of simulating the ion source the measured dimensions were used.

4.07 Modelling of the Ion Source using SIMION.

The gridless ion source was designed using the ray-tracing program SIMION, version 6 [44]. Figure 42 shows a schematic diagram of the ion source and associated lenses. Ions with various initial parameters were flown through the ion source to determine the properties of the ion source. The complex nature of the MALDI process, along with gaps in our knowledge, made accurate modelling of the ions initial properties difficult. It was difficult to accurately determine and relate the significance of the various statistical probability distributions, *i.e.* initial velocity distribution, initial angular distribution, initial spatial distribution and initial temporal distribution. The ion source was modelled at a mesh density of 50 grid units/mm and the ion mirrors at 1 grid unit/mm. The Over Relaxation Factor = 0.9, the Historical Memory Factor = 0.7 and the Convergence Criteria = $<5x10^{-5}$ V. The simplest approach, when modelling the ion source, was to consider the point of ion production to be constrained to a point

located on the surface of the repeller plate. The ions were then generated from

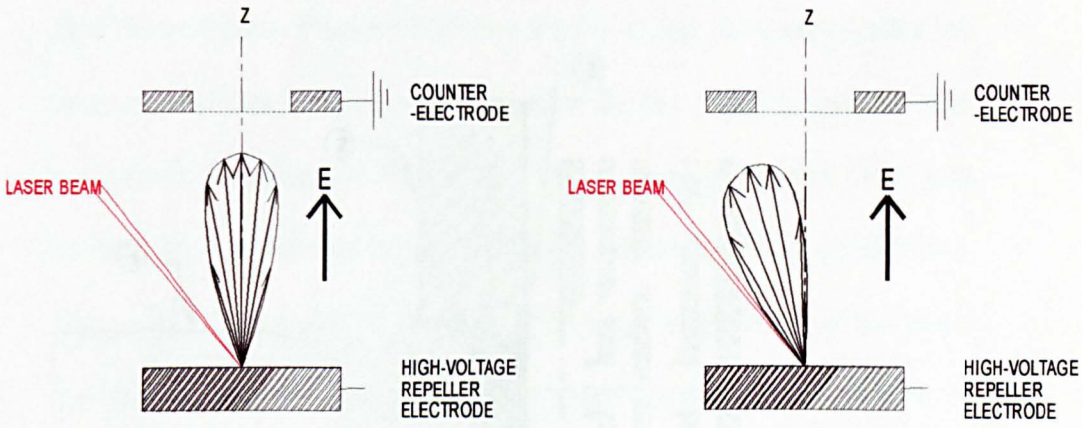

Fig. 40: Schematic diagram illustrating perpendicular velocity distribution (left) and skewed velocity distribution, angled towards the laser beam (right).

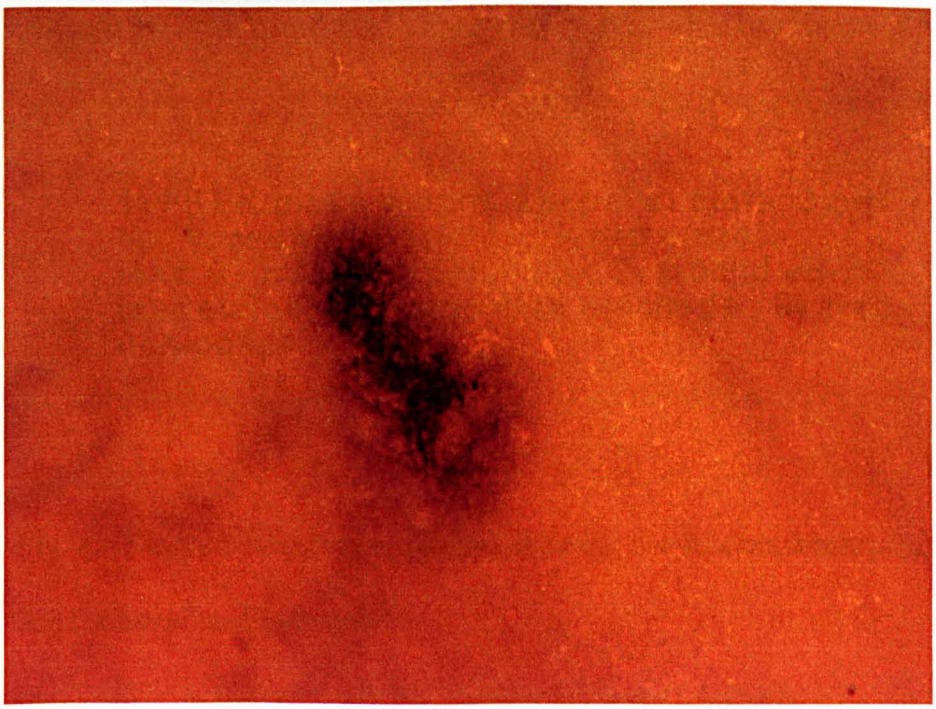

Fig. 41: CCD image of typical burn mark left by laser beam. The spot was 170 microns (longest axis) by 100 microns (perpendicular to longest axis).

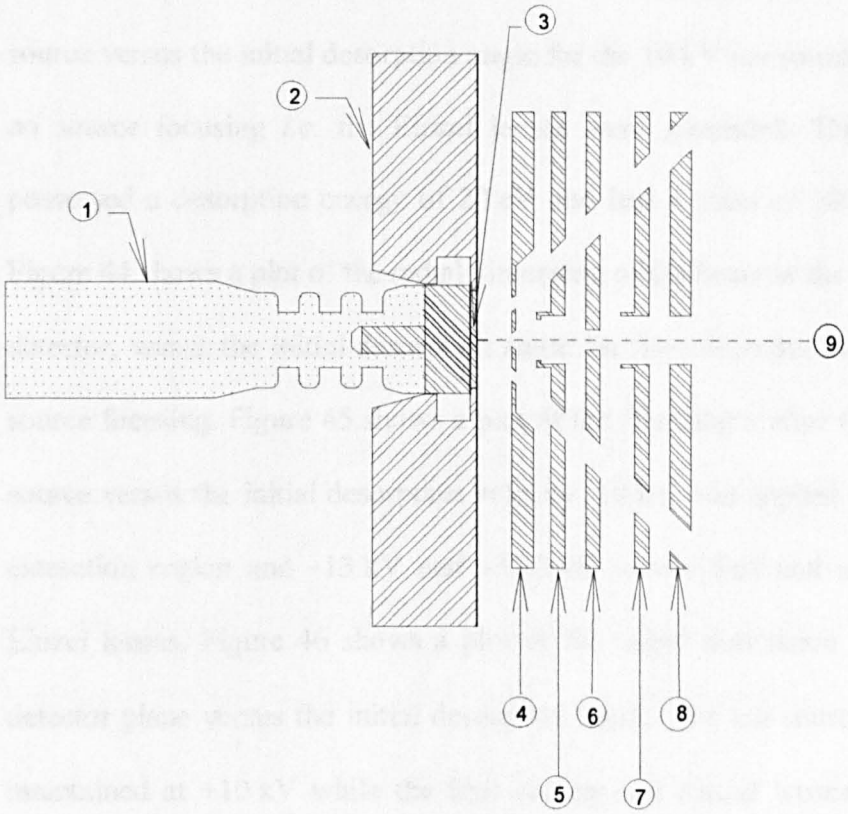

1) PEEK probe mount; 2)repeller plate; 3)probe tip; 4; counter-electrode; 5) first einzel lens; 6) grounded electrode; 7) second einzel lens element; 8) grounded electrode ; 9) z-axis (ion-optical axis).

Fig. 42: Diagram of the source region showing the acceleration region and the associated lens system.

this point with angular and energetic spreads. The focusing and collimating properties of the extraction region and lens system were then investigated. Figure 43 shows a plot of the final angle after the source versus the initial desorption angle for the 10 kV ion source with no source focusing *i.e.* the Einzel lenses were grounded. The ions possessed a desorption energy of 20 eV and had a mass of 1000 Da. Figure 44 shows a plot of the radial dimension of the beam at the linear detector, versus the initial desorption angle for the ion source with no source focusing. Figure 45 shows a plot of the final angle after the ion source versus the initial desorption velocity. 10 kV was applied to the extraction region and −13 kV and −12.7 kV to the first and second Einzel lenses. Figure 46 shows a plot of the radial dimension at the detector plane versus the initial desorption angle. The ion source was maintained at +10 kV while the first and second Einzel lenses were maintained at −13 kV and −12.7 kV respectively. The point source approximation estimated the beam divergence to be ±0.15°. The beam diameter at the linear detector was estimated to be 9 mm.

In order to model the effect of spatial spread on the beam diameter and angular divergence, ions possessing a range of initial radial positions were modelled. This allowed the effect of laser-spot size and laser alignment to be estimated. Figure 47 shows plot of the radial position at the linear detector versus the initial radial position. Figure 48 shows a plot of the angular divergence versus the initial radial position. The source was maintained at +10 kV and the Einzel lenses were grounded for both calculations. Figure 49 shows a plot of

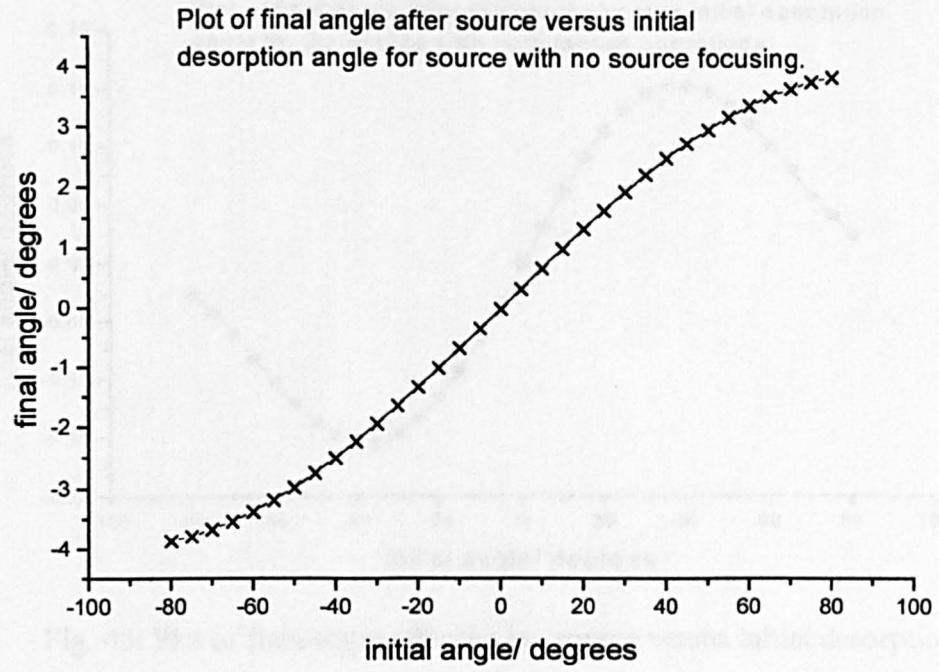

Fig. 43: Plot of final angle after the ion source versus initial desorption angle, for 10 kV accelerating potential with no source focusing.

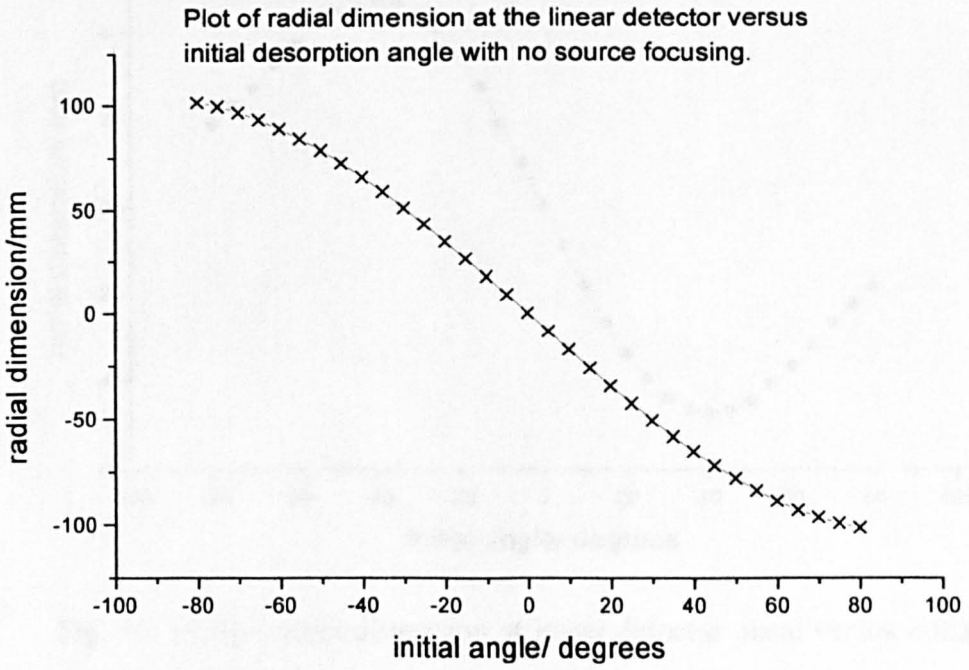

Fig. 44: Plot of radial dimension at linear detector versus initial desorption angle, for 10 kV ion source with no source focusing.

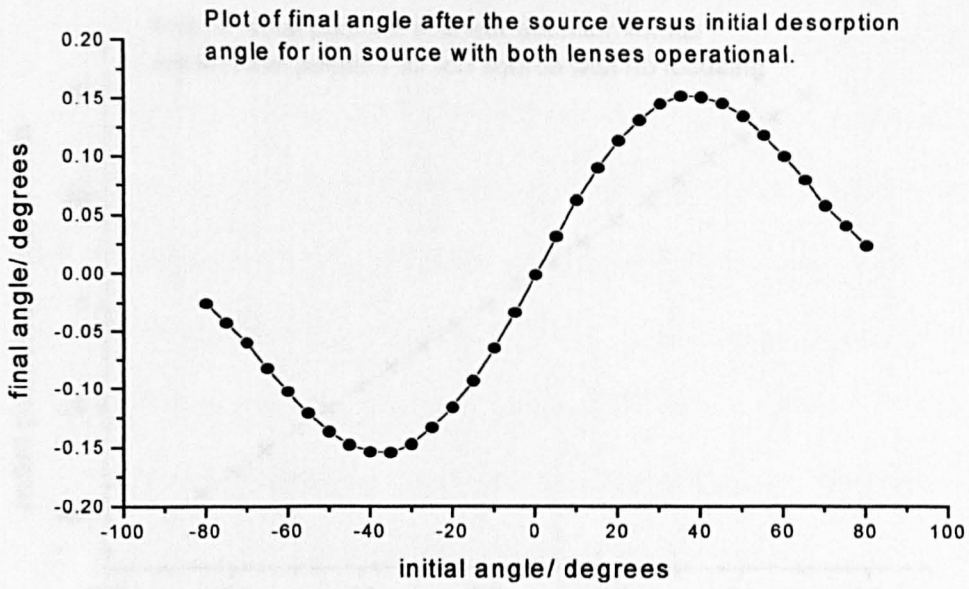

Fig. 45: Plot of final angle after the ion source versus initial desorption angle, for 10 kV acceleration with first Einzel lens at –13 kV and second at –12.7 kV.

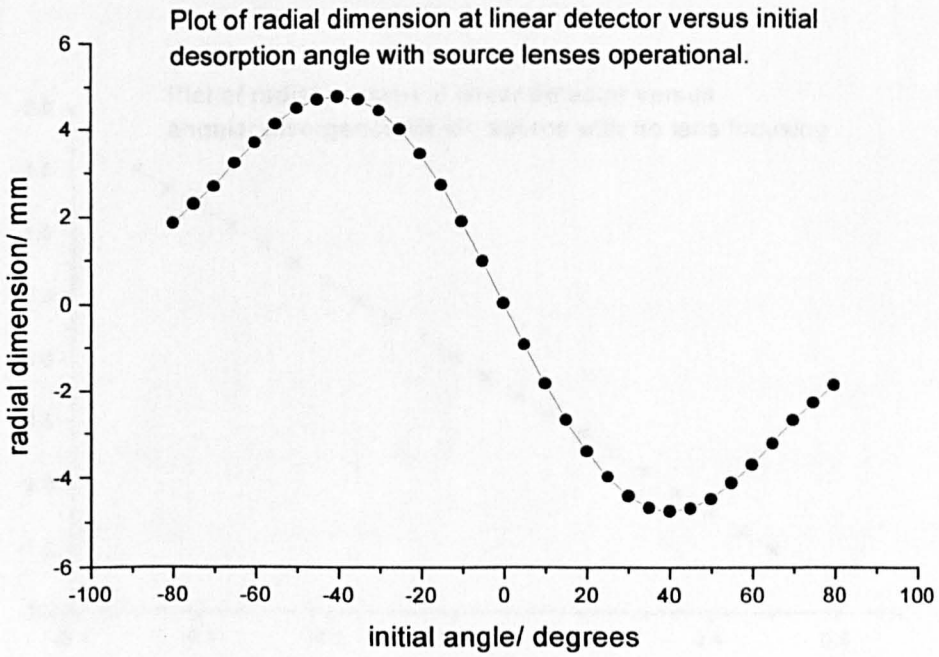

Fig. 46: Plot of radial dimension at linear detector plane versus initial desorption angle, for 10 kV extraction voltage with first Einzel lens at –13 kV and second at –12.7 kV.

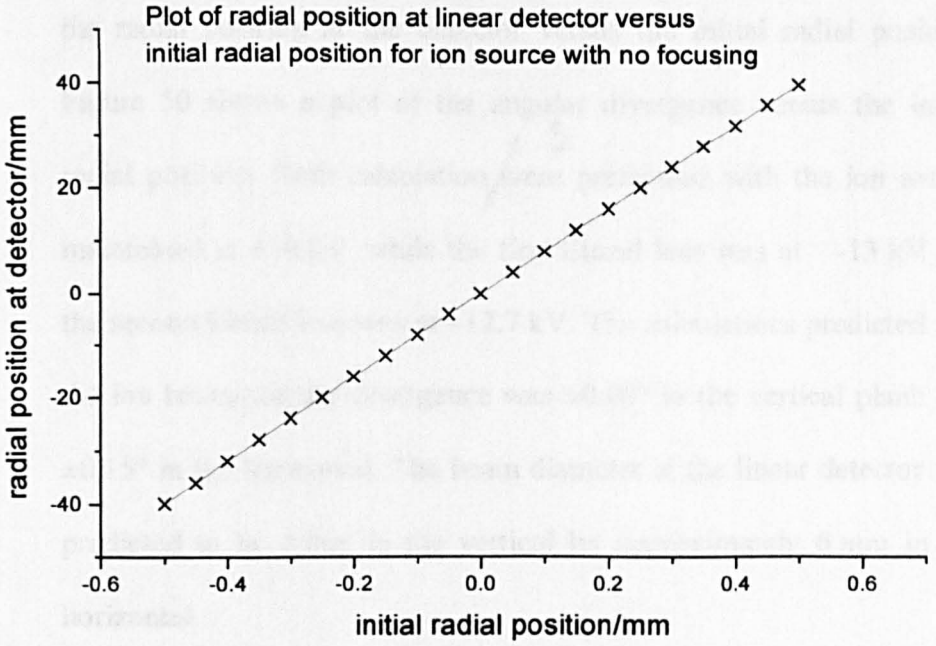

Fig. 47: Plot of radial position at detector plane versus initial radial position. The ion source was maintained at +10 kV, while the Einzel lenses were grounded.

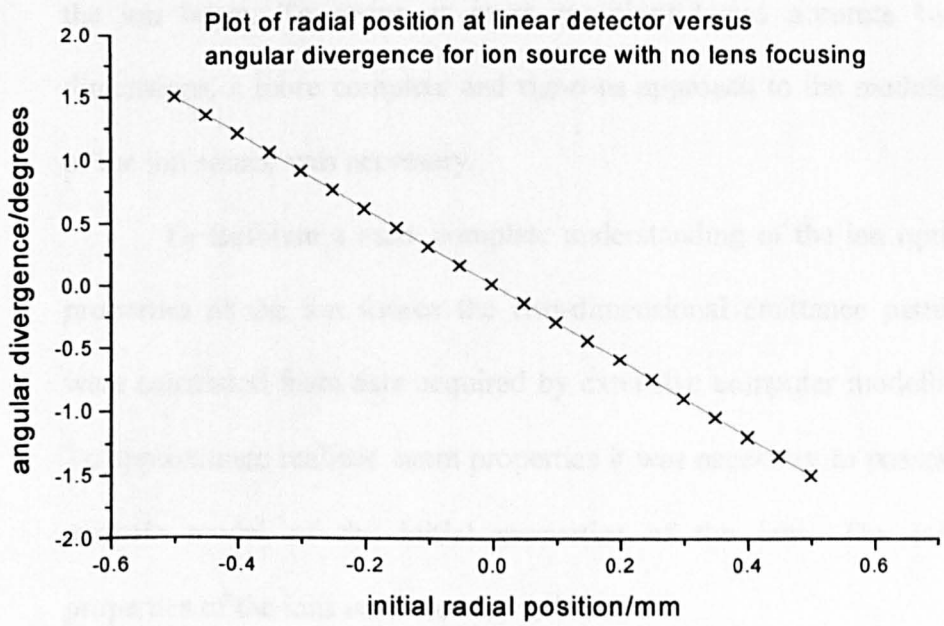

Fig. 48: Plot of angular divergence after the source versus initial radial position. The source was maintained at +10 kV, while the lenses were grounded.

the radial position at the detector versus the initial radial position. Figure 50 shows a plot of the angular divergence versus the initial radial position. Both calculation were performed with the ion source maintained at +10 kV, while the first Einzel lens was at -13 kV and the second Einzel lens was at –12.7 kV. The calculations predicted that the ion beam angular divergence was ±0.08° in the vertical plane and ±0.15° in the horizontal. The beam diameter at the linear detector was predicted to be 4 mm in the vertical by approximately 6 mm in the horizontal.

The point source approximation oversimplified the MALDI process as it negated the combined effects of energy spread, angular spread, temporal spread and spatial spread. The point source approximation under predicted the angular divergence and diameter of the ion beam. To arrive at more meaningful and accurate beam dimensions, a more complete and rigorous approach to the modelling of the ion source was necessary.

To facilitate a more complete understanding of the ion optical properties of the ion source the two-dimensional emittance patterns were calculated from data acquired by extensive computer modelling. To approximate realistic beam properties it was necessary to possess a realistic model of the initial properties of the ions. The initial properties of the ions used were as follows:

1) +/-0.085 mm spatial spread in the z-x (horizontal) plane. This dimension was estimated from the long axis of the elliptical laser spot.

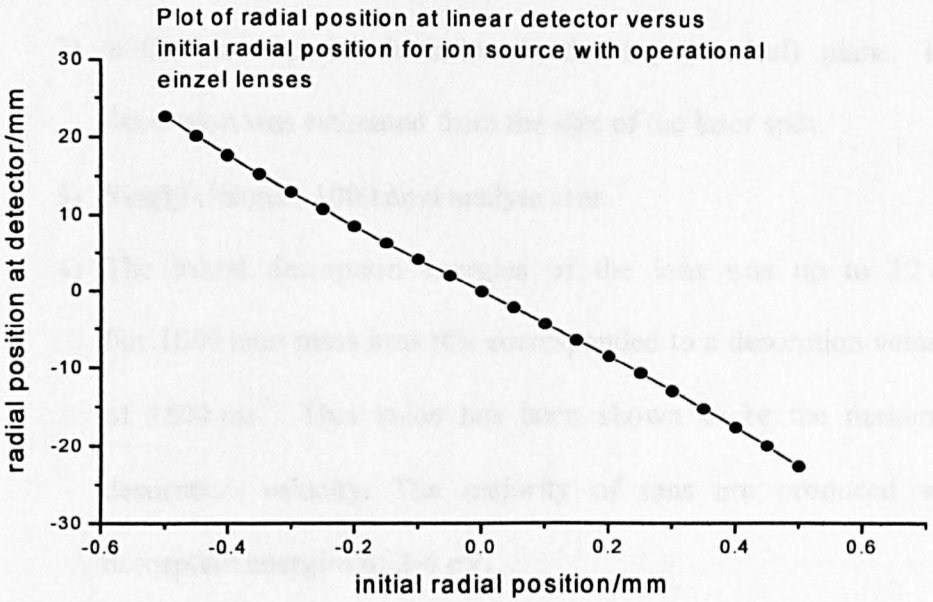

Fig. 49: Plot of radial position at the detector plane versus initial radial position. Ion source was at +10 kV, first Einzel lens =-13 kV, second Einzel lens =-12.7 kV.

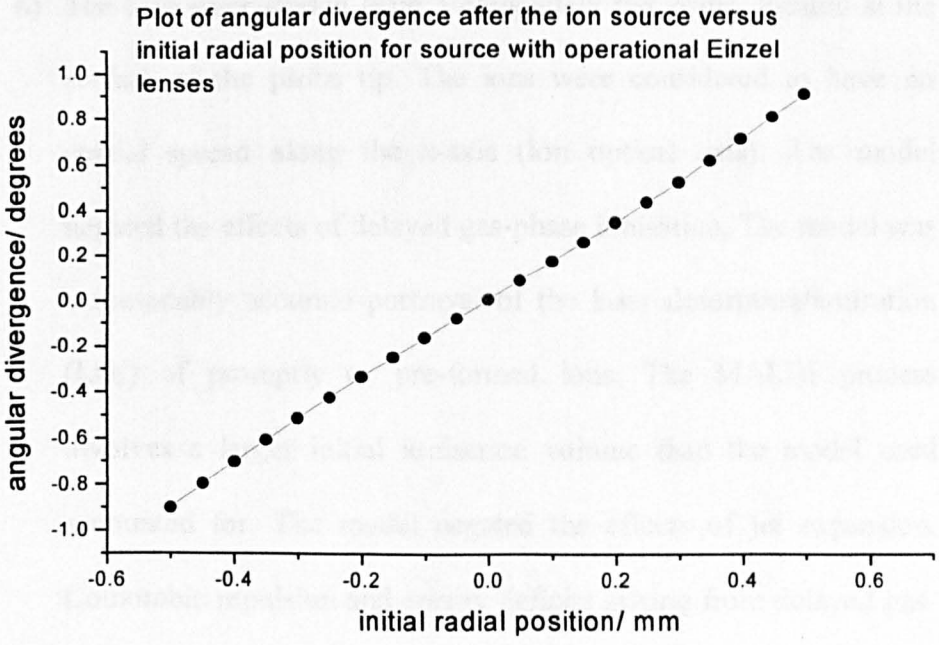

Fig. 50: Plot of angular divergence versus initial radial position. Source was maintained at +10 kV, first Einzel =-13 kV, second Einzel lens=-12.7 kV.

2) +/-0.05 mm spatial deviation in the z-y (vertical) plane. This dimension was estimated from the size of the laser spot.
3) Singly charged, 1000 amu analyte ions.
4) The initial desorption energies of the ions was up to 12 eV. For 1000 amu mass ions this corresponded to a desorption velocity of 1500 ms^{-1}. This value has been shown to be the maximum desorption velocity. The majority of ions are produced with desorption energies of 3-4 eV.
5) The ions maximum initial angular deviation from the normal was +/-80°. Literature published values showed that virtually all ions were produced within this angular spread while the majority were produced within +/-30°.
6) The ions were started from a completely flat plane, located at the surface of the probe tip. The ions were considered to have no spatial spread along the z-axis (ion optical axis). The model negated the effects of delayed gas-phase ionisation. The model was a reasonably accurate portrayal of the laser desorption/ionisation (LDI) of promptly or pre-formed ions. The MALDI process involves a larger initial ionisation volume than the model used accounted for. The model negated the effects of jet expansion, Coulombic repulsion and energy deficits arising from delayed gas-phase ionisation.
7) The angle and position of the ion trajectories were recorded at the entrance to the single-stage ion mirror (MS-1).

Figure 51 shows a diagram illustrating the relationship between the laser spot and the main axes.

4.08 Emittance Diagrams.

Emittance diagrams are a powerful method of displaying the spatial and angular characteristics of an ion beam. Consider an ideal point source. Downstream of the ion source the angular divergence results in a spatial spread. For a perfect point source ions with a certain radial position must possess a definite angular divergence. For a real source, in which the ionisation region is not confined to a point source, the ions may possess a range of angular divergences. The strength of the emittance plot is that it can represent the combined spatial and angular properties of an ion beam. Figure 52 shows a schematic diagram illustrating the emittance pattern from an ideal point source and the emittance pattern arising from a source with combined initial spatial and angular spread. Emittance diagrams are not necessary to represent ideal point sources.

By calculating the emittance pattern in the vertical plane (representing the spatial and angular spread in the vertical plane) and the emittance pattern in the horizontal plane (representing the spatial and angular spread in the horizontal plane) the dimensions and angular properties of the ion beam can be described. Emittance patterns do not relate the initial characteristics of the ions to the properties of the ions in the beam. It was therefore necessary to explicitly define the initial properties of the ions.

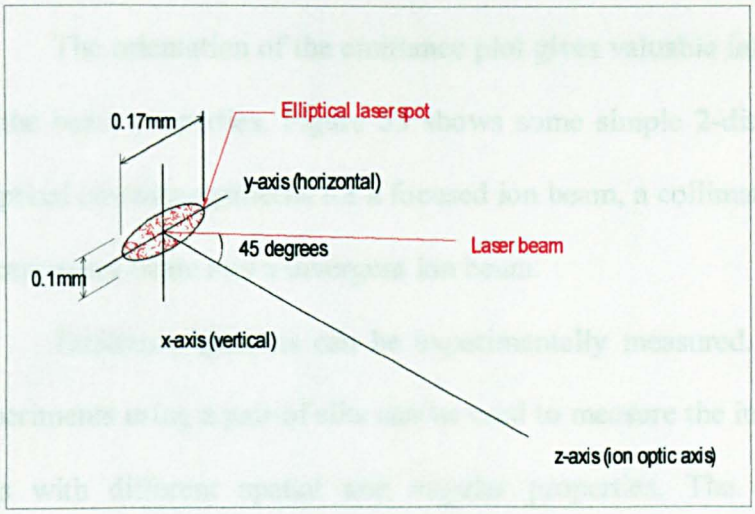

Fig. 51: Diagram showing relationship between the main axes, the laser beam and the laser spot.

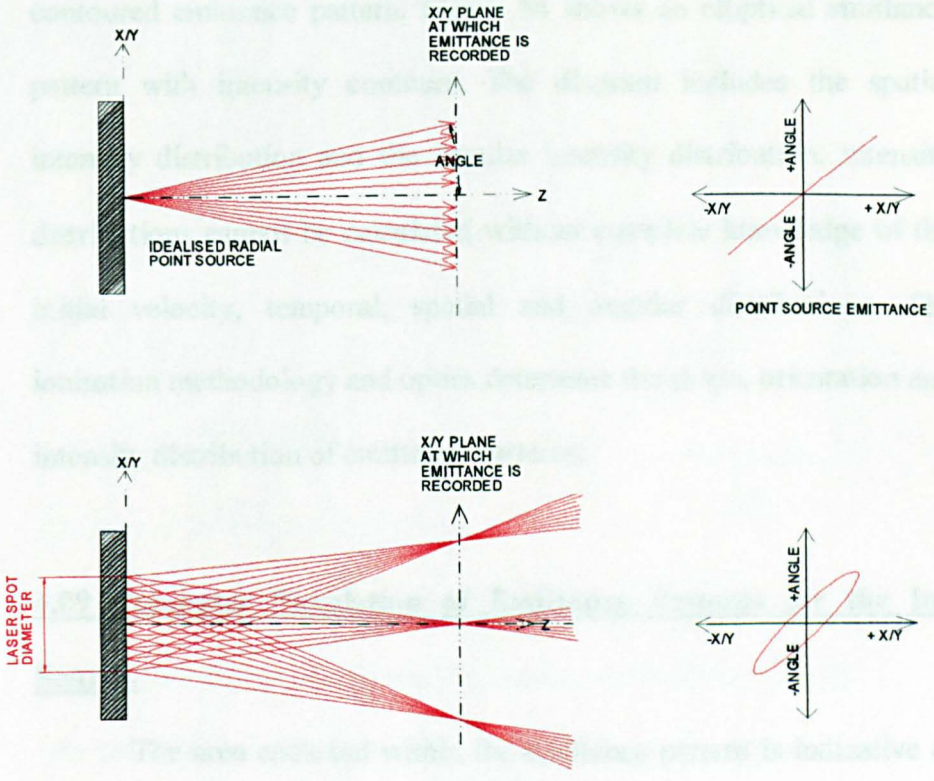

Fig. 52: Schematic diagram illustrating the simple emittance pattern of an ideal point source and the emittance pattern generated by a source when angular divergence and initial spatial spread are combined.

The orientation of the emittance plot gives valuable information on the beam properties. Figure 53 shows some simple 2-dimensional elliptical emittance patterns for a focused ion beam, a collimated beam, a convergent beam and a divergent ion beam.

Emittance patterns can be experimentally measured. Practical experiments using a pair of slits can be used to measure the intensity of ions with different spatial and angular properties. The emittance pattern can include information on the angular and spatial intensity distributions. The intensity distribution can be represented as a contoured emittance pattern. Figure 54 shows an elliptical emittance pattern with intensity contours. The diagram includes the spatial intensity distribution and the angular intensity distribution. Intensity distributions cannot be calculated without complete knowledge of the initial velocity, temporal, spatial and angular distributions. The ionisation methodology and optics determine the shape, orientation and intensity distribution of emittance patterns.

4.09 Computer Simulation of Emittance Patterns for the Ion Source.

The area enclosed within the emittance pattern is indicative of the beam properties. Figure 55 and figure 56 show the emittance patterns for the ion beam in the z-x (horizontal) and z-y (vertical) planes.

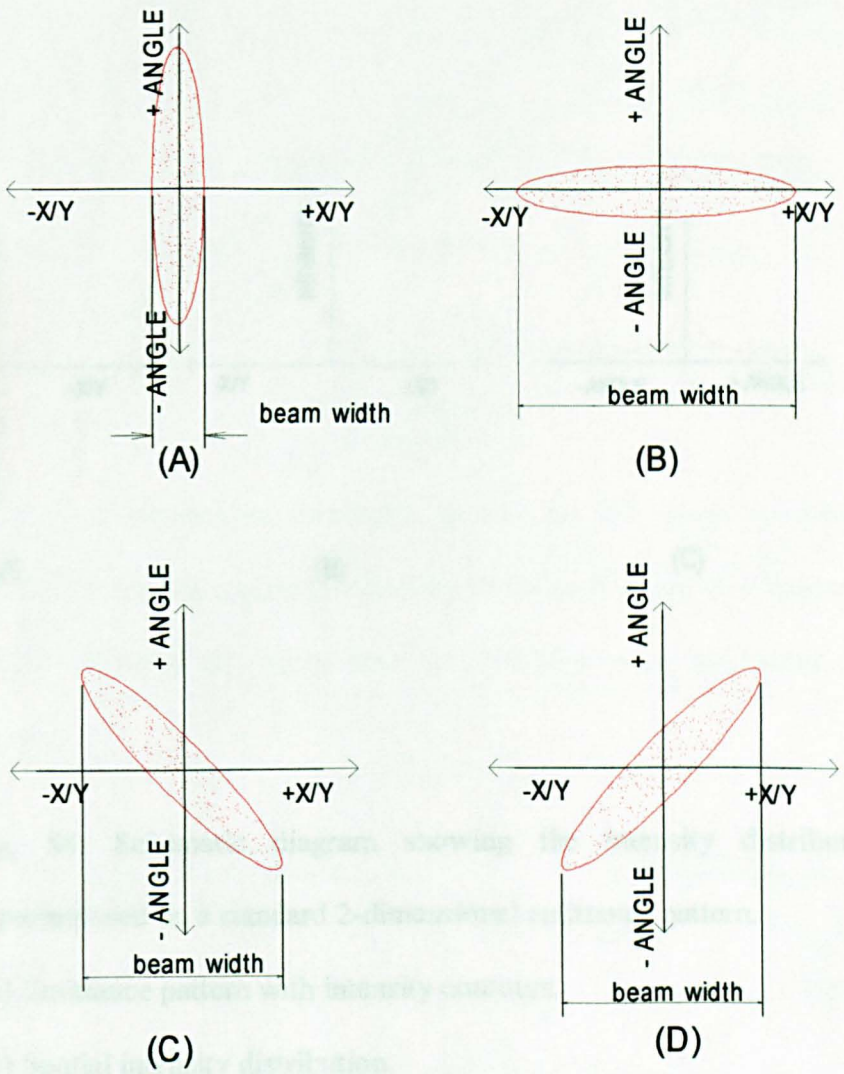

Fig. 53: Elliptical, 2-dimensional emittance patterns.

(A) At a focal point (large angular spread, small spatial spread).

(B) Collimated ion beam (small angular spread, larger spatial spread).

(C) Convergent ion beam.

(D) Divergent ion beam.

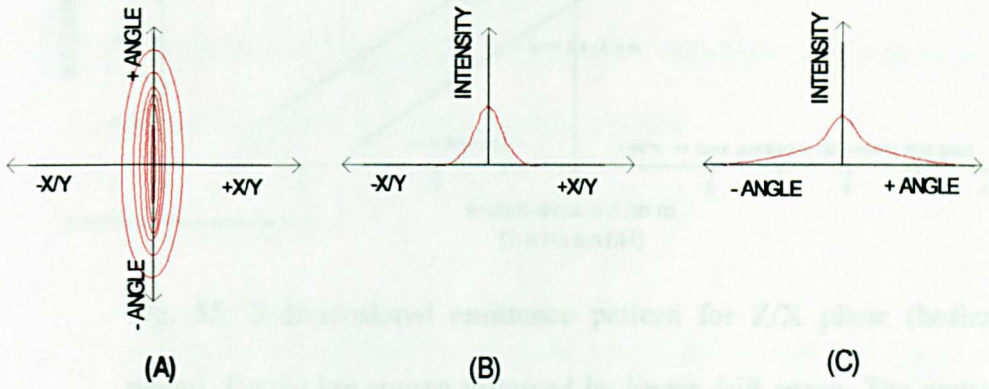

Fig. 54: Schematic diagram showing the intensity distribution superimposed on a standard 2-dimensional emittance pattern.

(A) Emittance pattern with intensity contours.

(B) Spatial intensity distribution.

(C) Angular intensity distribution.

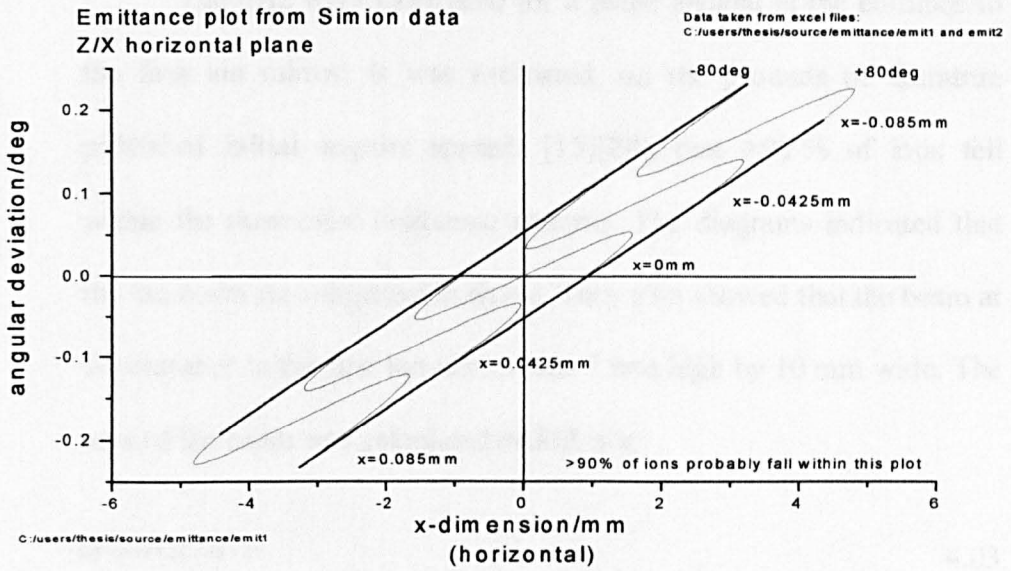

Fig. 55: 2-dimensional emittance pattern for Z/X plane (horizontal plane), for the ion source followed by linear drift space. The emittance pattern included the beam halo *i.e.* >90 % of ions fell within this pattern.

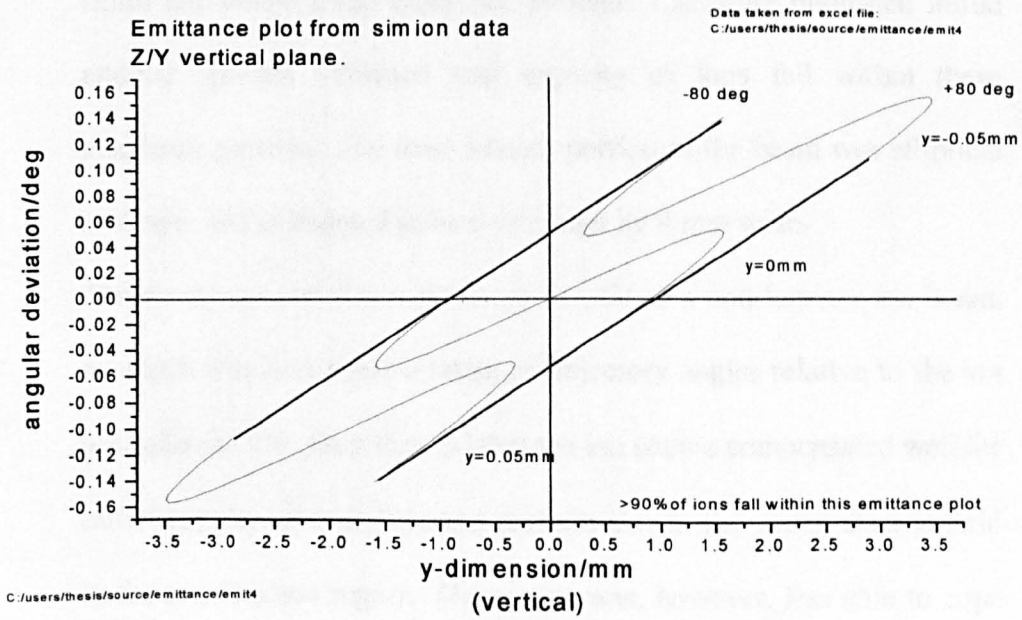

Fig. 56: Emittance pattern for Z/Y plane (vertical plane), for the ion source followed by drift space. Emittance patterns enclosed >90 % of ions.

The data were calculated for a plane located at the entrance to the first ion mirror. It was estimated, on the grounds of literature published initial angular spreads [15][28], that >90 % of ions fell within the theoretical emittance patterns. The diagrams indicated that the ion beam was elliptical in shape. They also showed that the beam at the entrance to the first ion mirror was 7 mm high by 10 mm wide. The area of the beam was calculated as follows:

$$area = \pi \cdot a \cdot b \qquad 4.03$$

a is half the length of the shortest axis and b is half the length of the longest axis.

Figure 57 and figure 58 show the z-x plane (horizontal) and z-y plane (vertical) emittance patterns. The most intense portion of the ion beam fell within these emittance patterns. Literature published initial angular spreads indicated that majority of ions fell within these emittance patterns. The most intense portion of the beam was elliptical in shape, and calculated to be 6 mm high by 9 mm wide.

The emittance patterns were characteristic of a non-laminar ion beam, in which ions possessed a range of trajectory angles relative to the ion optical axis. The plots showed that the ion source compensated well for initial angular spread. This was partially due to the strong electric field in the acceleration region. The source was, however, less able to cope with initial spatial spread (laser-spot diameter) and in particular the combined effects of initial spatial spread and initial

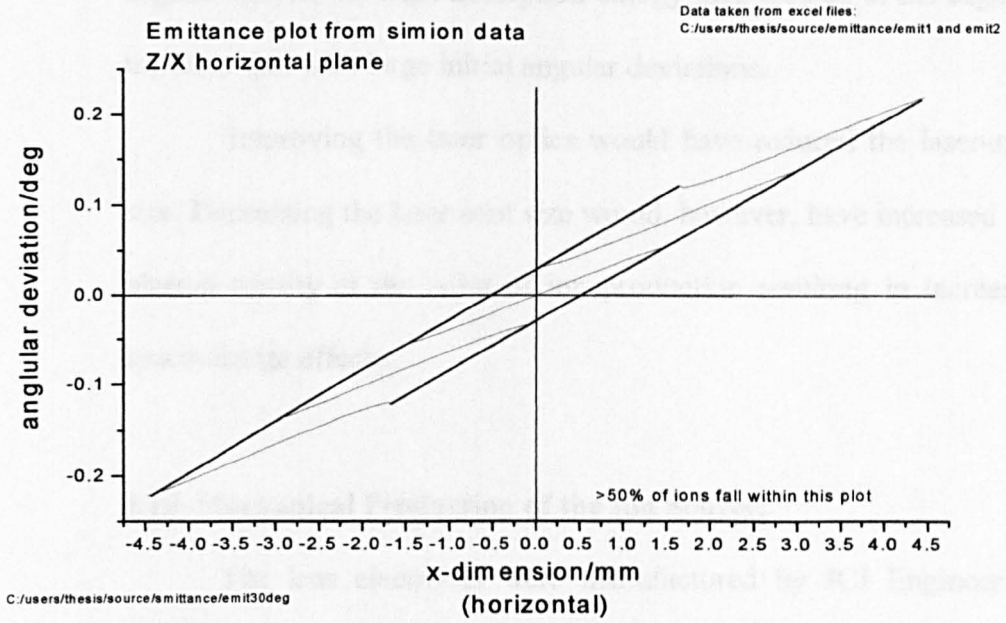

Fig. 57: Z/X plane (horizontal) emittance pattern. The emittance pattern encompassed the most intense portion of the ion beam. >50 % of ions fell within the emittance diagram.

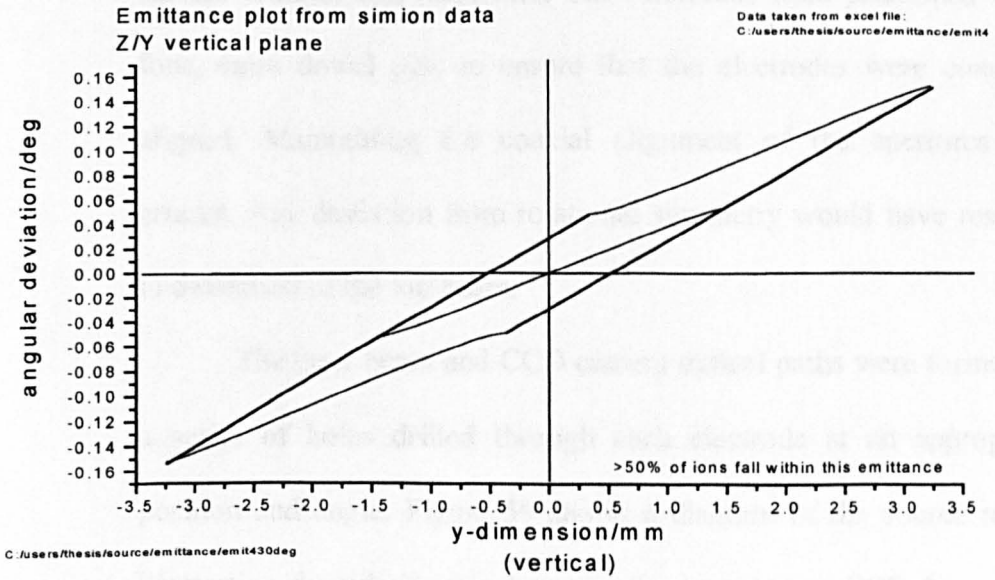

Fig. 58: Z/Y plane (vertical) emittance diagram for most intense region of beam.

angular spread, *i.e.* high desorption energy ions created at the edge of the laser spot with large initial angular deviations.

Improving the laser optics would have reduced the laser-spot size. Decreasing the laser-spot size would, however, have increased the plasma density at the point of ion production resulting in increased space-charge effects.

4.10 Mechanical Production of the Ion Source.

The lens electrodes were manufactured by JCJ Engineering (Southam, Warwickshire, UK). The electrodes were made from 316L stainless steel. 316L stainless steel was used because of its non-magnetic nature, corrosion resistance and desirable vacuum characteristics. The surface of each electrode was polished to remove surface features and blemishes. The electrodes were positioned using four, 4mm dowel pins to ensure that the electrodes were coaxially aligned. Maintaining the coaxial alignment of the apertures was crucial. Any deviation from rotational symmetry would have resulted in deflection of the ion beam.

The laser beam and CCD camera optical paths were formed by a series of holes drilled through each electrode at an appropriate position and angle. Figure 59 shows a diagram of the source region illustrating the relationship between the laser beam, CCD image and ion optical axis.

The in-vacuum aluminised mirrors were mounted on PEEK (polyetheretherketone) mirror supports. An electrical contact to each

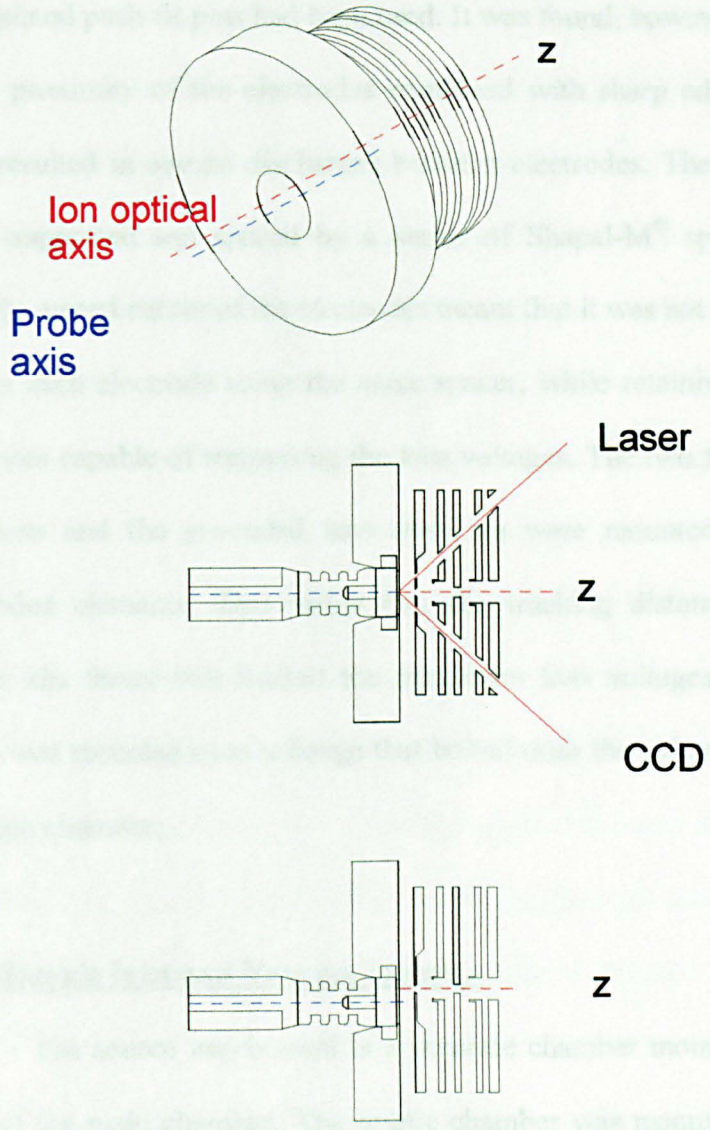

Fig. 59: Schematic diagrams of the ion source. (TOP) Diagram showing relationship between ion optical axis and the probe rotation axis. (MIDDLE) Horizontal section through source showing relationship between laser beam, CCD image and ion optical axis. (BOTTOM) Vertical section showing relationship between probe rotation axis and ion optical axis.

electrode was made by 1mm diameter tinned copper wire. Originally gold plated push-fit pins had been used. It was found, however, that the close proximity of the electrodes combined with sharp edges on the pins resulted in corona discharges between electrodes. The electrodes were supported and spaced by a series of Shapal-M® spacers. The closely spaced nature of the electrodes meant that it was not possible to mount each electrode using the same spacer, while retaining tracking distances capable of supporting the lens voltages. The two floated lens elements and the grounded lens elements were mounted from the grounded elements. This meant that the tracking distance was no longer the factor that limited the maximum lens voltages. The lens stack was mounted onto a flange that bolted onto the side of the main vacuum chamber.

4.11 Sample Inlet and Vacuum System.

The source was housed in a separate chamber mounted on the side of the main chamber. The source chamber was manufactured in-house from a single block of aluminium. All flanges were sealed using VITON® "o"-rings. Because the main chamber flanges sealed using Conflat® knife-edge/copper gasket seals, an adapter flange was manufactured in-house to connect the "o"-ring seal to the Conflat® seal. The source chamber was located on the main chamber by two 6 mm diameter dowel pins. A Turbovac 55 (pumping speed =55 l/s) turbomolecular pump (Leybold Heraeus, Germany) was mounted on the top flange. A water-cooled, aluminium flange was manufactured

in-house and mounted on the pump. A standard 4 way reducing cross (Caburn MDC, UK) was mounted on the bottom of the chamber. On the bottom of the cross another water-cooled Turbovac 55 turbomolecular pump was mounted. On one of the two DN40CF Conflat® side flanges, an ion gauge (Edwards, UK) was mounted in order to monitor the pressure in the source region. A four pin high-voltage feedthrough was mounted on the other flange.

Four viewports were mounted, two on each side, of the chamber. The viewports used UV grade quartz (Comar, UK), sealing directly onto VITON® "o"-rings. One port on one side allowed the laser beam into the chamber, while one port on the other side allowed the CCD camera to observe the laser spot. The remaining two viewports were positioned to allow the region of ion creation to be observed. This meant that experiments to examine the mechanism of MALDI ion generation could be conducted using the TOF-TOF instrument.

A sample probe and inlet system were designed and manufactured in-house. The probe was manufactured from 316L stainless steel tube (Goodfellows, UK). The end of the tube was sealed and made vacuum tight by welding a flange in position. The other end supported the sample stage. This consisted of a PEEK support that used a grooved structure in order to increase surface tracking. A stainless steel sample stage was mounted on top of the insulating spacer. The sample stage located into the repeller plate. The void inside the sample probe was pumped by suitable air bleed holes.

By mounting the rotational axis of the probe lower than the ion optical axis of the instrument, it was possible to load up to six individual sample spots and examine each by rotating the probe. Figure 56 shows a diagram of the source, showing the relationship between the probe rotation axis and the ion optical axis. Each sample spot was roughened by bead blasting the surface of the probe tip. This has been shown [45] to improve the sample spotting characteristics and improve shot-to-shot reproducibility. The effect of substrate roughening on energy spread and resolution was unclear, but was likely to be detrimental. The inlet system consisted of an atmospheric pressure region, a rotary pressure region and a high-vacuum region. The rotary-pumped stage was separated from the atmospheric and high-vacuum stages by spring energised PTFE Bal seals® (Bal Seal Engineering Company, CA). The spring seals sealed onto the shaft of the sample probe. When no sample probe was present inside the inlet system a 60 series ball valve (Swagelok, Birmingham Valve and Fitting Company, UK) sealed the high-vacuum region from the rotary pressure region. The valve body was drilled to facilitate the pumping of the void inside the valve. Figure 60 shows a schematic diagram of the probe inlet assembly. Tests showed that the ion source reached a pressure of $6x10^{-7}$ Torr after 5 minutes from the sample being introduced. Figure 61 shows a photograph of the source region.

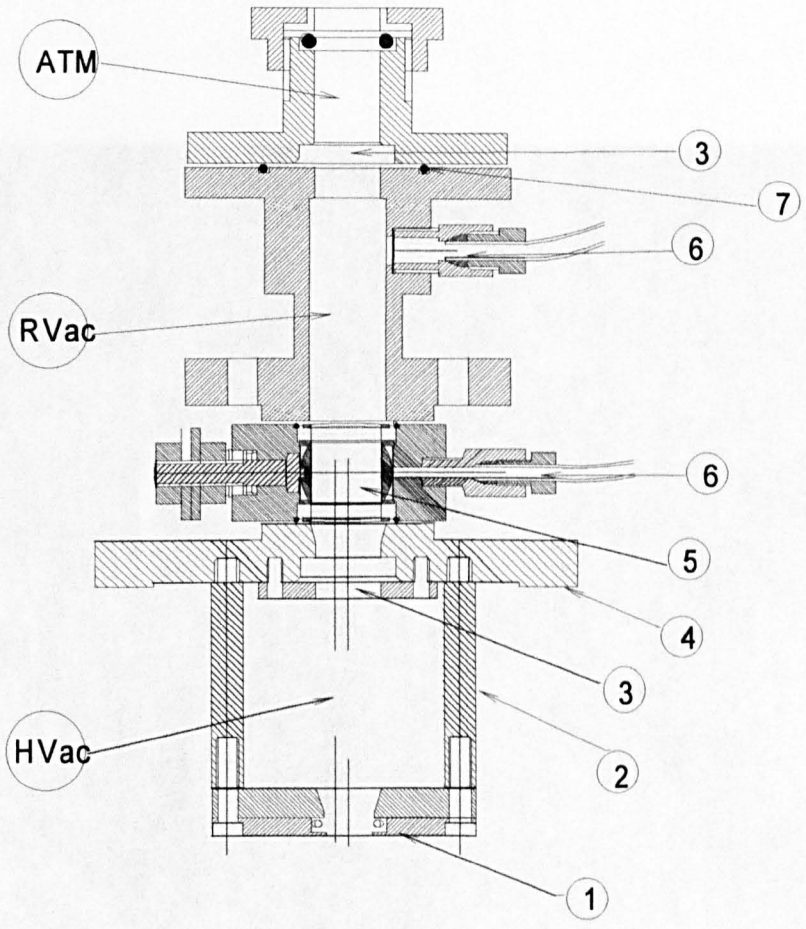

HVac) high vacuum region; RVac) rotary vacuum region; ATM) atmospheric region; 1) repeller electrode; 2) PEEK support spacers; 3) Bal seal; 4) source sealing flange; 5) Ball valve; 6) brass compression fitting(to rotary pump); 7) VITON O-ring.

Fig. 60: Schematic diagram of sample inlet system.

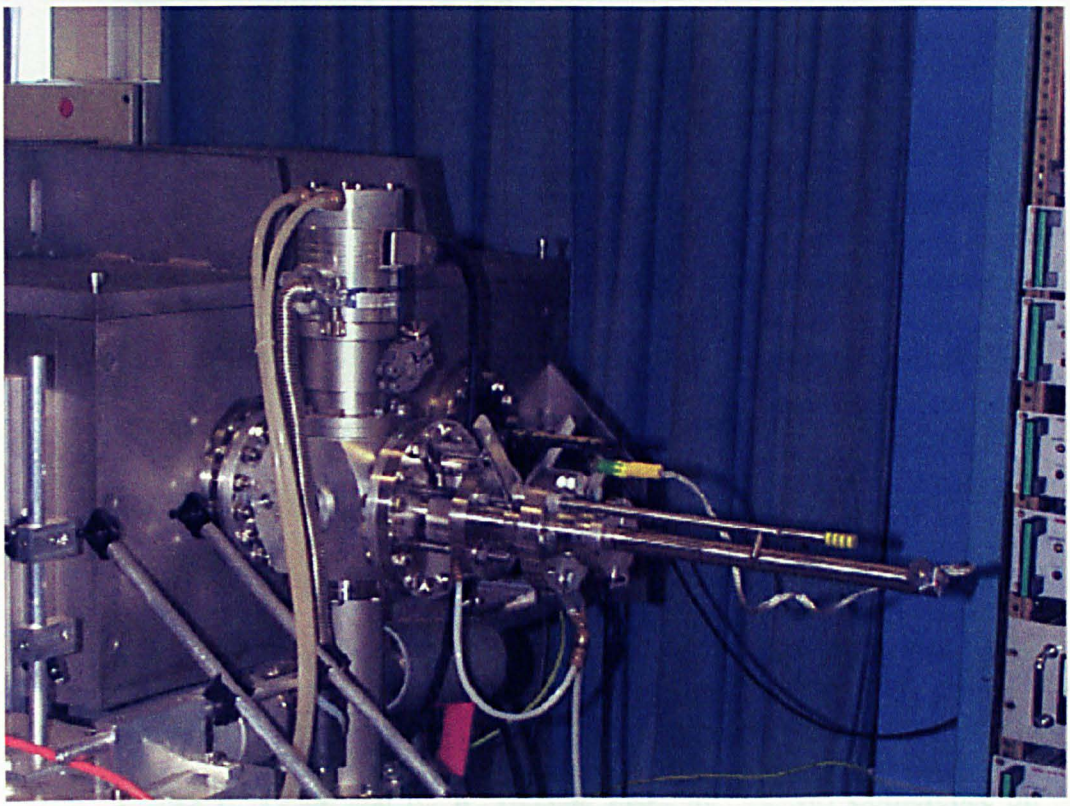

Fig. 61: Photograph of source chamber and probe inlet system.

4.12 References.

[1] K. Walter, U. Boesl and E. W. Schlag, Int. J. Mass Spectrom. Ion Processes, 71 (1986) 309.

[2] U. Boesl, R. Weinkauf and E. W. Schlag, Int. J. Mass Spectrom. Ion Processes, 112 (1992) 121.

[3] R. Grix, R. Kutscher, G. Li, U. Gruner and H. Wollnik, Rapid Commun. Mass Spectrom., 2 (1988) 83.

[4] X. Tang, R. Beavis, W. Ens, F. Lafortune, B. Schueler and K. G. Standing, Int. J. Mass Spectrom. Ion Processes, 85 (1988) 43.

[5] A. Brunelle, P. Chaurand, S. Della-Negra, J. Depauw, Y. LeBeyec and G. B. Baptista, Proc 39th ASMS Conference on Mass Spectrometry and Allied Topics, Nashville, TN, May 19-24, 1991, p.1703.

[6] F. J. Mayer, A. Holle, R. Schäfer and R. Frey, Proc. 40th ASMS Conference on Mass Spectrometry and Allied Topics, Washington, DC, May 31-June 5, 1992, p. 378.

[7] M. L. Vestal and R. W. Nelson, Proc. 40th ASMS Conference on Mass Spectrometry and Allied Topics, Washington, DC, May 31-June 5, 1992, p. 350.

[8] T. Bergmann, T. P. Martin and H. Schaber, Rev. Sci. Instrum., 60 (1990) 347 and 792.

[9] L. V. Zhigilei and B. J. Garrison, Rapid Comm. Mass Spectrom. 12 (1998) 1273.

[10] L. V. Zhigilei, P. B. S. Kodali and B. J. Garrison J. Phys. Chem. B 101 (1997) 2028.

[11] A. Vertes, G. Irinyi and R. Gijbels, Anal. Chem. 65 (1995) 2389.

[12] R. E. Johnson, Int. J. Mass Spectrom, Ion Processes, 139 (1994) 25

[13] R. C. Beavis and B. T. Chait, Chem. Phys. Lett. 181, 479 (1991).

[14] A. Verentchikov, W. Ens, J. Martens and K. G. Standing in Proc. of the 40th ASMS Conference on Mass Spectrometry and Allied Topics, Washington, DC, May 31- June 5, 1992, 360-361.

[15] B. Spengler and V. Bökelmann, Nucl. Instrum. Methods. Phys. Res. B. 82 (1993) 379

[16] Y. Pan and R. J. Cotter, Org. Mass Spectrom., 27, 3 (1992).

[17] T.-W. D. Chan, I. Thomas, A. W. Colburn and P. J. Derrick Chem. Phys. Lett., 222 (1994) 579.

[18] B. Spengler and R. J. Cotter, Anal. Chem., 62 (1990) 793.

[19] W. Zhang and B. T. Chait, Int. J. Mass Spectrom. Ion Processes, 160 (1997) 259.

[20] P. Juhasz, M. L. Vestal and S. A. Martin, J. Am. Soc. Mass Spectrom., 8 (1997) 209.

[21] R. Dworschak, W. Ens and K. G. Standing, Proceedings of the 45th, Conference on Mass Spectrometry and Allied Topics , Palm Springs, CA, June 1- June 6, 1997, 841.

[22] J. Zhou, W. Ens, K. G. Standing and A. Verentchikov, Rapid Commun. Mass Spectrom. 6, 671 (1992).

[23] A. E. Giannakopulos, D.J. Reynolds, T. –W. D. Chan, A. W. Colburn, and P. J. Derrick, Int. J. Mass Spectrom. Ion Processes, 131 (1994) 67.

[24] G. R. Kinsel, M. E. Gimon-Kinsel, K. J. Gillig and D. H. Russell,

J. Mass Spectrom., 34 (1999) 684.

[25] G. R. Kinsel and D. H. Russell, J. Am. Soc. Mass Spectrom., 6 (1995) 619.

[26] W. Ens, R. Dworschak, V. Spicer and K. G. Manitoba, 42nd ASMS Conference on Mass Spectrometry and Allied Topics, Chicago, IL, May 29 – June 3, 1994, pp 3.

[27] H. Ehring, M. Karas and F. Hillenkamp, Org. Mass Spectrom., 27 (1992) 427.

[28] V. Bökelmann, B. Spengler and R. Kaufmann, Eur. Mass Spectrom., 1 (1995) 81

[29] G. R. Kinsell, R. D. Edmondson and D. H. Russell, J. Mass Spectrom., 32 (1997) 714.

[30] B. H. Wang, K. Dreisewerd, U. Bahr, M. Karas and F. Hillenkamp, J. Am. Soc. Mass Spectrom. 4 (1993) 393.

[31] M. E. Belov, C. P. Myatt and P. J. Derrick, Chem. Phys. Lett., 284 (1998) 412.

[32] R. Kaufmann, P. Chaurand, D. Kirsch and B. Spengler, Rapid. Commun. Mass Spectrom., 10 (1996) 1199.

[33] H. Ehring, C. Costa, P. A. Demirev, B. U. R. Sundqvist Rapid Commun. Mass Spectrom. 10 (1996) 821.

[34] A. P. Quist, T. Huth-Fehre and B. U. R. Sundqvist, Rapid Commun. Mass Spectrom., 8 (1994) 149.

[35] A. A. Puretzky and D. B. Geohegan, Chem. Phys. Lett., 286 (1997) 425.

[36] P. Demirev, A. Westman, C. T. Reimann, P. Håkansson, D. Barofsky, B. U. R. Sundqvist, Y. D. Cheng, W. Seibt and K. Siegbahn, Rapid Commun. Mass Spectrom., 6 (1992) 187.

[37] M. R. Chevrier and R. J. Cotter, Rapid Commun. Mass Spectrom., 5 (1991) 611.

[38] K. Dreisewerd, M. Schurenberg, M. Karas and F. Hillenkamp, Int. J. Mass Spectrom. Ion Processes, 154 (1996) 171.

[39] E. Ayala, C. C. Vera, and P. Håkansson, Rapid Commun. Mass Spectrom., 13 (1999) 792.

[40] A. Westman, T. Huth-Fehre, P. Demirev, J. Bielawski, N. Medina and B. U. R. Sundqvist, Rapid Commun. Mass Spectrom. 8 (1994) 388.

[41] F. Aksouh, P. Chaurand, C. Deprun, S. Della-Negra, J. Hoyes, Le Beyec and R. Rosas Pinho, Rapid Commun. Mass Spectrom. 9 (1995) 515.

[42] P. Chaurand, S. Della Negra C. Deprun, J. Hoyes, Y. Le Beyec and F. Aksouh Proceedings of the 42nd ASMS Conference on Mass Spectrometry and Allied Topics, Chicago, IL, May 29 – June 3, 1994, 6.

[43] L. Schmidt, H. Jungclas, Hans-Walter Fritsch and P. Kohl, J. Am. Soc. Mass Spectrom., 4 (1993) 782.

[44] SIMION 3D, version 6, D. A. Dahl, Idaho National Engineering Laboratory.

[45] A. E. Giannakopulos, S. Bashir and P. J. Derrick, Eur. Mass Spectrom., 4 (1998) 127.

CHAPTER FIVE.

Linear Time-of-Flight Spectrometer, Single-Stage Ion Mirror and Pulsed Mass Gate.

5.01 Layout of the TOF-TOF Spectrometer.

The TOF-TOF instrument consisted of three basic time-of-flight spectrometers configured in such a way as to form an instrument capable of collision-induced dissociation. Figure 62 shows a plan view of the TOF-TOF instrument without the chamber lid. The schematic diagram shows the relationship between the ion source, the single-stage mirror, the quadratic-field ion mirror and all the associated optics. The diagram indicates the position of the three micro-channel plate detectors that constitute the linear time-of-flight spectrometer, the single-stage reflectron time-of-flight spectrometer and the tandem CID time-of-flight spectrometer.

Figure 63 shows a horizontal section through the ion optical plane of the instrument. The structure of the ion mirror's field-sustaining electrodes is clearly displayed. The components are as follows:

1) Sample probe tip; 2) Repeller electrode; 3) Source lenses;

4) First vertical deflector/lens; 5) Second vertical deflector/lens;

6) First horizontal deflector/lens; 7) Second horizontal deflector/lens;

8) Front electrode with apertures or covered in mesh; 9) Single-stage ion mirror and field-sustaining electrodes; 10) Linear TOF micro-

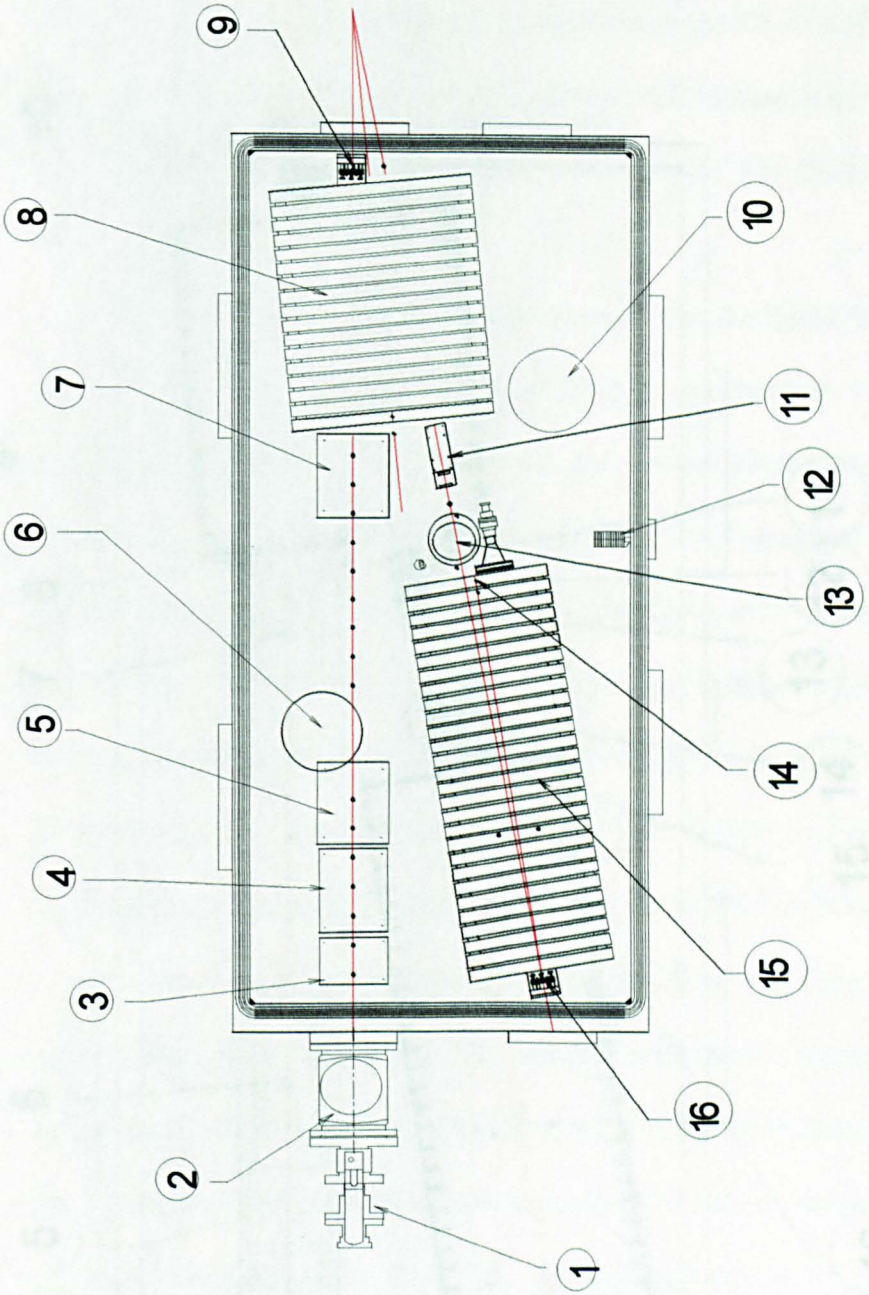

Fig. 62: Plan view of the TOF-TOF spectrometer.

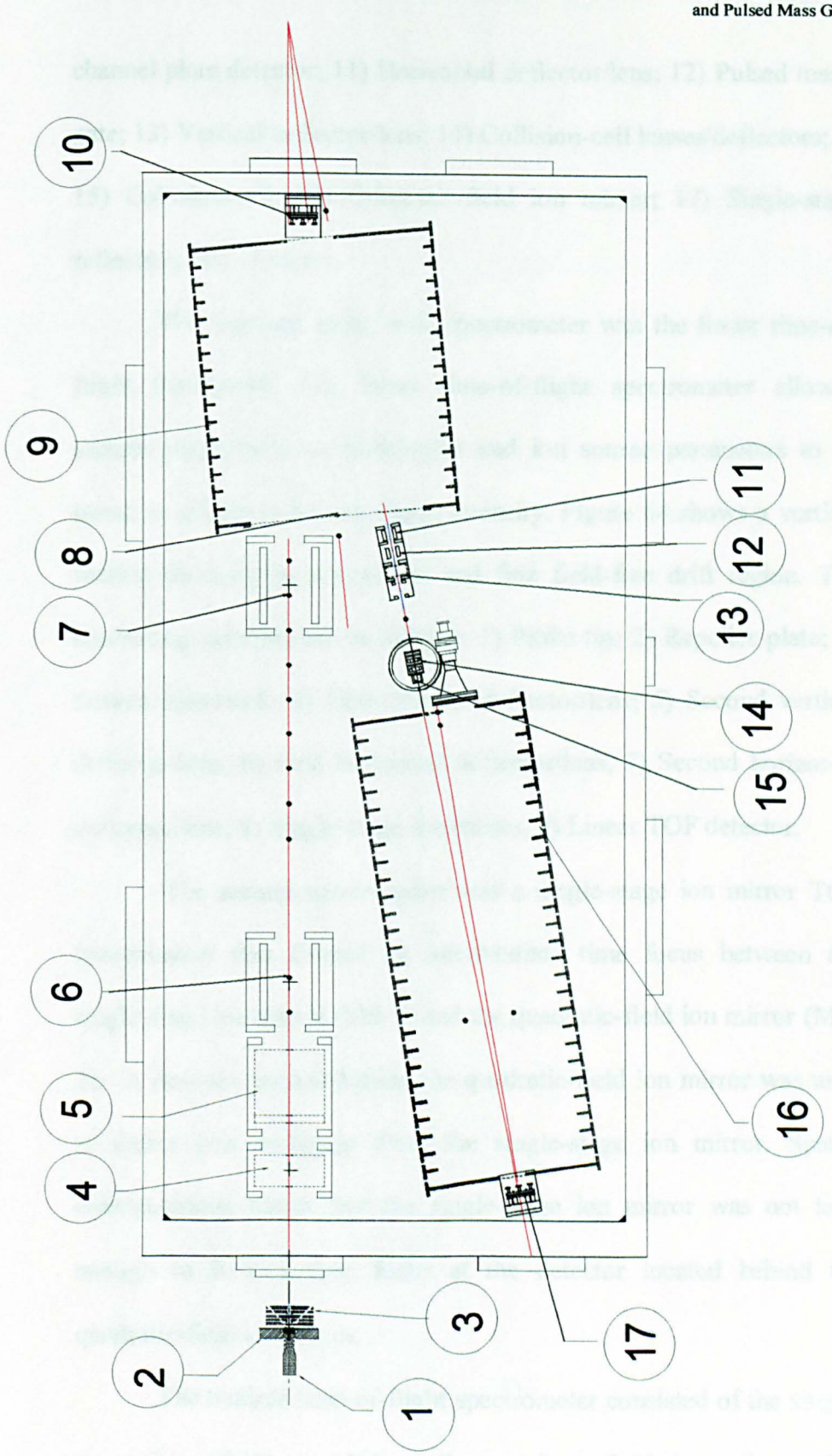

Fig. 63: Horizontal section through ion optical plane.

channel plate detector; 11) Horizontal deflector/lens; 12) Pulsed mass-gate; 13) Vertical deflector/lens; 14) Collision-cell lenses/deflectors; 15) Collision-cell; 16) Quadratic-field ion mirror; 17) Single-stage reflectron TOF detector.

The first and most basic spectrometer was the linear time-of-flight instrument. The linear time-of-flight spectrometer allowed sample preparation methodologies and ion source parameters to be tuned to achieve optimum signal intensity. Figure 64 shows a vertical section through the ion source and first field-free drift region. The annotating numbers are as follows: 1) Probe tip; 2) Repeller plate; 3) Source lens-stack; 4) First vertical deflector/lens; 5) Second vertical deflector/lens; 6) First horizontal deflector/lens; 7) Second horizontal deflector/lens; 8) Single-stage ion mirror; 9) Linear TOF detector.

The second spectrometer was a single-stage ion mirror TOF spectrometer that formed an intermediate time focus between the single-stage ion mirror (MS-1) and the quadratic-field ion mirror (MS-2). A detector located behind the quadratic-field ion mirror was used to detect ions emerging from the single-stage ion mirror. Spatial considerations meant that the single-stage ion mirror was not long enough to form a time focus at the detector located behind the quadratic-field ion mirror.

The tandem time-of-flight spectrometer consisted of the single-stage ion mirror coupled to the quadratic-field ion mirror. The quadratic-field ion mirror was capable of simultaneously time focusing the complete fragment mass envelope at the detector plane.

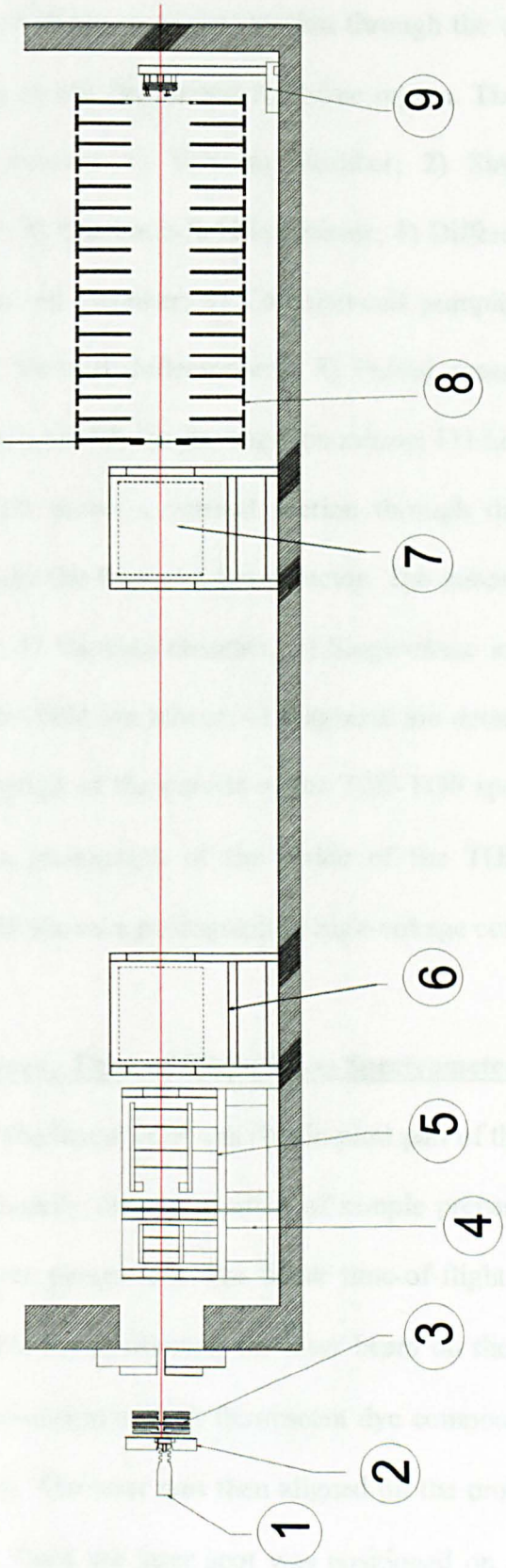

Fig. 64: Vertical section through first field-free region.

Figure 65 shows a vertical section through the collision-cell, the two ion mirrors and the second field-free region. The annotating numbers are as follows: 1) Vacuum chamber; 2) Single-stage ion mirror detector; 3) Quadratic-field ion mirror; 4) Differentially pumped outer collision-cell chamber; 5) Collision-cell pumping port; 6) Collision-cell; 7) Vertical deflector/lens; 8) Pulsed mass gate; 9) Horizontal deflector/lens; 10) Single-stage ion mirror; 11) Linear TOF detector. Figure 66 shows a vertical section through the quadratic-field ion mirror and the fragment ion detector. The annotating numbers are as follows: 1) Vacuum chamber; 2) Single-stage ion mirror detector; 3) Quadratic-field ion mirror; 4) Fragment ion detector. Figure 67 shows a photograph of the outside of the TOF-TOF spectrometer. Figure 68 shows a photograph of the inside of the TOF-TOF spectrometer. Figure 69 shows a photograph of high-voltage control units.

5.02 Linear Time-of-Flight Mass Spectrometer.

The linear TOF was the simplest part of the instrument and was used primarily for optimisation of sample preparation procedures and ion source parameters. The linear time-of-flight spectrometer proved invaluable for positioning the laser beam on the sample spot and the ideal ion-optical axis. A fluorescent dye compound was placed on the probe tip. The laser was then aligned on the probe tip using the CCD camera. Once the laser spot was positioned on the probe tip the dye was replaced with an alkali metal halide salt. The laser spot was rastered across the surface of the probe tip, using the external mirror

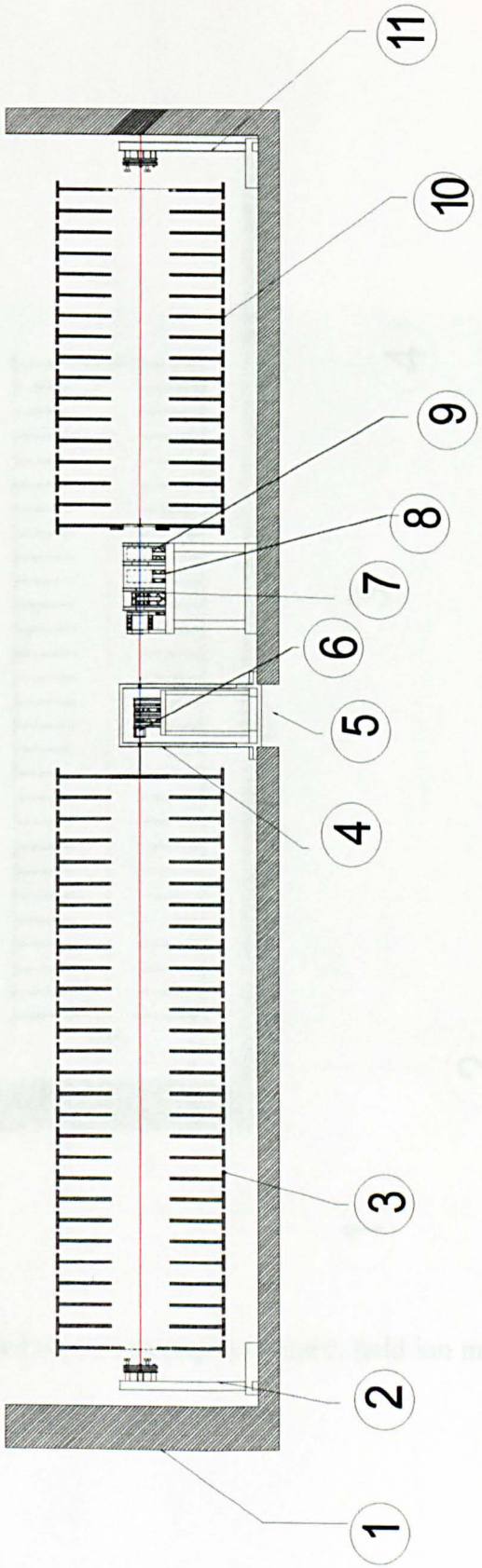

Fig. 65: Vertical section through second field-free region and collision-cell.

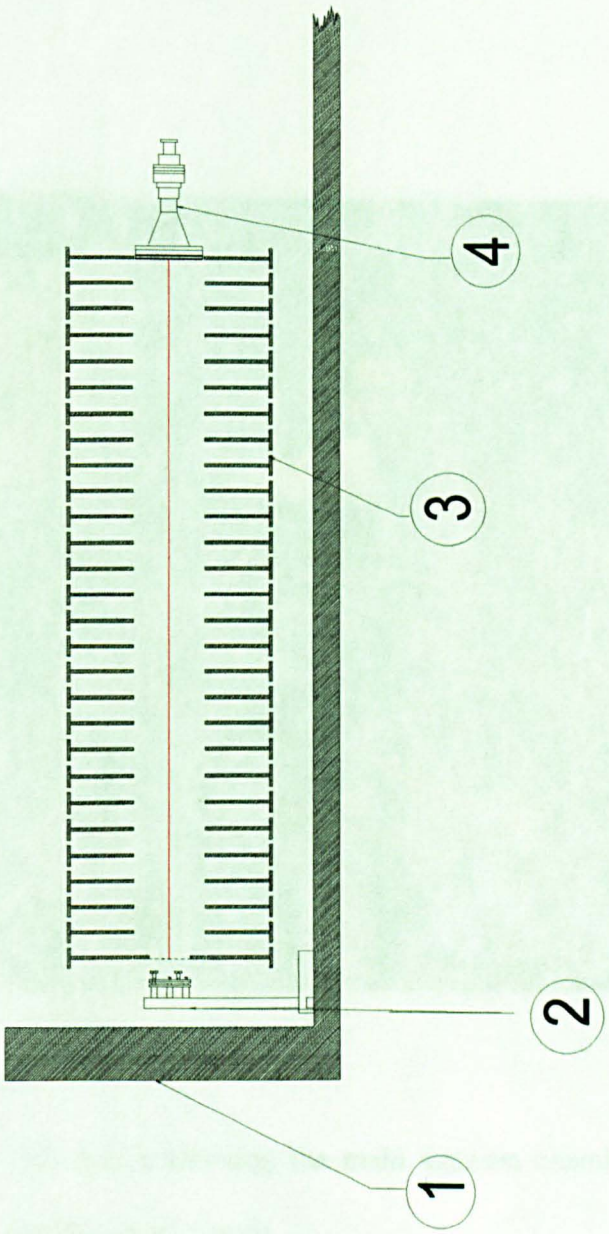

Fig.66: Vertical section through quadratic-field ion mirror.

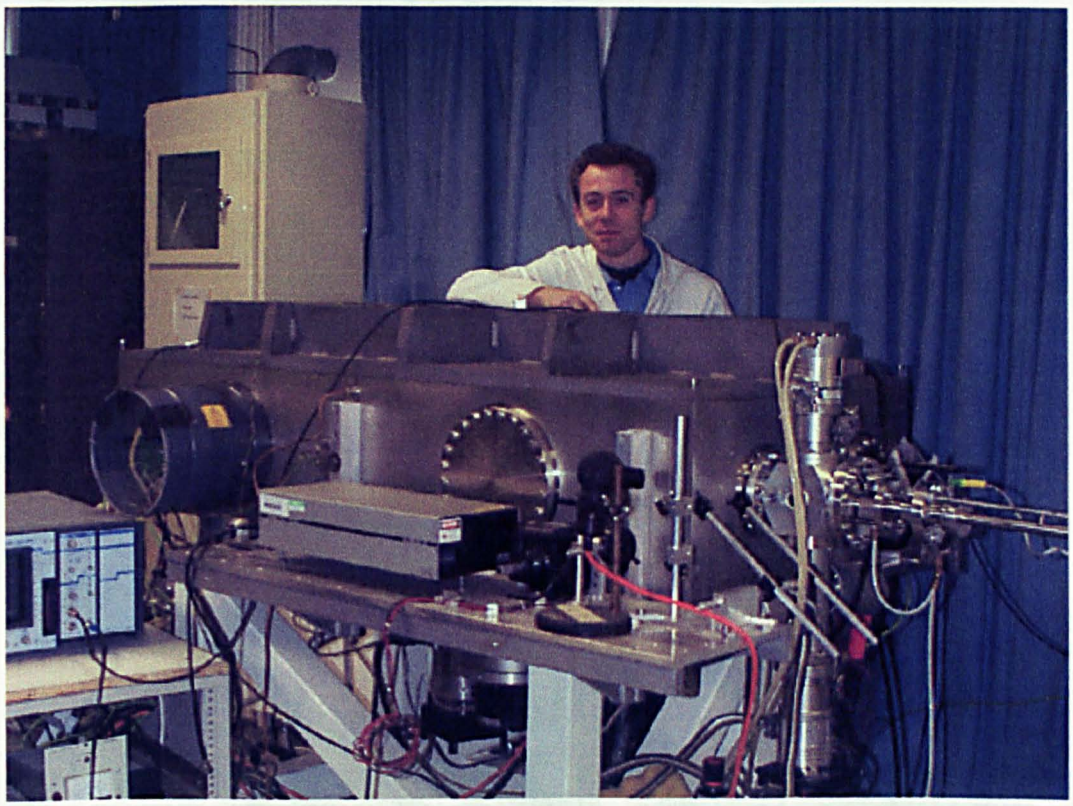

Fig. 67: Photograph showing the main vacuum chamber, the source chamber and the optics bench.

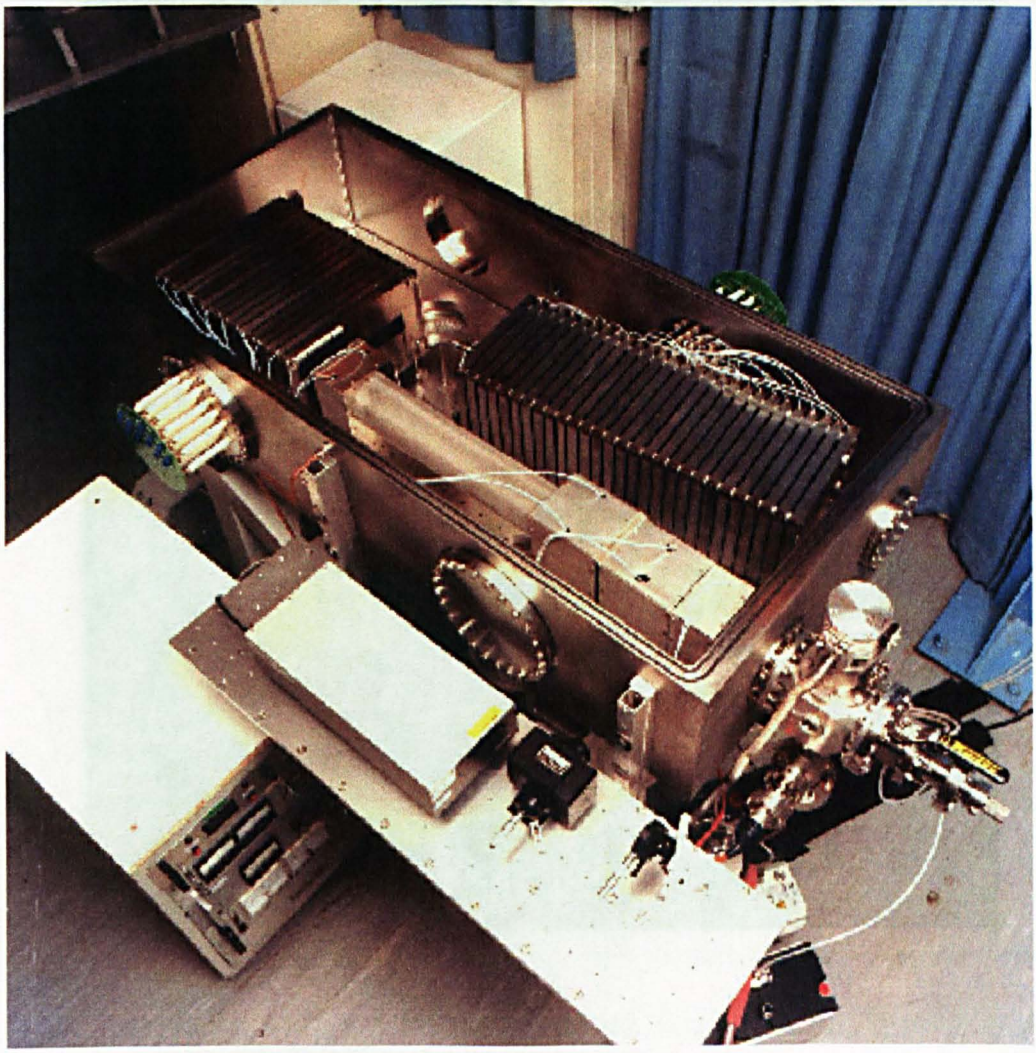

Fig. 68: Photograph of main chamber without lid.

Fig. 69: Photograph of the instrument control racks.

mounts, until optimum signal intensity was obtained. It was found that small differences in alignment dramatically reduced signal intensity. Placing a chevron micro-channel plate detector in the line-of-sight of the MALDI ion source formed the linear time-of-flight instrument. The detector was positioned behind the rear electrode of the single-stage ion mirror. The length of the field-free flight path was 1.56 m. The ion beam passed through a slit shaped aperture in the front of the single-stage ion mirror. SIMION calculations showed that the aperture did not attenuate the ion beam.

The rear electrode of the single-stage ion mirror (MS-1) had a 68mm diameter hole drilled in it to ensure that the ion beam reached the linear TOF detector. The hole was covered with a 30-wires/inch stainless steel mesh to ensure that the desired electric field was formed inside the single-stage ion mirror. The optical transmission of the mesh was determined by optical microscopy to be approximately 42 %. The mesh was held in place by a retaining plate that ensured the mesh was held flat.

SIMION ion trajectory calculations were conducted to determine the emittance pattern at the linear time-of-flight detector. The initial ion conditions were outlined previously. The simulations showed that the beam was elliptical in shape with a maximum horizontal beam width of 19 mm. The vertical beam width was less than 14mm at the linear TOF detector. The majority of ions were contained within this beam area *i.e.* the beam halo was included. Figure 70 shows the emittance pattern for the Z/X plane (horizontal

plane) at the linear TOF detector. The emittance pattern included the low intensity beam halo region. The beam was approximately 19 mm wide in the horizontal plane at the linear TOF detector. Figure 71 shows the emittance pattern for the Z/Y plane (vertical plane) at the linear TOF detector. The emittance pattern included the low intensity beam halo region. The emittance pattern showed that the beam was less than 14 mm wide in the vertical. For the purposes of the calculations the source was maintained at the following voltages:

1) The acceleration voltage was +10 kV.
2) The first Einzel lens was maintained at –14 kV.
3) The second Einzel lens was maintained at –13 kV.

The ions used had the following properties:

1) 1000 amu, singly charged ions.
2) Up to 12 eV desorption energy.
3) The ions were formed at the surface of the probe tip.
4) Initial spatial spread of ±50 microns in the vertical by ±85 microns in the horizontal.
5) Initial angular distribution of ±80°, including the beam halo. Initial angular distribution of ± 30°, excluding the low intensity beam halo region.

Figure 72 shows the emittance pattern for the Z/X plane (horizontal plane) at the linear TOF detector. The emittance pattern includes only the most intense region of the ion beam. The emittance pattern showed that the brightest region of the ion beam was approximately 10mm wide in the horizontal direction. Figure 73 shows

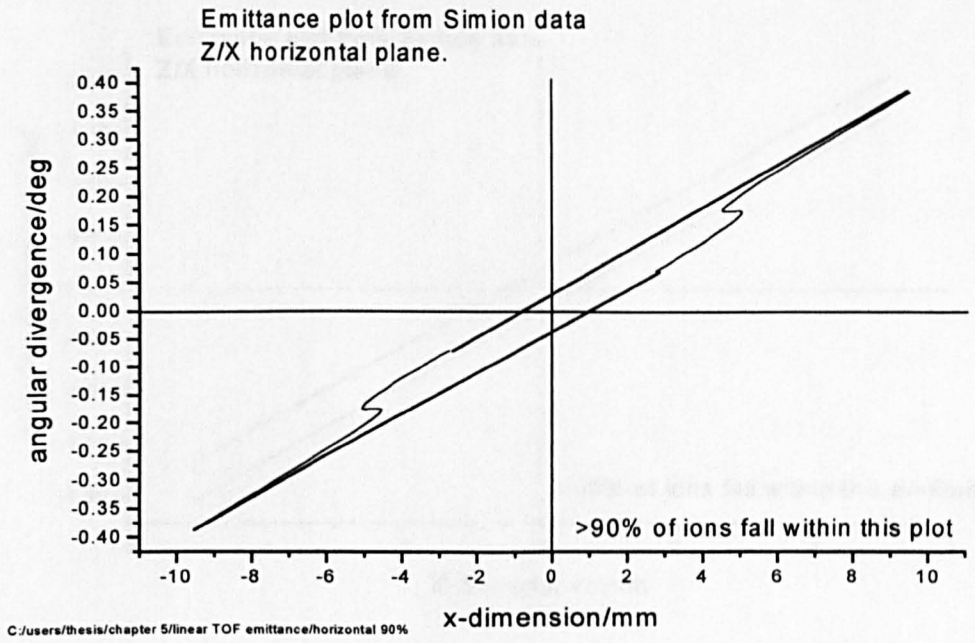

Fig. 70: Emittance pattern for Z/X plane (horizontal plane) at the linear TOF detector. >90 % of ions fell within this emittance pattern *i.e.* the beam halo was included.

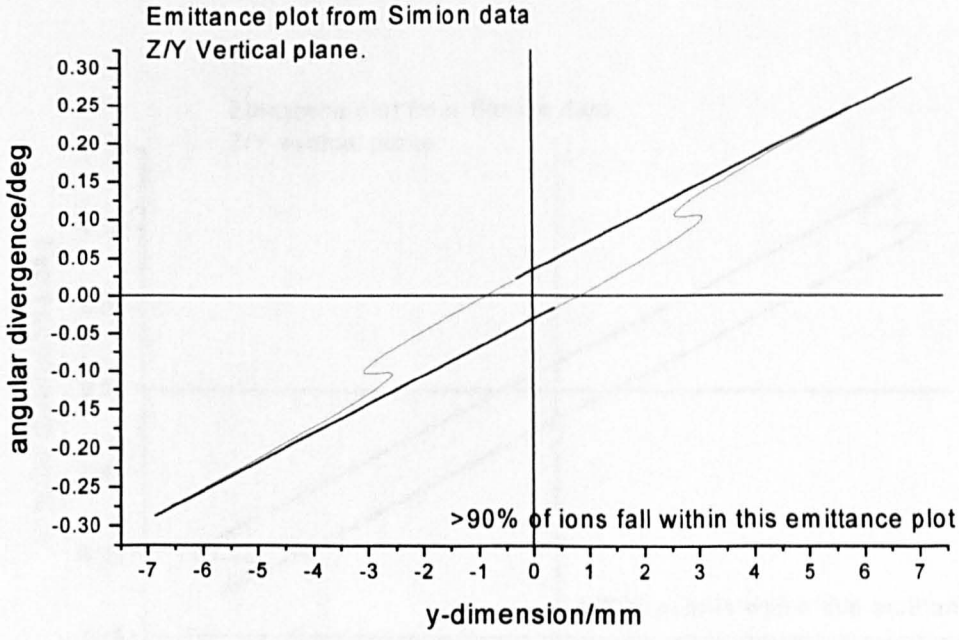

Fig. 71: Emittance pattern for Z/Y plane (vertical plane) at the linear TOF detector. >90 % of ions fell within the emittance pattern.

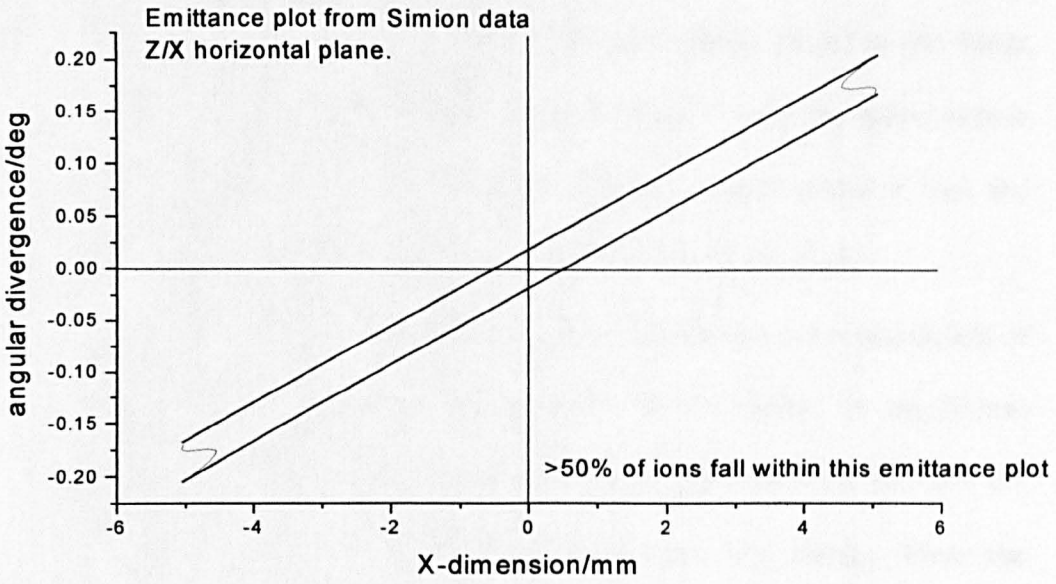

Fig. 72: Emittance pattern for Z/X plane (horizontal plane) at the linear TOF detector. The emittance pattern includes >50 % of ions. Only the most intense portion of the ion beam was included, while the beam halo was excluded.

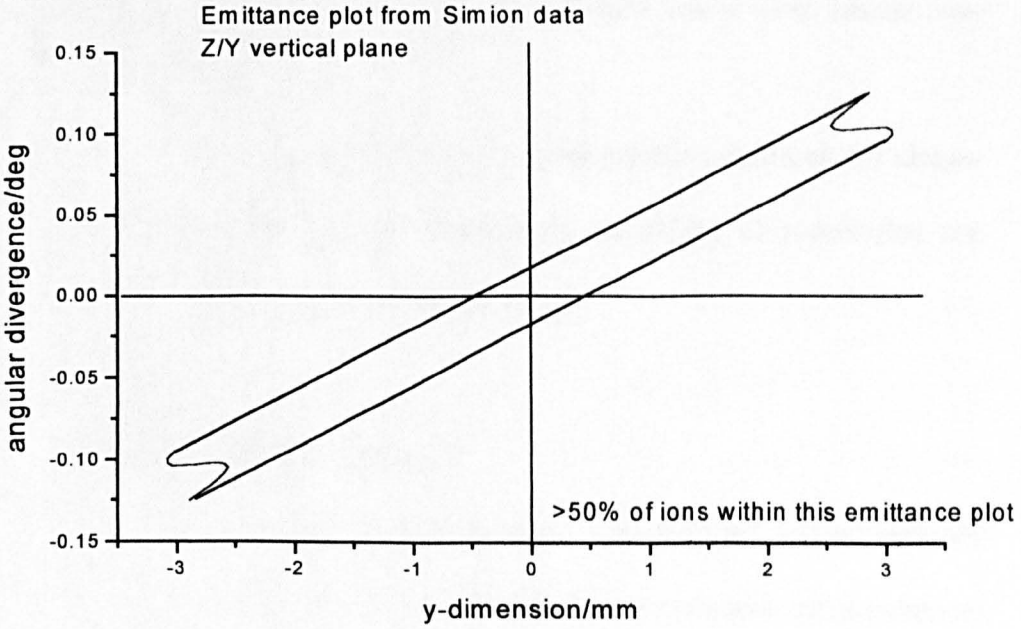

Fig. 73: Emittance pattern for the Z/Y plane (vertical plane) for the linear TOF detector. Emittance pattern encloses >50 % of all ions.

the emittance pattern for the Z/Y plane (vertical plane) at the linear TOF detector. The emittance pattern includes only the most intense portion of the ion beam. The emittance pattern showed that the brightest portion of the ion beam was less than 6 mm high.

The theoretical emittance plots showed that the transmission of the linear time-of-flight spectrometer was not limited by the 20 mm diameter active-area of the micro-channel plate detector. Nor did the aperture at the front of the single-stage ion mirror limit the transmission. The transmission of the linear time-of-flight spectrometer was, however, limited by the transmission of the mesh covering the aperture in the rear electrode of the ion mirror. The transmission of the linear time-of-flight spectrometer was estimated to be 40 %. If a more transparent mesh were available it would be a trivial task to upgrade the transmission of the linear time-of-flight spectrometer. The mass resolving power of the linear time-of-flight mass spectrometer was typically 150 (FWHM).

The linear time-of-flight detector, positioned behind the single-stage ion mirror (MS-1), afforded the capability of monitoring the neutral products of postsource decay [1].

5.03 Ion Detection System.

A micro-channel plate detector was designed and constructed in-house for use in the linear time-of-flight instrument. Micro-channel plates (MCP) are solid-state detectors consisting of millions of individual channel electron multipliers (10^6 channels cm^{-2}) fused

together to form a single, rigid, parallel array. Figure 74 shows a schematic diagram illustrating the operating principles of a micro-channel plate electron multiplier.

Micro-channel plate detectors are ideally suited to time-of-flight mass spectrometry. They are available in a range of shapes and sizes and possess large, flat active-areas. A single channel plate provides a typical gain of 10^3-10^4. When combined in a chevron stack the gain can be of the order of 10^6-10^7. Micro-channel plate detectors possess rapid response times (1.8 ns is a typical response time [2]). Thus minimising resolution degrading effects.

Micro-channel plate detectors are not, however, without problems. The secondary electron yield rapidly decreases with increasing molecular mass [3]. This means that micro-channel plate detectors are not as sensitive at the high-mass end of the spectrum as they are at the low-mass end. This situation can be mitigated by the addition of a post-acceleration stage to increase the kinetic energies/velocities of the incident ions. Another reason for decreased high-mass sensitivity is detector saturation [4]. Low-mass ions reach the detector first and trigger secondary electron emission. Once triggered a channel has a dead-time of several milliseconds [5]. This means that subsequent high-mass ions are not detected. This reduces the probability of high-mass ions triggering an electron cascade. Several methods have been utilised to circumvent this problem. These include gating systems, which deflect low-mass matrix species from the detector [5][6][7][8], and the delayed application of the high-

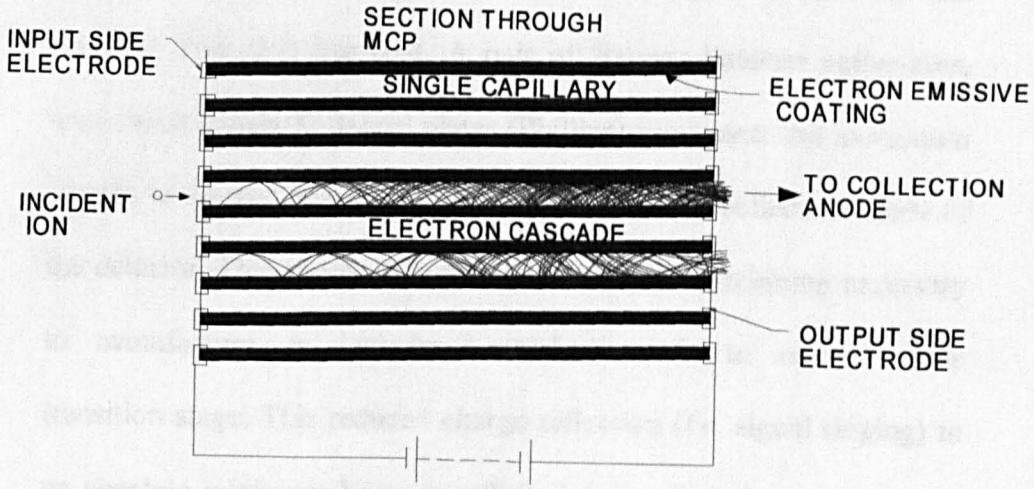

Fig. 74: Schematic diagram illustrating the operating principles of a micro-channel plate detector.

voltage to the channel plates. The transmission of a time-of-flight instrument is limited by the open area ratio (OAR) of the micro-channel plates. The OAR is typically 60 % [9], although higher values are commercially available.

The linear TOF detector was a chevron (two-stage) micro-channel plate detector. The detector offered good sensitivity and response time at a low-cost. A pair of 20 mm diameter active-area, impedance matched channel plates (Phillips) were used. An in-vacuum current-to-voltage amplifier was located behind the collection anode of the detector. This approach avoided the complex machining necessary to manufacture an impedance-matched anode to coaxial cable transition stage. This reduced charge reflection (*i.e.* signal ringing) to an absolute minimum because reflected pulses had short propagation times and were rapidly damped [3]. The chevron stack micro-channel plates were clamped between two stainless steel retaining plates. Three PEEK screws, fitted with springs, compressed the two retaining plates and ensured that the channel plates were secure. An amplifier was designed and manufactured in-house. The amplifier and collection anode were mounted behind the channel plates. The collection anode was maintained at +1.6 kV in order attract secondary electrons. The front micro-channel plate was maintained at ground potential. The lack of post-acceleration limited the sensitivity of the detector to high-mass analytes and at low accelerating voltages. The lack of a post-acceleration stage meant, however, that metastable fragments did not limit mass resolving power. Also, no transmission limiting, field-

defining mesh was required in front of the detector. Figure 75 shows a simple circuit diagram of the detector. A series of PEEK spacers separated the amplifier from the channel plates. A metal spacer ensured that high-voltage was supplied from the amplifier to the channel plates. Six PEEK spacers screwed into the mount that supported the amplifier and the channel plates. The detector mount was manufactured in-house from 316L stainless steel. Figure 76 shows a schematic diagram of the detector assembly. The figure annotations are as follows: 1) PEEK retaining screws and compression springs; 2) Micro-channel plates and retaining plates; 3) Amplifier and collector anode mounted on PCB; 4) PEEK supports; 5) support mount.

The mount was a free-standing design, which meant that the detector could be repositioned anywhere in the vacuum chamber. The disadvantage of the design was that the detector could not always be guaranteed to hold the correct angular relationship with respect to the ion beam. If the detector surface were not positioned perpendicular to the ion beam or parallel to the time focus, the resolution of the spectrometer would be degraded because different portions of the beam would travel different distances. Figure 77 shows a schematic diagram of a micro-channel plate detector illustrating the effective path-length difference resulting from an incorrectly orientated detector. The effective path-length difference can be expressed as:

$$\Delta L = 2B \tan \alpha \qquad 5.01$$

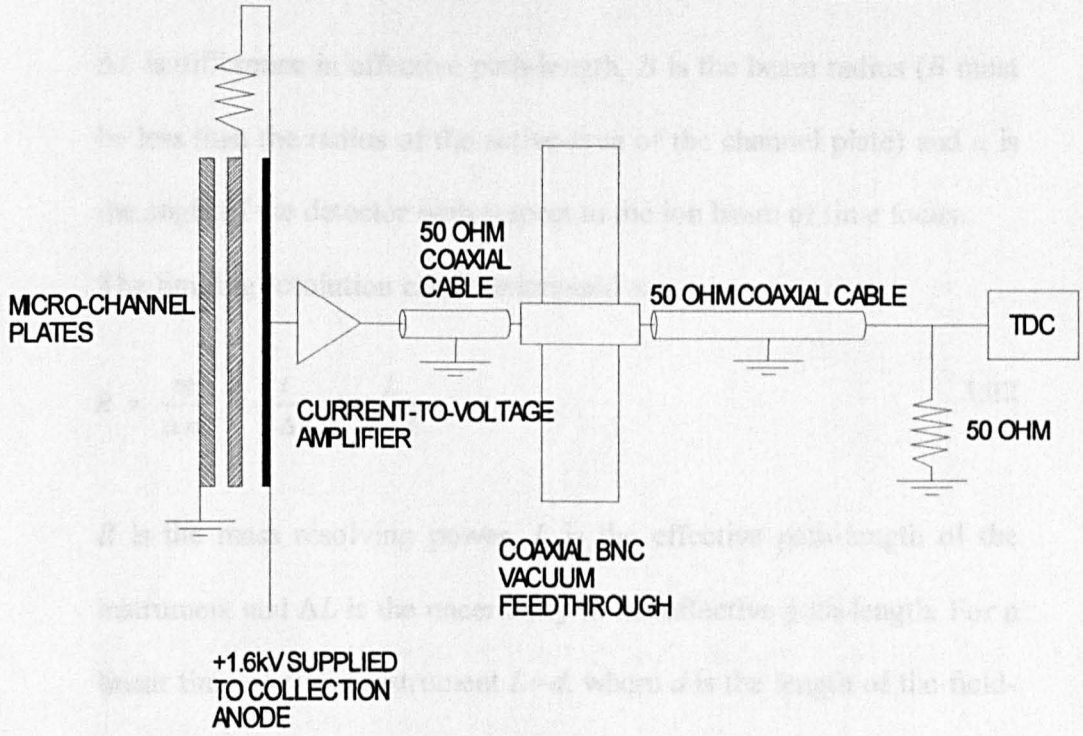

Fig. 75: Circuit diagram of detector.

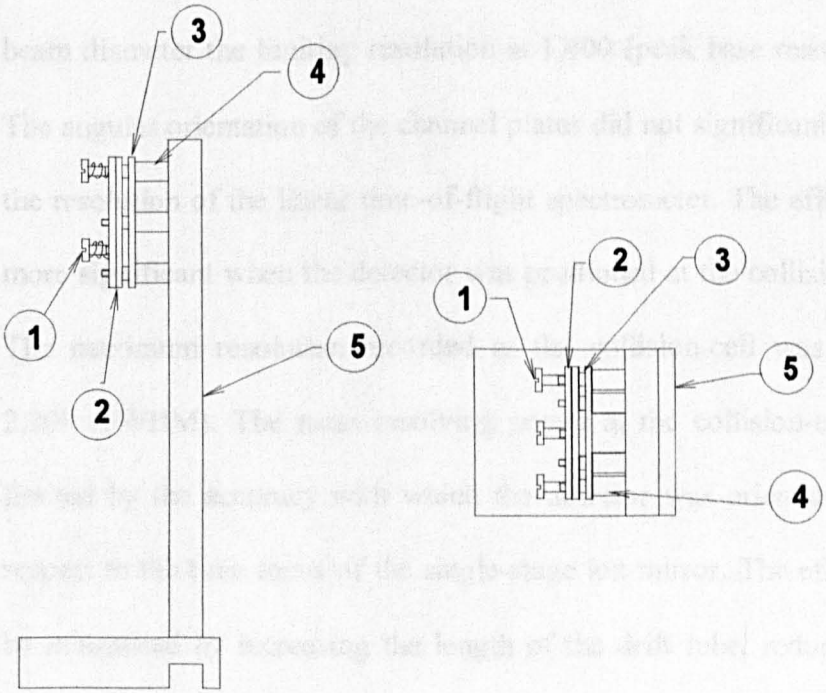

Fig. 76: Schematic diagram showing side view and plan view of detector.

ΔL is difference in effective path-length, B is the beam radius (B must be less than the radius of the active-area of the channel plate) and α is the angle of the detector with respect to the ion beam or time focus. The limiting resolution can be expressed as:

$$R = \frac{m}{\Delta m} = \frac{t}{2\Delta t} = \frac{L}{2\Delta L} \qquad 5.02$$

R is the mass resolving power, L is the effective path-length of the instrument and ΔL is the uncertainty in the effective path-length. For a linear time-of-flight instrument $L=d$, where d is the length of the field-free drift tube. For a detector positioned with an angular accuracy of 2° with respect to the time focus, a 2 m effective flight path and a 20 mm beam diameter the limiting resolution is 1,400 (peak base resolution). The angular orientation of the channel plates did not significantly limit the resolution of the linear time-of-flight spectrometer. The effect was more significant when the detector was positioned at the collision-cell. The maximum resolution recorded at the collision-cell was 2,000-2,200 (FWHM). The mass resolving power at the collision-cell was limited by the accuracy with which the detector was orientated with respect to the time focus of the single-stage ion mirror. The effect can be minimised by increasing the length of the drift tube, reducing the beam diameter/active-area of the channel plates or increasing the angular precision of the micro-channel plate detector.

The physical geometry of the individual channels of the micro-channel plates result in an uncertainty in the effective path-length. Figure 78 shows a schematic diagram illustrating the uncertainty in

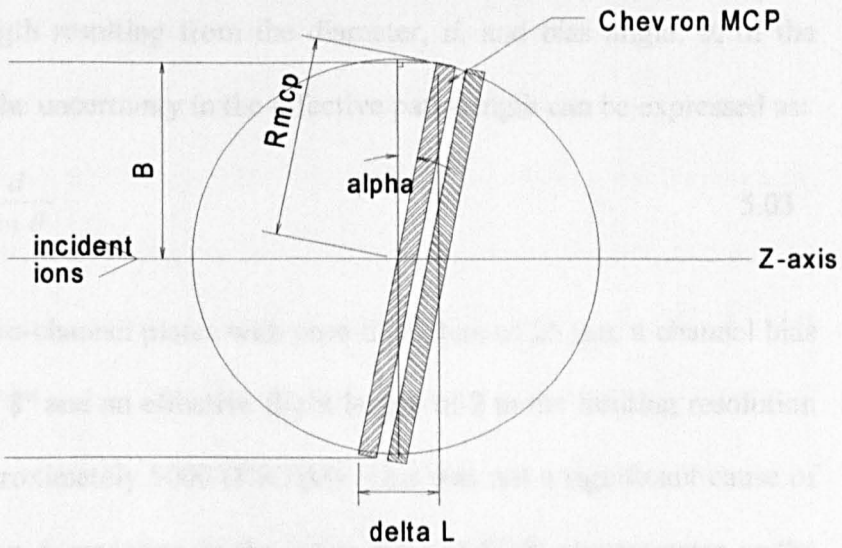

Fig. 77: Schematic diagram illustrating the resolution degrading effect of an incorrectly orientated detector.

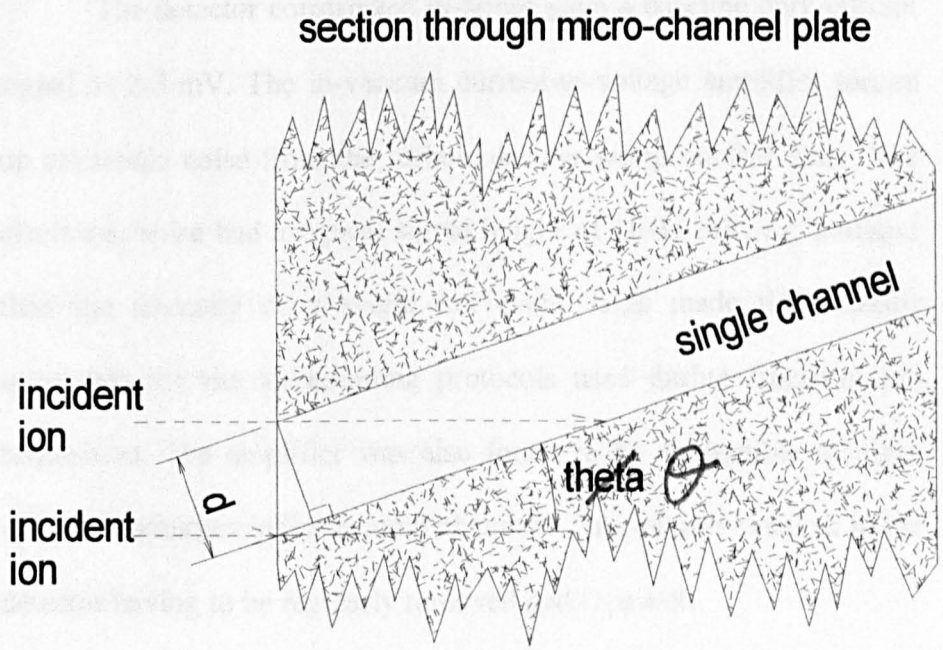

Fig. 78: Schematic diagram illustrating the resolution degrading effect resulting from the bias angle, θ, and the pore diameter, d, of the micro-channel plates.

path-length resulting from the diameter, d, and bias angle, θ, of the pores. The uncertainty in the effective path-length can be expressed as:

$$\Delta L = \frac{d}{\sin \theta} \qquad 5.03$$

For micro-channel plates with pore diameters of 25 μm, a channel bias angle of 8° and an effective flight length of 2 m the limiting resolution was approximately 5000 (FWHM). This was not a significant cause of resolution degradation in the linear time-of-flight spectrometer or the single-stage ion mirror time-of-flight spectrometer. The resolution degradation can be minimised by using a longer flight path, decreasing the pore diameter or increasing the channel bias angle.

The detector constructed in-house gave a baseline dark-current signal of 2-3 mV. The in-vacuum current-to-voltage amplifier picked up electronic noise from the turbomolecular pump control units. The electronic noise had a typical signal height of 10-15 mV, *i.e.* stronger than the intensity of a single ion event. This made the detector unsuitable for the ion-counting protocols used during fragment ion acquisition. The amplifier was also found to be susceptible to high-voltage discharges in the vacuum chamber. This initially resulted in the detector having to be regularly removed and repaired.

5.04 Beam Deflection/Focusing Assemblies.

Correct alignment of the ion beam with respect to the ion optical axis was of critical importance if the instrument was to achieve high ion transmission. Angular deflection from the ion optical axis

arises when the region of ion formation is not coincident with the ion optical axis. This was minimised by careful alignment of the laser beam on the probe target. Deflections also occur when the electrostatic field in the source region does not possess cylindrical symmetry. This may arise because the field shaping electrodes are not coaxially aligned or individual electrodes are not perfectly machined. The inclusion of suitable beam deflection assemblies was therefore important. The geometry of the ion mirrors used in the TOF-TOF spectrometer meant that the beam transmission was especially sensitive to angular deflection of the ion beam in the vertical plane.

It was not possible to restore a deflected beam to the ion optical axis using a single pair of vertical/horizontal deflection plates. In order to completely correct for angular deflection of the ion beam it was necessary to use two pairs of vertical and two pairs of horizontal defection plates. The simplest deflection system consisted of a pair of parallel metal plates, to which a differential voltage could be applied. Other groups have used obliquely cut cylindrical electrode deflection systems [10]. For our purposes it was decided that four pairs of parallel deflection plates (two vertical deflection pairs and two horizontal deflection pairs) would be adequate. The deflection assemblies were designed using the SIMION ray-tracing program. Figure 79 shows a series of plots of the angle of axial ion deflection versus the deflecting voltage for a series of deflection plate geometries. The data were extracted from a SIMION model of deflection assemblies for 10 keV, 1000 amu, singly charged ions. The results showed that

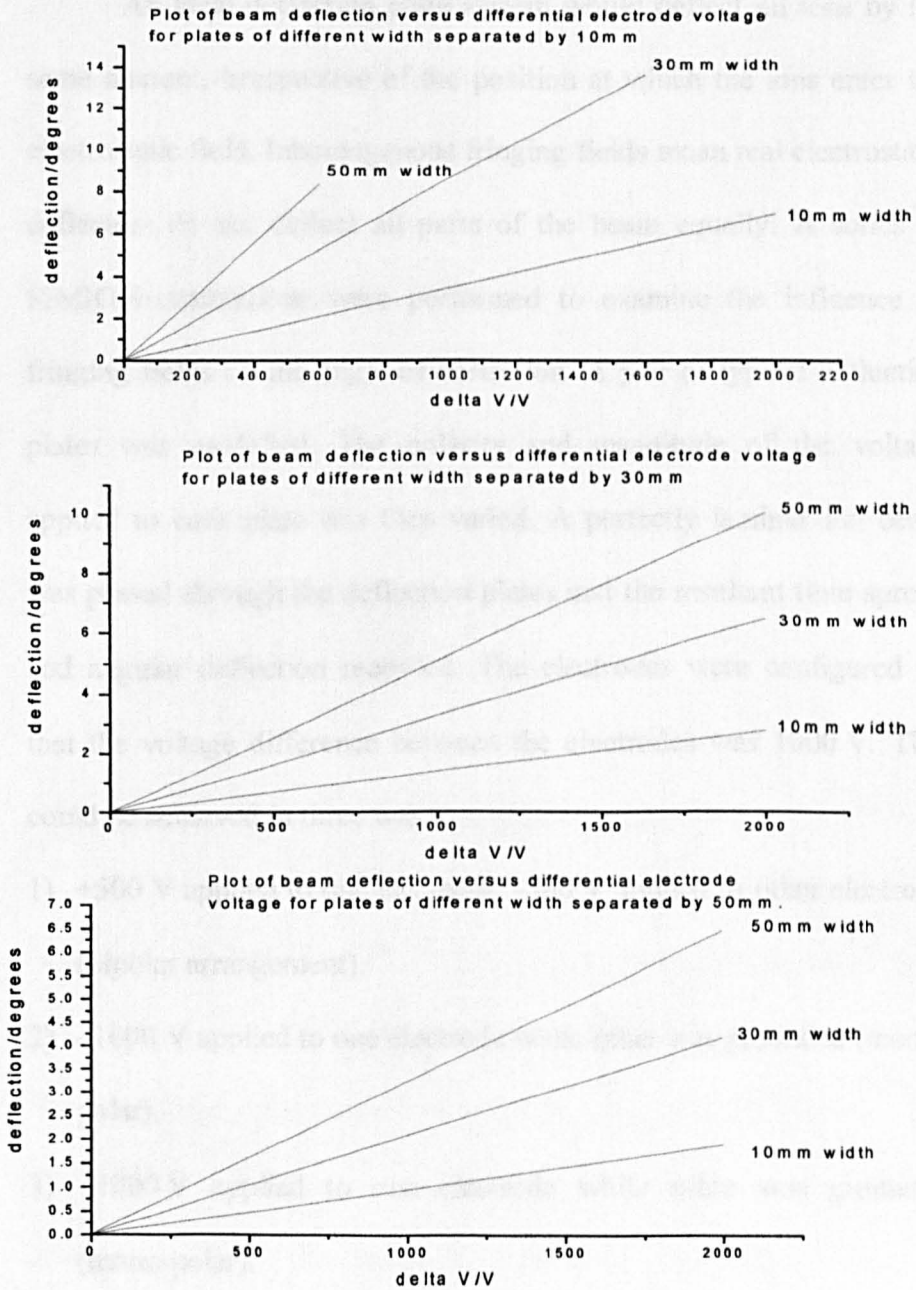

Fig. 79: SIMION study of the effects of different deflection plate geometries on the axial ion deflection. 10 mm plate separation (TOP), 30 mm plate separation (MIDDLE) and 50 mm plate separation (BOTTOM).

longer deflection plates and smaller plate separations resulted in larger deflection angles. Smaller plate separations and longer plates meant, however, that the maximum deflection range was reduced.

An ideal deflection plate system would deflect all ions by the same amount, irrespective of the position at which the ions enter the electrostatic field. Inhomogenous fringing fields mean real electrostatic deflectors do not deflect all parts of the beam equally. A series of SIMION calculations were performed to examine the influence of fringing fields on the angle of deflection. A pair of typical deflection plates was modelled. The polarity and magnitude of the voltage applied to each plate was then varied. A perfectly laminar ion beam was passed through the deflection plates and the resultant time spread and angular deflection recorded. The electrodes were configured so that the voltage difference between the electrodes was 1000 V. This could be achieved in three ways:

1) +500 V applied to one electrode, -500 V applied to other electrode (bipolar arrangement).
2) −1000 V applied to one electrode while other was grounded (mono-polar).
3) +1000 V applied to one electrode while other was grounded (mono-polar).

Figure 80 shows a plot of theoretical angular deflection versus beam diameter. The plot clearly shows that different portions of the beam were deflected by different amounts. The effect results in loss of transmission. The bipolar voltage configuration minimised this.

Figure 81 shows a plot of the theoretical time spread versus beam width for a typical deflection plate assembly. The time spread can be minimised by applying a negative voltage to an electrode or operating the electrodes in a bipolar voltage configuration. The plot clearly shows that the degradation in mass resolving power arising from the deflectors can be significant. The calculations were performed for a standard pair of deflection plated followed by a 4 m field-free region. Ideally the deflection voltages and beam diameter should be minimised to ensure high transmission and resolution. Figure 82 shows a SIMION diagram showing the extent of the 10 V equipotential contour for the bipolar and mono-polar voltage configurations. The fringing field of the mono-polar configuration extends three times further than the bipolar configuration because of field asymmetry.

5.05 Mechanical Production of Deflection Plates.

Four sets of deflection plates were designed and manufactured in-house. The deflection plates and housing were manufactured from 316L stainless steel. All deflection plates used a similar basic design. The deflection plates were spaced by four PEEK spacers. The deflection plates were mounted on PEEK supports to ensure that high-voltage breakdown did not occur. Each pair of deflection plates was housed in a grounded case that minimised the extent of the fringing fields and limited stray fields. The sides of the grounded cases were covered with a coarse woven stainless steel mesh (Potter and Soar, Banbury, U.K.). This ensured that the ground plane was well defined

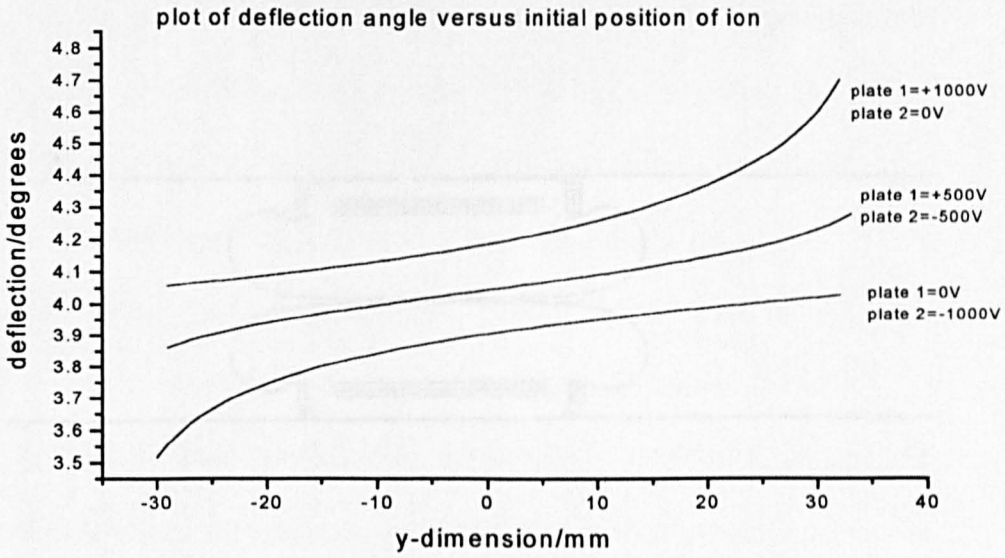

Fig. 80: Plot of angle of deflection versus beam width for a typical set of deflection plates configured so that the potential difference between the electrodes was 1000 V. Field asymmetry results in different parts of the beam being retarded by different amounts.

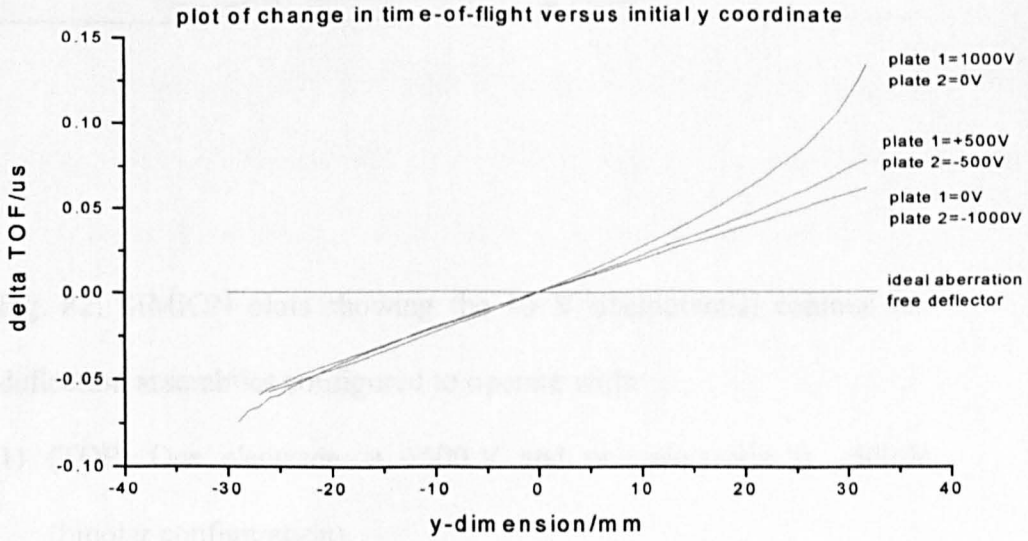

Fig. 81: Plot of difference in flight-time versus the position at which ion entered the deflector. Data shown for deflection assembly configured with 1000 V potential difference between the electrodes.

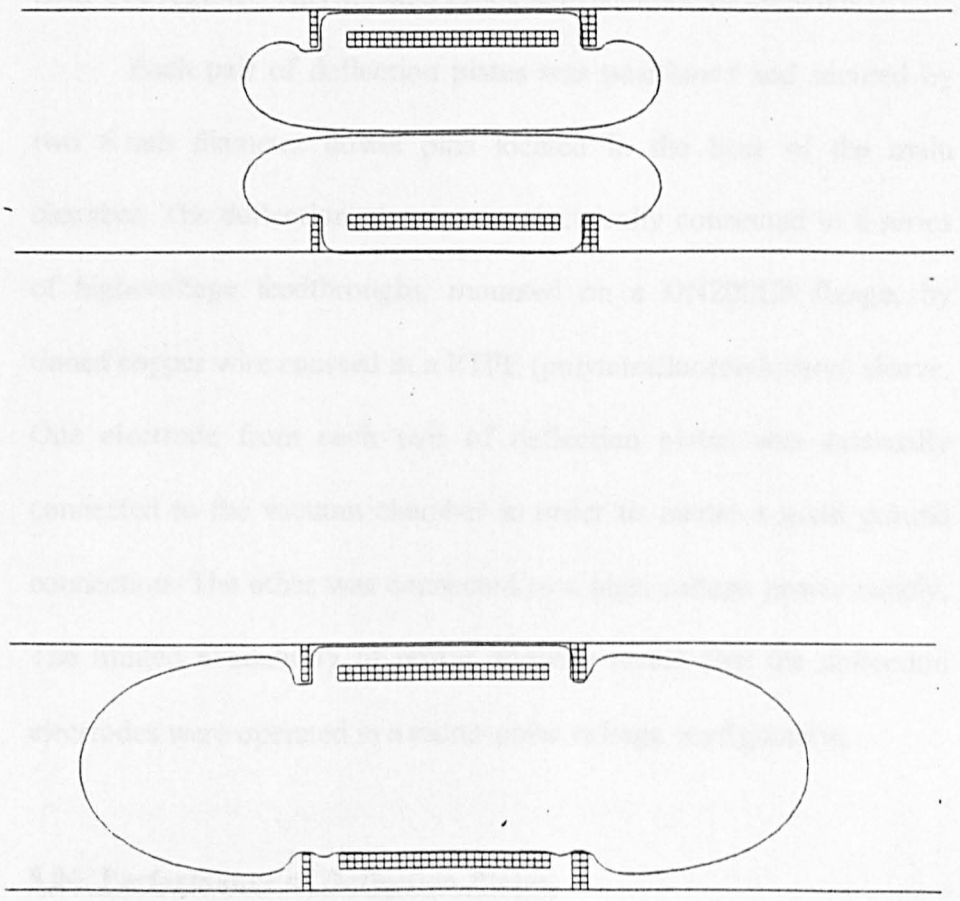

Fig. 82: SIMION plots showing the 10 V equipotential contour for deflection assemblies configured to operate with:

1) (TOP) One electrode at +500 V and one electrode at –500 V (bipolar configuration).
2) (BOTTOM) One electrode grounded and one floated at ±1000 V (mono-polar configuration). Field asymmetry results in different parts of the beam being retarded by different amounts.

and that the internal void was easily evacuated. Mesh tubes, supported on the grounded housings of the deflection assemblies, isolated all field-free regions. This allowed efficient evacuation of the voids.

Each pair of deflection plates was positioned and secured by two 6 mm diameter dowel pins located in the base of the main chamber. The deflection plates were electrically connected to a series of high-voltage feedthroughs, mounted on a DN200CF flange, by tinned copper wire encased in a PTFE (polytetrafluoroethylene) sleeve. One electrode from each pair of deflection plates was externally connected to the vacuum chamber in order to ensure a good ground connection. The other was connected to a high-voltage power supply. The limited availability of power supplies meant that the deflection electrodes were operated in a mono-polar voltage configuration.

5.06 Performance of Deflection Plates.

The first pair of horizontal deflection plates was used to alter the entrance angle of the ion beam with respect to the single-stage mirror axis. By scanning the deflection voltage it was possible to optimise the transmission of the ion beam through the apertures of the differentially pumped collision-cell. The last pair of horizontal deflection plates was found to be largely unnecessary. During normal operation these deflection plates were grounded.

The two pairs of vertical deflection plates proved to be invaluable. Ions emerging from the ion source were found to possess a large downwards vertical deflection. The deflection plates corrected

the deflection when 500-800 V was applied across the electrodes. The deflection was subsequently found to be due to a slight machining error in one of the electrodes in the source Einzel lenses. The electrode was subsequently replaced and the deflection cured.

5.07 Single-Stage Ion Mirror.

The purpose of the first ion mirror was to form a time focus at the collision-cell in order to maximise fragment ion resolution. The ion mirror was required to transmit an ion beam with angular and spatial properties within the acceptance criteria of the collision-cell and the quadratic-field ion mirror. An emergent beam with unsuitable properties would not have passed through the small apertures of the collision-cell or the defocusing field inside the quadratic-field ion mirror. In order to ensure that the TOF-TOF spectrometer achieved efficient transmission of ions from the source region to the final detector, it was important that the first ion mirror did not impart a large angular divergence to the ions. This could have been achieved using two possible mirror configurations.

The first possibility was to design an ion mirror capable of simultaneously spatially and temporally focusing the ion packet at the collision-cell. Figure 83 shows a schematic diagram illustrating the principle of operation of a spatially focusing ion mirror. The source region and the associated optics form a collimated ion beam. The ion mirror simultaneously time focuses and spatially focuses the ion beam at the collision-cell without the need for further lenses.

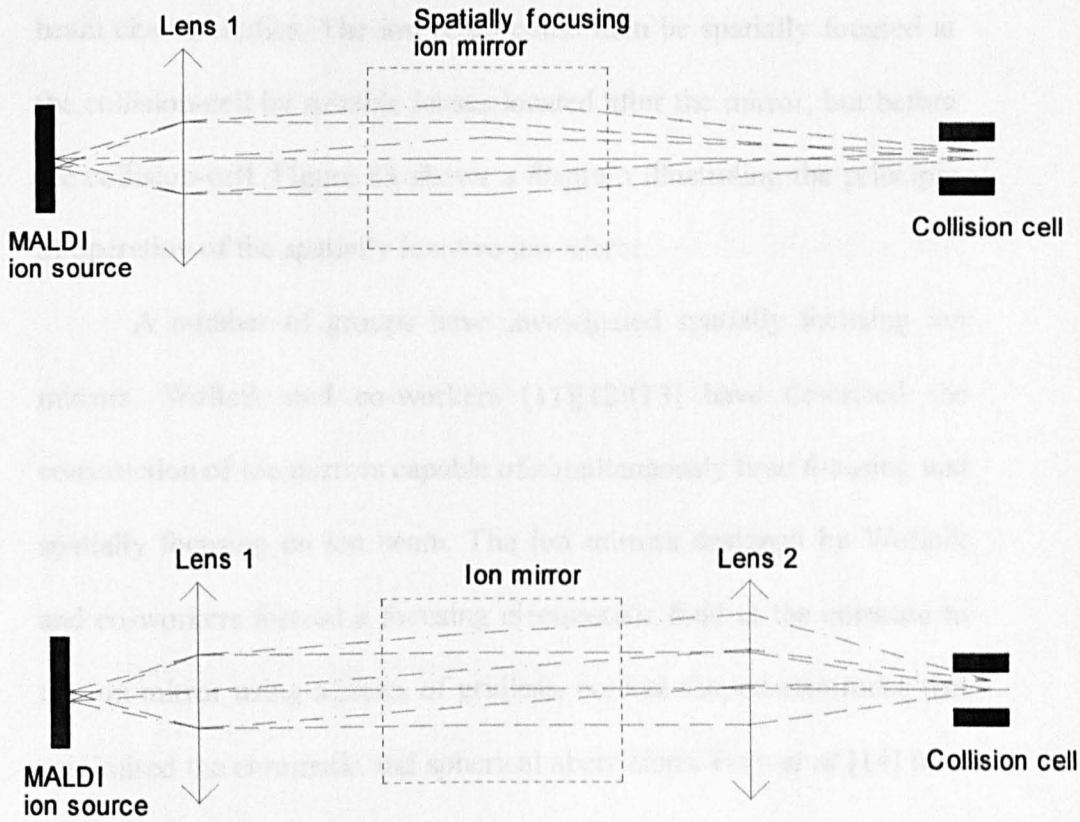

Fig. 83: Schematic diagram illustrating the instrument configuration of a simultaneously spatially and temporally focusing ion mirror (TOP). Schematic diagram illustrating the instrument configuration for a temporally focusing but spatially inactive ion mirror (BOTTOM).

The second option was to design an ion mirror capable of transmitting a collimated ion beam without significantly degrading the beam characteristics. The ion beam could then be spatially focused at the collision-cell by suitable lenses located after the mirror, but before the collision-cell. Figure 83 shows a diagram illustrating the principle of operation of the spatially inactive ion mirror.

A number of groups have investigated spatially focusing ion mirrors. Wollnik and co-workers [11][12][13] have described the construction of ion mirrors capable of simultaneously time focusing and spatially focusing an ion beam. The ion mirrors designed by Wollnik and co-workers formed a focusing electrostatic field at the entrance to the ion mirror using a series of gridless, conical shaped electrodes that minimised the chromatic and spherical aberrations. Frey *et al* [14] have constructed a gridless ion mirror capable of spatial focusing. Gridless ion mirrors, while offering transmission gains, are complex to design and optimise, and for this reason are not widely used.

By comparison ion mirrors that are spatially inactive are relatively simple to design. The spatially inactive ion mirror was developed further because it was felt that the ion mirror would be simpler to design and optimise than an ion mirror capable of simultaneous temporal and spatial focusing. Subsequent experiments showed, however, that an ion mirror capable of spatially focusing the ion beam was necessary to achieve high transmission and sensitivity.

5.08 Optimisation of the Design of the First Ion Mirror.

One of the most important features of the first ion mirror was that its design should allow for future modifications and improvements. The first ion mirror was a single-stage ion mirror because it was simple to design, gave good transmission and suitably high mass resolving power. The physical length of the ion mirror was governed by the basic time focusing criteria discussed in chapter one. For a single-stage ion mirror to achieve first-order time focusing:

$$\frac{dt}{du} = 0 \qquad 5.04$$

The following conditions must be satisfied:

$$\frac{2mu}{qE} = \frac{L}{u} \qquad 5.05$$

$$E = \frac{2mu^2}{qL} = \frac{4U}{qL} \qquad 5.06$$

m is the mass of the ion, u is the velocity of the ion, q is the charge, E is the electric field strength inside the mirror, L is the length of the field-free flight path. $U=lqE$, where l is the penetration depth. Under these conditions the residence time inside the ion mirror, t_m, is equal to the time spent in the field-free regions, t_L,:

$$t_m = t_L = \frac{L}{u} \qquad 5.07$$

The average velocity of an ion through an ideal, homogenous single-stage mirror is $u/2$. Therefore the flight path through the ion mirror

must be $L/2$. This corresponds to a mirror penetration depth of $L/4$. The physical length of the ion mirror is therefore ¼ L, the total length of the field-free drift regions. In reality, if the ion mirror were equal to ¼L, the ions would pass through the fringing fields at the rear of the ion mirror. This would increase the temporal dispersion of the ion packet and degrade the mass resolving power of the spectrometer. The fringing fields are the result of electrode surface irregularities, grids and physical imperfections. The ion mirror is therefore always longer than ¼L.

The total length of the field free-regions between the source and the collision-cell in the TOF-TOF spectrometer was approximately 1.4 m. The minimum length of the single-stage ion mirror was therefore 0.35 m. The final mirror had a physical length of 0.4 m. This meant that the ions did not come into close proximity with the rear electrode. Adjusting the electric-field strength inside the ion mirror allowed the depth of mirror penetration, and hence the position of the time focus, to be controlled.

Once the length of the ion mirror had been determined, it was necessary to determine the width and height of the mirror. These dimensions were governed by a number of considerations. These included the physical dimensions of the vacuum chamber, the layout and size of the ion optical components, the symmetry of the electrostatic field inside the ion mirror and the geometry of the field sustaining electrodes. In order to optimise these dimensions it was necessary to characterise and optimise the ion mirror using SIMION.

The width of the ion mirror was determined in part by the Z shaped ion trajectory through the instrument. In order that there to was sufficient space for the positioning of the collision-cell, the steering optics and the quadratic-field ion mirror it was necessary that the ion beam entered the reflectron at an angle with respect to the mirror axis. A coaxial mirror arrangement was unsuitable for the tandem CID instrument. The minimum mirror width was determined by the angle between the mirror axis and the ion optical axis. Figure 84 shows a schematic diagram illustrating the pertinent relationships between different mirror dimensions [15]. The distance between the entrance and exit point of the ion beam can be expressed as:

$$s_x = 4s_p \sin\alpha \cos\alpha \qquad 5.08$$

s_x is the distance between the entry and exit point, α is the angle of the reflectron with respect to the ion beam (tilt angle) and s_p can be expressed as:

$$4s_p = L_1 + L_2 \qquad 5.09$$

For an ion mirror with a tilt angle of 5.5° and a penetration depth of 0.35 m, s_x was equal to 0.143 m. This dimension represented the minimum width of the aperture. Fringing fields and electrostatic considerations meant that the aperture was wider than this.

In order to shape the field and prevent ground potential penetrating the field from the side, it was necessary to use a number of field-sustaining electrodes. Seventeen electrodes were used in the final

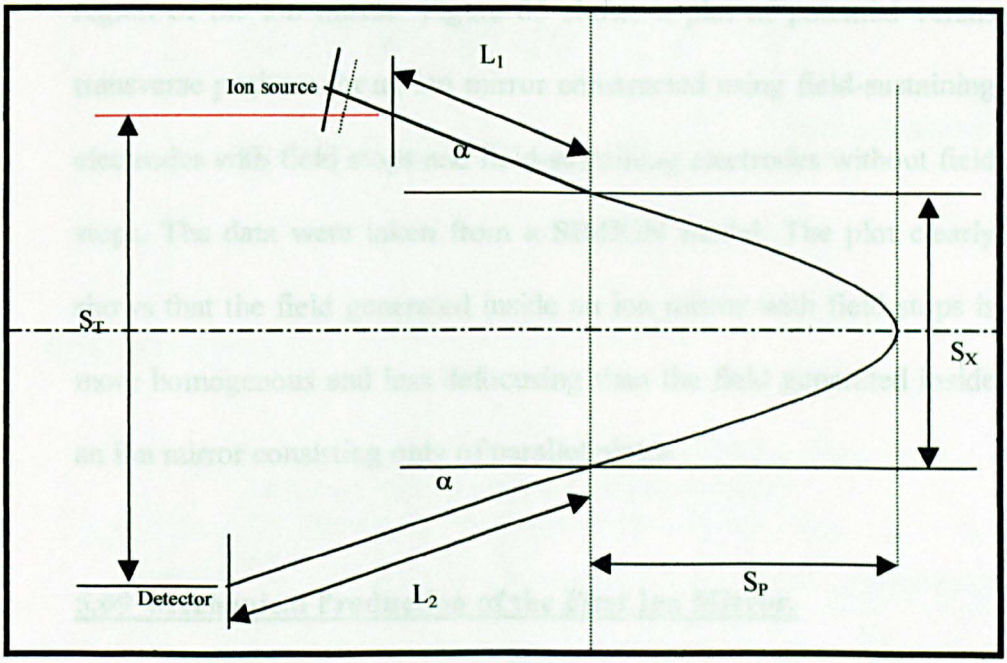

$$4S_P = L_1 + L_2$$
$$S_X = 4S_p \sin\alpha \cos\alpha$$
$$S_T = (L_1 + L_2) \sin\alpha (1 + \cos\alpha)$$

Fig. 84: Diagram illustrating relationships between mirror dimensions.

ion mirror: one front electrode, 15 standard field-sustaining electrodes and one rear electrode. SIMION calculations showed that this provided a suitable field with sufficient electrodes to allow the field to be shaped. The mirror consisted of a series of parallel metal plates with field stops to reduce ground potential penetration into the reflecting region of the ion mirror. Figure 85 shows a plot of potential versus transverse position for an ion mirror constructed using field-sustaining electrodes with field stops and field-sustaining electrodes without field stops. The data were taken from a SIMION model. The plot clearly shows that the field generated inside an ion mirror with field stops is more homogenous and less defocusing than the field generated inside an ion mirror consisting only of parallel plates.

5.09 Mechanical Production of the First Ion Mirror.

There are several methods of physically constructing an ion mirror. Derrick and co-workers [16] have described a quadratic-field reflectron in which the field-sustaining electrodes were formed by copper tracks etched on the surface of printed circuit boards. Hansen and Myerholtz [17] have patented an ion mirror in which the retarding field was generated by a continuous resistive film formed into a cylinder. The most wide spread means of producing a reflecting field is by use of a series of discrete, resistively coupled metal electrodes supported by a series of insulating spacers. The discrete metal electrode design has been proven to be compatible with high-vacuum systems.

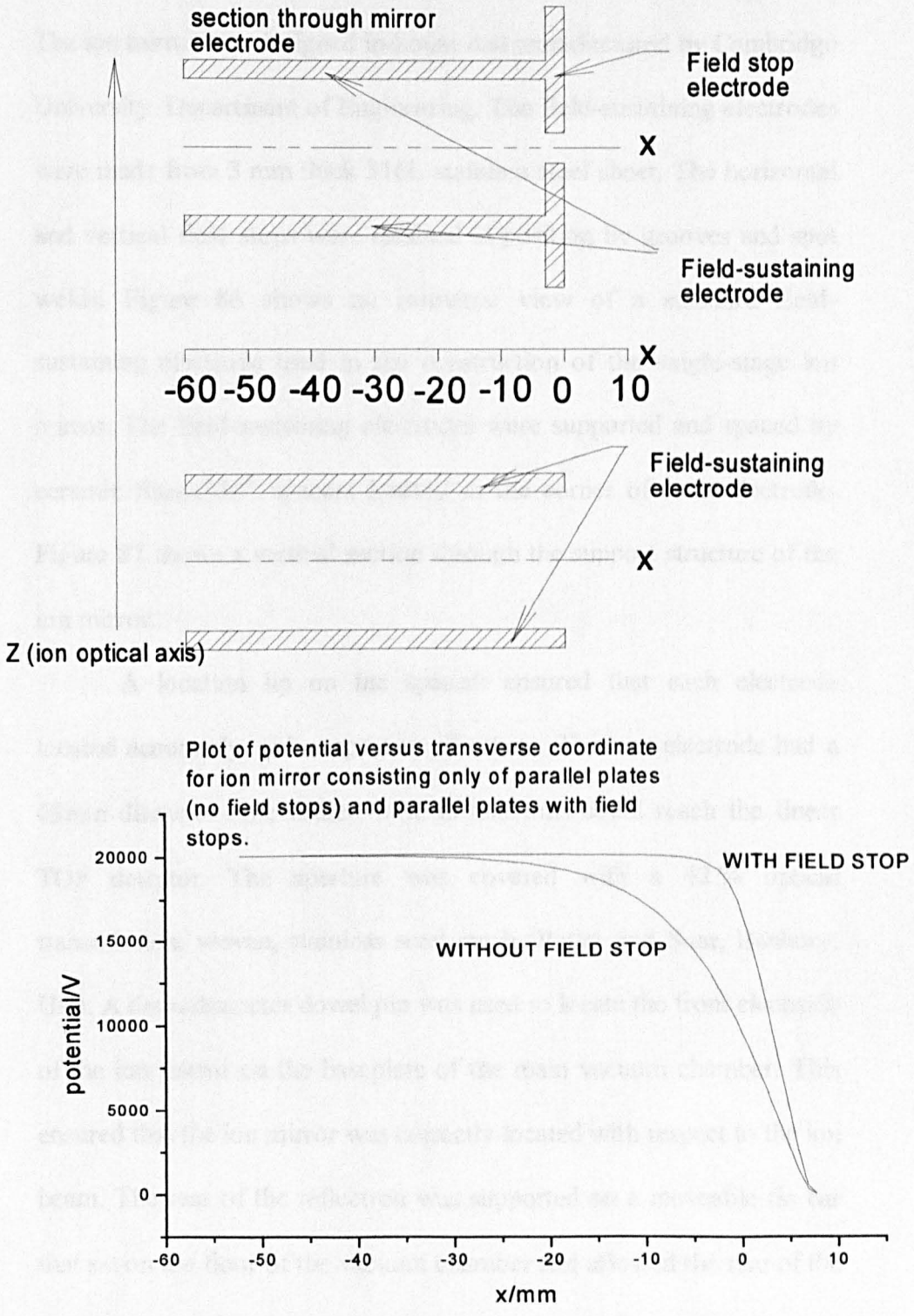

Fig. 85: Schematic diagram showing section through field-sustaining electrodes, with and without field stops electrodes (TOP). Plot of theoretical potential versus radial dimension (BOTTOM).

The ion mirror was designed in-house and manufactured by Cambridge University, Department of Engineering. The field-sustaining electrodes were made from 3 mm thick 316L stainless steel sheet. The horizontal and vertical field stops were retained in position by grooves and spot welds. Figure 86 shows an isometric view of a standard field-sustaining electrode used in the construction of the single-stage ion mirror. The field-sustaining electrodes were supported and spaced by ceramic Shapal-M® spacers located in the corner of each electrode. Figure 87 shows a vertical section through the support structure of the ion mirror.

A location lip on the spacers ensured that each electrode located accurately with respect to all others. The rear electrode had a 68mm diameter hole drilled in it so that ions could reach the linear TOF detector. The aperture was covered with a 42 % optical transmission, woven, stainless steel mesh (Potter and Soar, Banbury, UK). A 6mm diameter dowel pin was used to locate the front electrode of the ion mirror on the baseplate of the main vacuum chamber. This ensured that the ion mirror was correctly located with respect to the ion beam. The rear of the reflectron was supported on a moveable tie bar that sat on the floor of the vacuum chamber and allowed the rear of the ion mirror to rotate freely. The mirror was electrically isolated from the grounded chamber by Shapal-M® ceramic spacers. The front electrode had a rectangular aperture. Six M3 tapped holes meant that a grid or smaller aperture could be mounted across the aperture to modify the electrostatic field at the entrance to the ion mirror. Figure 88 shows an

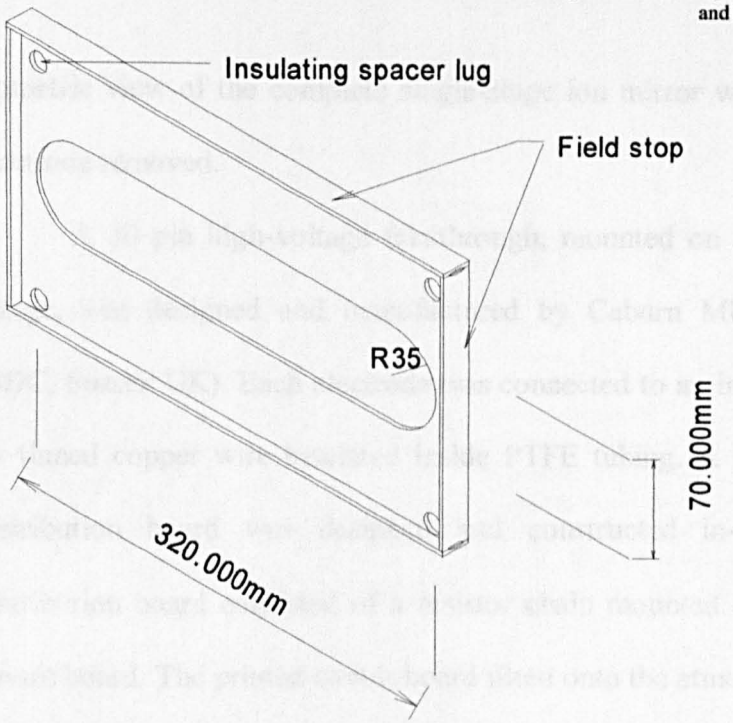

Fig. 86: Diagram of a standard field-sustaining electrode used in the construction of the single-stage ion mirror.

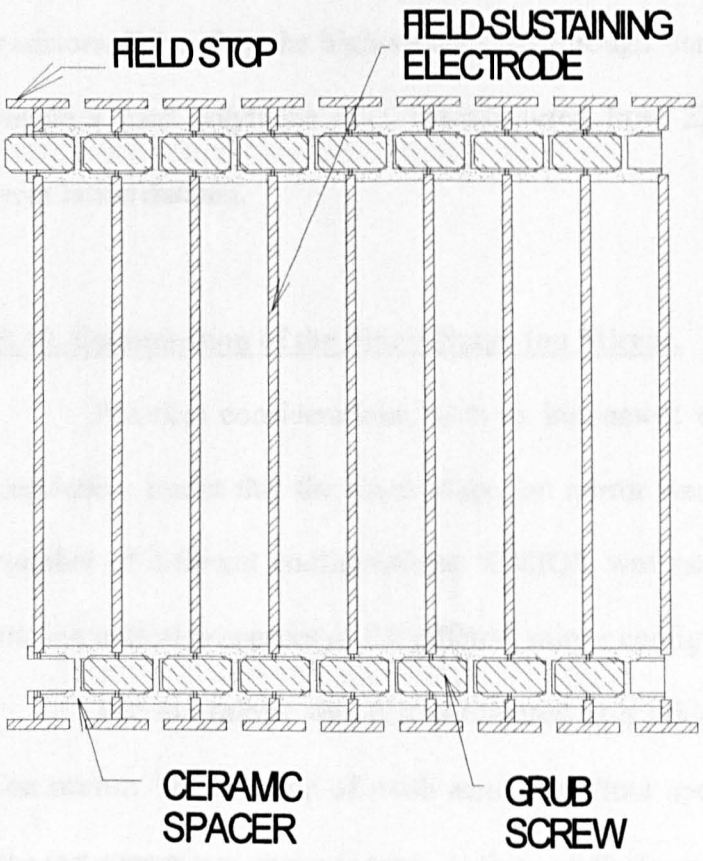

Fig. 87: Vertical section through mirror support structure.

isometric view of the complete single-stage ion mirror with the front electrode removed.

A 30 pin high-voltage feedthrough, mounted on a DN200CF flange, was designed and manufactured by Caburn MDC (Caburn MDC, Sussex UK). Each electrode was connected to an individual pin by tinned copper wire insulated inside PTFE tubing. A high-voltage distribution board was designed and constructed in-house. The distribution board consisted of a resistor chain mounted on a printed circuit board. The printed circuit board fitted onto the atmospheric side of the high-voltage feedthrough flange. The voltage supplied to each field-sustaining electrode was optimised by adjusting the variable resistors. For safety the high-voltage feedthrough flange was isolated inside a hard polythene case, manufactured from 220 mm diameter ventilation ducting.

5.10 Optimisation of the Single-Stage Ion Mirror.

Practical considerations, such as instrument transmission and resolution, meant that the single-stage ion mirror was configured in a number of different configurations. SIMION was used to understand the ion optical properties of the different mirror configurations.

The ion mirror was first configured as a gridded, single-stage ion mirror. The addition of mesh across the front aperture meant that the instrument was easier to tune. A piece of 42 % optical transmission grid was placed across the entrance aperture and retained in place by a

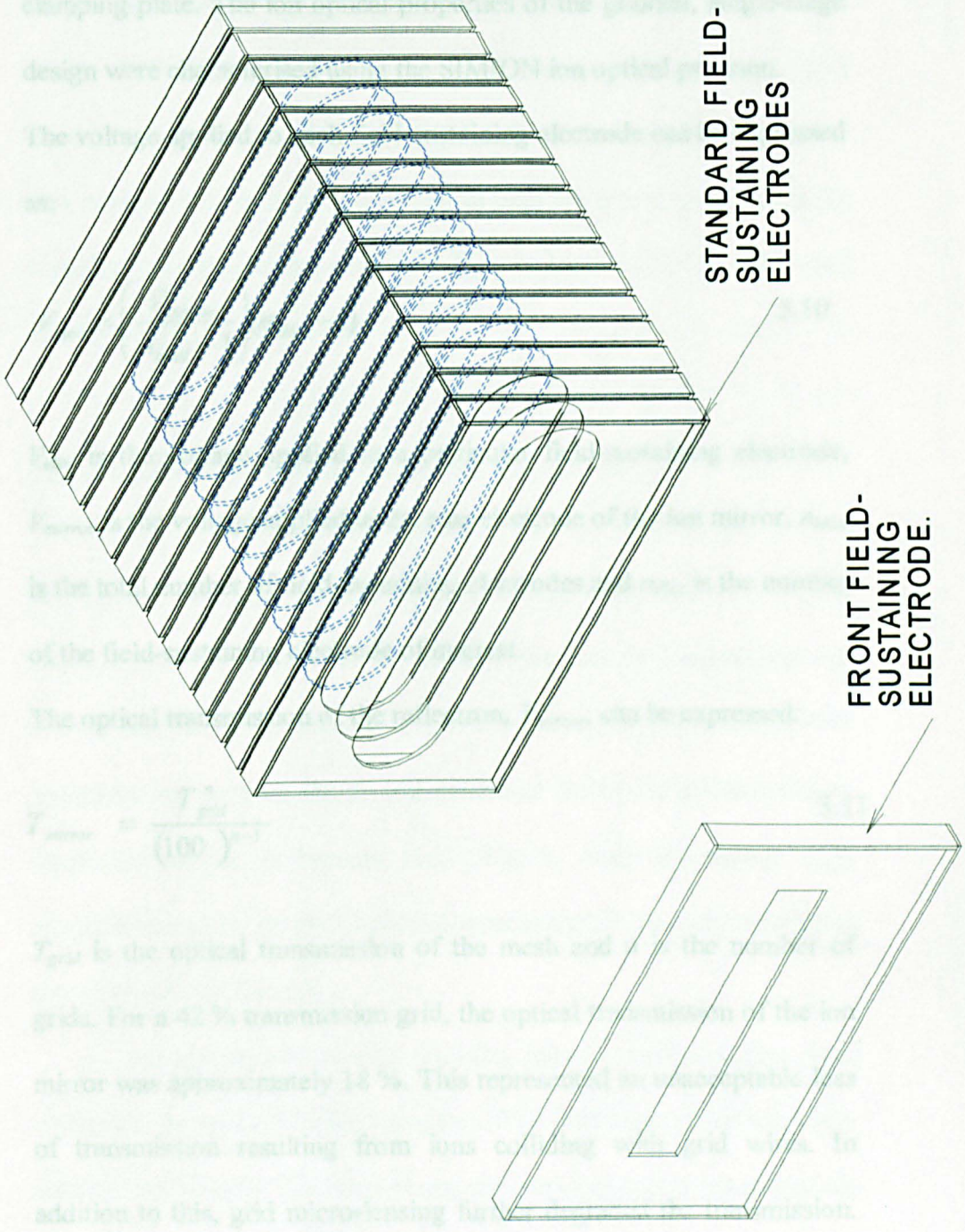

Fig. 88: Isometric view of the complete single-stage ion mirror.

The front electrode has been removed for clarity.

clamping plate. The ion optical properties of the gridded, single-stage design were characterised using the SIMION ion optical program.

The voltage applied to each field-sustaining electrode can be expressed as:

$$V_{elec} = \left(\frac{V_{mirror}}{n_{total} - 1} \right) (n_{elec} - 1) \qquad 5.10$$

V_{elec} is the voltage applied to a particular field-sustaining electrode, V_{mirror} is the voltage applied to the rear electrode of the ion mirror, n_{total} is the total number of field-sustaining electrodes and n_{elec} is the number of the field-sustaining electrode of interest.

The optical transmission of the reflectron, T_{mirror}, can be expressed:

$$T_{mirror} = \frac{T_{grid}^{n}}{(100)^{n-1}} \qquad 5.11$$

T_{grid} is the optical transmission of the mesh and n is the number of grids. For a 42 % transmission grid, the optical transmission of the ion mirror was approximately 18 %. This represented an unacceptable loss of transmission resulting from ions colliding with grid wires. In addition to this, grid micro-lensing further degraded the transmission. The mesh could have either been replaced with an 80-90 % transmission grid or have been removed altogether. A solid electrode with entrance and exit apertures subsequently replaced the grid. This resulted in the formation of a uniform reflecting field without the loss in transmission resulting from collisions with grid wires. This improvement significantly increased the sensitivity and transmission of

the instrument. Subsequent experiments showed that the transmission of the TOF-TOF spectrometer was still unacceptably low. It was therefore necessary to propose a solution to the transmission problem. One solution was to convert the single-stage ion mirror into a spatially focusing ion mirror that would allow the ion beam to traverse the small apertures of the collision-cell.

5.11 SIMION Simulation of the First Ion Mirror.

Extensive computer modelling of the homogenous electric field ion mirror and the proposed spatially focusing ion mirror was conducted to determine the critical beam parameters. Simulations had shown that the field generated inside the single-stage ion mirror with apertures was very similar to that generated inside the gridded single-stage ion mirror. It became clear that in order to achieve high transmission through the TOF-TOF spectrometer the first ion mirror must be spatially focusing.

The emittance patterns for the mirror configurations were calculated using the SIMION program. The initial ion conditions were outlined previously. The ions possessed initial desorption energies up to 12 eV, angular spreads of up to ±80° and spatial spreads of ±50 microns (vertical) and ±85 microns (horizontal). The ions were created at the surface of the probe tip.

Figure 89 shows the horizontal emittance pattern at the collision-cell for the gridded single-stage ion mirror. Figure 90 shows the vertical emittance pattern at the collision-cell for the gridded

single-stage ion mirror. Both plots include the low intensity beam halo region. The potential applied to the rear of the ion mirror was 12 kV, while the source conditions were: accelerating potential = 10 kV, first Einzel lens = -14 kV, second Einzel lens = -13 kV. Figure 91 shows the horizontal emittance without the beam halo region. Figure 92 shows the vertical emittance pattern at the collision-cell without the beam halo region. The emittance patterns showed that the beam was elliptical in shape and approximately 24 mm wide in the horizontal by 16mm high in the vertical. The model neglected the effects of grid micro-optics, which would further defocus the ion beam. The most intense portion of the beam fell within an area 20 mm wide by 14 mm high. The results clearly showed that the majority of ions did not pass through the 2mm diameter holes used to define the differentially pumped collision-cell region. The computer modelling results were supported by experimentally determined transmission values, which are discussed later.

These results clearly showed that the first ion mirror was not producing an ion beam with properties matching the acceptance criteria of the collision-cell. A study was therefore undertaken to determine a mirror configuration that would increase the transmission while retaining high resolution. Ideally the ion mirrors field-sustaining electrodes would not have to be re-designed. This meant that the

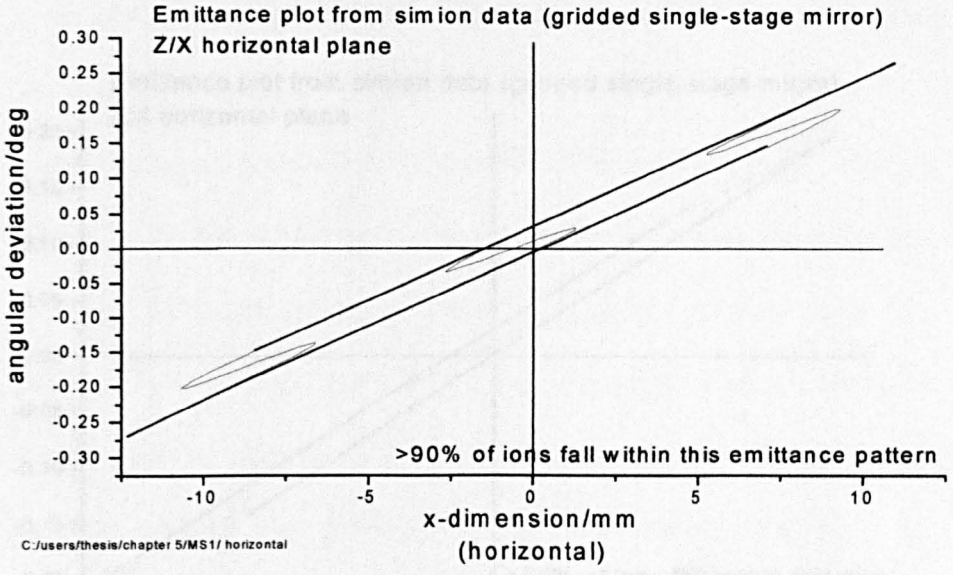

Fig. 89: Emittance (horizontal plane) pattern at the collision-cell for gridded single-stage ion mirror. Emittance pattern includes beam halo.

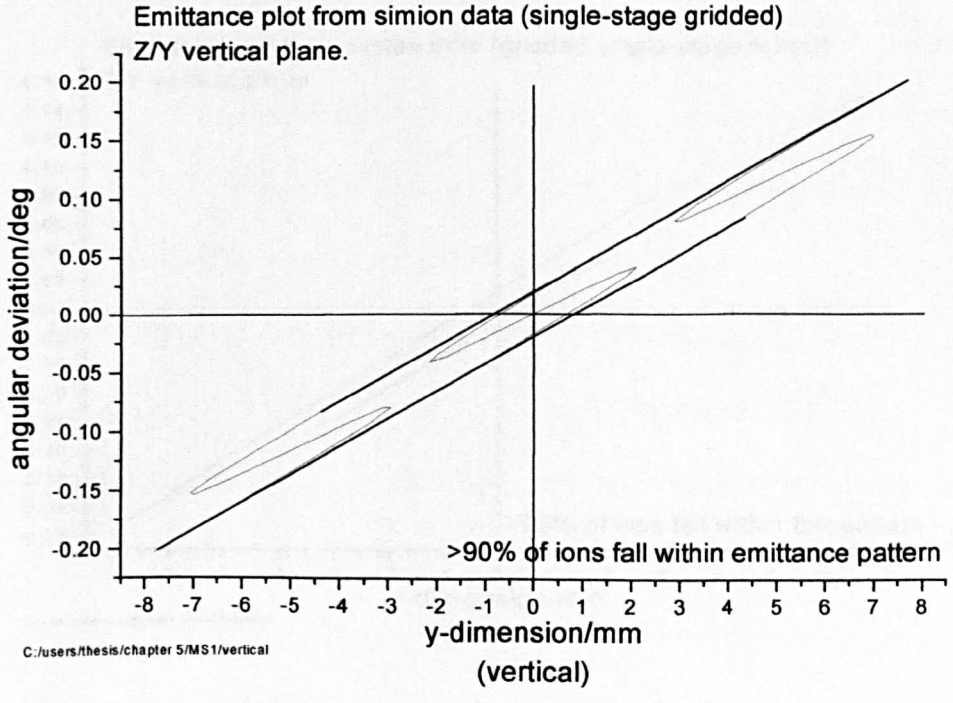

Fig. 90: Emittance (vertical plane) pattern at the collision-cell for gridded single-stage ion mirror. Beam halo included.

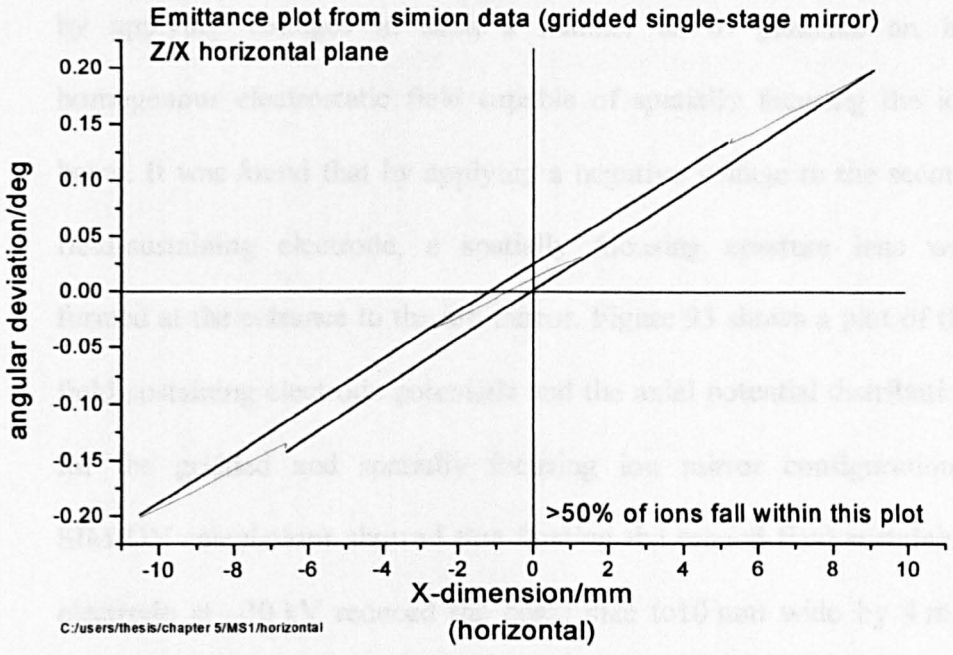

Fig. 91: Emittance (horizontal plane) pattern at the collision-cell for gridded single-stage ion mirror. Beam halo region excluded.

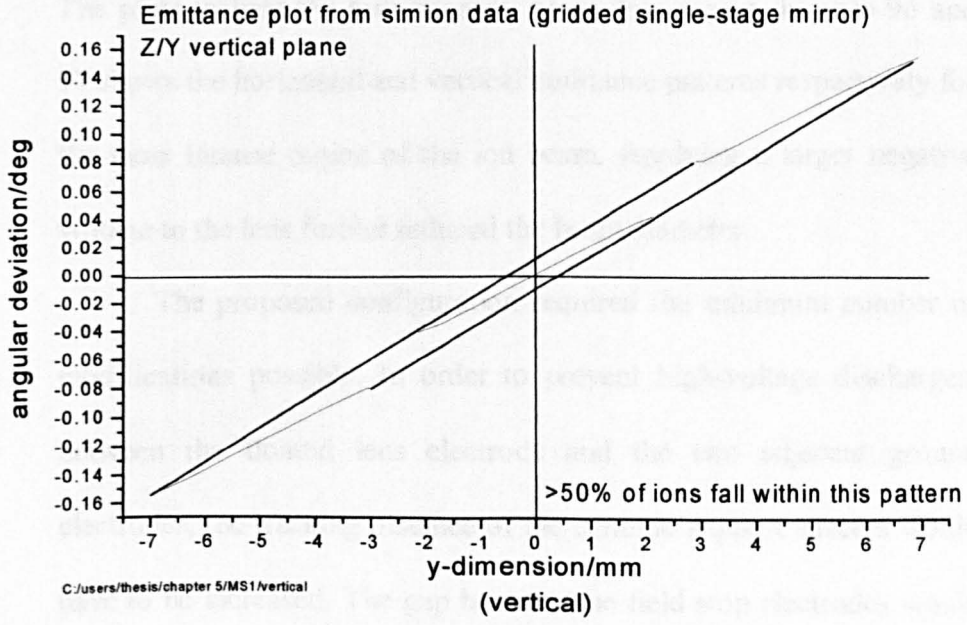

Fig. 92: Emittance (vertical plane) pattern at the collision-cell for gridded single-stage ion mirror. Beam halo region excluded.

spatial focusing properties of the ion mirror would have to be realised by applying voltages in such a manner as to generate an in-homogenous electrostatic field capable of spatially focusing the ion beam. It was found that by applying a negative voltage to the second field-sustaining electrode, a spatially focusing aperture lens was formed at the entrance to the ion mirror. Figure 93 shows a plot of the field-sustaining electrode potentials and the axial potential distribution for the gridded and spatially focusing ion mirror configurations. SIMION calculations showed that floating the second field-sustaining electrode at –30 kV reduced the beam size to10 mm wide by 4 mm high. The most intense region of the ion beam fell within an area 6 mm wide by 2 mm high. Figures 94 and 95 show the horizontal and vertical emittance patterns respectively, for the spatially focusing ion mirror. The plots include the low intensity beam halo region. Figures 96 and 97 shows the horizontal and vertical emittance patterns respectively for the most intense region of the ion beam. Applying a larger negative voltage to the lens further reduced the beam diameter.

The proposed configuration required the minimum number of modifications possible. In order to prevent high-voltage discharges, between the floated lens electrode and the two adjacent ground electrodes, the tracking distance of the ceramic support spacers would have to be increased. The gap between the field stop electrodes would also have to be increased.

A series of theoretical SIMION calculations was performed to compare the spatial properties of the focusing and gridded mirror

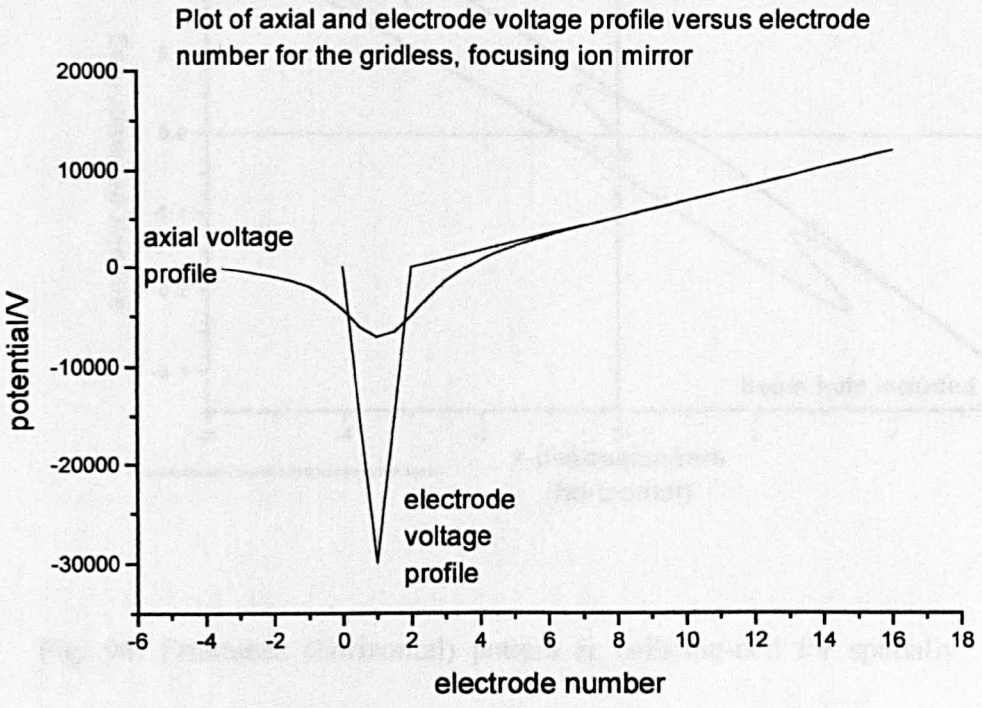

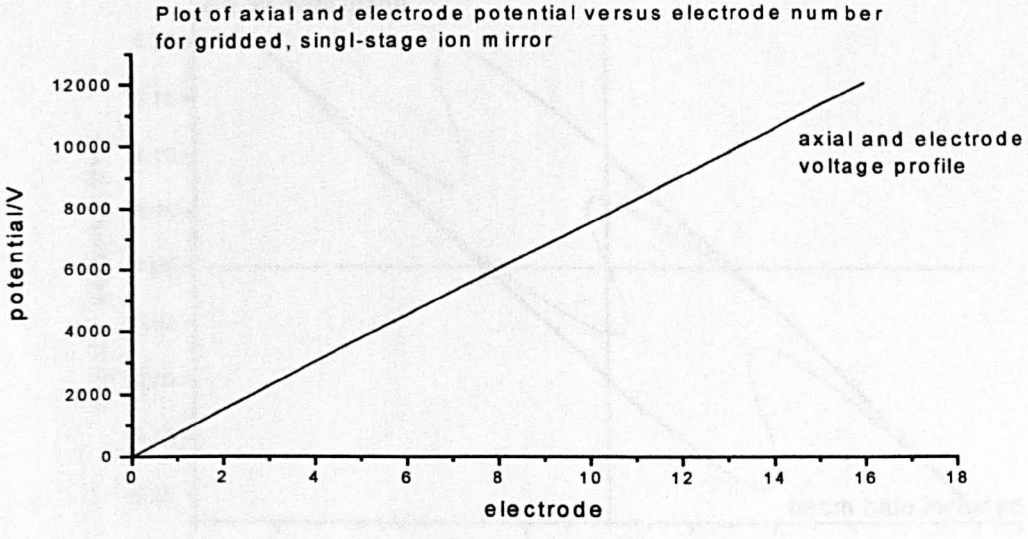

Fig. 93: Plot of axial voltage profile and voltage applied to the field-sustaining electrodes in the gridless, spatially focusing ion mirror (TOP). Plot of axial voltage profile and voltage applied to the field-sustaining electrodes for the gridded ion mirror (BOTTOM).

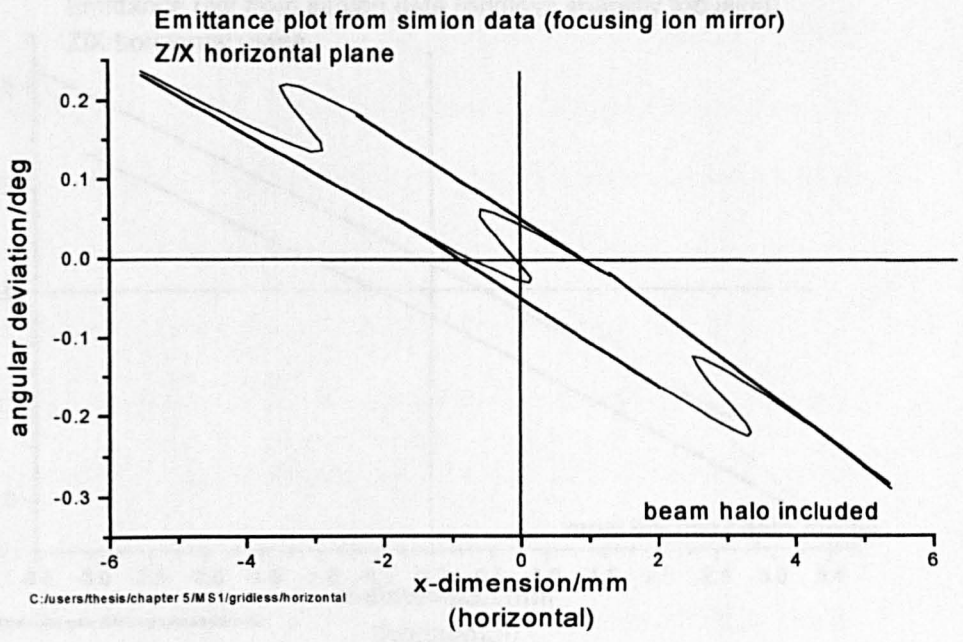

Fig. 94: Emittance (horizontal) pattern at collision-cell for spatially focusing ion mirror. Beam halo region included.

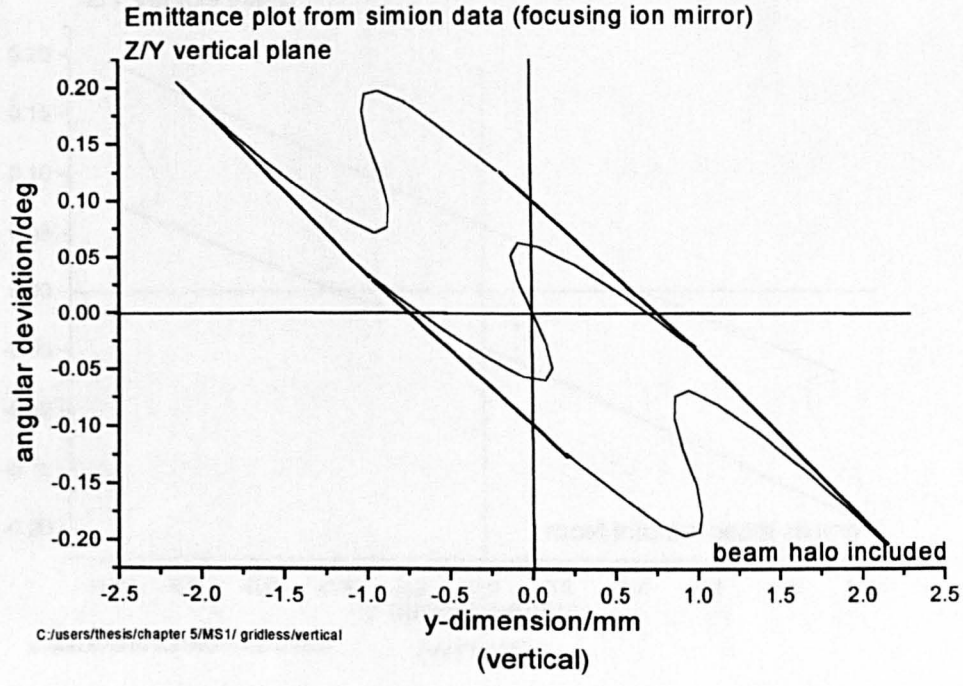

Fig. 95: Emittance (vertical) pattern at the collision-cell for spatially focusing ion mirror. Beam halo region included.

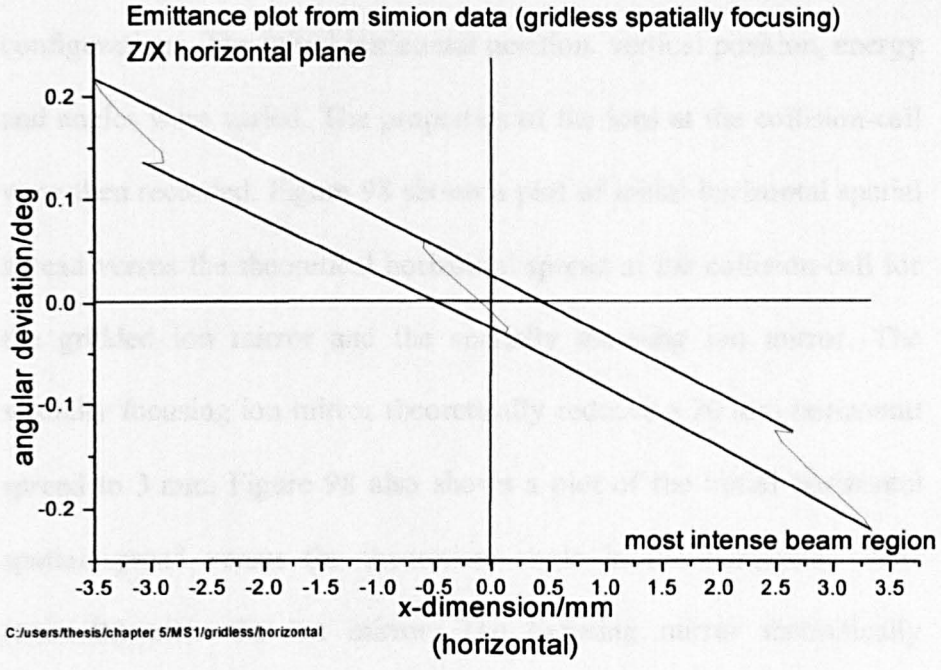

Fig. 96: Emittance (horizontal) pattern at collision-cell for spatially focusing ion mirror. Beam halo region excluded.

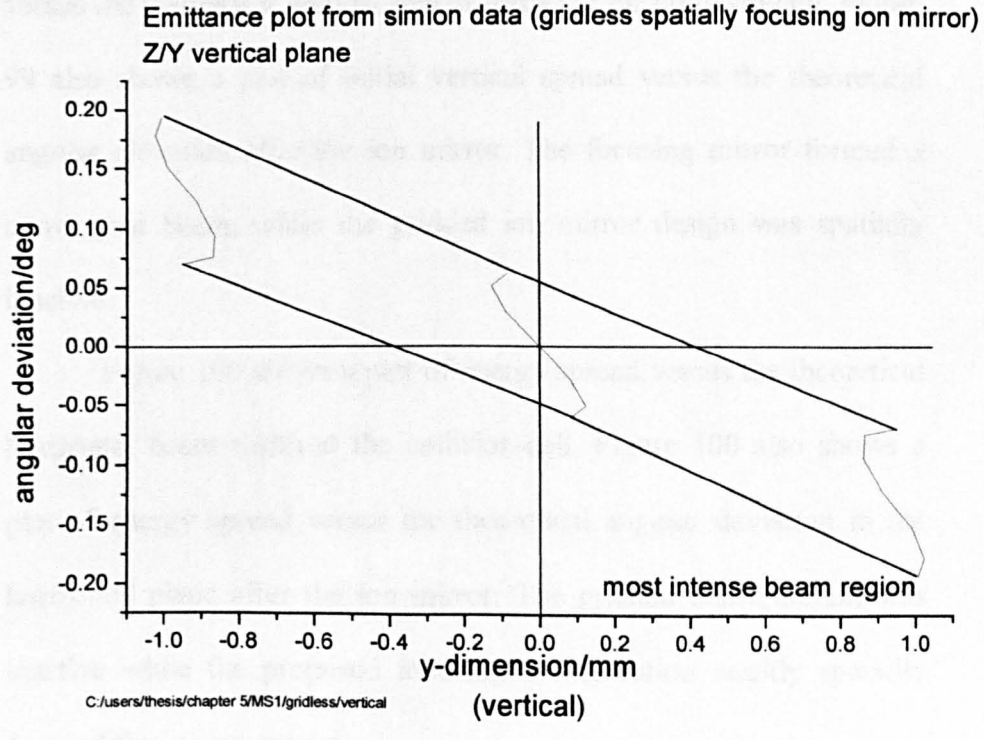

Fig. 97: Emittance (vertical) pattern at collision-cell for spatially focusing ion mirror. Beam halo region excluded.

configurations. The initial horizontal position, vertical position, energy and angles were varied. The properties of the ions at the collision-cell were then recorded. Figure 98 shows a plot of initial horizontal spatial spread versus the theoretical horizontal spread at the collision-cell for the gridded ion mirror and the spatially focusing ion mirror. The spatially focusing ion mirror theoretically reduces a 20 mm horizontal spread to 3 mm. Figure 98 also shows a plot of the initial horizontal spatial spread versus the theoretical angle in the horizontal plane (azimuth) after the ion mirror. The focusing mirror theoretically formed a convergent beam while the gridded ion mirror was almost inactive.

Figure 99 shows a plot of the initial vertical spatial spread versus the theoretical vertical spatial spread at the collision-cell. Figure 99 also shows a plot of initial vertical spread versus the theoretical angular elevation after the ion mirror. The focusing mirror formed a convergent beam, while the gridded ion mirror design was spatially inactive.

Figure 100 shows a plot of energy spread versus the theoretical horizontal beam width at the collision-cell. Figure 100 also shows a plot of energy spread versus the theoretical angular deviation in the horizontal plane after the ion mirror. The gridded configuration was inactive while the proposed focusing configuration weakly spatially focused the energy spread.

Figure 101 shows plots of initial angular elevation (angular deviation in vertical plane) versus the angular elevation after the

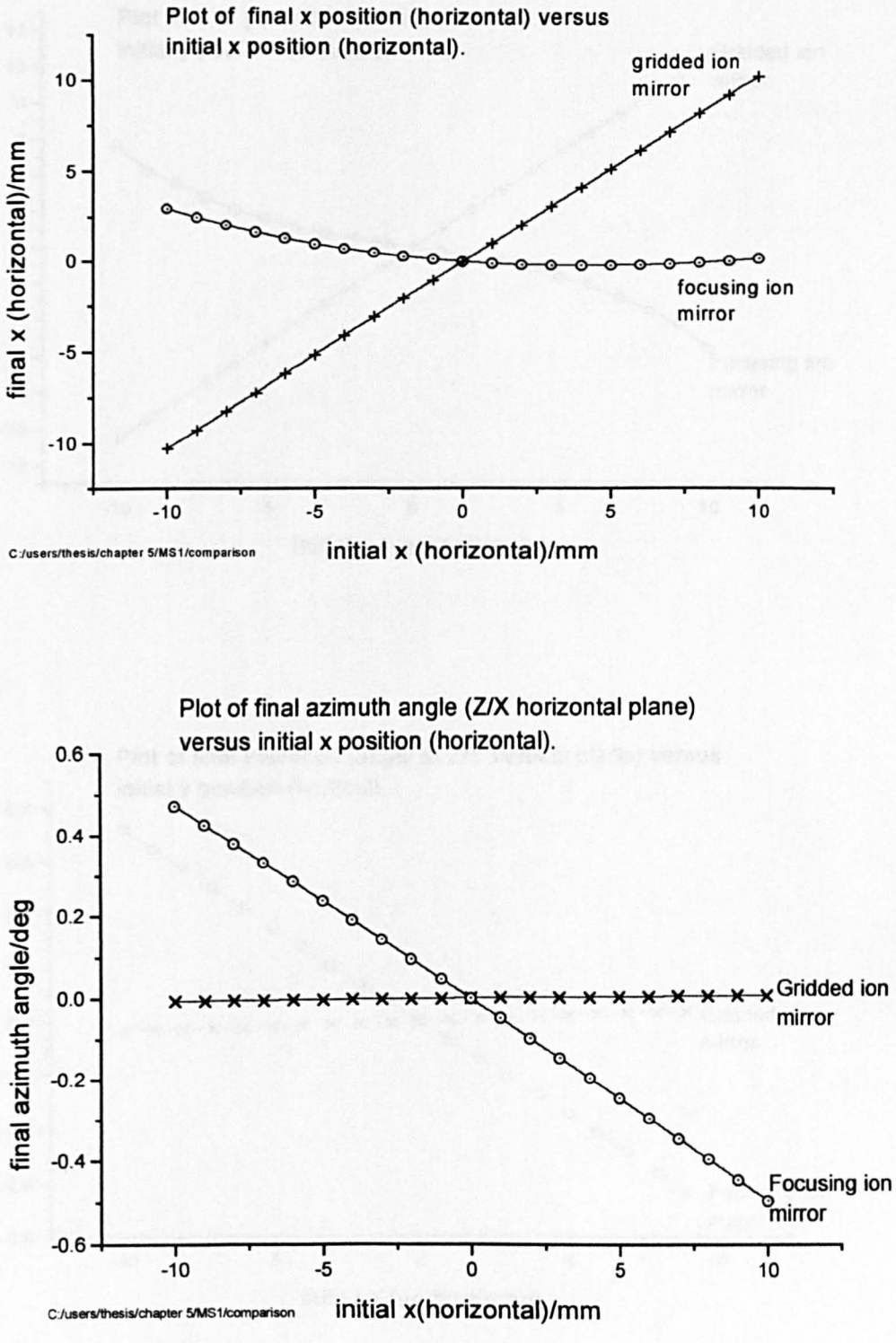

Fig. 98: Plot of initial horizontal position versus final horizontal position (TOP). Plot of initial horizontal position versus angle in horizontal plane (azimuth) after ion mirror (BOTTOM).

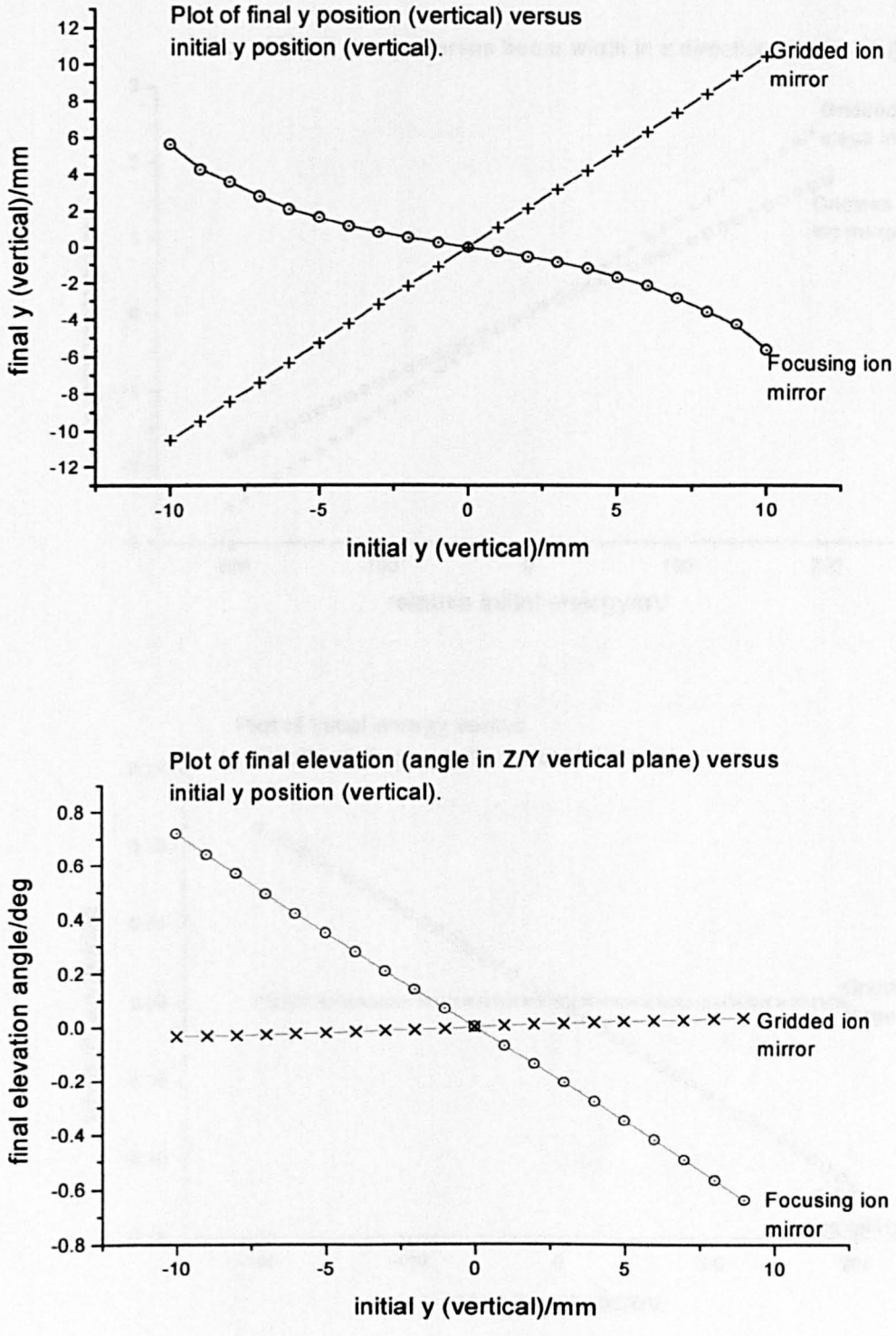

Fig. 99: Plot of initial vertical position versus vertical position at the collision-cell (TOP). Plot of initial vertical position versus final elevation angle (BOTTOM).

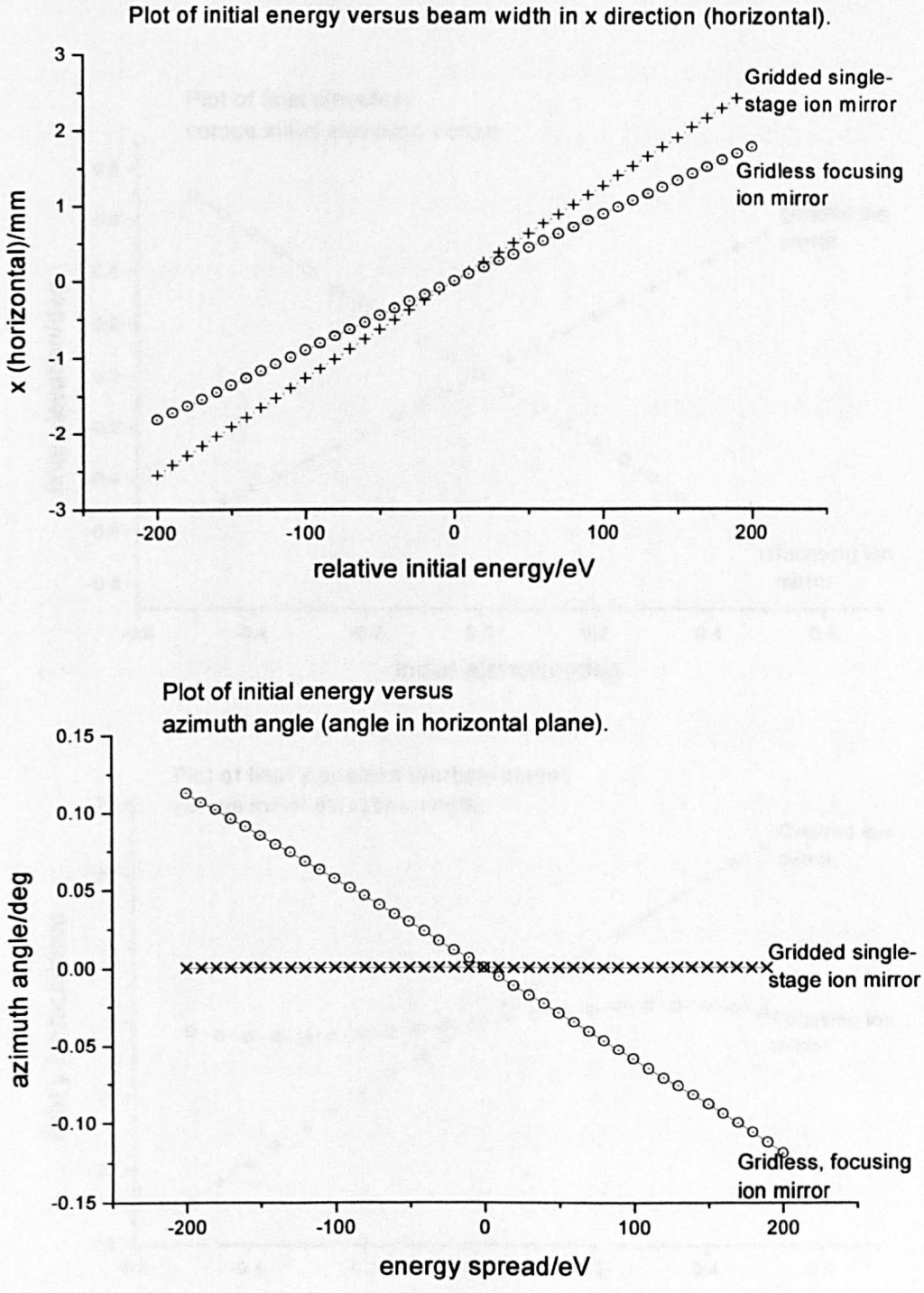

Fig. 100: Plot of initial energy versus horizontal spatial spread at collision-cell (TOP). Plot of initial energy versus angular spread in horizontal plane (BOTTOM).

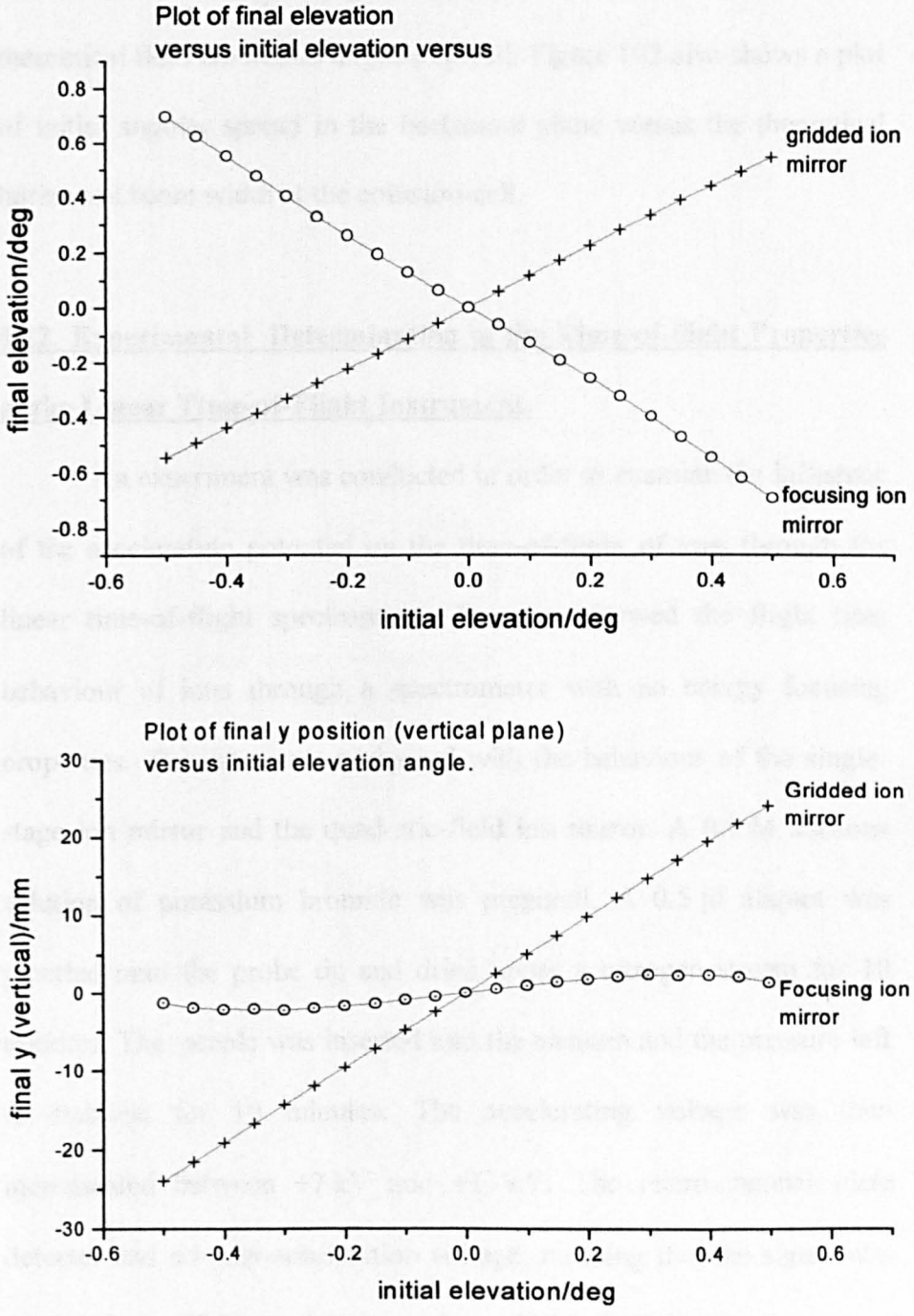

Fig. 101: Plot of initial elevation versus final elevation after ion mirror (TOP). Plot of initial elevation versus final vertical position at collision-cell (BOTTOM).

mirror. Figure 101 also shows a plot of initial angular elevation versus the vertical beam width at the-collision cell. Figure 102 shows a plot of the initial azimuth angle (angular spread in horizontal plane) versus the theoretical final horizontal angular spread. Figure 102 also shows a plot of initial angular spread in the horizontal plane versus the theoretical horizontal beam width at the collision-cell.

5.12 Experimental Determination of the Time-of-flight Properties of the Linear Time-of-Flight Instrument.

An experiment was conducted in order to examine the influence of the accelerating potential on the time-of-flight of ions through the linear time-of-flight spectrometer. The data showed the flight time behaviour of ions through a spectrometer with no energy focusing properties. The data were compared with the behaviour of the single-stage ion mirror and the quadratic-field ion mirror. A 0.1 M aqueous solution of potassium bromide was prepared. A 0.5 µl aliquot was pipetted onto the probe tip and dried under a nitrogen stream for 10 minutes. The sample was inserted into the vacuum and the pressure left to stabilise for 10 minutes. The accelerating voltage was then incremented between +7 kV and +13 kV. The micro-channel plate detector had no post-acceleration voltage, meaning that the signal was weak below +7 kV accelerating voltage. Thirty individual spectra were recorded and averaged using a 7200A series A Lecroy digital oscilloscope (Lecroy, Chesnut Ridge, NY, USA). The time-of-flight of the potassium cation was then measured and recorded. Figure 103

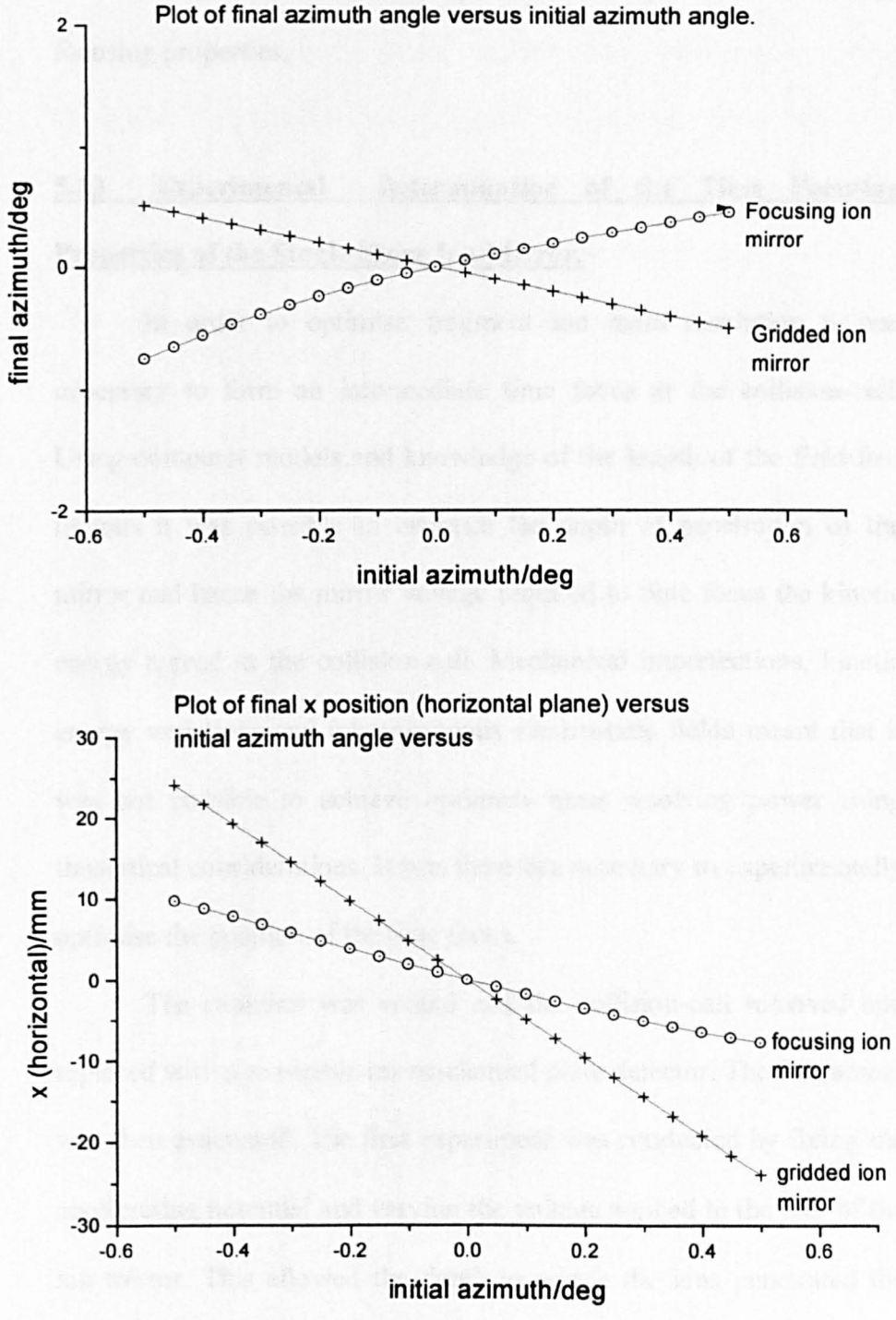

Fig. 102: Plot of initial angle in horizontal plane (azimuth) versus angle in horizontal plane after ion mirror (TOP). Plot of initial azimuth angle versus horizontal position at the collision-cell (BOTTOM).

shows a plot of flight time versus accelerating potential. The plot shows that the linear time-of-flight instrument possessed no energy focusing properties.

5.13 Experimental Determination of the Time Focusing Properties of the Single-Stage Ion Mirror.

In order to optimise fragment ion mass resolution it was necessary to form an intermediate time focus at the collision-cell. Using computer models and knowledge of the length of the field-free regions it was possible to estimate the depth of penetration of the mirror and hence the mirror voltage required to time focus the kinetic energy spread at the collision-cell. Mechanical imperfections, kinetic energy variations and inhomogenous electrostatic fields meant that it was not possible to achieve optimum mass resolving power using theoretical considerations. It was therefore necessary to experimentally optimise the position of the time focus.

The chamber was vented and the collision-cell removed and replaced with a moveable micro-channel plate detector. The instrument was then evacuated. The first experiment was conducted by fixing the accelerating potential and varying the voltage applied to the rear of the ion mirror. This allowed the depth to which the ions penetrated the mirror to be adjusted, with the aim of making the time spent in the field-free regions equal to the time spent inside the ion mirror. A 0.1 M aqueous potassium bromide solution was made up. A 0.5 µl sample

was pipetted onto the probe tip and dried under a nitrogen stream for 10 minutes.

The accelerating potential was fixed at +10 kV and the voltage applied to the rear field-sustaining electrode scanned. Thirty individual spectra were recorded and averaged. The flight time and peak width (FWHM) of the potassium cation signal were measured and recorded. The mass resolution, R, was calculated as follows:

$$R = \frac{t}{2\Delta t} \qquad 5.12$$

The experiment was repeated a further five times using the procedure outlined above. The mean average value of R at each mirror voltage was then calculated according to:

$$\overline{R} = \frac{\sum R}{n} \qquad 5.13$$

Where n, the number of samples, was equal to 6. The sample variance, s^2, was calculated as follows:

$$s^2 = \frac{\sum (R - \overline{R})^2}{n-1} \qquad 5.14$$

The sample standard deviation was calculated as follows:

$$s = \sqrt{s^2} \qquad 5.15$$

An estimate of the variability of the mean was obtained by calculating the standard error:

$$st.error = \frac{s}{\sqrt{n}} \qquad 5.16$$

Figure 104 shows a plot of the potassium cation resolution (FWHM) versus mirror reflecting voltage for a 10 kV accelerating potential. Error bars of the standard error are included. A mass resolution of approximately 900 (FWHM) was achieved when
12.4 kV was applied to the rear of the ion mirror. The time focus was located at the collision-cell when the following quotient was satisfied:

$$\frac{V_{acc}}{V_{mirror}} = \frac{10{,}000}{12{,}400} \qquad 5.17$$

The technique of fixing the accelerating voltage, while scanning the mirror voltage and recording the mass resolution, posed difficulties. The shot-to-shot reproducibility of ions formed by MALDI was poor. This resulted in shot-to-shot variations in signal intensity and resolution.

It was possible to determine the conditions under which the time focus was located at the collision-cell by fixing the mirror voltage and scanning the acceleration potential. Under these conditions it was not necessary to measure the peak width, but the time-of-flight of the ion instead. It was possible to determine the flight time with a greater degree of accuracy and reproducibility than the peak width.

A 0.1 M aqueous solution of potassium bromide was made up and applied to the probe tip using the sample preparation protocol outlined previously. The voltage applied to the rear field-sustaining electrode was maintained at +12.4 kV for the duration of the experiment. The voltage applied to the accelerating electrode was incremented and the time-of-flight of the potassium cation to the

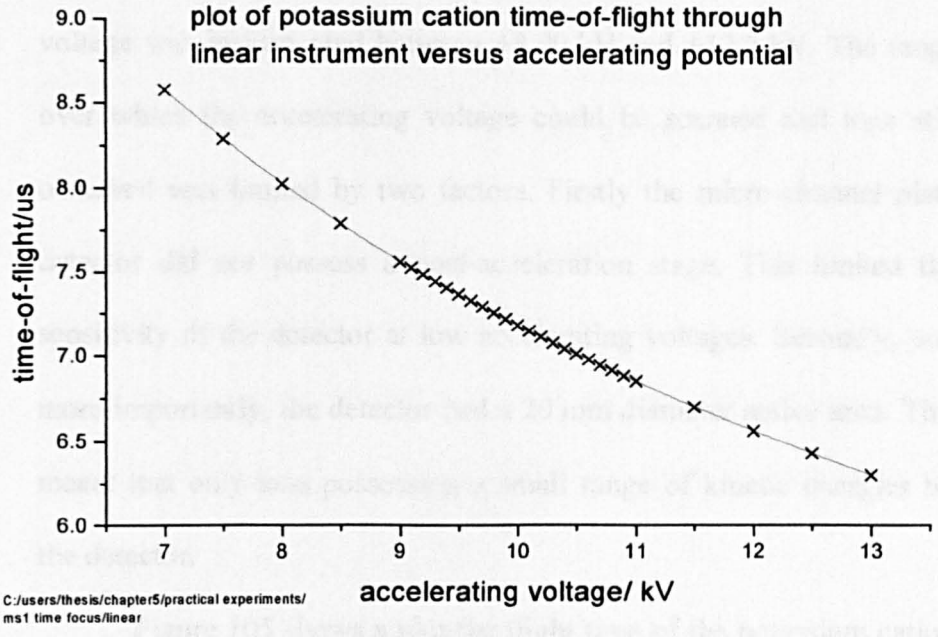

Fig. 103: Plot of potassium cation flight-time through the linear time-of-flight instrument versus accelerating potential.

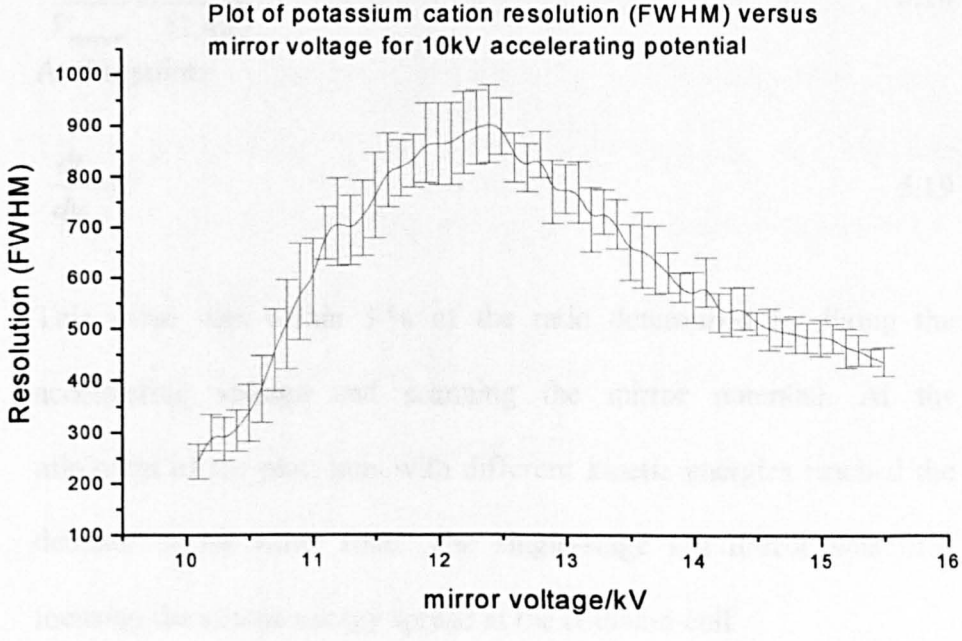

Fig. 104: Plot of potassium cation resolution versus mirror reflecting voltage.

detector located at the collision-cell measured. The accelerating voltage was incremented between +8.00 kV and +12.2 kV. The range over which the accelerating voltage could be scanned and ions still observed was limited by two factors. Firstly the micro-channel plate detector did not possess a post-acceleration stage. This limited the sensitivity of the detector at low accelerating voltages. Secondly, and more importantly, the detector had a 20 mm diameter active area. This meant that only ions possessing a small range of kinetic energies hit the detector.

Figure 105 shows a plot the flight time of the potassium cation versus the voltage applied to the acceleration electrode. The time-of-flight of the potassium cation reached a minimum when the ratio of the accelerating potential to the mirror voltage was:

$$\frac{V_{acc}}{V_{mirror}} = \frac{10{,}300}{12{,}400} \qquad 5.18$$

At this point:

$$\frac{dt}{du} = 0 \qquad 5.19$$

This value was within 3 % of the ratio determined by fixing the accelerating voltage and scanning the mirror potential. At the minimum of the plot, ions with different kinetic energies reached the detector at the same time. The single-stage ion mirror was time focusing the kinetic energy spread at the collision-cell.

The residence time of the ion inside the mirror can be expressed as:

$$T_{mirror} = T_{observed} - \left[\left(\frac{L}{\sqrt{V_{acc} \times 1.60219 \times 10^{-19} / 0.5 \times m \times 1.66054 \times 10^{-27}}} \right) + T_{source} \right] \quad 5.20$$

T_{mirror} is the residence time of the ion inside the ion mirror, $T_{observed}$ is the recorded total flight time, L is the total length of the drift regions, V_{acc} is the accelerating potential in volts and m is the atomic mass of the ion in atomic mass units. T_{source} is the time spent in acceleration:

$$T_{source} = \frac{2s}{\sqrt{V_{acc} \times 1.60219 \times 10^{-19} / 0.5 \times m \times 1.66054 \times 10^{-27}}} \quad 5.21$$

s is the distance over which the ion is accelerated.

Figure 106 shows a plot of the residence time of the potassium cation inside the single-stage ion mirror versus the kinetic energy of the ion. The residence time data was used to assess the linearity and homogeneity of the electrostatic field in the turnaround region of the ion mirror. A best-fit line was fitted to the data using a linear least-squares analysis software program (Origin 5, Microcal Software Inc.). The linear correlation coefficient, or R-value, of the data was 0.99935. The standard deviation was 1.36557×10^{-8} s or 14 ns. Visual inspection of figure 106 shows that the most significant deviation in flight time from idealised linear behaviour occurred when the ions passed close to the rear electrode of the ion mirror. The meshed aperture in the rear

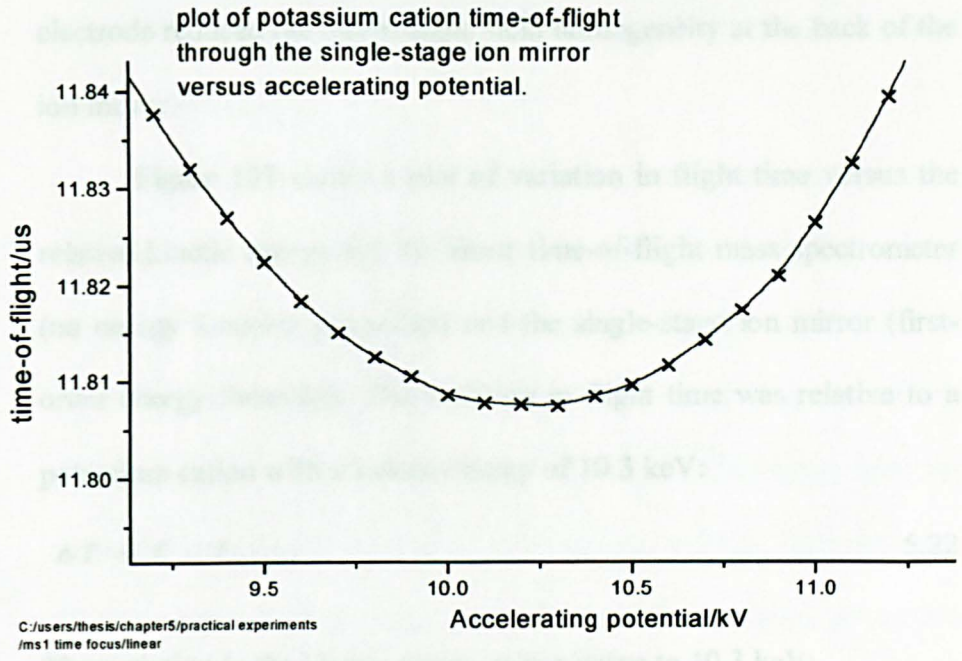

Fig. 105: Plot of potassium cation time-of-flight to the collision-cell versus accelerating voltage. The single-stage ion mirror was maintained at 12.4 kV.

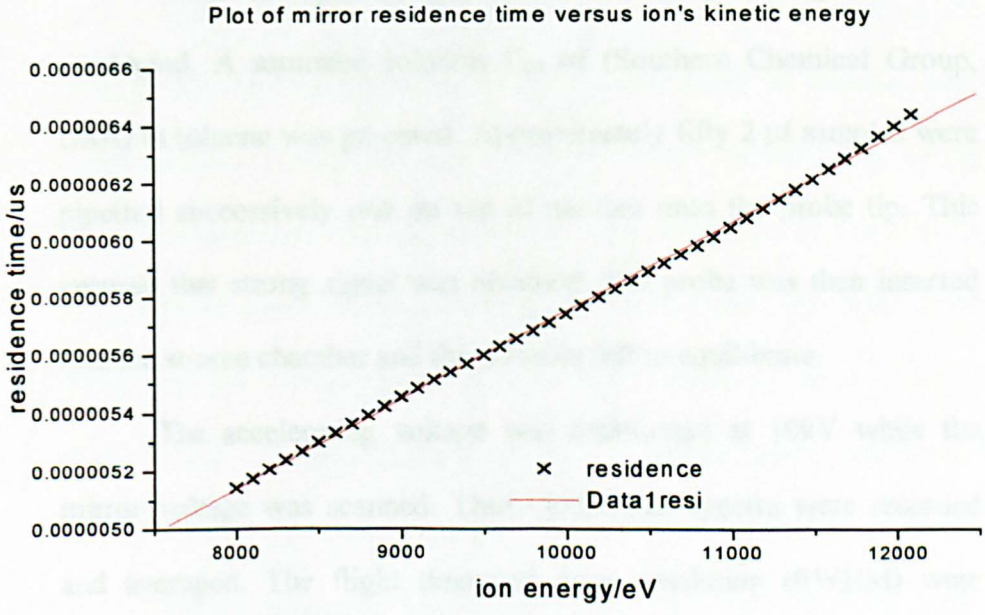

Fig. 106: Plot of potassium cation residence time inside the single-stage ion mirror versus the kinetic energy of the ion. Best-fit line fitted using linear least-squares analysis.

electrode reduced the electrostatic field homogeneity at the back of the ion mirror.

Figure 107 shows a plot of variation in flight time versus the relative kinetic energy for the linear time-of-flight mass spectrometer (no energy focusing properties) and the single-stage ion mirror (first-order energy focusing). The variation in flight time was relative to a potassium cation with a kinetic energy of 10.3 keV:

$$\Delta T = T - T_{10.3\,keV} \qquad 5.22$$

The variation in the kinetic energy was relative to 10.3 keV:

$$\Delta U = U - 10,300 \qquad 5.23$$

5.14 Optimisation of Mirror Reflecting Voltage for C_{60}.

Work to optimise the mirror reflecting voltage for was conducted. A saturated solution C_{60} of (Southern Chemical Group, USA) in toluene was prepared. Approximately fifty 2 µl samples were pipetted successively one on top of another onto the probe tip. This ensured that strong signal was obtained. The probe was then inserted into the source chamber and the pressure left to equilibrate.

The accelerating voltage was maintained at 10kV while the mirror voltage was scanned. Thirty individual spectra were recorded and averaged. The flight time and mass resolution (FWHM) were recorded at a detector located at the collision-cell. The experiment was repeated a further four times. The data was plotted to determine the conditions under which C_{60} was time focused at the collision-cell.

Figure 108 shows a plot of mass resolution (FWHM) versus mirror reflecting voltage.

The error bars indicated that the spectra-to-spectra reproducibility of the fullerene sample was less than that of the potassium cation. The maximum resolution of 1800 (FWHM) was obtained when the mirror was maintained at a voltage of approximately 11.7 kV. Figure 109 shows a series of spectra illustrating how the resolution was dependent upon the reflecting voltage. Note how the ^{13}C isotopomers become resolved. Optimum mass resolving power was achieved when 11.7 kV was applied to the rear of the mirror.

5.15 Experiment to Determine the Electrode Potentials of the First Ion Mirror.

Seventeen discrete field-sustaining electrodes generated the field inside the first ion mirror. An externally mounted resistor chain controlled the voltage on each electrode. Direct measurement of the electrode potential was impracticable. The resistance of the resistor chain resistors were measured using a precision digital voltmeter. From these data the voltage applied to each field-sustaining electrode could be calculated. Figure 110 shows a plot of the ideal electrode potentials and the actual electrode potentials. The plot also shows the deviation from the ideal potential. The deviation from the ideal potential in the critical turnaround region was less than 0.1 %.

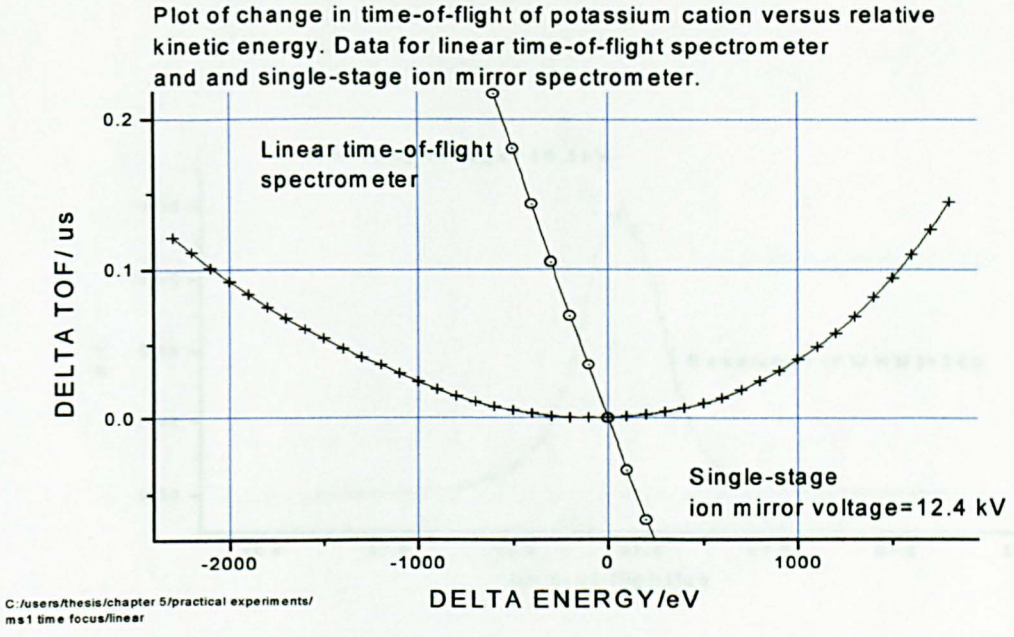

Fig. 107: Plot of deviation in flight-time versus deviation in kinetic energy for the linear time-of-flight spectrometer and the single-stage ion mirror spectrometer.

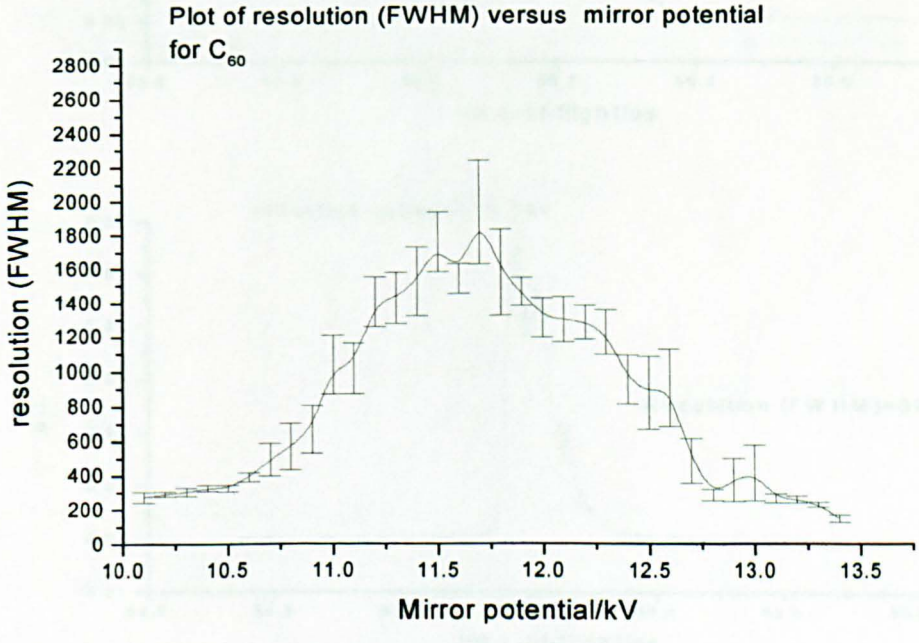

Fig. 108: Plot of $C_{60}^{+\cdot}$ resolution (FWHM) versus mirror reflecting voltage.

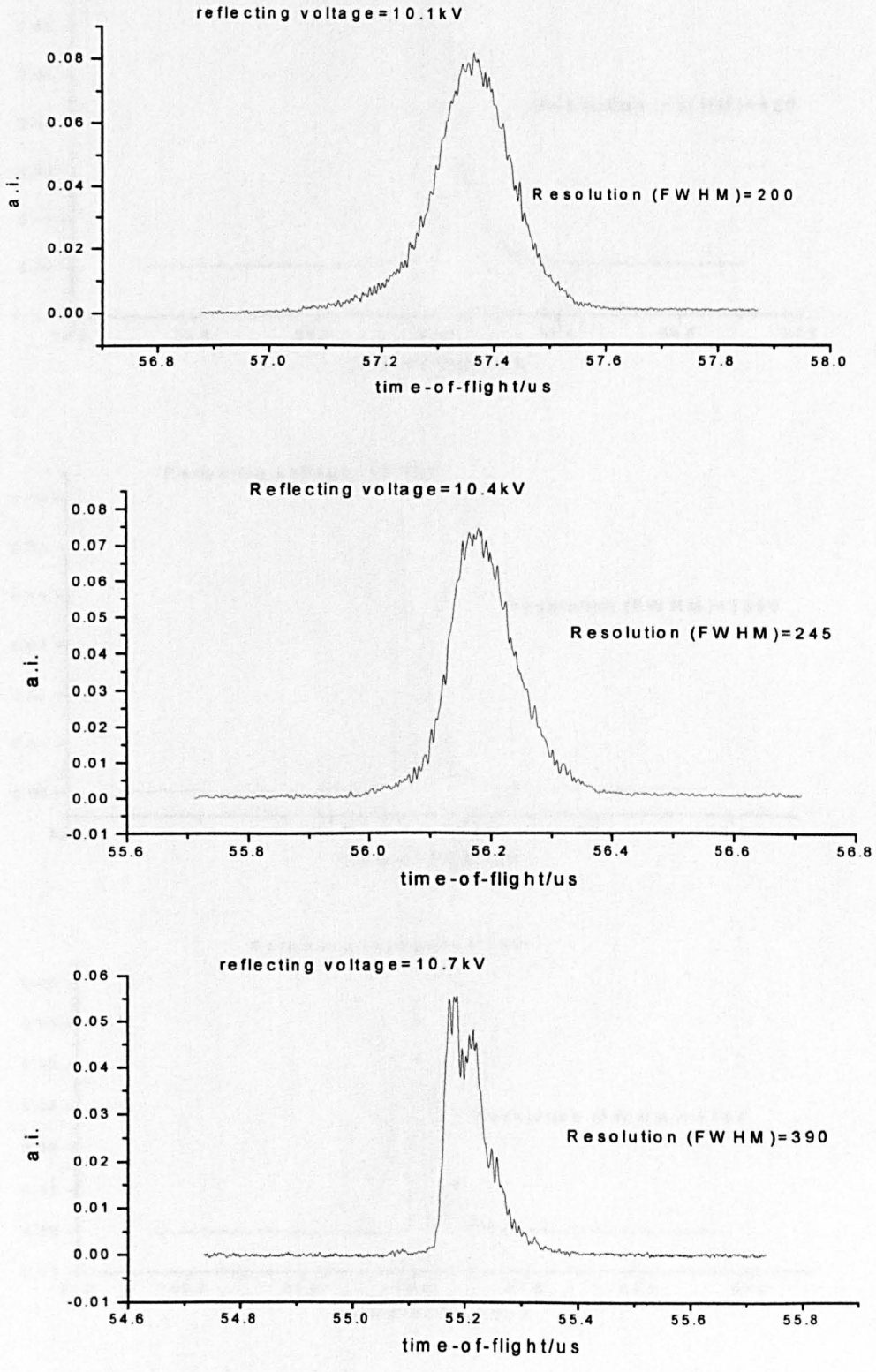

Fig. 109: $C_{60}^{+\cdot}$ spectra for different single-stage mirror reflecting voltages

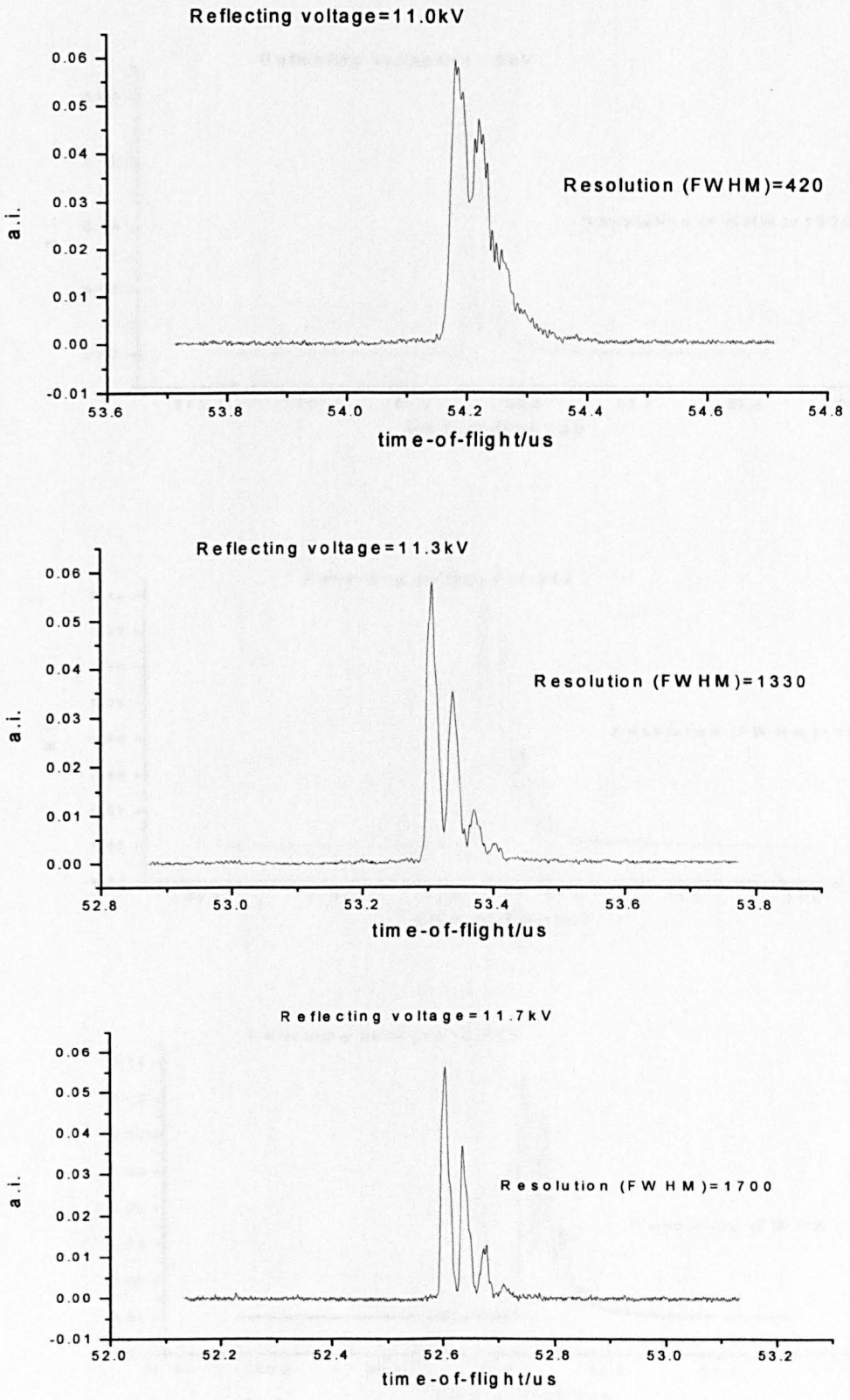

Fig. 109 (continued): $C_{60}^{+\cdot}$ spectra.

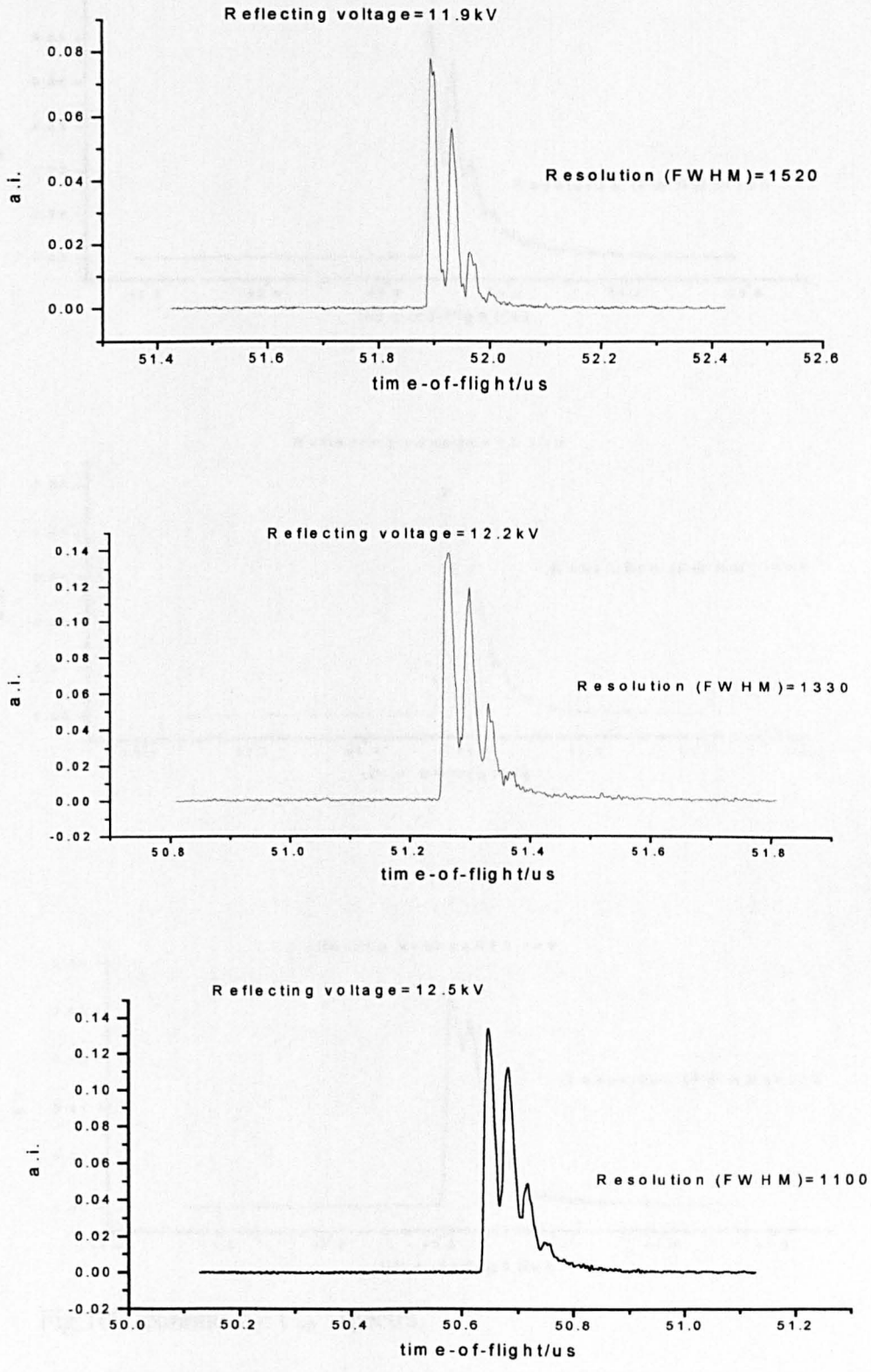

Fig.109 (continued): $C_{60}^{+\cdot}$ spectra.

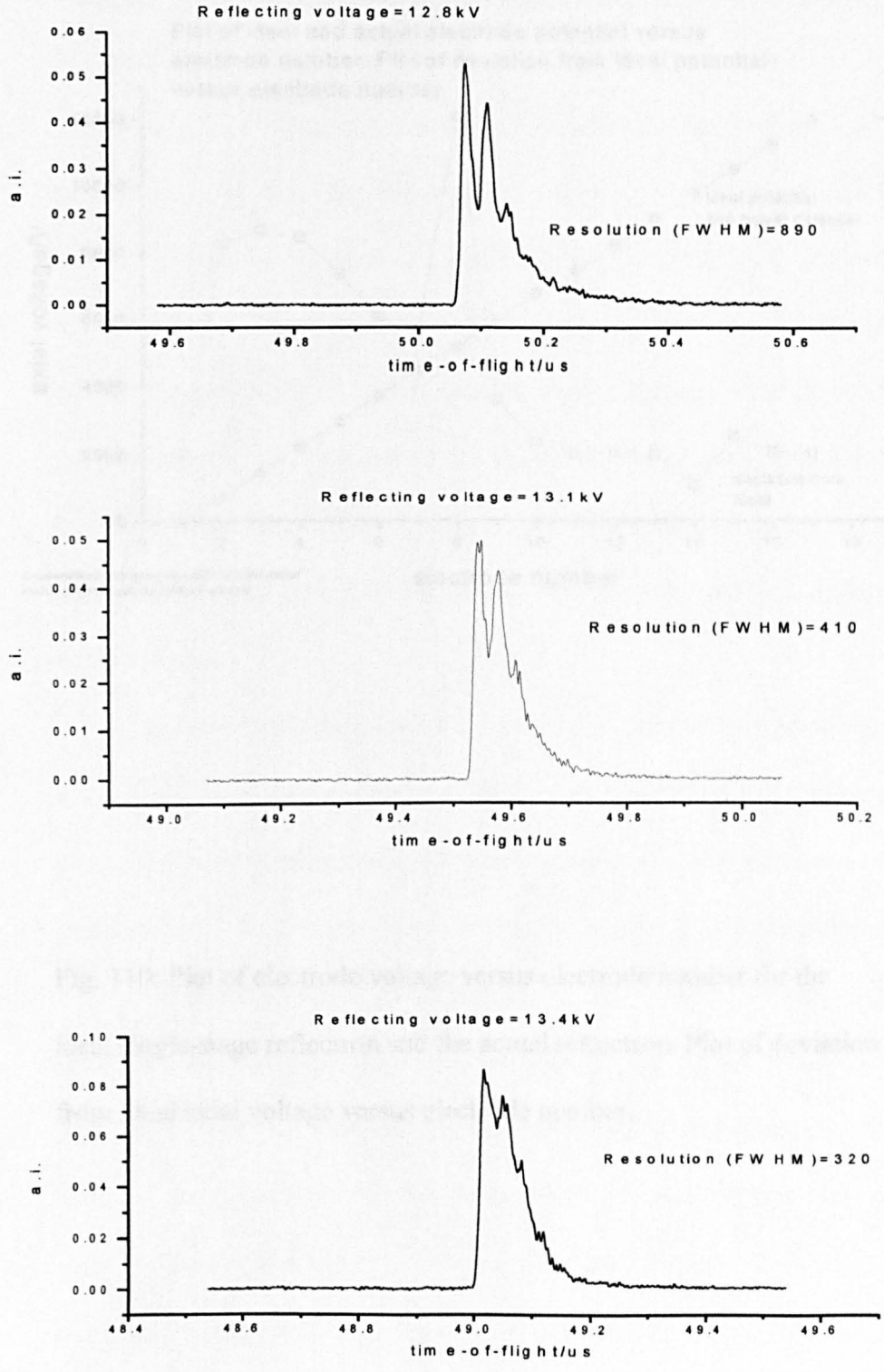

Fig.109 (continued): $C_{60}^{+\cdot}$ spectra.

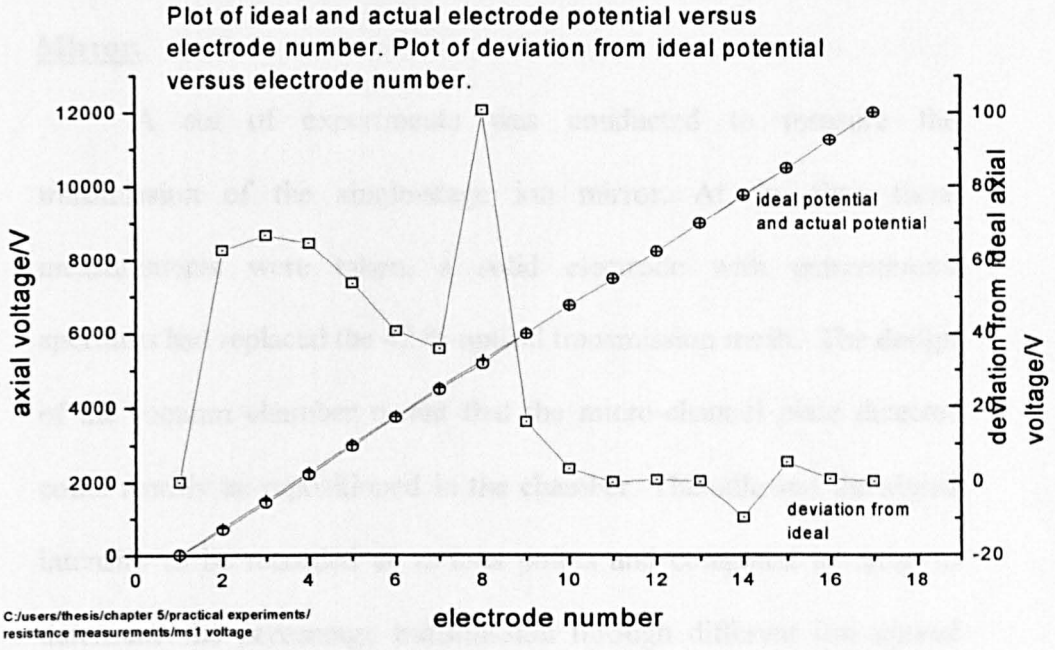

Fig. 110: Plot of electrode voltage versus electrode number for the ideal single-stage reflectron and the actual reflectron. Plot of deviation from ideal axial voltage versus electrode number.

5.16 Determination of the Transmission of the Single-Stage Ion Mirror.

A set of experiments was conducted to measure the transmission of the single-stage ion mirror. At the time these measurements were taken, a solid electrode with entrance/exit apertures had replaced the 42 % optical transmission mesh. The design of the vacuum chamber meant that the micro-channel plate detector could readily be repositioned in the chamber. This allowed the signal intensity to be recorded at various points and compared in order to determine the percentage transmission through different ion optical components.

An aqueous solution of 0.5 M lithium bromide was made up. Six 0.5 µl samples were pipetted onto the probe and then dried under a nitrogen stream. Lithium bromide was used because the lithium cation provided good shot-to-shot intensity reproducibility. The lithium cation did not fragment as it traversed the spectrometer. Sodium and potassium halides were originally considered, but it was found that their cation signals saturated the detector when it was positioned in front of the source. A 20 mm diameter (active-area) micro-channel plate detector was positioned 580 mm from the extraction region. The extraction voltage was set at +10kV and the detector was maintained at +1.6kV. The voltages applied to the source Einzel lenses were tuned so as to optimise lithium cation signal at the detector. The laser attenuator was tuned to provide consistent, strong signal. Once the attenuator was set no further adjustments to instrument parameters were made.

A minimum of thirty individual spectra were accumulated and averaged on the Lecroy digital oscilloscope for each lithium bromide sample spot. In total, thirty individual sample spots were loaded and examined. A baseline spectrum, in the absence of ions was also recorded. The oscilloscope settings were optimised so as to record only the lithium cation signal. The averaged spectra were saved to a floppy disc and transferred to an IBM compatible, Pentium 75 MHz personal computer for analysis. The Lecroy digital oscilloscope recorded 1 Gsample/s, resulting in data points separated by 1ns.

By summing the signal height of each data point it was possible to estimate the area under the signal:

$$\overline{a} = \frac{1}{n}\sum_{i=1}^{n}\left[\sum x - b\right] \qquad 5.24$$

a is the average signal peak area, x is the signal height of the data point, b is the signal height of the baseline data point and n is the number of samples examined.

The vacuum system was then vented and the detector re-positioned at the collision-cell. The chamber was pumped down to operating pressure. The accelerating voltage, detector voltage and laser attenuator settings remained fixed. The source lenses were tuned to provide optimum signal intensity at the collision-cell detector. Thirty individual sample spots were pipetted using the sample preparation protocol outlined above. For each individual sample spot at least thirty single-shot spectra were recorded and averaged on the oscilloscope. The data was then processed using the procedure outlined above. The

areas of the averaged lithium cation signal before and after the single-stage ion mirror were compared to determine the percentage transmission. It was found that the detector produced some signal ringing (charge reflection). The signal ringing peaks were not included in the determination of the peak area. Data analysis showed that the signal ringing peaks did not greatly change the percentage transmission value. Figure 111 shows a plot of the average lithium cation signal before and after the single-stage ion mirror. The error bars were calculated from the standard error of the signal intensity measurements. The mean percentage transmission of the single-stage ion mirror was found to be 36 %. Calculation of the area contained within the error bars showed that the mean percentage transmission lay between 26 % and 51 %.

When the single-stage ion mirror was first installed in the vacuum chamber the front aperture was covered with a 42% optical transmission mesh. This ensured that the field inside the mirror was homogenous. It was subsequently found that the mesh resulted in unacceptable beam attenuation. The mesh was replaced with a solid electrode with entrance and exit apertures. This ensured that a homogenous field was formed, while the critical part of the beam path was devoid of grids. A set of experiments was conducted in order to determine the relative transmission of the two configurations.

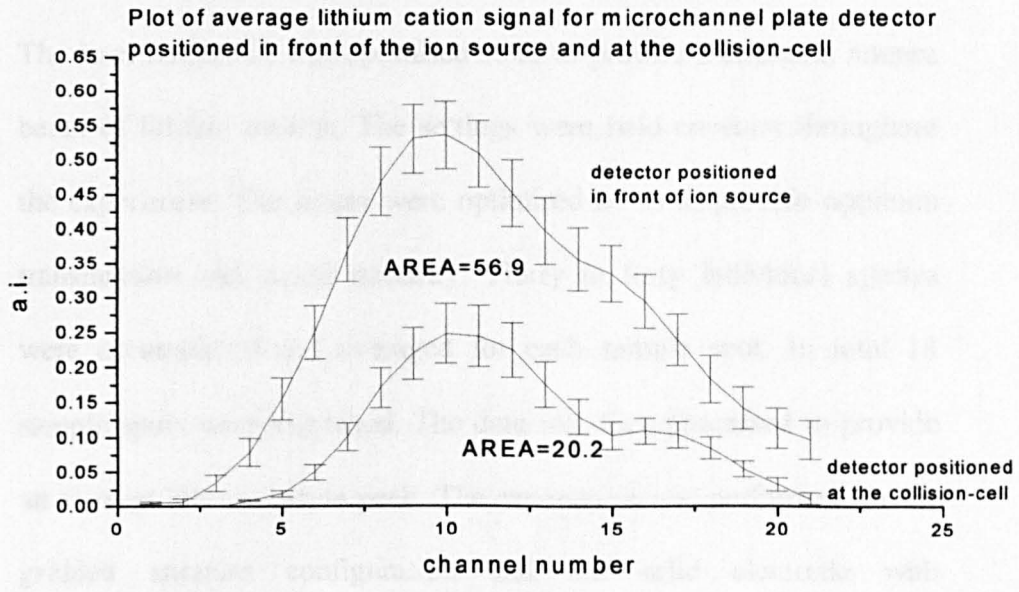

Fig. 111: Average lithium cation signal before and after the single-stage ion mirror.

A 25mm diameter active-area micro-channel plate detector (Galileo, MA, USA) was positioned in front of the collision-cell. Spatial constraints meant that the detector could not be positioned at the collision-cell without removing the parabolic ion mirror. An aqueous solution of 0.5M lithium bromide was made up and 0.5 µl aliquots were pipetted onto the sample probe. The accelerating voltage was maintained at +10kV, the detector at –1.8kV and the mirror at 12.4kV. The laser attenuator was optimised so as to provide a constant, intense beam of lithium cations. The settings were held constant throughout the experiment. The lenses were optimised so as to provide optimum transmission and signal intensity. Thirty to forty individual spectra were accumulated and averaged for each sample spot. In total 18 sample spots were examined. The data was then processed to provide an average lithium cation peak. The experiment was performed for the gridded aperture configuration and the solid electrode with entrance/exit apertures. Figure 112 shows a plot of average lithium cation signal for both mirror configurations. The shoulder feature on both signals was due to charge reflection (signal ringing). The trailing, damped oscillations were neglected from the calculation of the signal areas.

By comparing the areas under the signals it was possible to determine the relative transmission of the two mirror configurations. The lithium cation signal intensity using the solid electrode with apertures was 2.52 times that of the gridded design. Analysis of the errors showed that the value was between 2.3 and 2.7 times

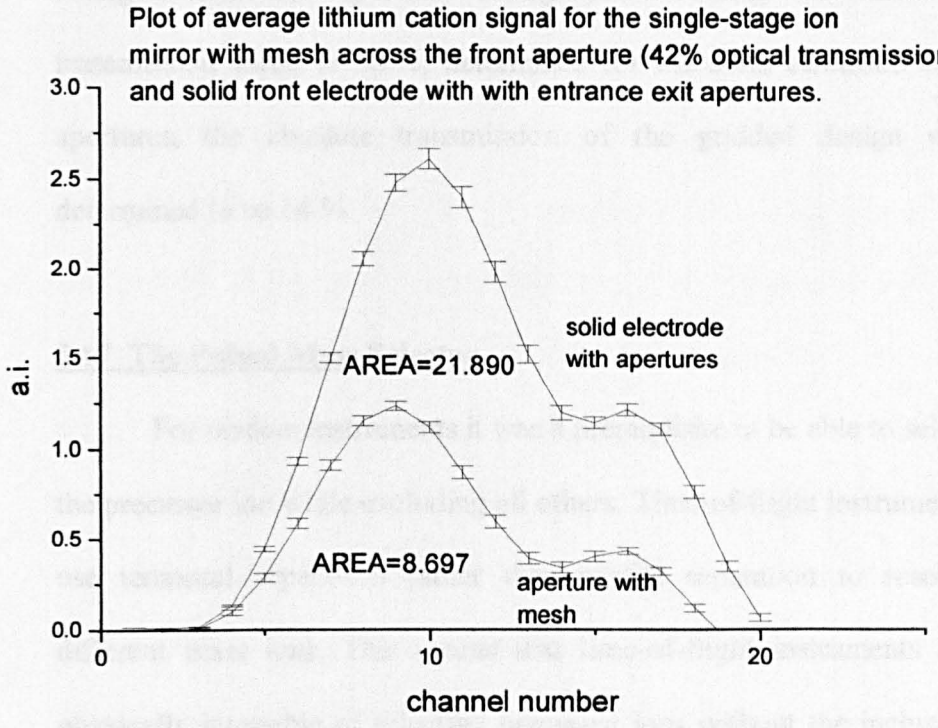

Fig. 112: Lithium cation signal intensity at the collision-cell with gridded front electrode and solid electrode with apertures.

stronger than the gridded configuration. Using the absolute transmission value of 36 %, determined for the solid electrode with apertures, the absolute transmission of the gridded design was determined to be 14 %.

5.17 The Pulsed Mass Selector.

For tandem instruments it was a prerequisite to be able to select the precursor ion while excluding all others. Time-of-flight instruments use temporal separation rather than spatial separation to resolve different mass ions. This means that time-of-flight instruments are physically incapable of selecting precursor ions without the inclusion of a pulsed deflection system, or mass gate, to deflect unwanted ions. All mass gates use the same basic principles. A set of metal electrodes generates an electrostatic field capable of deflecting ions from the flight path. The deflection system is pulsed to ground in order to allow the precursor ion into the fragmentation region. The deflecting field is then re-established.

There are a number of basic designs of mass selector in operation with different research groups. They range from simple, low resolution, low transmission devices to mechanically and electronically complex systems capable of high resolution and transmission.

The most basic form of ion selector is a pair of pulsed deflection plates. The most basic configuration uses one pulsed electrode and one grounded electrode. The advantage of this design is its simplicity. Only one mono-polar power supply is required and the

switching electronics are relatively simple. The bipolar configuration floats one electrode at a positive polarity while the other is maintained at a negative polarity. This configuration requires two power supplies and more complicated switching electronics. A major advantage of the bipolar gate is that the fringing fields are less extensive than those present in the mono-polar mass gate. This results in higher ion transmission and mass resolving power.

Pulsed deflection plates have been widely used by a number of research groups [18][19][20][21]. Spengler and co-workers [22] reported achieving a mass selectivity $m/\Delta m$ =60. Spengler [23] subsequently reported improved mass selectivity, $m/\Delta m$ =110 (FWHM) for PEG 6000. The authors reported parent ion attenuation of greater than 90 %.

The extent of the fringing fields at the entrance and exit to the gate assembly can be minimised by placing a high transmission grid across the apertures. This construction method has been used by Williams *et al* [24] to improve the transmission and resolution of their mass gate. The authors reported an attenuation of 65 % and unit mass selection up to m/z 200.

A further development of the parallel plate selector was the double-pulse mass gate [25]. The gate consisted of two sets of parallel deflection plates in series. Figure 113 shows a schematic of the gate with the pulse timings. The authors reported achieving a gate resolution of $m/\Delta m$=50.

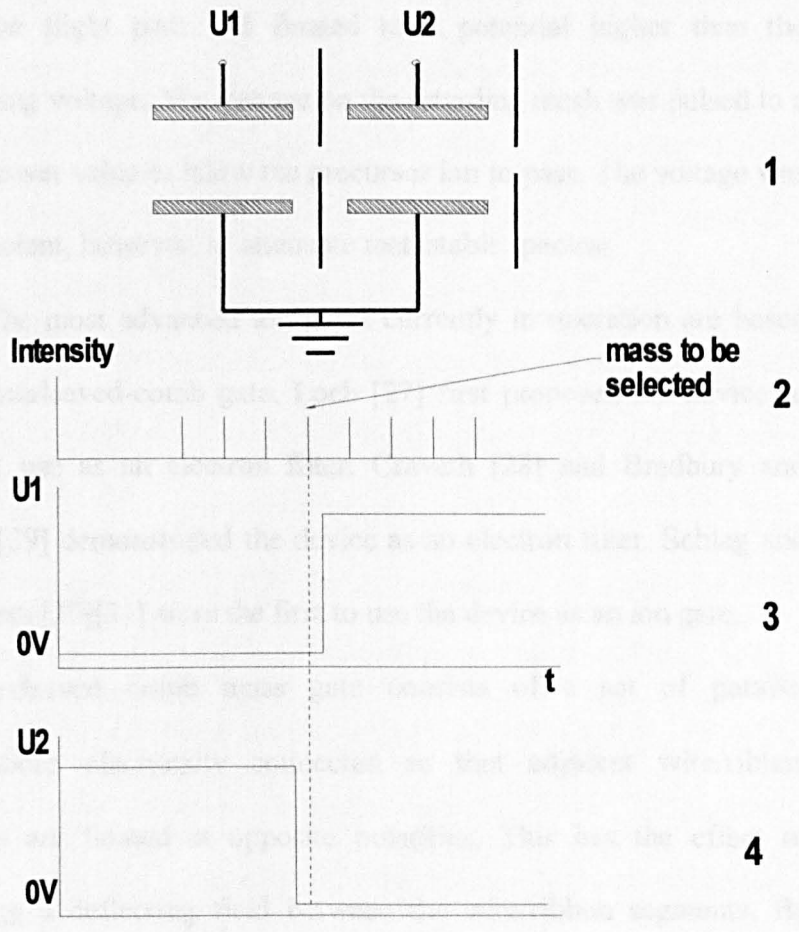

Fig. 113: Schematic diagram showing operating mode of a dual mass gate (1). Simulated mass spectrum (2). Voltage pulse timing applied to first gate (3). Voltage pulse timing applied to second gate (4).

Becker and Cheshnovsky [26] have designed a gate that stopped ions using a kinetic energy barrier. A fine mesh was placed across the flight path and floated to a potential higher than the accelerating voltage. The voltage on the retarding mesh was pulsed to a slightly lower value to allow the precursor ion to pass. The voltage was still sufficient, however, to attenuate metastable species.

The most advanced ion gates currently in operation are based on the interleaved-comb gate. Loeb [27] first proposed the device to Lusk for use as an electron filter. Cravath [28] and Bradbury and Nielsen [29] demonstrated the device as an electron filter. Schlag and co-workers [30][31] were the first to use the device as an ion gate.

The interleaved comb mass gate consists of a set of parallel wires/ribbons electrically connected so that adjacent wire/ribbon segments are floated at opposite polarities. This has the effect of generating a deflecting field between the wire/ribbon segments. By pulsing the voltage applied to the interleaved comb mass gate the precursor ion can be selected. The small mechanical size and small fringing fields mean that the interleaved comb device is capable of high mass-selectivity with relatively little attenuation of the selected ion signal.

Enke and co-workers [32][33] have described, in detail, the construction of an interleaved comb mass gate for use in a tandem reflectron instrument. Enke and co-workers reported achieving unit mass selectivity up to *m/z* 167, when the gate was positioned at the time focus of the first ion mirror. An attenuation of just 12 % of the

selected ion signal intensity was reported when the gate was in operation.

Piyadasa *et al* [34] have described a mass gate composed of two interleaved comb gates in series. Deflecting elements made of metal ribbon were used instead of wire. The dual interleaved comb mass gate works on a similar principle to that of the dual mass gate described by Haberland *et al* [25]. The transmission of the device was determined to be 80 %. Mass resolving powers of between 1100 (*m/z* 1350, substance P) and 5200 (PEG 6000) were reported by Piyadasa *et al* [34].

Stoermer *et al* [35] have reported constructing a dual interleaved comb mass gate similar to that described by Piyadasa *et al* [34]. The device used two interleaved comb mass gates in series. The gate used wire defecting elements rather than the metal ribbon elements used by Piyadasa *et al*. The authors reported achieving a resolution of 400.

5.18 Mass Gate Design Considerations.

To achieve maximum gating resolution it was important that the physical dimensions of the gate electrodes and the fringing fields were minimised. Minimising the extent of the fringing fields also limited precursor ion attenuation. The rise-time and fall-time of the high-voltage switching electronics had to be as short as possible to ensure high mass-selectivity. The position of the mass gate was important in determining the resolution, as the further along the flight

path the gate was placed the greater the temporal dispersion. In post-source decay (PSD) instruments, the gate is usually positioned in close proximity to the source to ensure a suitably long field-free region is present for fragmentation to occur in.

The position of the gate with respect to any time focus was important in determining the mass selectivity of the gate. For tandem CID/photodissociation instruments it may be important to exclude metastable fragments formed in the field-free regions. Currently the mass gate and energy discriminator described by Becker and Cheshnovsky [26] is the only device capable of effectively discriminating against metastable fragment ions. The kinetic energy of the ion beam was an important factor in determining the performance of the gate. It is easier to achieve high performance gating with low kinetic energy ion beams than with high-energy beams.

The gate was to be located after the single-stage ion mirror and before the collision-cell. The position of the gate with respect to the ion source determined the temporal and spatial dispersion of the ions. This determined both the resolution and transmission of the ion gate. A series of SIMION calculations for different mass-to-charge ratio ions was carried out in order to determine the time-of-flight, temporal dispersion and spatial dispersion of the ions at the mass gate. The time-of-flight determined the gate delay-time. The temporal dispersion between different mass ion packets determined the resolution, transmission and the time required for the gate to switch between ON-

OFF-ON. The spatial dispersion determined the physical size of the gate and the associated fringing fields.

Figure 114 shows a plot of the time-of-flight of ions to the gate versus the mass-to-charge ration of the ions. Figure 115 shows a plot of temporal separation at the mass gate versus mass-to-charge ratio. The time separation between 1 amu (isotopic), 16 amu (sodiated/potassiated) and 22 amu (protonated/sodiated) is shown

In order to achieve isotopic mass selection it was necessary that the gate be switched between ON-OFF-ON, in less time than the time separation between ions. The only mass gate that has been shown to be capable of such mass resolving powers is the dual interleaved comb mass gate described by Piyadasa *et al* [34]. Figure 116 shows a plot of spatial separation between ions, at the mass gate, versus their mass-to-charge ratio. The spatial separation between ions separated by 1 amu, 16 amu and 22 amu is shown.

In order to achieve isotopic mass-selection it was necessary that the gate and associated fringing field be smaller than the spatial separation between one mass unit. In order to achieve isotopic mass selection it would be necessary to locate the gate at the position of the time focus of the single-stage ion mirror. An ion-bunching device would have to be installed after the gate to form a time focus at the collision-cell. It was decided to incorporate a simple deflection plate mass gate into the prototype instrument. Figure 117 shows a photograph of the ion gate and collision-cell optics.

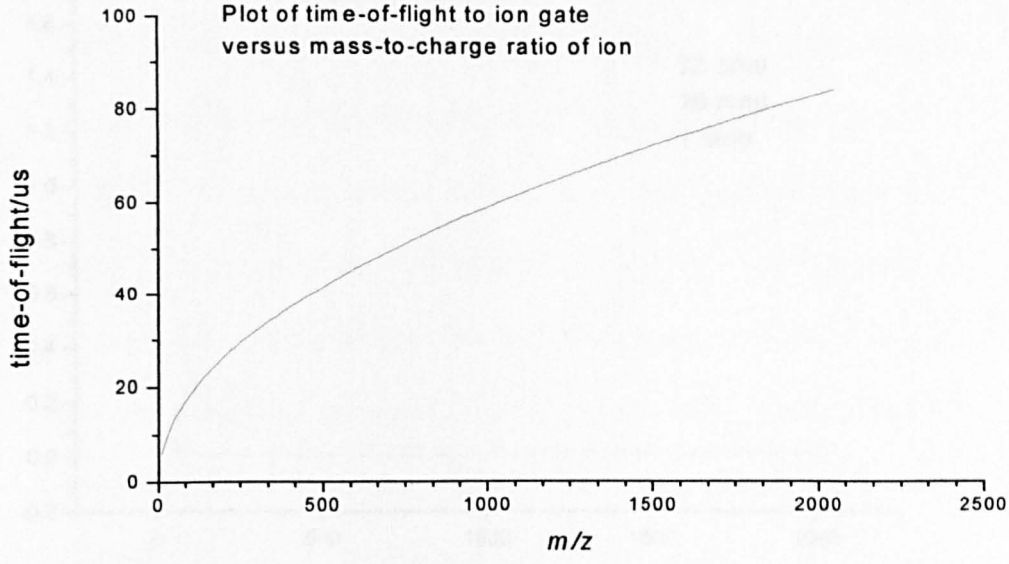

Fig. 114: Plot of time-of-flight to mass gate versus mass-to-charge ratio.

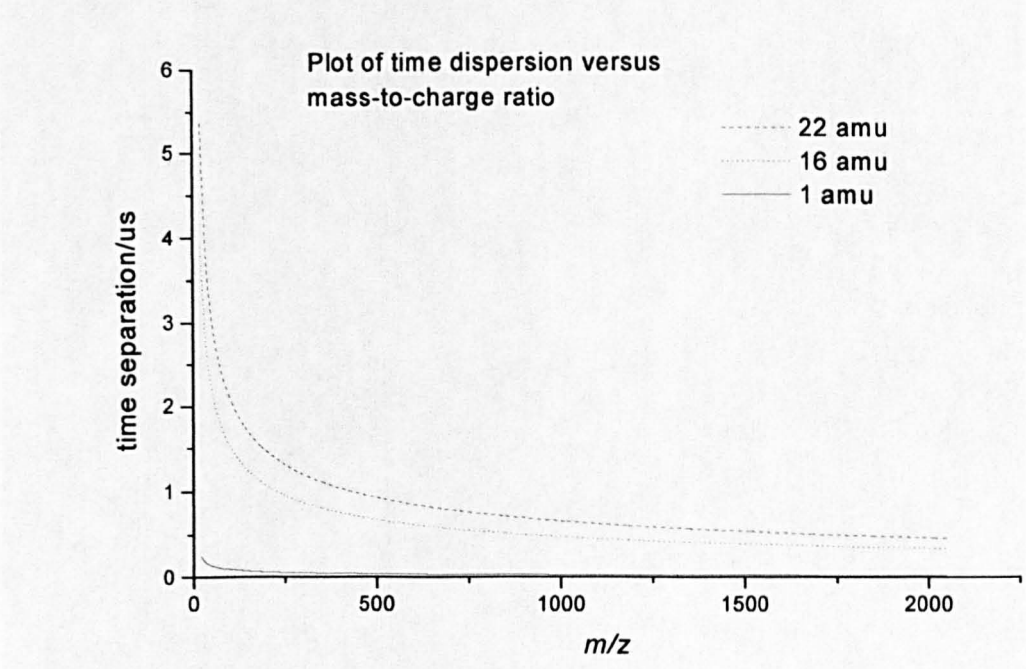

Fig. 115: Plot of time separation versus mass-to-charge ratio. Time separation between 1 amu, 16 amu and 22 amu shown.

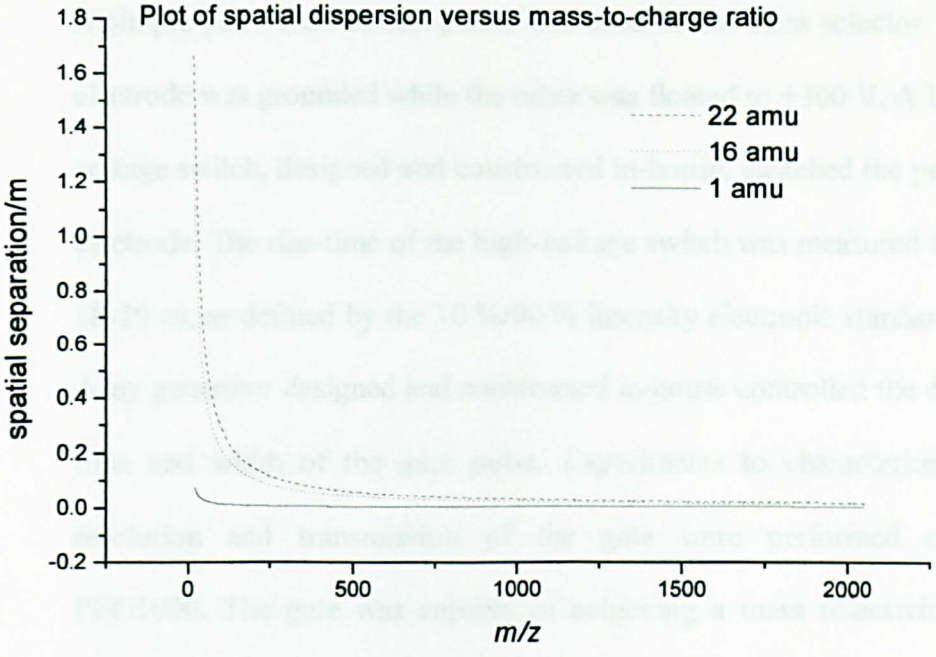

Fig. 116: Plot of spatial separation at mass gate versus mass-to-charge ratio. Spatial separation between 1 amu, 16 amu and 22 amu shown.

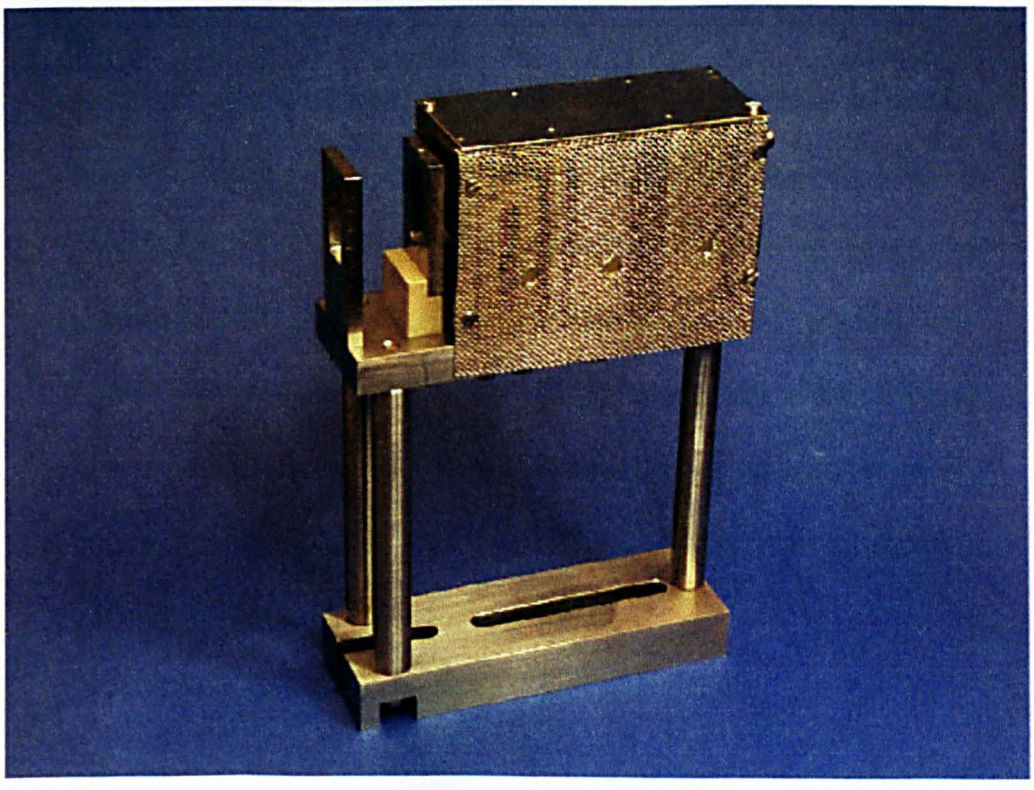

Fig. 117: Photograph of the ion optics and mass gate located before the collision-cell.

A simple pair of deflection plates was used as the mass selector. One electrode was grounded while the other was floated to +300 V. A high-voltage switch, designed and constructed in-house, switched the pulsed electrode. The rise-time of the high-voltage switch was measured to be 18-20 ns, as defined by the 10 %/90 % intensity electronic standard. A delay generator designed and constructed in-house controlled the delay time and width of the gate pulse. Experiments to characterise the resolution and transmission of the gate were performed using PEG1000. The gate was capable of achieving a mass selectivity of $m/\Delta m$ =20. The attenuation of the selected ion at the final detector was determined to be greater than 90 % (determined using peak height). SIMION calculations showed that the fringing fields extended for a considerable distance. This resulted in the selected ion being deflected by the fringing fields as it approached the gate. Using a bipolar configuration, in which one electrode is floated to a positive polarity while the other is floated to a negative polarity, would reduce the extent of the fringing fields. Covering the entrance/exit apertures with high transmission mesh would also reduce the extent of the fringing fields and help improve the gate transmission. The long-term aim must, however, be to replace the present mass gate with a superior interleaved comb mass gate.

5.19 References.

[1] R. Kaufmann, D. Kirsch and B. Spengler, Int. J. Mass Spectrom., Ion Processes, 131 (1994) 355-385.

[2] B. N. Laprade and R. J. Labich, Spectroscopy 9 (1994) 26.

[3] M. Gonin, Y. H. Chen, Th. Horvath, M. Theiss and H. Wollnik, Nuc. Instrum. Meth. Phys. Res. B, 136-138 (1998) 1244.

[4] R. Beavis and B. Chait, Rapid Commun. Mass Spectrom., 3 (1989) 233.

[5] C. D. Hanson and C. G. Just, Anal. Chem., 66 (1994) 3676.

[6] W. deHeer, and P. Milani, Rev. Sci. Instrum., 62 (1991) 670.

[7] R. Brown and N. Gilfrich, Anal. Chim. Acta., 248 (1991) 541.

[8] Klaus-Dieter Rinnen, D. A. V. Kliner, R. S. Blake and R. N. Zare, Rev. Sci. Instrum., 60 (1989) 717.

[9] Hamamatsu Photonics Technical Information, MCP Assembly, May 1994.

[10] A. I. Pikin, C. A. Morgan, E. W. Bell, L. P. Ratliff, D. A. Church and J. D. Gillaspy, Rev. Sci. Instrum., 67 (1996) 2528.

[11] R. Kutscher, R. Grix, G. Li and H. Wollnik, Int. J. Mass Spectrom. Ion Processes, 103 (1991) 117.

[12] H. Wollnik, U. Gruner, G. Li, Ann., Physik Leipzig 48 (1991) 215.

[13] R. Kutscher, R. Grix, G. Li, H. Wollnik, US patent 5,017,780.

[14] R. Frey, G. Weiss, H. Kaminski, E. W. Schlag Z. Naturforsch 40a (1985) 1349.

[15] E. Axelsson and L. Holmlid, Int. J. Mass Spectrom. Ion Processes, 59 (1984) 231.

[16] U. N. Andersen, A. E. Colburn, A. A. Makarov, E.N. Raptakis, D. J. Reynolds, P. J. Derrick, S. C. Davis, A. D. Hoffman and S. Thomson, Rev. Sci. Instrum., 69 (1998) 1650.

[17] S. C. Hansen and C. A. Myerholtz, 1996 US patent Number: 5,661,300.

[18] K. Schey, R. G. Cooks, R. Grix and H. Wollnik, Int. J. Mass Spectrom. Ion Processes, 77 (1987) 49.

[19] P. J. Brucat, L.-S. Zheng, C. L. Pettiette, S. Yang and R. E. Smalley, J. Chem. Phys., 84 (1986) 3078.

[20] L. A. Bloomfield, M. E. Geusic, R. R. Freeman and W. L. Brown, Chem. Phys. Letts., 121 (1985) 33.

[21] L. A. Bloomfield, R. R. Freeman and W. L. Brown, Phys. Rev. Letts., 54 (1985) 2246.

[22] R. Kaufmann, B. Spengler and F. Lützenkirchen, Rapid Commun. Mass Spectrom., 7 (1993) 902.

[23] B. Spengler, J. Mass Spectrom., 32 (1997) 1019.

[24] E. R. Williams, L. Fang and R. N. Zare, Int. J. Mass Spectrom. Ion Processes, 123 (1993) 233.

[25] H. Haberland, H. Kornmeier, C. Ludewigt and A. Risch, Rev. Sci. Instrum., 62 (1991) 2368.

[26] I. Becker and O. Cheshnovsky, Rev. Sci. Instrum., 68 (1997) 4625.

[27] L. B. Loeb in Basic Processes in Gaseous Electronics; University of California Press: Berkeley, CA, 1961.

[28] A. M. Cravath, Phys. Rev., 33 (1929) 605.

[29] N. E. Bradbury and R. E. Nielsen, Phys. Rev., 49 (1936) 388.

[30] R. Weinkauf, K. Walter, C. Weickhardt, U. Boesl, and E. W. Schlag, Z. Naturforsch, 44a (1989) 1219.

[31] U. Boesl, E. W. Schlag, K. Walter and R. Weinkauf, US Patent No. 5,032,722 (1991).

[32] P. R. Vlasak, D. J. Beussman, M. R. Davenport and C. D. Enke, Rev. Sci. Instrum., 67 (1996) 68.

[33] D. J. Beussman, P. R. Vlasak, R. D. McLane, M. A. Steerlin and C. D. Enke, Anal. Chem., 67 (1995) 3952.

[34] C. K. G. Piyadasa, P. Håkansson, T. R. Ariyaratne and D. F. Barofsky, Rapid Commun. Mass Spectrom., 12 (1998) 1655.

[35] C. W. Stoermer, S. Gilb, J. Friedrich, D. Schooss and M. M. Kappes, Rev. Sci. Instrum., 69 (1998) 1661.

CHAPTER SIX.

Collision-Cell and Quadratic-Field Ion Mirror.

6.01 Collision-Cell Ion Optics.

In order to obtain high transmission through the instrument, it was important that a large percentage of the ion beam pass through the small apertures of the differentially pumped collision-cell. To form a collimated beam after the single-stage ion mirror it was necessary to incorporate a set of lenses. It was also necessary to incorporate steering electrodes into the region before the collision-cell to correct for angular deflection arising from the beam's passage through the single-stage ion mirror. The limited availability of space between the single-stage ion mirror and the collision-cell pumping port meant that the focusing and deflection optics had to be small. In order to minimise the space required, the lenses and deflecting electrodes were combined. The lenses/deflection assemblies consisted of four pairs of rectangular electrodes: two pairs to deflect and focus the beam in the horizontal plane and another two pairs to deflect and focus the beam in the vertical plane. By applying a differential high-voltage to the electrodes the beam could be steered and focused simultaneously. The first set of vertical and horizontal steering lenses was located in the field-free region after the single-stage ion mirror. The second set of steering/focusing electrodes was incorporated into the differentially pumped collision-cell chamber. Figure 118 shows a schematic diagram

illustrating the principle of operation of the focusing/deflection electrodes located before the collision-cell. The horizontal and vertical focusing properties of the lenses were de-coupled in order to allow beam deflection. The first lens formed a spatial focus before the second lens. The second lens then collimated the ion beam.

The electrode assemblies were designed and manufactured in-house. The electrodes were constructed from 316L stainless steel. Electrodes were fixed in position on insulating PEEK supports. The floated electrodes were contained within a grounded, mesh box, which allowed for efficient evacuation of the intervening voids and prevented stray fields. The first set of lenses was mounted on a stainless steel stand that located onto the baseplate of the main vacuum chamber using two 6 mm diameter dowel pins. The second set of lenses was mounted inside the collision-cell chamber. The collision-cell and associated optics located onto a lip on the pumping port. Four differential power-supplies were designed and constructed in-house to control the steering/focusing assemblies.

When steering potentials were applied to the lens electrodes the signal intensity at the final detector could be increased five-fold to ten-fold. It proved difficult to optimise the lens' potentials so that the first lens formed a spatial focus at the second lens, which would in turn have formed a tightly collimated beam through the apertures of the collision-cell. Figure 119 shows a photograph of the collision-cell region.

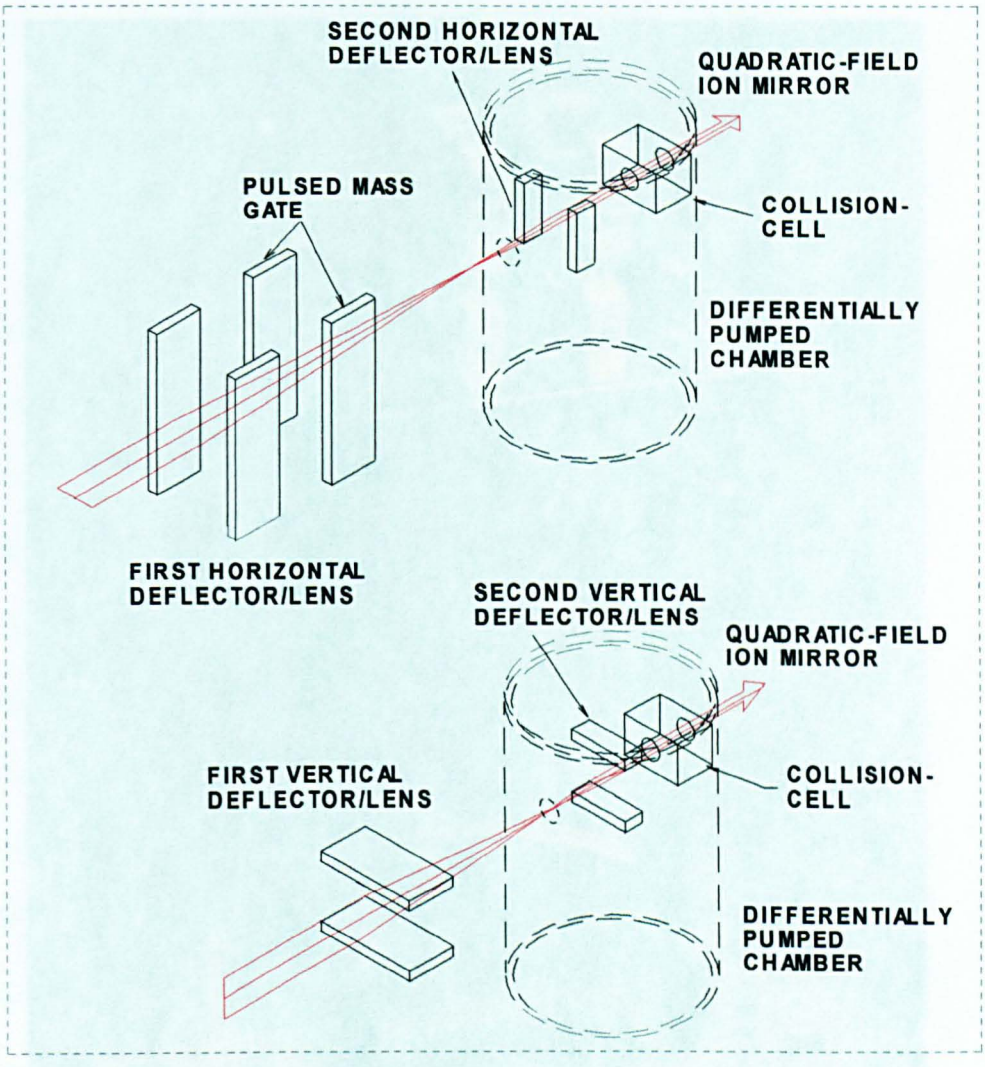

Fig. 118: Schematic diagram showing the horizontal steering and focusing electrodes (TOP). Schematic diagram showing the vertical deflection and focusing electrodes (BOTTOM).

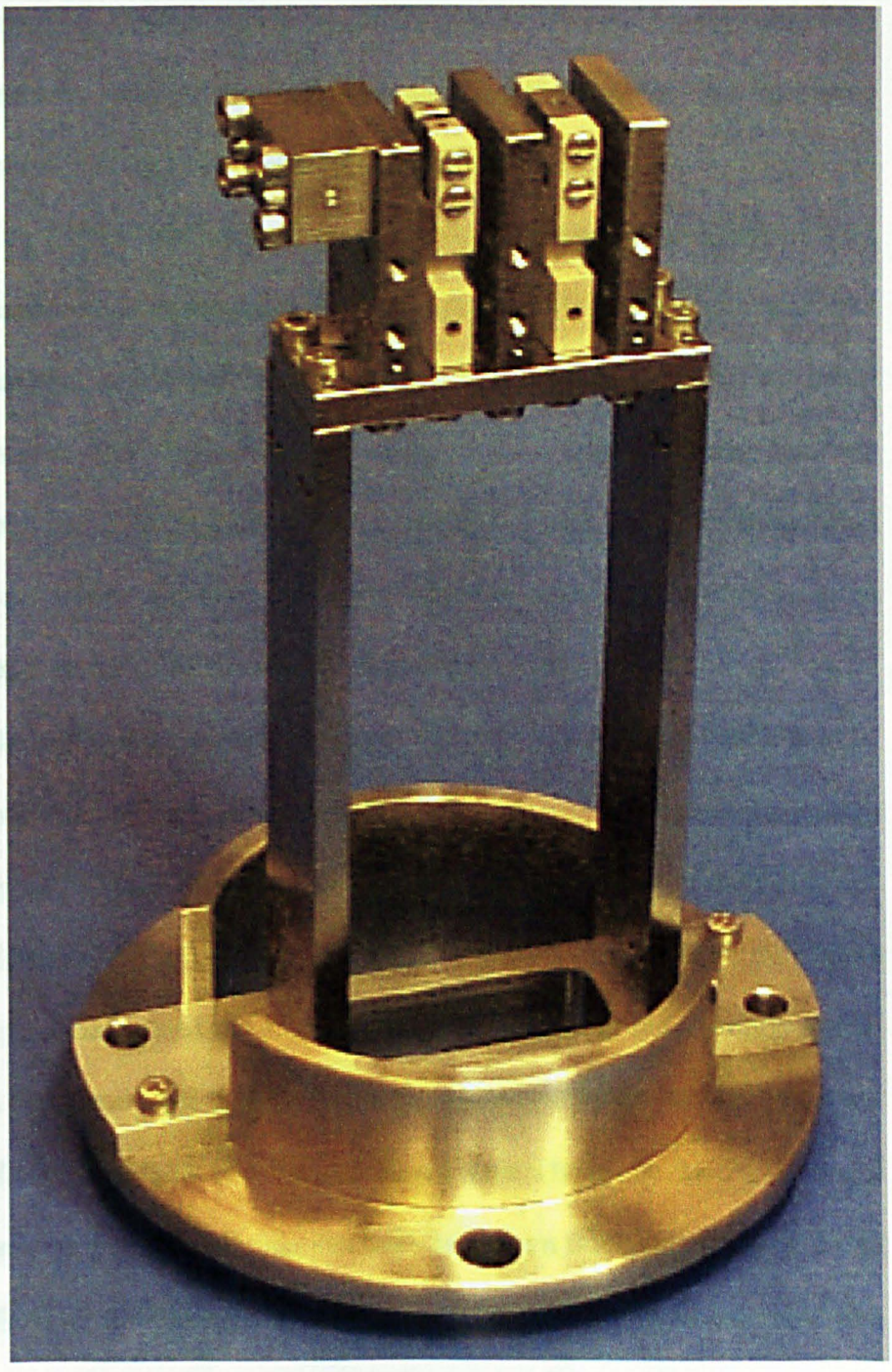

Fig. 119: Photograph of the collision-cell with outer chamber removed.

6.02 The Collision-Cell Region.

The collision-cell region consisted of a 1 cm long collision-cell chamber located inside a differentially pumped outer chamber. Pressure calculations indicated the pressure inside the cell was approximately $5x10^{-5}$ mbar during CID operation.

The collision-cell and associated optics were designed and manufactured in-house. The outer differentially pumped chamber was manufactured from 75 mm diameter aluminium tube. The ion beam entered the differentially pumped cell through 2 mm diameter apertures. The collision-cell and associated optics were manufactured from 316L stainless steel. The steering and lens electrodes were supported on PEEK mounts screwed onto metal supports.

The outer differentially pumped chamber was held in position by a stainless steel retaining ring. The retaining ring located into a seating lip in the baseplate of the chamber above the pumping port. Two 6 mm diameter dowel pins ensured that the collision-cell and associated optics maintained the correct angle with respect to the ion optical axis. A stainless steel plate capped the chamber. Holes in the cap plate allowed the gas line and electrical contacts to be made. The cell consisted of a small chamber with two 1mm thick endplates. A 2 mm diameter hole in each endplate allowed the ion beam to enter and exit the collision-cell. A piece of tapped 2 mm internal diameter stainless steel tube screwed into the bottom of the collision-cell. A piece of PTFE tube connected this, through the differentially pumped chamber, to a length of 2 mm internal diameter stainless steel tube in the main-

chamber vacuum region. The stainless steel tube sealed into a Swagelok compression fitting (Birmingham Valve and Fitting Company, UK) in the baseplate of the chamber. A Negretti precision leak-valve allowed the flow of collision gas to be controlled. Electrical connections to the steering/focusing optics were made by tinned copper wire insulated using PTFE tubing. The high-voltage lines were connected to a 4 pin high-voltage feedthrough (Caburn MDC, Sussex, UK) mounted on a DN200CF.

Practical experiments, described below, showed that the transmission of the collision-cell was poor. The 2 mm diameter apertures did not match the beam characteristics of ions emerging from the ion mirror. SIMION models, supported by practical experiments to characterise the ion beam, showed that the beam at the collision-cell was 20 mm wide. One solution would be to incorporate a pulsed-valve gas introduction system. This would allow the pressure within the main vacuum chamber to be kept within acceptable limits without the need for small apertures. Figure 120 shows a diagram of the proposed pulsed-valve system. The trigger unit would open the pulsed-valve and control the duration of the gas pulse. The delay generator would control the delay time between when the pulsed-valve was opened and the time when laser was fired. This delay time would be critical to controlling fragmentation of the analyte ions. The time-of-flight clock would be triggered in the usual manner from a reflection from the laser beam. Diffusive broadening of the gas pulse would mean that the pulse-width of the gas pulse would be in excess of 100 ms (FWHM)

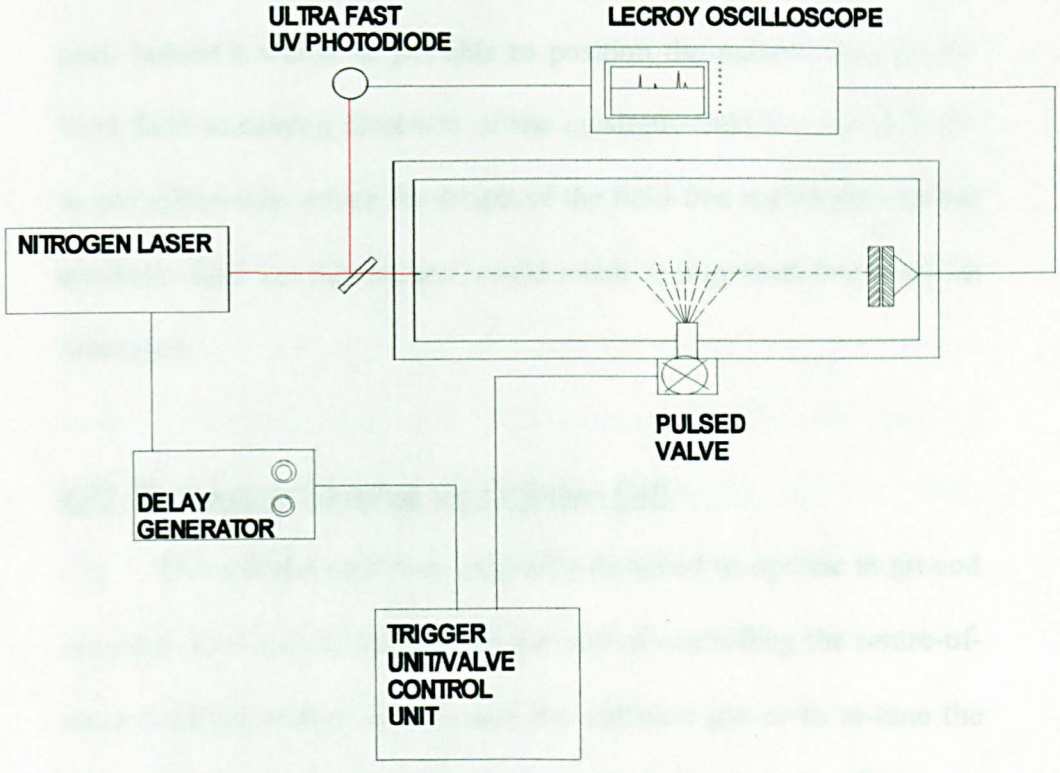

Fig. 120: Diagram of the proposed pulsed-valve collision region.

[1]. The pulse duration could be minimised by careful design of the valve system.

An advantage of the pulsed-valve gas inlet system would be that it would not have to be located over the collision-cell pumping port. Indeed it would be possible to position the pulsed-valve on the front field-sustaining electrode of the quadratic-field ion mirror. This would effectively reduce the length of the field-free region prior to the quadratic-field ion mirror, and would result in improved fragment-ion resolution.

6.03 Prospects of Floating the Collision-Cell.

The collision-cell was originally designed to operate at ground potential. This meant that the only method of controlling the centre-of-mass collision energy was to alter the collision gas or to re-tune the instrument to lower accelerating potentials. Selection of collision gas allowed only a few discrete values of centre-of-mass collision energy to be accessed, while re-tuning the instrument was complex and time consuming. The sensitivity of the micro-channel plates toward ions possessing low kinetic energies also limited the minimum accelerating voltage.

A preliminary investigation of the possibility of floating the collision-cell was conducted. The simplest approach to floating the collision-cell was to isolate the cell body using a set of PEEK spacers. Figure 121 shows a schematic diagram of one simple floated collision-cell configuration. The problem with this design, however, was that the

small apertures and high-voltages meant that the collision-cell formed a strong lens. Figure 122 shows a SIMION trajectory plot illustrating the lensing effect of the collision-cell apertures. The resultant beam was over-focused, resulting in a divergent ion beam inside the quadratic-field ion mirror. Experiments showed that this configuration resulted in virtually undetectable signal intensity at the final detector. Incorporating a deceleration and acceleration lens-stack before and after the cell would solve the problem. Figure 121 shows a schematic diagram of a collision-cell incorporating deceleration/acceleration lenses. By including a set of resistively coupled electrodes it would be possible to shape the field to minimise the divergence of the beam inside the quadratic-field ion mirror. Figure 122 shows a SIMION plot of the ion trajectories through the hypothetical deceleration/acceleration lens assembly. One major difficulty with such a design would be the amount of space required for the field-sustaining electrodes.

It is possible to conceive of a floated pulsed-valve system. It would prove difficult to float the pulsed-valve at high-voltages. Suitable mesh electrodes could be used to form the deceleration/acceleration regions. A major advantage of this design would be that the meshed apertures could be relatively large. This would lead to improved ion transmission. Another advantage would be that the system would fit in a relatively small space, meaning that the floated cell could be positioned in close proximity to the entrance to

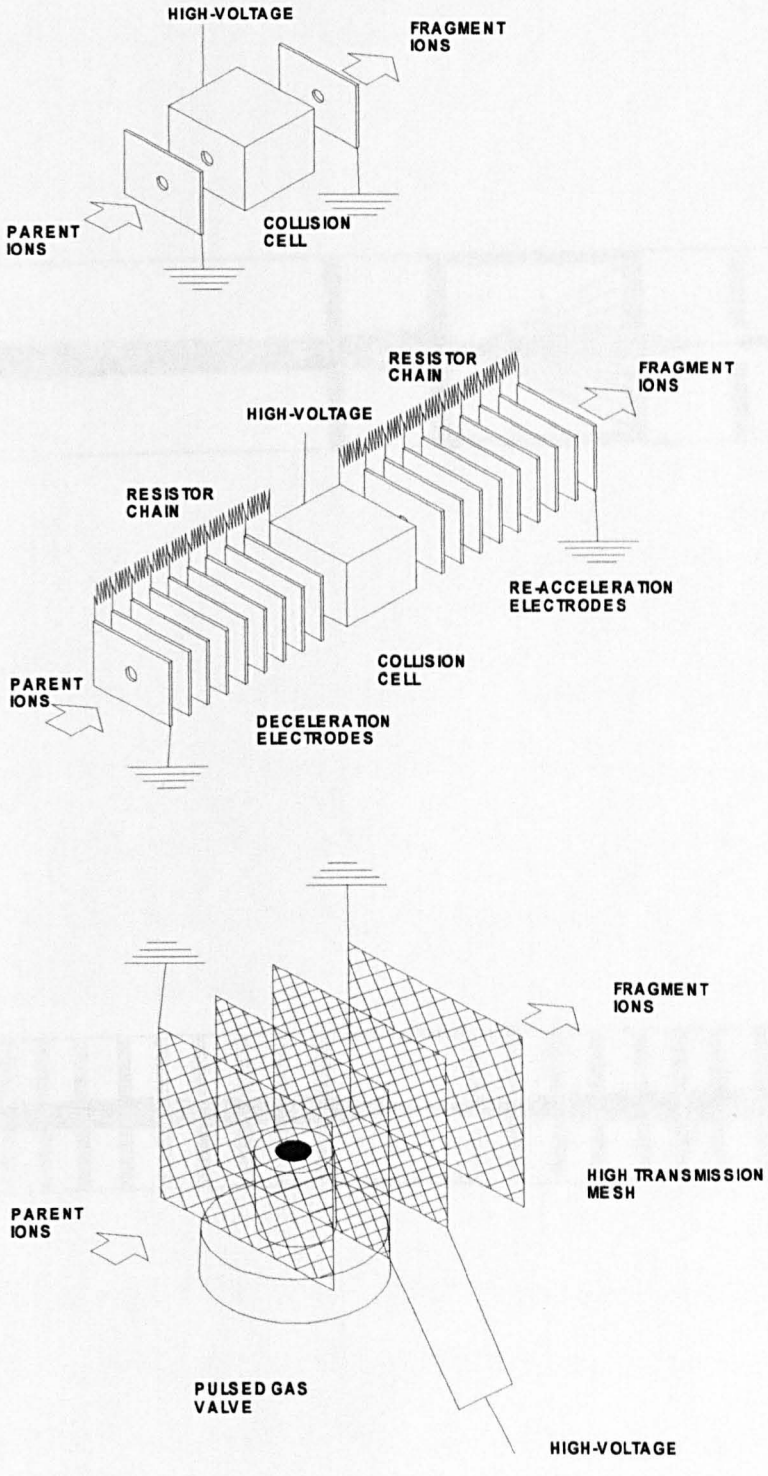

Fig. 121: Schematic diagram of simple floated collision-cell (TOP). Schematic diagram of floated collision-cell with field-sustaining electrodes (MIDDLE). Schematic diagram of floated pulsed-valve system (BOTTOM).

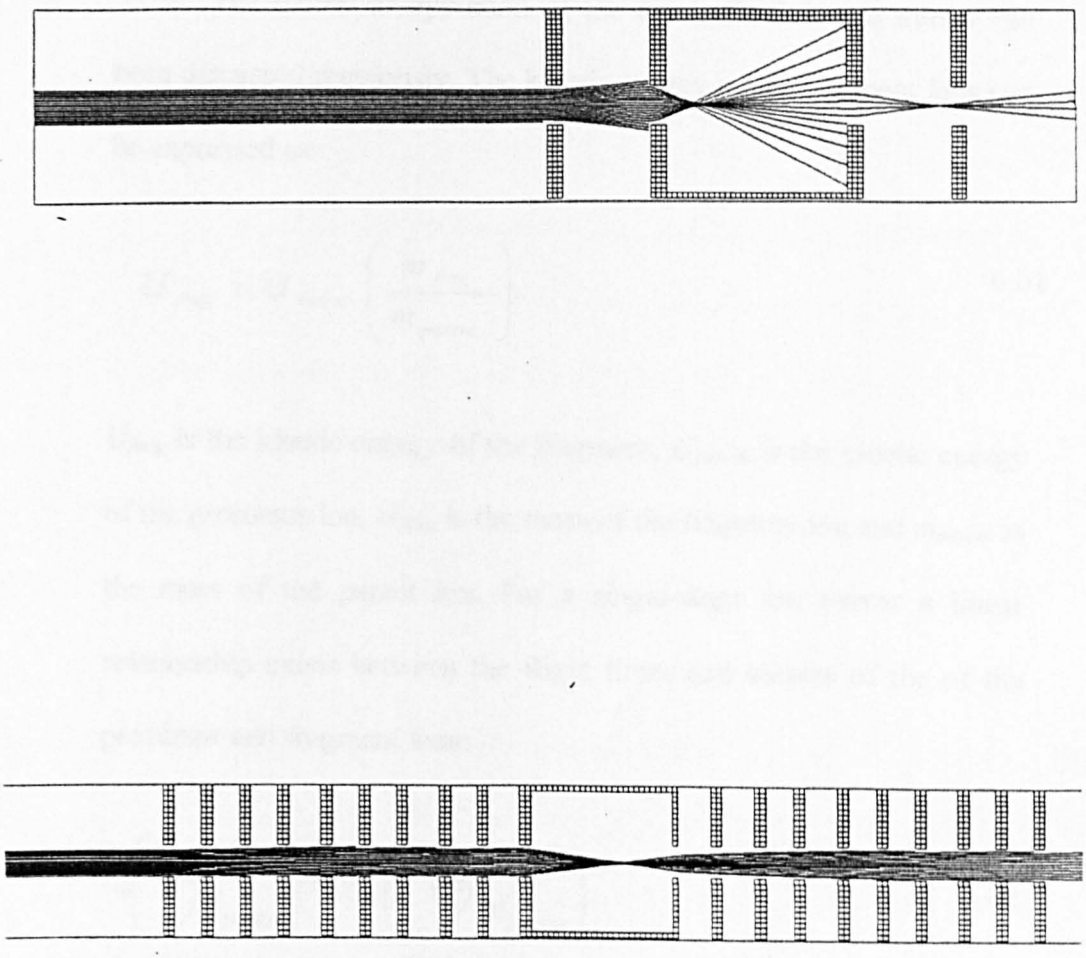

Fig. 122: SIMION ion trajectory plot for a simple floated collision-cell (TOP). SIMION ion trajectory plot for a collision-cell with field-sustaining electrodes (BOTTOM). 10,000 eV ions; 9000 V cells.

the quadratic-field ion mirror. Figure 121 shows a schematic diagram of the proposed pulsed-valve collision region.

6.04 Quadratic-Field Ion Mirror.

The theory of operation of the quadratic-field ion mirror has been discussed previously. The kinetic energy of the fragment ions can be expressed as:

$$U_{frag} = U_{parent}\left(\frac{m_{frag}}{m_{parent}}\right) \qquad 6.01$$

U_{frag} is the kinetic energy of the fragment, U_{parent} is the kinetic energy of the precursor ion, m_{frag} is the mass of the fragment ion and m_{parent} is the mass of the parent ion. For a single-stage ion mirror a linear relationship exists between the flight times and masses of the of the precursor and fragment ions:

$$2\left(t_{frag}/t_{parent}\right) = 1 + \left(m_{frag}/m_{parent}\right) \qquad 6.02$$

t_{frag} is the flight time of the fragment ion and t_{parent} is the flight time of the parent ion. The single-stage ion mirror is capable of time resolving the fragments. Standing and co-workers [2] have utilised the approach to study the metastable decay of various peptides. The problem with this approach is that the penetration depth of the ions inside the mirror determines the time focusing characteristics of the single-stage mirror. It is therefore possible to time focusing only a very small portion of the

fragment mass envelope at the detector plane at any one time. Mass resolution rapidly degrades for all other fragment masses. It is possible to time focus all fragment masses by "tuning" the mirror voltage to focus individual fragment masses. To achieve optimum time focusing for all fragment masses would, however, require a large number of individual portions of the spectrum to be acquired, stitched together and mass calibrated.

Two-stage ion mirrors are better suited to fragment-ion mass analysis, because of their ability to time focus a larger portion of the fragment-ion mass envelope at the detector plane. Kaufmann *et al* [3] have shown that the complete fragment mass spectrum can be acquired at high resolution by scanning the mirror reflecting-voltage through 10 to 14 consecutive voltages. This approach gave sufficient segment overlap to allow the individual portions of the spectrum to be stitched together to form a complete fragment mass spectrum.

The quadratic-field ion mirror [4] permits the complete fragment- mass envelope to be time focused at the detector plane without changing the reflecting voltage. This means that it is no longer necessary to scan the mirror potential and stitch together the resultant spectra. The approach is simpler and less time consuming. A significant problem with the quadratic-field ion mirror is the inherently defocusing nature of the electrostatic field. This degrades the transmission of the ion mirror, resulting in reduced sensitivity.

A quadratic-field ion mirror was designed and manufactured for use in the TOF-TOF spectrometer. A number of theoretical

considerations governed the resolution and design of the ion mirror.

Makarov *et al* [5] discussed the implications of field-free regions on achievable mass resolution and outlined methods for its treatment. If the constant C is chosen so that $U(0)=0$, *i.e.* the front electrode of the mirror is maintained at ground potential, the axial mirror potential can be expressed as:

$$U(z)=\frac{k}{2}\cdot(z-a)^2-\frac{k}{2}\cdot a^2=\frac{k}{2}\cdot z^2-k\cdot z\cdot a \qquad 6.03$$

$U(z)$ is the axial potential, z is the axial position and k and a are constants. If a field-free region of length L_d is introduced between the time focus of MS-1 and the entrance to MS-2, the quadratic-field ion mirror will achieve first-order time focusing when an appropriate value of a is selected [5]:

$$-k\cdot a=2\frac{U_{frag}}{L_d}\cdot\left\{1-\left[1-\left(\frac{L_d}{L}\right)^2\right]^{1/2}\right\} \qquad 6.04$$

U_{frag} is the kinetic energy of the fragment ion. L_d is the distance from the time focus of MS-1 to the entrance to the quadratic-field ion mirror. L is equal to the penetration depth of the ion with energy U_{frag}. For short field-free regions ($L_d/L<<1$):

$$a\approx-\frac{L_d}{2}-\frac{L_d}{8}\left(\frac{L_d}{L}\right)^2+.... \qquad 6.05$$

Higher-order terms are insignificant for instruments in which the field-free region is much shorter than mirror. All ions are time compressed at an image plane located at $z=2a$. Makarov *et al* [5] have shown that for short field-free regions high fragment-ion resolutions are achieved for fragments with kinetic masses greater than 0.4 m_{parent}. Mass resolution is limited for low-mass fragment ions possessing kinetic energies of the order 0.1-0.3 that of the parent ion. For the TOF-TOF instrument this meant that the mass resolution of fragment ions possessing kinetic energies <3000 eV was limited. Makarov *et al* [5] have shown that the degradation of mass resolving power becomes more significant when the length of the field-free region is in the range L_d >0.1-0.2L. For the TOF-TOF instrument, the geometry of the chamber and the mirror meant that L_d=0.08L.

The degraded resolution at low fragment-ion kinetic energies could be mitigated by reducing the length of the field-free region, *i.e.* moving the time focus of MS-1 towards the entrance to the quadratic-field ion mirror. Increasing the kinetic energy of the fragment ions after collision can also increase fragment ion resolution. This can be accomplished by floating the front of the quadratic-field ion mirror to a negative voltage. The TOF-TOF instrument would require the mirror front voltage to be –3 kV.

6.05 The Quadratic-Field Ion Mirror and the Collision-Cell.

The design of the collision-cell was determined by a number of considerations. The requirement to maintain pressures in the main

vacuum region of the order $1x10^{-7}$ mbar determined the size of the apertures. Makarov *et al* [5] have outlined the theoretical considerations governing the length of the collision-cell.

According to the impulsive collision theory (ICT) [6] the change in axial ion velocity after collision can be expressed as:

$$\Delta u_z = -2 \cdot \frac{m_g}{m_{parent}} \cdot \frac{m_a}{(m_a + m_g)} \cdot u \cdot \cos^2 \varphi \qquad 6.06$$

Δu_z is the velocity change post collision, m_g is the mass of the collision gas, m_{parent} is the mass of the parent ion, m_a is the mass of the atom or group of atoms involved in the collision, u is the velocity of the ion prior to collision and φ is the impact angle. The radial velocity change can be expressed as:

$$\Delta u_x = 2 \cdot \frac{m_g}{m_{parent}} \cdot \frac{m_a}{(m_a + m_g)} \cdot u \cdot \cos\varphi \cdot \sin\varphi \qquad 6.07$$

Δu_x is the radial velocity change.

For a situation in which the average number of collisions inside the cell is 1, the maximum axial, Δz, and radial, Δx, velocity spreads can be expressed as:

$$\Delta_z = 2 \cdot \frac{m_g}{m_{parent}} \cdot \frac{m_a}{(m_a + m_g)} \cdot u \qquad 6.08$$

$$\Delta_x = \pm \frac{m_g}{m_{parent}} \cdot \frac{m_a}{(m_a + m_g)} \cdot u \qquad 6.09$$

Kinetic energy spread may also arise from kinetic energy release associated with the unimolecular decay process. For a parent ion undergoing unimolecular decay to form a fragment ion of mass m_{frag}, accompanied by kinetic energy release equal to zw, the resultant velocity in the laboratory frame can be expressed as:

$$u_1 = \left[2 \cdot \frac{zw}{m_{parent}} \cdot \left(\frac{m_{parent}}{m_{frag}} - 1 \right) \right]^{1/2} = u \cdot \left[\frac{w}{U} \cdot \left(\frac{m_{parent}}{m_{frag}} - 1 \right) \right]^{1/2} \qquad 6.10$$

u_1 is the velocity spread, zw is the kinetic energy release associated with unimolecular decay and U is the kinetic energy of the precursor ion. In the centre-of-mass frame the velocity is isotropically distributed *i.e.* that is to say that the unimolecular decay process has no memory of the activation process. The velocity is distributed such that $\Delta_{z1} = \pm u_1$ and $\Delta_{x1} = \pm u_1$.

Figure 123 shows theoretical plots of axial velocity spread versus parent-ion mass caused by CID. The velocity spread becomes increasingly significant at high target-gas mass and low parent-ion

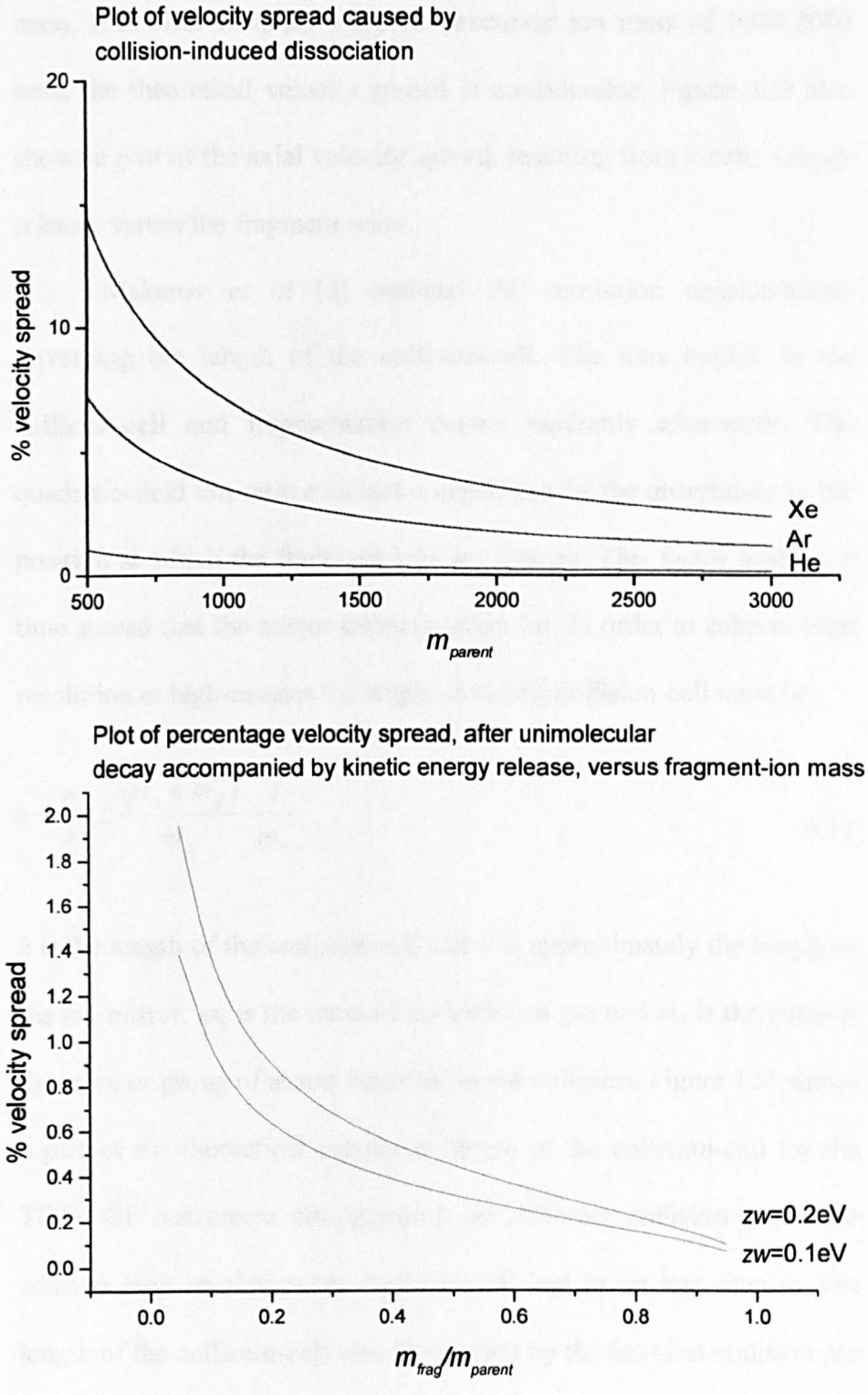

Fig.123: Plot of axial velocity spread caused by CID versus precursor mass (TOP). Plot of axial velocity spread caused by kinetic energy release during unimolecular decay versus fragment-ion mass (BOTTOM).

mass. It is clear that, for a typical precursor ion mass of 1000-2000 amu, the theoretical velocity spread is considerable. Figure 123 also shows a plot of the axial velocity spread, resulting from kinetic energy release, versus the fragment mass.

Makarov *et al* [5] outlined the resolution considerations governing the length of the collision-cell. The ions collide in the collision-cell and fragmentation occurs randomly afterwards. The quadratic-field ion mirror cannot compensate for the uncertainty in the position at which the fragment ions are formed. This factor leads to a time spread that the mirror cannot correct for. In order to achieve high resolution at high-masses the length, *h*, of the collision-cell must be:

$$h < \frac{\pi}{4} \cdot L \frac{(m_a + m_g)}{m_a} \cdot \frac{1}{m_g} \qquad 6.11$$

h is the length of the collision-cell and *L* is approximately the length of the ion mirror. m_g is the mass of the collision gas and m_a is the mass of the atom or group of atoms involved in the collision. Figure 124 shows a plot of the theoretical maximum length of the collision-cell for the TOF-TOF instrument configuration for different collision gases. To achieve high resolution the collision-cell had to be less than *h*. The length of the collision-cell was determined by the heaviest collision gas likely to be used, in this case xenon. The length of the collision-cell had to be less than 11 mm. The collision-cell was designed to be 10 mm long.

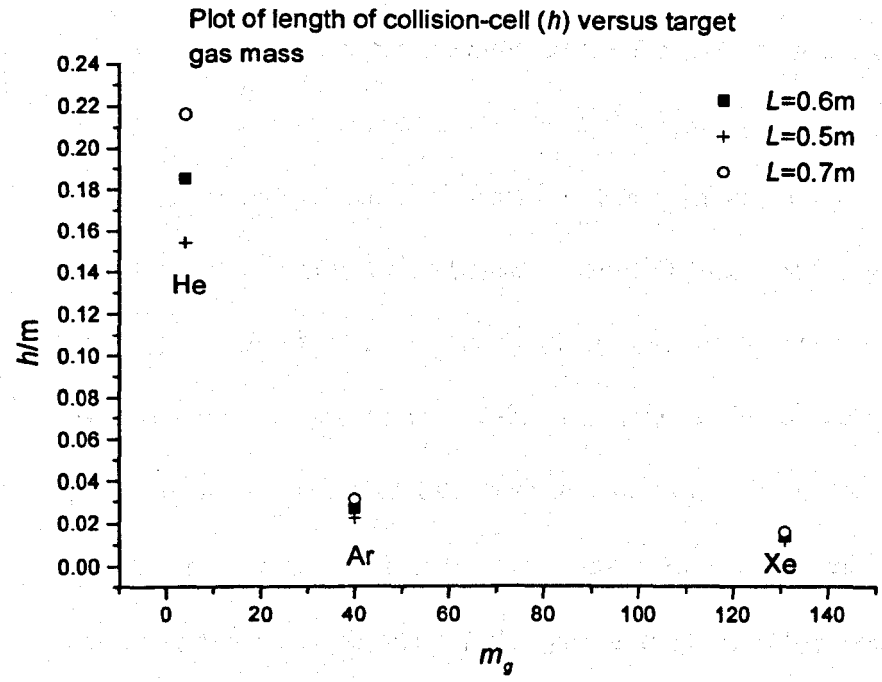

Fig. 124: Plot of length of collision-cell (h) versus mass of target gas (m_g) for different length quadratic-field ion mirrors.

6.06 Metastable Decay in the TOF-TOF spectrometer.

Metastable decay/post-source decay is widely used in the structural analysis of peptides. The ions are thought to acquire excess internal energy through a number of processes. Spengler *et al* [7] found a strong correlation between PSD fragment yield and residual gas pressure. This was interpreted as evidence for collisional activation of the precursor through collision with background gas molecules followed by unimolecular dissociation. Spengler and co-workers [8] reported a strong correlation between the PSD fragment ion yield and accelerating field strength, suggesting in-source activation. The mechanism was thought to involve multiple collisions between the precursor molecule-ion and the neutral species present in the MALDI desorption plume. Spengler and co-workers [9] subsequently demonstrated that the use of delayed extraction (DE) resulted in reduced post-source decay compared to that observed using prompt extraction (PE). Spengler and co-workers accounted for the observation thus: ions in the DE ion source were generated in a field-free region. The ions experienced low-energy ion-neutral collisions in the desorption plume. After a time delay, in which the neutral species in the desorption-plume had reduced in density, a voltage pulse extracted the ions. The probability of collision in the delayed extraction source was therefore lower than that encountered in the prompt extraction source. As will be shown later, this had important ramifications for the prompt extraction ion source fitted to the TOF-TOF spectrometer.

Metastable species were observed to undergo fragmentation on transit through the TOF-TOF instrument. Ions undergoing fragmentation in the first field-free region were time resolved by MS-1. The trajectories of low-mass metastable fragment ions were outside of the tight acceptance parameters of the collision-cell. Only metastable fragments with masses close to that of the precursor ion had trajectories that fell within the acceptance parameters of the collision-cell. The mass gate was shown to be capable of excluding the time-resolved metastable fragment species generated in the first field-free region.

The mass gate did not exclude PSD fragments generated in the second field-free region, prior to the quadratic-field ion mirror. The length of the field-free region and the kinetic energy release associated with the unimolecular decay process determined the mass resolution of these metastable species. Makarov *et al* [5] derived an expression describing how the length of the field-free region limits metastable fragment resolution:

$$R_{0\%} = \frac{\pi}{4} \cdot \frac{L}{L_{ff}} \cdot \frac{\left(\frac{m_{frag}}{m_{parent}}\right)^{1/2}}{\left[\frac{w}{U} \cdot \left(\frac{m_{parent}}{m_{frag}} - 1\right)\right]^{1/2}} \qquad 6.12$$

$R_{0\%}$ is mass resolution defined using the base of the peak, L is the penetration depth, and L_{ff} is the length of the field-free region between MS-1 and MS-2. zw is the kinetic energy released during unimolecular decay and U is the kinetic energy of the precursor ion.

The resolution can be expressed as:

$$R_{0\%} = \frac{1}{2\Delta t / t} \qquad 6.13$$

The full-width half-maximum resolution can be expressed as R (FWHM)=$2R_{0\%}$. Figure 125 shows a plot of the limiting metastable fragment ion resolution (FWHM) for the TOF-TOF instrument versus fragment mass. L_{ff} = 0.3 m; zw = 0.1 eV; U =10,000 eV. The metastable fragment ion resolution was determined by the kinetic energy release associated with unimolecular decay.

Ions dissociating inside the quadratic-field ion mirror are detected. The time-of-flight of the fragment ion will depend upon the position at which the fragment ion was formed. The fact that fragments are formed at different potentials results in peak broadening. The quadratic-field ion mirror, and indeed any ion mirror, cannot compensate for this source of peak broadening. Fragmentation inside the mirror may also result in "ghost peaks".

6.07 Detector Considerations and Mass Discrimination.

The shape and size of the fragment ion detector were important considerations. The shape of the detector determined the sensitivity of the detector towards different mass fragment ions. The ion mirror temporally resolved and spatially separated the fragment ions at the detector plane. The shape and size of the detector can result in fragment ion mass discrimination. Figure 126 shows schematic diagrams of ion mirrors fitted with rectangular and circular channel

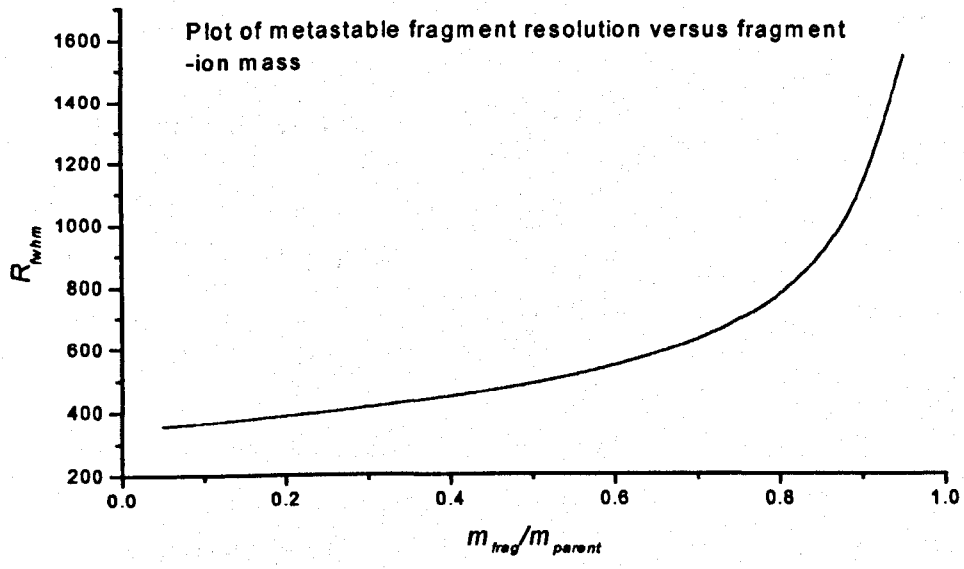

Fig. 125: Plot of metastable fragment-ion resolution versus fragment-ion mass for the TOF-TOF spectrometer.

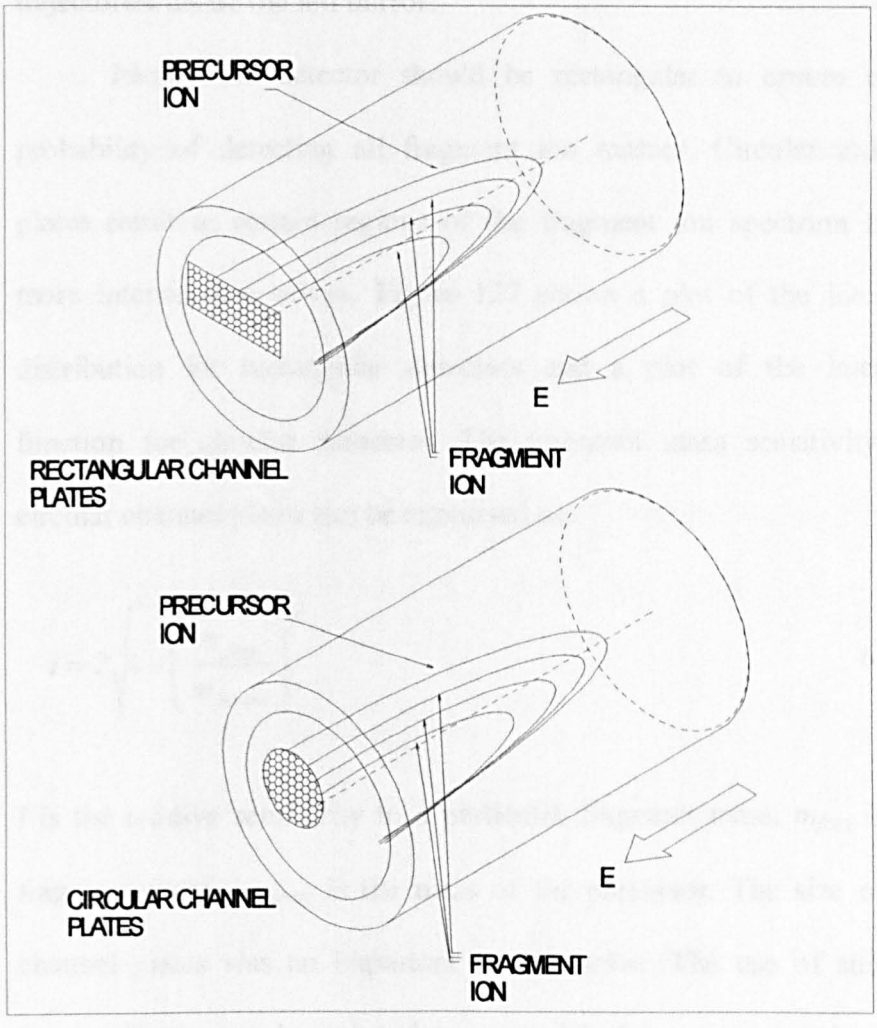

Fig. 126: Schematic diagram showing parent and daughter ion trajectories through ion mirror. The shape of the detector determines the sensitivity of the spectrometer towards different mass fragments.

plates. Note the spatial separation of the fragment and parent ion trajectories inside the ion mirror.

Ideally the detector should be rectangular to ensure equal probability of detecting all fragment ion masses. Circular channel plates result in certain regions of the fragment ion spectrum being more intense than others. Figure 127 shows a plot of the intensity distribution for rectangular detectors and a plot of the intensity function for circular detectors. The fragment mass sensitivity for circular channel plates can be expressed as:

$$i = 2\sqrt{1-\left(\frac{m_{frag}}{m_{parent}}\right)^2} \qquad 6.14$$

i is the relative sensitivity to a particular fragment mass, m_{frag} is the fragment mass, m_{parent} is the mass of the precursor. The size of the channel plates was an important consideration. The use of suitably large diameter channel plates would have prevented mass discrimination. Correct choice of detector dimensions was therefore important in order to minimise mass discrimination.

The beam width at the detector plane was determined by a number of factors. For coaxial mirrors the angular scattering associated with CID, the kinetic energy release associated with unimolecular decay, the beam characteristics and the properties of the electrostatic field determine the beam dimensions at the detector plane.

For reflectron mirrors in which the mirror axis is at an angle with respect to the entry axis of the ions, the length and tilt angle of the mirror determine the beam dimensions. Ignoring scattering caused by CID and kinetic energy release the beam width at the front of the mirror for a complete fragment ion spectrum can be estimated:

$$l_{det} = 2L\tan\theta \qquad 6.15$$

l_{det} is the width of the detector, L is the penetration depth/length of the mirror and θ is the tilt angle of the ion mirror. Performing the calculation for the TOF-TOF instrument gave a minimum detector width, l_{det}, of 66mm.

Scattering, resulting from CID and unimolecular decay, increases the beam size at the detector plane. Makarov *et al* [5] have derived an expression governing the relationship between these processes and the size of detector for planar hyperbolic ion mirrors:

$$D_x \approx \pm\left\{\frac{m_g}{m_{parent}}\cdot\frac{m_a}{(m_a+m_g)}+\left[\frac{w}{U}\cdot\left(\frac{m_{parent}}{m_{frag}}-1\right)\right]^{1/2}\right\}\cdot L\cdot\sqrt{\frac{m_{frag}}{m_{parent}}}\cdot\sinh(\pi) \qquad 6.16$$

D_x is the horizontal width of the detector and $D_y \approx 0.272 D_x$, where D_y is the vertical dimension of the detector. Heavier collision gases require larger detector areas in order to achieve 100 % transmission.

In order to achieve 100 % fragment ion transmission the detector must be larger than the dimensions shown in figure 128. For collision gases heavier than helium, it was not possible to achieve 100 % fragment ion transmission.

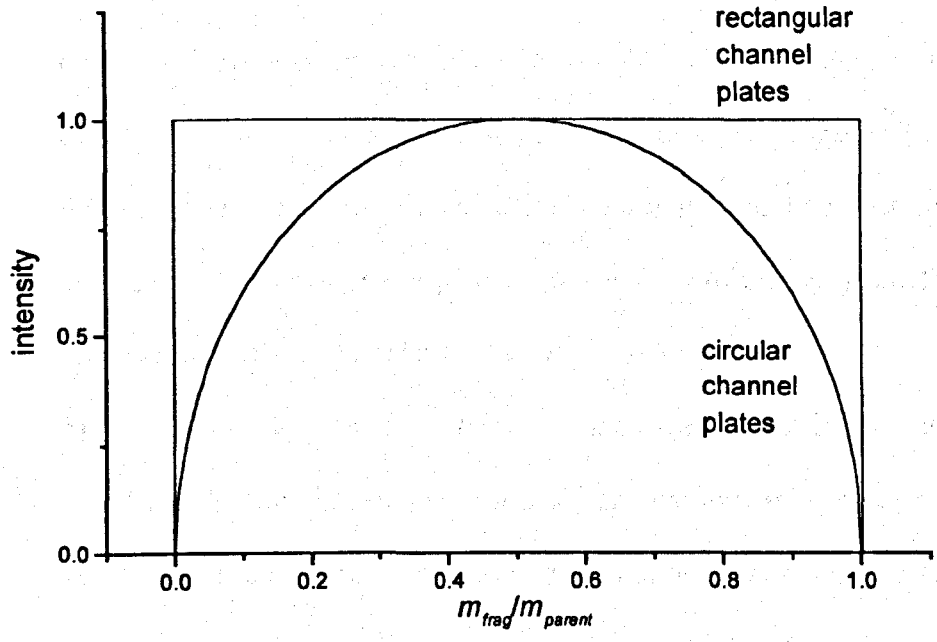

Fig. 127: Plot of intensity versus fragment mass. The plot displays the relationship between the shape of the channel plates and their sensitivity towards different mass fragment ions.

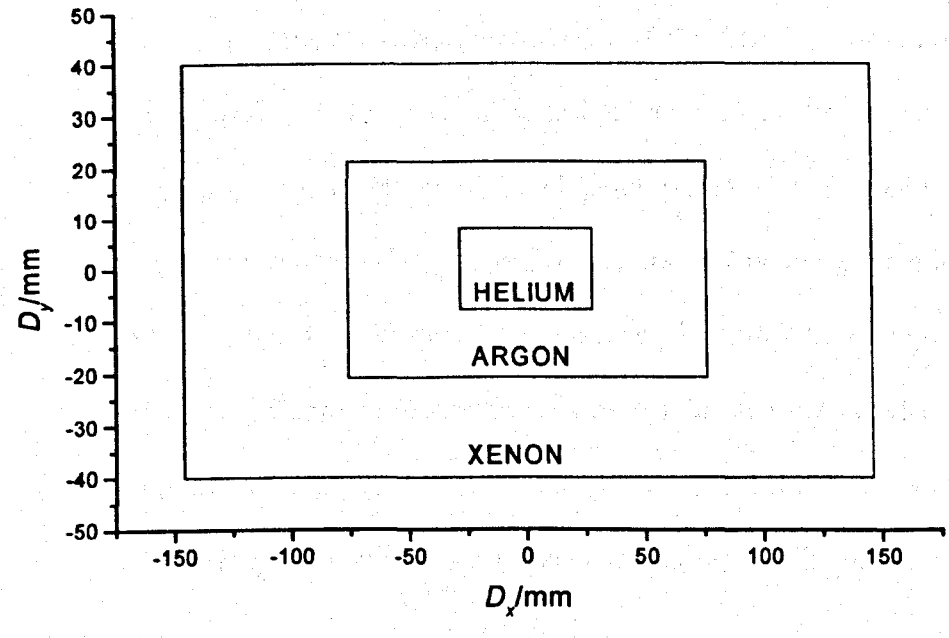

Fig. 128: Size of detector required for 100 % ion transmission with different target gases.

To account for fringing fields it was necessary to examine the quadratic-field ion mirror using SIMION. The ion mirror was accurately modelled in three dimensions and the trajectories of fragment ions analysed. Figure 129 shows a plot of fragment mass versus the fragment-ion exit position at the front of the quadratic-field ion mirror. The analysis raised several important points.

1) Ions entered through a 6 mm diameter aperture in the front electrode. Simulations showed that fragment ions with m_{frag}/m_{parent} $\leq$0.04 were reflected back through the entrance aperture. For 1000 amu precursor ions this meant that the signal intensity of ions with m/z $\leq$40 was significantly reduced. This region of the spectrum included the cation species, Na^+ and K^+.
2) The 25mm diameter active area of the channel plates meant that the detector was sensitive to only a small portion of the fragment ion spectrum, in the range m_{frag}/m_{parent}=0.18-0.54. The circular channel plates also led to mass discrimination across the detectable fragment mass envelope. The channel plates showed optimum fragment mass sensitivity at m_{frag}/m_{parent}=0.36. Changing the mirror voltage altered the fragment mass sensitivity. Angular divergence meant that fragment ions with masses outside the predicted range were observable. SIMION calculations showed that a channel plate 80mm long was required to detect the complete fragment mass range.

6.08 Design and Construction of the Quadratic-Field Ion Mirror.

The quadratic-field ion mirror was designed in-house and manufactured by Cambridge University, Department of Engineering. The mirror consisted of 28 field-sustaining electrodes manufactured from 3 mm thick 316L stainless steel. Field-stop electrodes, similar to those of the first ion mirror, were spot welded in position to minimise ground potential penetration. The mirror consisted of 26 standard field-sustaining electrodes with elliptical apertures, a rear electrode and a front electrode. Figure 130 shows a schematic diagram of a standard field-sustaining electrode.

The front electrode was solid with a 6 mm diameter entrance aperture and 68 mm diameter detector aperture. Figure 131 shows a schematic diagram of the front electrode. The rear electrode was designed so that the central portion of the electrode could be floated at a potential ±4 kV different from that of the rest of the electrode. This allowed the field inside the mirror to be shaped. The central portion of the electrode was mounted on four Shapal-M® spacers. A hole in the centre of the rear electrode allowed ions to be detected on a MCP detector located behind the mirror.

The mirror was constructed in a manner identical to that used for the first ion mirror. Each electrode was connected to its adjacent electrodes by four Shapal-M® ceramic spacers attached by M12 grub screws. The front and rear electrodes were held in position by M12 bolts. The front electrode of the mirror located on a 6mm diameter dowel pin in the baseplate of the chamber. A tie bar supported the rear

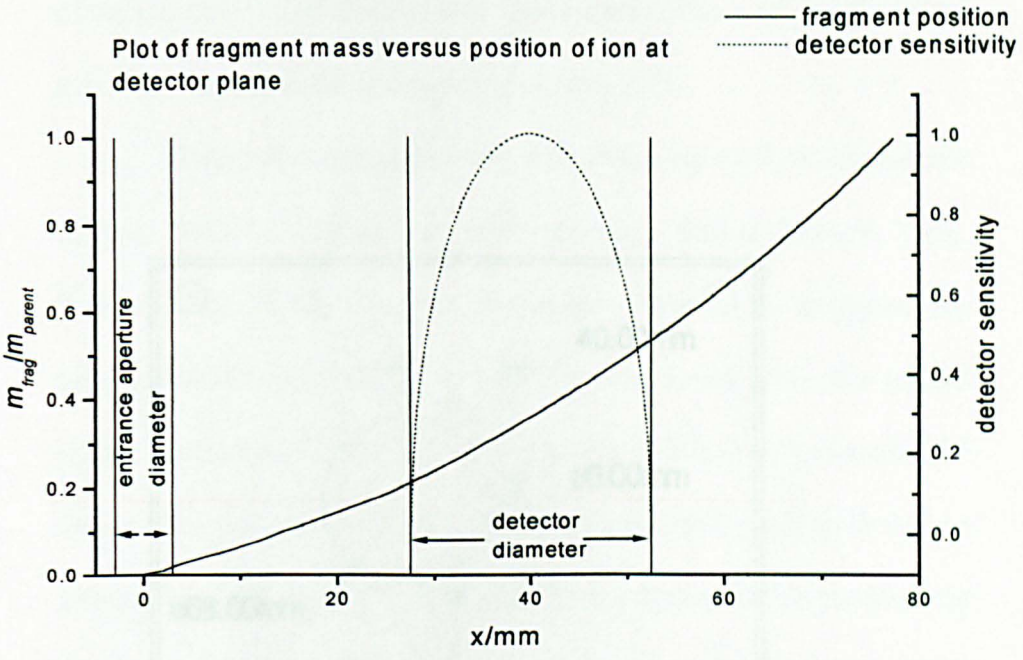

Fig. 129: Plot showing relationship between fragment ion mass and the position of fragment ion at the detector plane. The dimensions of the entrance aperture and the detector's active area are shown. The detector sensitivity towards different fragment masses is also plotted (x=0 is the centre of the entrance aperture).

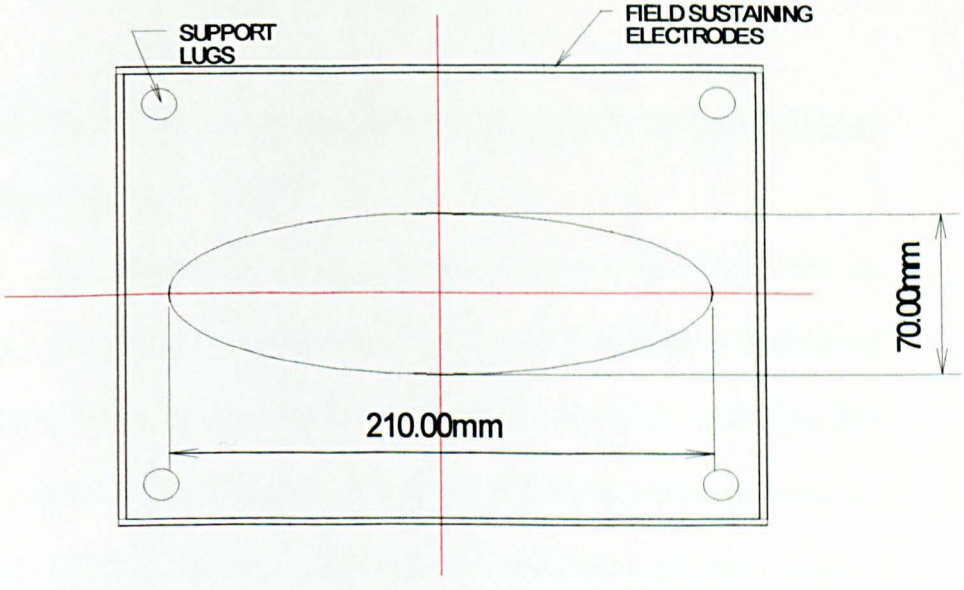

Fig. 130: Schematic diagram of standard MS-2 field-sustaining electrode.

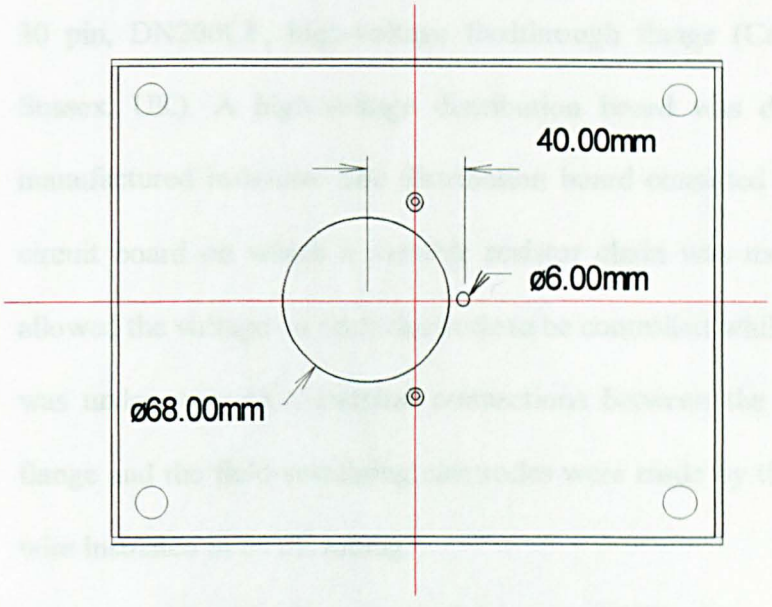

Fig. 131: Schematic diagram of the front electrode of MS-2.

of the ion mirror and allowed it to rotate freely. The angle of the mirror axis with respect to the ion optical axis was 2.7°.

Electrical connections were made via a specially manufactured 30 pin, DN200CF, high-voltage feedthrough flange (Caburn MDC, Sussex, UK). A high-voltage distribution board was designed and manufactured in-house. The distribution board consisted of a printed circuit board on which a variable resistor chain was mounted. This allowed the voltage on each electrode to be controlled while the system was under vacuum. Electrical connections between the feedthrough flange and the field-sustaining electrodes were made by tinned copper wire insulated in PTFE tubing.

A 25 mm diameter active area MCP detector (Galileo, Sturbridge, MA) was positioned at the front of the ion mirror to detect fragment ion. Figure 132 shows an isometric view of the completed ion mirror.

6.09 Experiments to Characterise the Instrument and Mirror Transmissions.

Experiments to characterise the transmission of the first ion mirror have already been outlined. A similar procedure was followed to characterise the transmission of the collision-cell and quadratic-field ion mirror. A 0.1 M aqueous solution of lithium bromide was made up. 0.5 µl aliquots were pipetted onto the probe tip and dried under a nitrogen stream. The source voltage was fixed at +10 kV. The laser power was tuned to provide strong, consistent signal. The MCP

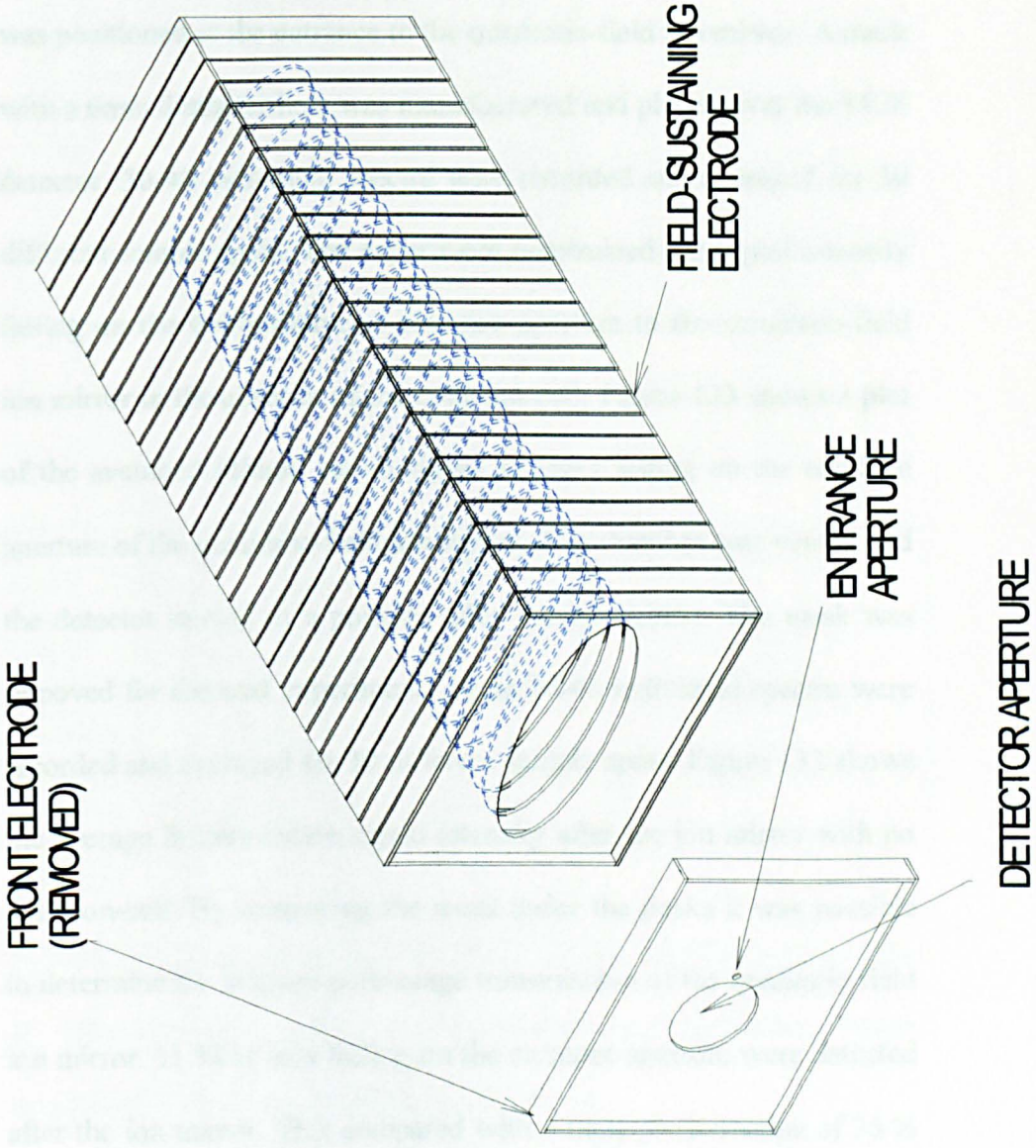

Fig. 132: Schematic diagram of the quadratic-field ion mirror.

detector was maintained at –1.8 kV. The single-stage ion mirror was maintained at +12.4 kV. The settings were held constant for subsequent experiments. The potentials applied to the lenses and steering electrodes were tuned to provide optimum transmission.

A 25 mm diameter MCP detector (Galileo, Sturbridge, MA) was positioned at the entrance to the quadratic-field ion mirror. A mask with a 6mm diameter hole was manufactured and placed over the MCP detector. 30-40 individual spectra were recorded and averaged for 30 different sample spots. The experiment determined the signal intensity falling on the 6 mm diameter entrance aperture to the quadratic-field ion mirror in the absence of the collision-cell. Figure 133 shows a plot of the averaged lithium cation signal intensity falling on the entrance aperture of the quadratic-field ion mirror. The chamber was vented and the detector moved to a position after the ion mirror. The mask was removed for the next experiment. Again 30-40 individual spectra were recorded and averaged for 30 different sample spots. Figure 133 shows the average lithium cation signal intensity after the ion mirror with no collision-cell. By comparing the areas under the peaks it was possible to determine the average percentage transmission of the quadratic-field ion mirror. 11 % of ions falling on the entrance aperture were detected after the ion mirror. This compared with a transmission value of 36 % for the single-stage ion mirror.

The chamber was vented again and the collision-cell installed. Again 30-40 individual spectra were recorded and averaged for 30 individual sample spots. Figure 133 shows a plot of the average lithium

cation intensity with the collision-cell in place. The chamber was vented again and the detector positioned 60 cm in front of the ion source. The experiment was repeated in order to determine the signal produced in the source region. Figure 134 shows a plot of the lithium cation signal intensity produced by the ion source. From the experiments it was possible to determine the percentage transmission of the instrument. With no collision-cell in place, 5 % of ions fell on the entrance aperture of MS-2. Of these 0.5 % reached the final detector. The situation, however, was far worse when the collision-cell was in position. The total transmission of the instrument, for a non-metastable species, with the collision-cell in place was 0.06 %. The table below summarises the findings:

Position	Percentage Transmission
MS-1 (20 mm diameter MCP)	36 %
MS-2 (25 mm diameter MCP)	11 %
Absolute transmission without collision-cell	0.5 %
Absolute transmission with collision-cell	0.06 %

Table 6.1

Subsequent design modifications improved the absolute transmission by approximately a factor of 30 (estimated on comparison of peak heights) to 2 %. These modifications included:

1) Steering/lenses in the second field-free region.
2) Increased diameter of collision-cell apertures.
3) Improved alignment of source electrodes (no deflection generated in source).
4) Improved tuning.

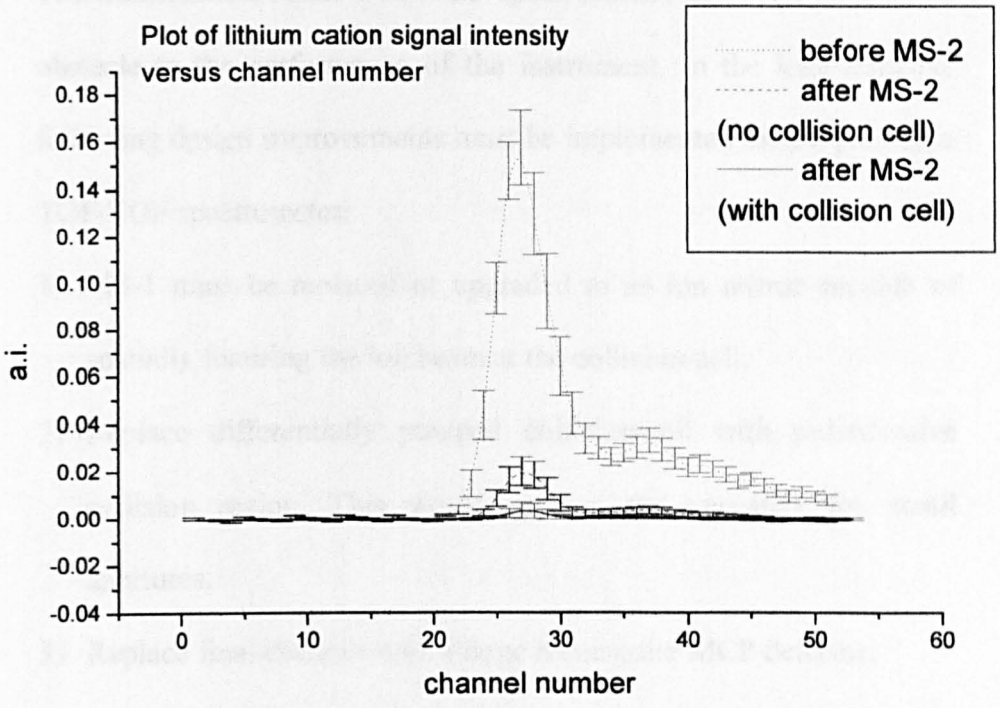

Fig. 133: Lithium cation signal intensity before and after MS-2. Signal intensity with and without the collision-cell shown.

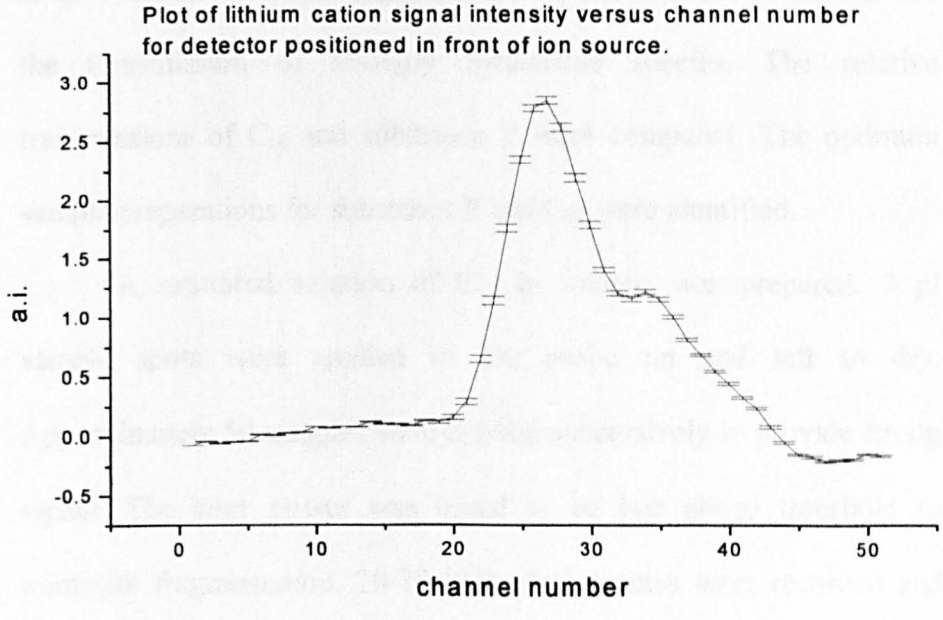

Fig.134: Lithium cation intensity after the ion source. For clarity figures 133 and 134 are plotted separately. The intensity scales are comparable.

The transmission of the TOF-TOF spectrometer, however, remains an obstacle to the performance of the instrument. In the long-term the following design improvements must be implemented on the prototype TOF-TOF spectrometer:

1) MS-1 must be replaced or upgraded to an ion mirror capable of spatially focusing the ion beam at the collision-cell.
2) Replace differentially pumped collision-cell with pulsed-valve collision region. This would remove the necessity for small apertures.
3) Replace final detector with a large rectangular MCP detector.

Experiments had shown that it was possible to generate sufficient $C_{60}^{+\cdot}$ ion current for CID. It proved impossible, however, to detect sufficient ion current from buccalin, bradykinin and substance P at the final detector. A set of experiments was conducted to determine the transmission of strongly metastable species. The relative transmissions of C_{60} and substance P were compared. The optimum sample preparations for substance P and C_{60} were identified.

A saturated solution of C_{60} in toluene was prepared. 2 µl sample spots were applied to the probe tip and left to dry. Approximately 50 samples were applied successively to provide strong signal. The laser power was tuned to be just above threshold to minimise fragmentation. 20-30 individual spectra were recorded and averaged. The signal intensity at the linear TOF detector was recorded for a total of 12 sample spots. The experiment was repeated and the signal intensity at the final detector recorded. The linear TOF

instrument could not resolve the parent and fragment ions and so recorded the total fullerene signal.

A 0.1 mg/ml solution of substance P in water/methanol (50:50) was made up. A 0.2 M solution of α-cyano-4-hydroxy-cinnamic acid (α-CHC) in acetone/water (70:30) was made up. 0.5 µl of α-CHC solution was spotted and dried under nitrogen. 0.5 µl of the substance P solution was spotted on top of the matrix and dried under nitrogen. The laser power was tuned so as to be just above threshold. Again 20-30 individual spectra were recorded for 12 sample spots. The signal intensity of the protonated substance P at the linear TOF detector was recorded. The experiment was repeated and the signal intensity at the final detector measured.

The experiment was repeated for substance P with 2,5-dihydroxybenzoic acid (DHB) as the matrix. The following optimised sample preparation was used: 0.5 µl of 0.1 M DHB in acetone/water (70:30) spotted and dried followed by 0.5 µl of 0.1 mg/ml substance P in water/methanol (50:50) spotted and dried. The signal intensities recorded are outlined in the table below.

Sample Preparation	Detector	Average Signal Height/mV	Percentage Signal Height	Laser attenuator (micrometer)
0.1 mg/ml substance P, 0.2 M α-CHC	Linear detector	39		3+95
0.1 mg/ml substance P, 0.2 M α-CHC	Final detector	2.04	5.2 %	3+95
0.1 mg/ml substance P, 0.1M DHB	Linear detector	14.5		7+05
0.1 mg/ml substance P, 0.1 M DHB	Final detector	1.31	9.0 %	7+05
C_{60}	Linear detector	67		5+55
C_{60}	Final detector	20.7	31 %	5+55

Table 6.2

The values could not be used to determine absolute transmission values because the detectors at the linear TOF and MS-2 TOF were different. By assuming that the $C_{60}^{+\cdot}$ did not fragment during transit through the instrument and comparing the signal intensities for different analytes it was possible to estimate the signal reduction arising from metastable fragmentation. The signal height at the final detector was $1/3^{rd}$ that at the linear TOF detector. If substance P did not undergo metastable fragmentation the signal intensity at the final detector would be expected to be $1/3^{rd}$ that of the linear detector. It was found, however, that the signal was $1/10^{th}$ (with DHB) to $1/20^{th}$ (with α-CHC). The total transmission of metastable peptides was of the order of 0.01% to 0.02%.

To reduce metastable peptide transmission a number of future modifications must be made:

1) Reduce the field strength in the acceleration region, currently >20 kV/cm, by increasing the separation of the acceleration and counter-electrode.
2) Reconfigure the ion source to a delayed extraction ion source.
3) Improve the pumping of the neutral desorption plume.

6.10 Experiments to Characterise the Energy Focusing Properties of the Quadratic-Field Ion Mirror.

A set of experiments was conducted to examine the energy-focusing properties of the quadratic-field ion mirror. The experiment to determine the time focusing properties of the quadratic-field ion mirror was complicated by the presence of the first ion mirror. Simply scanning the accelerating voltage would mean that the result would not separate the time focusing behaviours of MS-1 and MS-2. Performing a linked scan, in which the ratio of the first ion mirror voltage to the accelerating potential was held constant, solved this problem. This ensured that the penetration depth of ions inside the first mirror was constant and that the time focus was always at the same position. For the purposes of the experiment the ratio was maintained at:

$$\frac{V_{mirror}}{V_{acc}} = \frac{12{,}400}{10{,}000} \qquad 6.17$$

Experiments had shown that MS-1 formed a time focus at the collision-cell under these conditions.

An aqueous solution of 0.1 M potassium bromide was made up. 0.5 µl aliquots were pipetted onto the probe tip and dried under a nitrogen stream. The voltage applied to the quadratic-field ion mirror was maintained at +16 kV. The accelerating potential was scanned between +4 kV (determined by the sensitivity of the MCP detector) and +10 kV. The flight time of the potassium cation to a detector located after the quadratic-field ion mirror was recorded. In order to determine the time spent inside the quadratic-field ion mirror it was necessary to calculate or measure the time spent in the rest of the instrument. Accurately calculating the time spent in the rest of the instrument was difficult. The 25 mm diameter detector was therefore moved to a position in the second field-free region. The linked scan experiment was repeated and the flight times of the potassium cation recorded. The physical length of the detector assembly meant that the detector could not be positioned at the entrance to MS-2. An additional flight time correction term was calculated to correct for the length of the detector assembly. This simply assumed flight time through a field-free region.

The time spent inside the ion mirror was calculated as follows:

$$t_{mirror} = t_{total} - \left(t_{MS-1} + \frac{l_d}{\sqrt{2 \cdot U/m}} \right) \qquad 6.18$$

t_{mirror} is the residence time inside the quadratic-field ion mirror, t_{total} is the total measured flight time, t_{MS-1} is the time-of-flight measured to a detector located in the second field-free region, l_d is the length of the

detector assembly, U is the kinetic energy of the ion and m is the mass of potassium.

Figure 135 shows a plot of the residence time of the potassium cation inside the quadratic-field ion mirror versus the kinetic energy of the ion. The total variation in flight time, Δt, over a kinetic energy range of 6,000 eV was determined to be less than 45 ns. The scatter, especially prominent at low kinetic energies, was due to the accuracy with which the V_{mirror}/V_{acc} ratio could be maintained. The high-voltage power supplies meant that voltages could be dialled with an accuracy of ± 10 V. The trend to shorter residence times at higher kinetic energies was due to a number of factors.

1) Field anharmonicity, *i.e* field imperfections resulting in the formation of a non-ideal quadratic-field. The plot indicated that the field was at its least ideal at the back of the mirror.
2) Detector not perpendicular to the time focus.

6.11 Mass Calibration and Resolution.

Mass calibration of the precursor ion spectrum was relatively simple:

$$(m/z)^{1/2} = At + B \qquad 6.19$$

m/z is the mass-to-charge ratio, t is the time-of-flight and A and B are calibration coefficients. The calibration constants were instrument-dependent parameters that had to be calculated. The coefficients were determined using two known masses and the spectrum calibrated. The

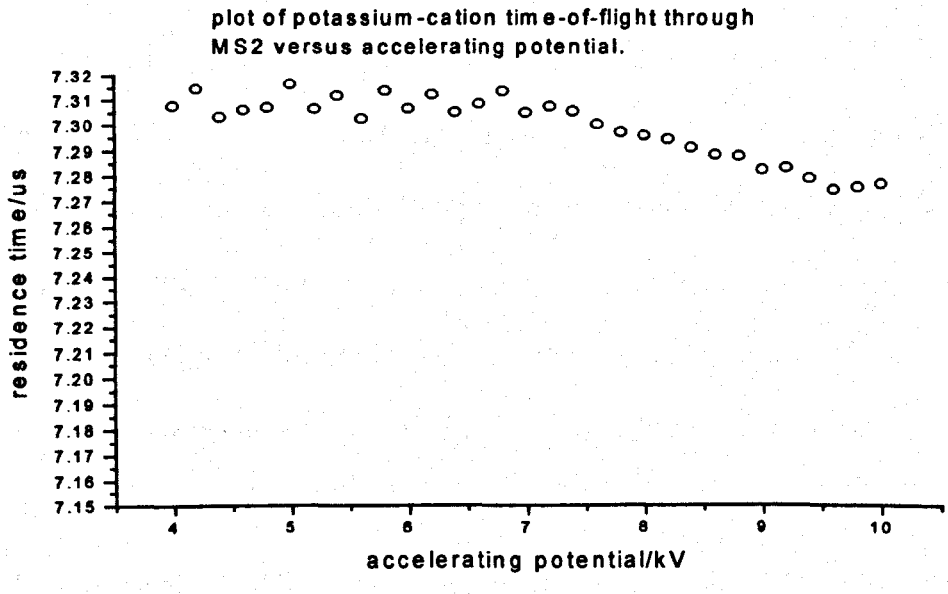

Fig. 135: Plot of residence time inside the quadratic-field ion mirror versus accelerating potential.

calibration method was used to calibrate the precursor ion spectrum in the linear, single-stage ion mirror and quadratic-field ion mirror spectrometers.

Fragment ion calibration was more problematic. The fragment spectrum was calibrated using a second order polynomial:

$$(m/z) = A + Bt + Ct^2 \qquad 6.20$$

A, *B* and *C* are coefficients. The coefficients were determined using polynomial curve-fitting software. In order to be able to mass calibrate the spectrum a detailed knowledge of the fragments was required. 15-20 known fragment masses were required to determine the coefficients and thus calibrate the spectrum. In order to calibrate an unknown fragment spectrum it was necessary to run a sample with a regular, known cleavage pattern such as C_{60}. Cotter and Cornish [10] used $(pro)_{14}Arg$ to calibrate fragment spectra obtained using a curved-field ion mirror. The coefficients were then applied to the unknown.

6.12 Mass Resolution.

Experiments were conducted to determine the optimum penetration depth/reflecting voltage for the quadratic-field ion mirror. The spectra of C_{60} were recorded for various quadratic-field ion mirror voltages, in order to optimise resolution. The experiment was replicated five times. The accelerating potential was +10 kV and the single-stage ion mirror was maintained at +11.6 kV.

Figure 136 shows a plot of resolution versus reflecting voltage. The optimum resolution was found to occur when the mirror was maintained at +15-16 kV.

Careful adjustment of the laser power proved critical for optimum resolution. For laser desorbed $C_{60}^{+\cdot}$ resolution values of the order 6,000-7,000 (FWHM) were readily achievable. Figure 137 shows a spectrum consisting of 30 averaged individual C_{60} spectra. The peak width was 6-7 ns and the resolution was 6,400. At threshold a mass resolution of the order of 7,500-8,000 (FWHM) was achievable. The signal strength was weak.

Single-shot spectra with mass resolution in excess of 10,000 were recorded. Figure 138 shows a single-shot spectrum of C_{60}. The peak width (FWHM) of the isotopomers was 3.0 ns-3.6 ns. The resolution (FWHM) was 11,700-14,000. Spectra of MALDI generated substance P ions showed peak widths of 13 ns-16 ns and maximum mass resolving powers (FWHM) of 3,500-4,400. The signal ringing, present in all spectra, was the result of charge reflection in the Galileo MCP detector assembly.

6.13 Collision-Induced Dissociation Results.

Initial CID spectra were obtained using PEG 1000 (polyethyleneglycol 1000) with α-CHC matrix. 0.2 M α-CHC in 70/30 acetone/water was made up. 0.5 µl aliquots were pipetted onto the probe tip and dried. 0.5 µl of aqueous, 7 mg/ml PEG 1000 was spotted on top of the matrix and dried. The gate was optimised to select

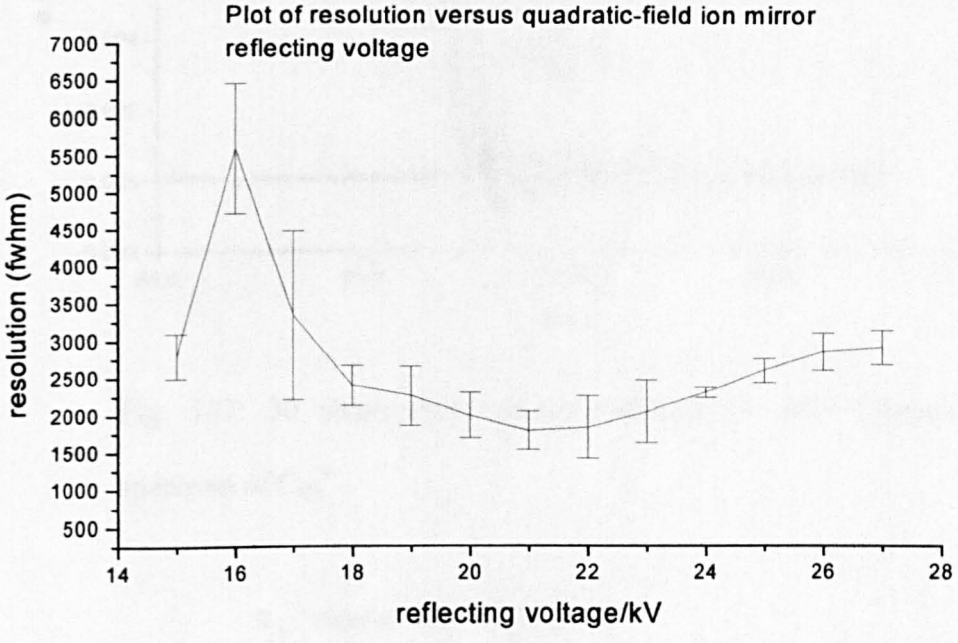

Fig. 136: Plot of $^{12}C_{60}^{+\cdot}$ resolution (FWHM) versus quadratic-field ion mirror reflecting voltage.

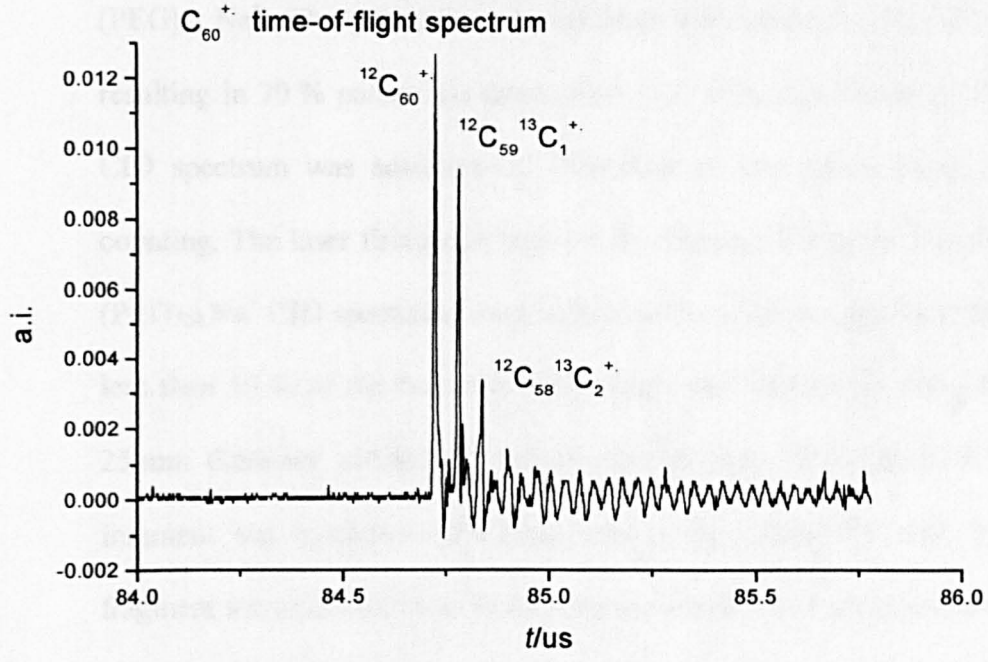

Fig. 137: 30 single-shot spectra averaged to form time-of-flight spectrum of $C_{60}^{+\cdot}$.

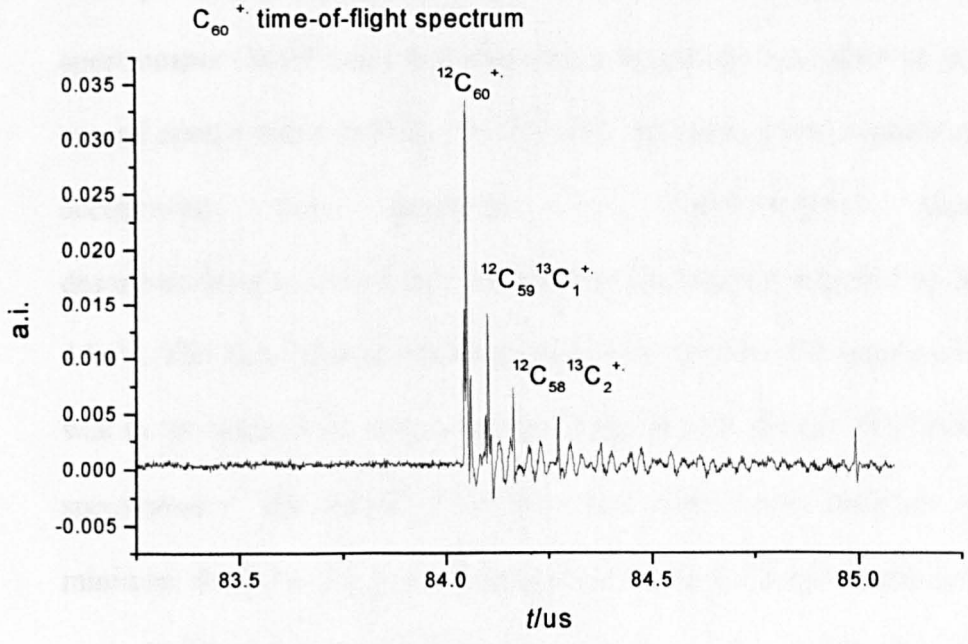

Fig. 138: Single shot time-of-flight spectrum of $C_{60}^{+\cdot}$ obtained using the TOF-TOF spectrometer.

$(PEG)_{24}$ Na^+. The precursor was collided with helium collision gas resulting in 70 % parent ion attenuation (*i.e.* 30 % transmission). The CID spectrum was accumulated over four to five hours using ion counting. The laser firing rate was 2-3 Hz. Figure 139 shows a typical $(PEG)_{24}$ Na^+ CID spectrum using helium as the collision gas. Note that less than 50 % of the fragment mass range was observable using the 25 mm diameter active area micro-channel plate. The typical CID fragment ion resolution (FWHM) was in the range 200-400. The fragment ion resolution was limited by the number of data points used to plot the spectrum. Figure 140 shows a helium CID spectrum of PEG 1000 obtained using the EB-TOF instrument constructed at the University of Warwick [11]. The EB-TOF instrument used a Kratos, Concept-H double-focusing mass spectrometer and buncher as the first spectrometer (MS-1), and an in-line planar hyperbolic ion mirror as the second spectrometer (MS-2). The EB-TOF instrument was capable of accelerating ions generated by matrix-assisted laser desorption/ionisation to 8 keV. In addition the buncher supplied up to 4 keV. The total laboratory-frame energy of the EB-TOF instrument was in the range 8-12 keV, compared with 10 keV for the TOF-TOF spectrometer. The planar hyperbolic ion mirror was designed to minimise fragment ion mass discrimination. The ion mirror combined an inclination and a slight vertical deflection in the region after the collision-cell. The instrument also used a pair of large rectangular micro-channel plates. The active area of the detector assembly was 19-20 times larger than that used on the TOF-TOF spectrometer.

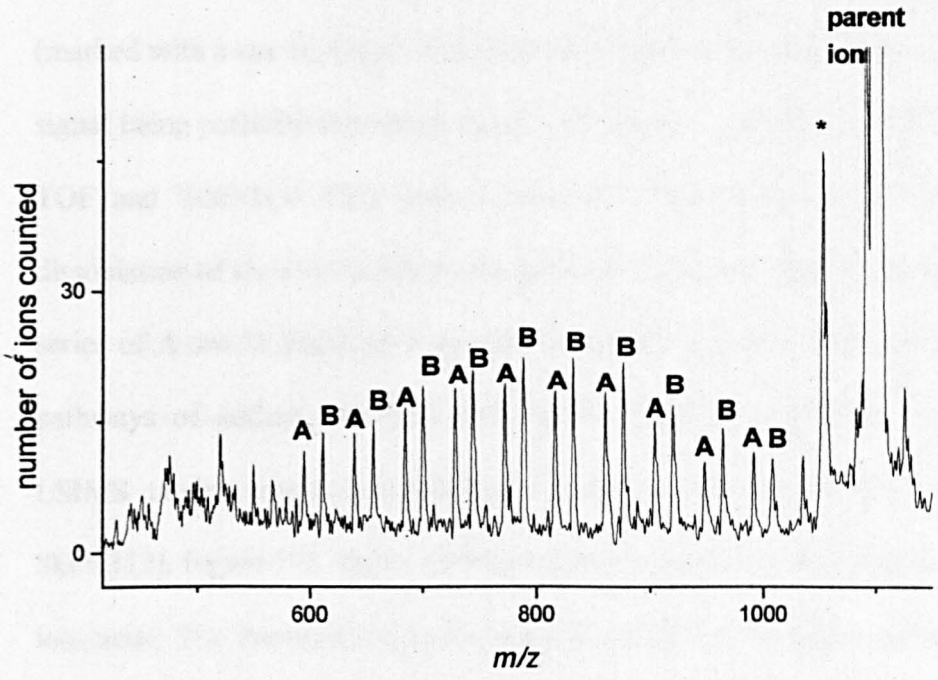

Fig. 139: Helium CID spectrum of $(PEG)_{24}Na^+$ obtained on the TOF-TOF spectrometer.

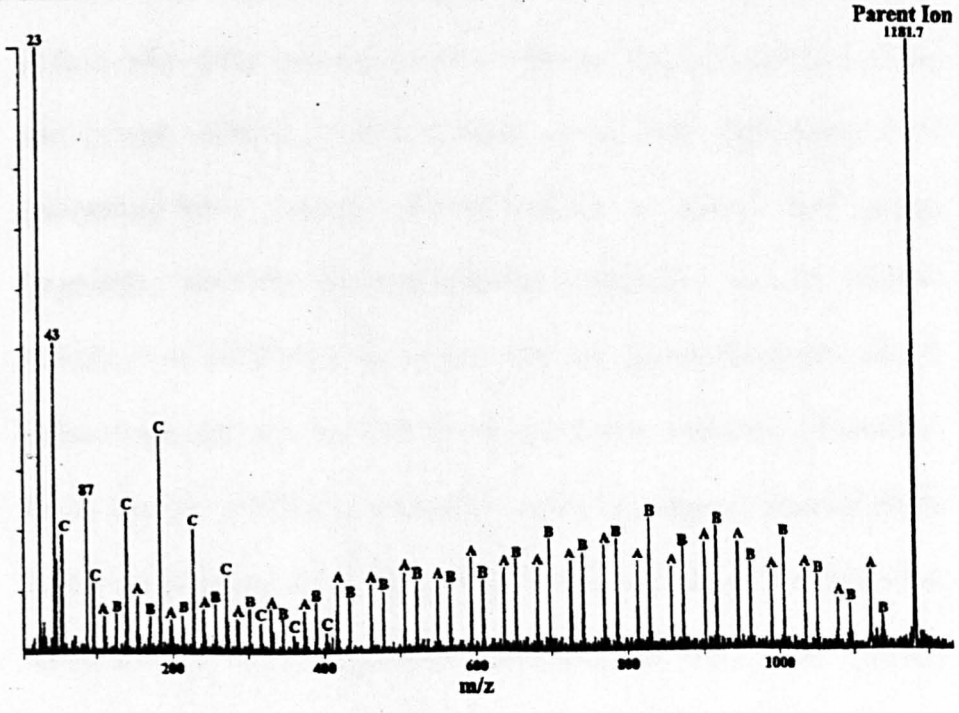

Fig. 140: Helium CID spectrum of sodiated PEG 1000 obtained on the EB-TOF spectrometer.

The TOF-TOF CID spectrum contained a strong artefact signal (marked with a star in figure 139), believed to be due to a precursor ion signal being partially attenuated by the pulsed mass gate. Both the EB-TOF and TOF-TOF CID spectra showed A and B series, due to dissociation of the C-O bonds in the polymer backbone. The repeating series of A and B fragment ions were consistent with the dissociation pathways of adducts of PEG with alkali metal ions proposed for LSIMS tandem mass spectrometry at laboratory-frame energies of 8keV [12]. Figure 141 shows a diagram illustrating how A and B series ions arise. The fragment ion mass range of the TOF-TOF spectrometer was limited to ions with a mass-to-charge ratio greater than 600 by the physical dimensions of the final detector. The TOF-TOF spectrometer did not detect the C series fragments present below *m/z* 400 in the EB-TOF spectrum. The C series fragments were proposed by Bottrill *et al* [13] to arise from cleavage of the backbone without retention of the end groups. Bottrill *et al* [13] have shown that high-energy CID (laboratory-frame energy >8 keV) results in intense end group fragments, allowing the unambiguous assignment of end groups. Bottrill *et al* [13][14] have shown that end group fragments and C series fragments are weak at the low collision energies (laboratory-frame energy <800 eV) obtainable using orthogonal time-of-flight mass spectrometry and absent from Fourier transform ion cyclotron resonance (FTICR), sustained off-resonance irradiation (SORI) spectra. This gives a clear indication that high-energy collisions are

required to gain unambiguous structural and end group information on synthetic polymer.

Bottrill *et al* [14] have proposed that the formation of the A and B series ions involves initial homolytic cleavage of a C-H bond, resulting in the loss of $H^{\bullet}$ and the formation of an intermediate species that subsequently fragments to form A or B series ions. Figure 142 and figure 143 shows the mechanism proposed by Bottrill *et al* [14]. The proposed process involves localised activation, followed by rapid homolytic cleavage of the C-H bond. The homolytic cleavage of the C-H bond would be highly endoergic, with the required energy largely supplied by the collision. If homolytic cleavage of the C-H bond is assumed to be possible, direct scission of the C-C and C-O backbone bonds must also occur when collisions occur directly with the backbone. Evidence for the localised activation is supplied [14] by observation of the behaviour of the intensity of the Na^+ fragment at different centre-of-mass collision energies. Statistical rate theories (quasi-equilibrium theory (QET) and Rice-Ramsperger-Kassel-Marcus (RRKM) theories) could not account for the observed Na^+ intensities at different collision energies.

Experiments were conducted to acquire the low-mass, PEG 1000 CID fragments not observed on the TOF-TOF spectrometer. The quadratic-ion mirror voltage was reduced to below 10 kV to focus the low-mass fragments onto the detector. Experiments showed that although intense low-mass fragments were detectable, many fragments

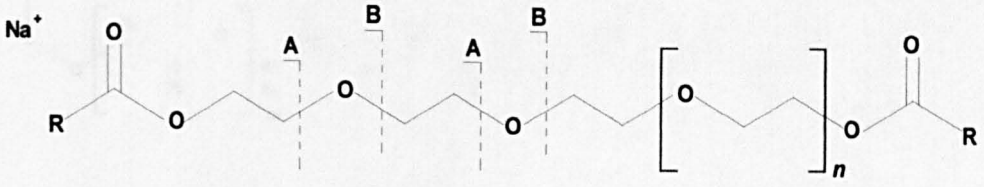

Fig. 141: Diagram showing where backbone bonds cleave in PEG to form A and B fragments.

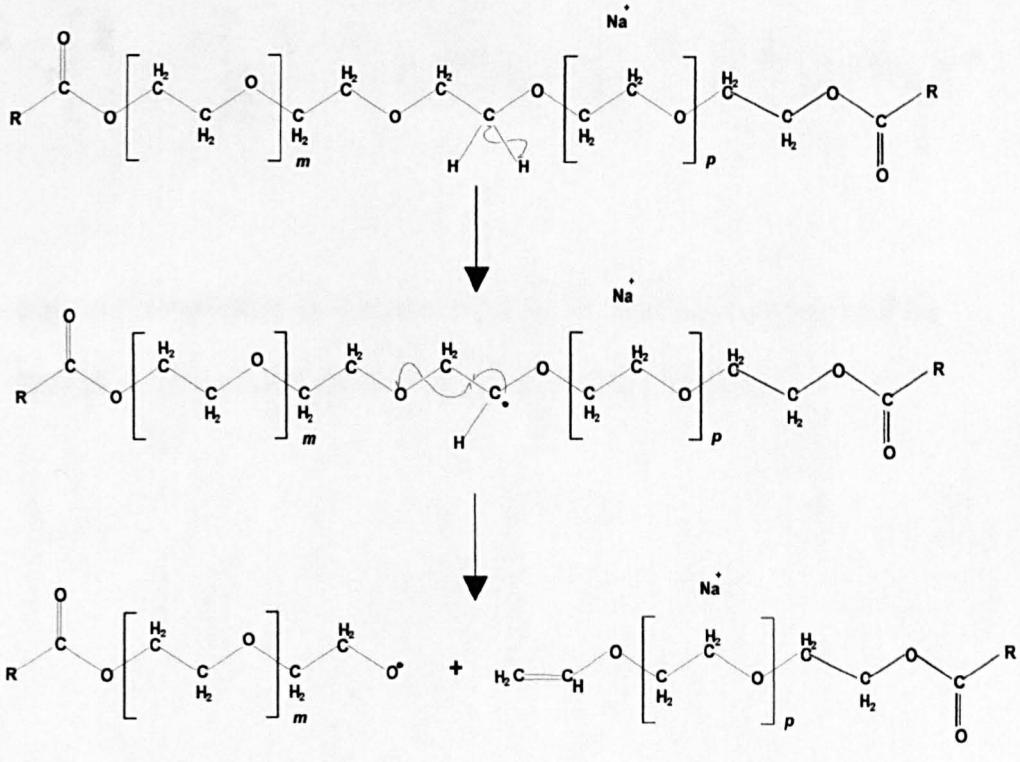

Fig. 142: Fragmentation scheme showing mechanism proposed by Bottrill *et al* to explain A series fragments.

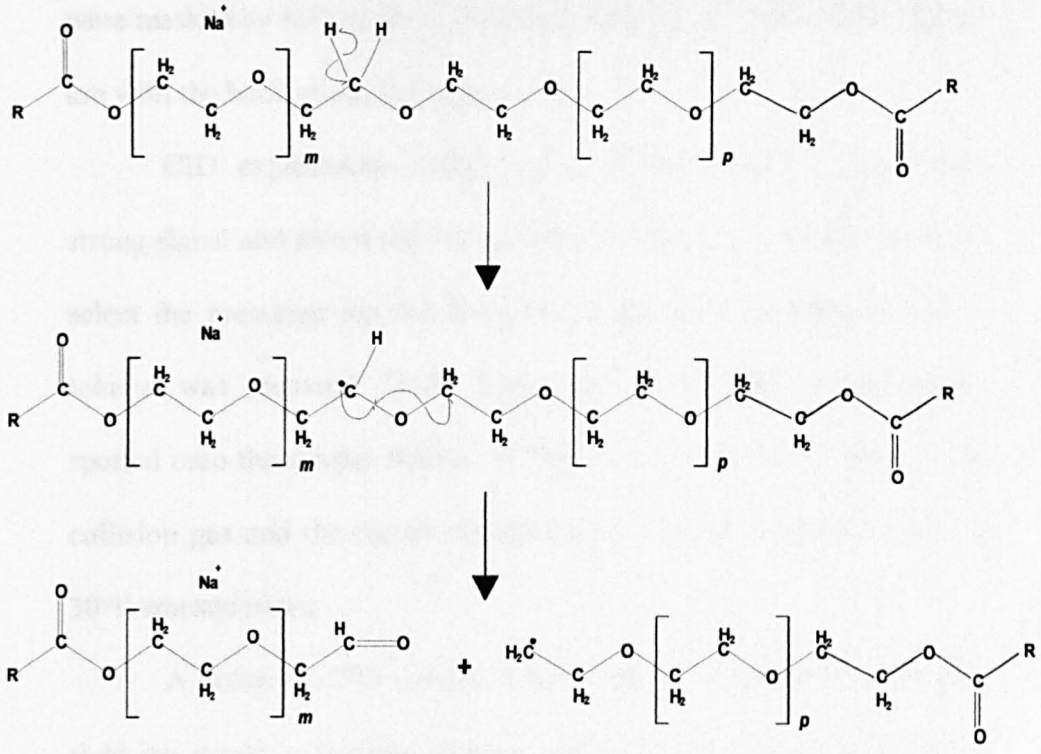

Fig. 143: Fragmentation scheme showing the mechanism proposed by Bottrill *et al* to explain the formation of B series fragments.

were masked by SID products resulting from the collision of the parent ion with the back of the ion mirror.

CID experiments using C_{60} were conducted. C_{60} provided strong signal and meant that the gate did not have to be used in order to select the precursor ion for collision. A saturated solution of C_{60} in toluene was prepared. 50-80 2 µl sample spots were consecutively spotted onto the sample holder and left to dry. Argon was used as the collision gas and the signal attenuation was approximately 70 % (*i.e.* 30 % transmission).

A series of CID spectra were recorded at different quadratic-field ion mirror reflecting voltages. Optimum resolution was found to occur when 15 kV was applied to the rear of the quadratic-field ion mirror. Figure 144 shows a typical argon CID spectrum of $C_{60}^{+\cdot}$. The fragment resolution (FWHM) was in the range of 50-180. The spectrum shows metastable decay fragment species resulting from unimolecular decay in the first field-free region. Experiments conducted in the absence of collision gas confirmed the assignment of these peaks as metastable fragments. The metastable fragments are marked with stars in figure 144. The metastable fragments were the result of C_2 loss, leading the formation of closed fullerene cages. Figure 144 includes fragment species resulting from collision-induced dissociation. Loss of C_m fragments (m=2,4,6.....) was observed up to m=22. Certain C_m losses were obscured by the presence of intense metastable species. According to the "shrink-wrap" mechanism proposed by Curl and Smalley [15], loss of C_m results in the formation

of a "repaired" closed cage. Figure 145 shows a diagram illustrating the "shrink-wrap" mechanism. Closed fullerene structures are accessible down to C_{32}. The smallest closed fullerene structure observable using the TOF-TOF spectrometer was C38. The low-mass portion of the spectrum consisted of non-fullerene (unclosed structure) carbon clusters.

C_{60} spectra acquired at different quadratic-field ion mirror reflecting voltages clearly showed mass discrimination. A series of C_{60} CID spectra using argon (70 % attenuation) were acquired for different reflecting voltages. The CID spectra was acquired over 45 minutes with a laser firing rate of 3 Hz. The experiment was repeated for a range of reflecting voltages between 12 kV and 20 kV. Figure 146 shows a C_{60} CID spectrum with 13 kV applied to MS-2. Note intensity discrimination against high-mass fragment species. Figure 147 shows a CID spectrum acquired at 20 kV reflecting voltage. The spectrum shows intensity discrimination against low-mass fragments. The conclusion is that 25 mm diameter detector was not sufficiently large to prevent mass discrimination.

6.14 Conclusions.

In conclusion, a novel tandem time-of-flight mass spectrometer coupled to a laser ion source has been designed and constructed at the University of Warwick. The instrument has successfully demonstrated the applicability of quadratic-field ion mirrors to high-energy collision-

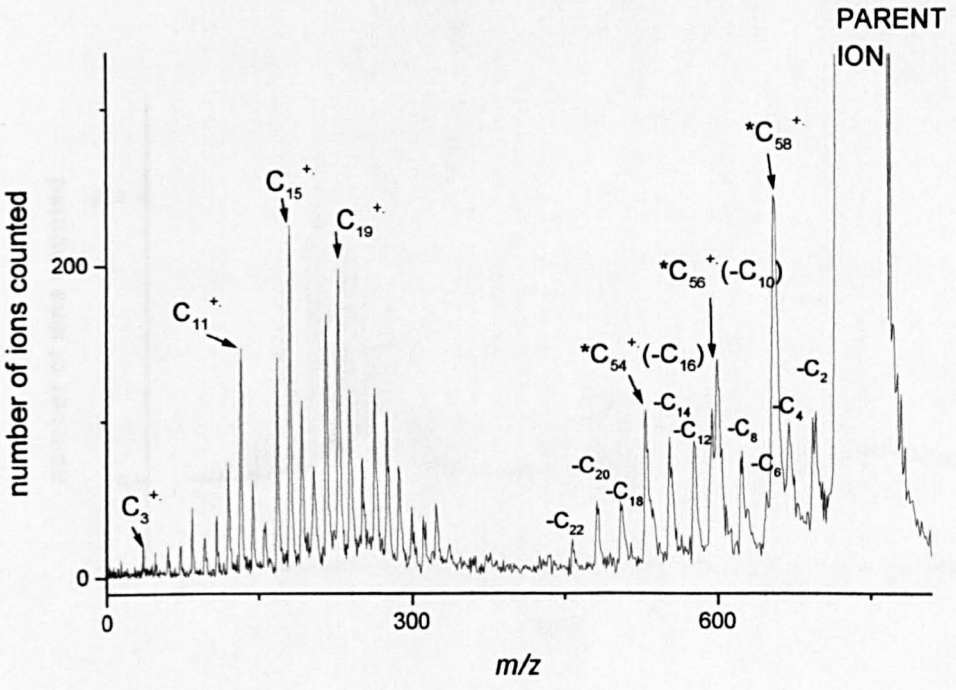

Fig. 144: Argon CID spectrum of $C_{60}^{+\cdot}$ obtained using the TOF-TOF spectrometer.

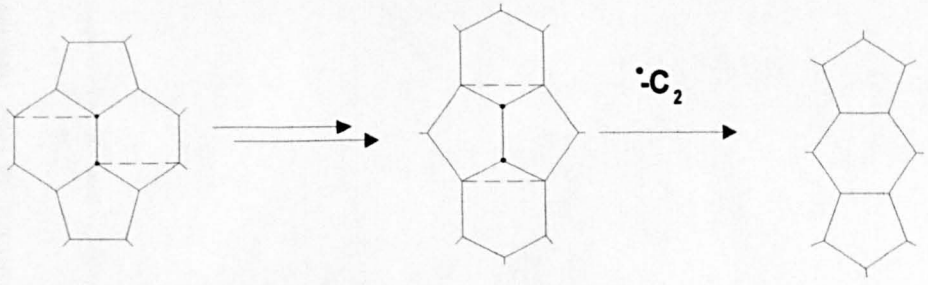

Fig. 145: "Shrink-wrap" mechanism proposed by Curl and Smalley [15] to explain C_2 loss from fullerenes.

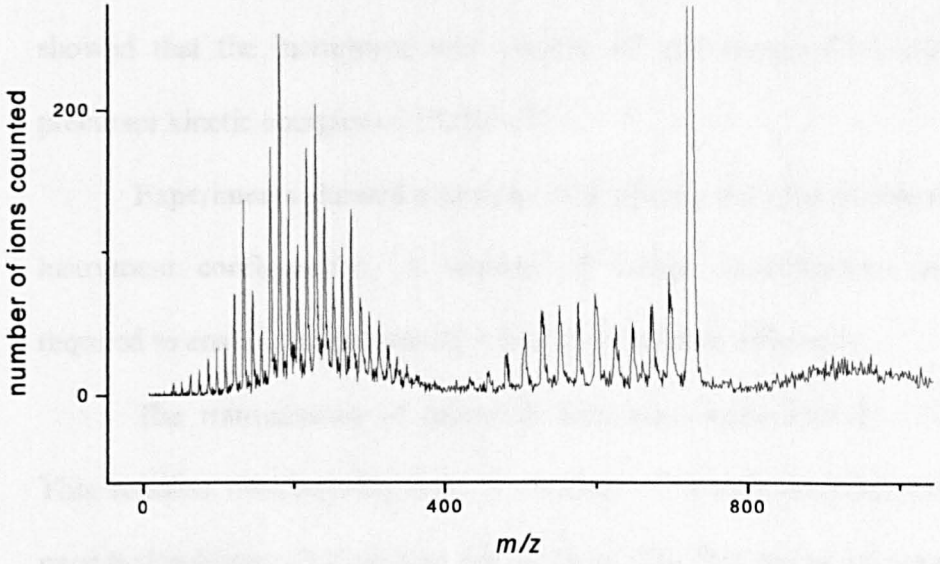

Fig. 146: C_{60} argon CID spectrum. Quadratic-field ion mirror reflecting voltage =13 kV. Note mass discrimination at high fragment masses.

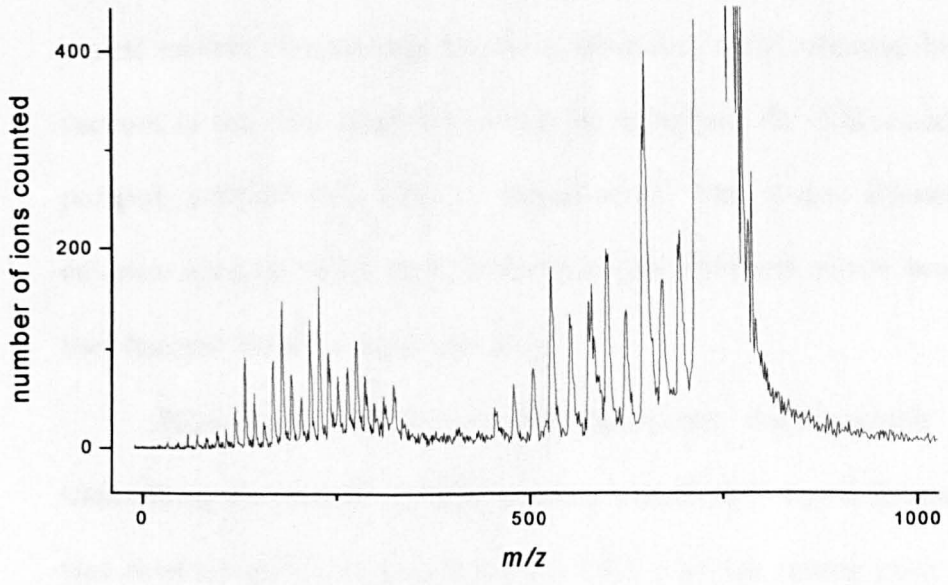

Fig. 147: C_{60} argon CID spectrum. Quadratic-field ion mirror reflecting voltage =20 kV. Note mass discrimination at low fragment

induced dissociation. The instrument has been shown to be capable of achieving high resolving powers for precursor ions. Experiments showed that the instrument was capable of high-energy CID with precursor kinetic energies of 10,000 eV.

Experiments showed a number of problems with the prototype instrument configuration. A number of design modifications are required to enable the instrument to work at optimum efficiency.

The transmission of precursor ions was approximately 2 %. This remains unacceptably low. A number of design modifications must be implemented to resolve this problem. The first ion mirror must be upgraded to allow simultaneous temporal and spatial focusing of the ion beam at the collision-cell. This would dramatically increase the transmission of precursor ions. The small pressure defining apertures of the collision-cell should be replaced. Practical experiments showed that a significant number of ions were lost at the collision-cell. The easiest method of removing the small apertures, while retaining high vacuum in the main chamber, would be to replace the differentially pumped collision-cell with a pulsed-valve. The 6 mm diameter entrance aperture at the front of the quadratic-field ion mirror would then become the attenuating aperture.

Experiments showed that the instrument was incapable of transmitting metastable peptide species. Insufficient signal intensity was detected at the final detector for CID. The ion source must be upgraded and replaced with a delayed extraction ion source capable of reducing in-source activation. Improving the pumping efficiency of the

gap between the acceleration and counter-electrodes would reduce the density of the desorption plume and reduce in-source activation.

Mass discrimination was observed in CID spectra. This was the result of using a small circular detector in the prototype instrument as the fragment detector. A large rectangular MCP assembly must be used to replace the current detector assembly. Calculations showed that the detector must be a minimum of 80 mm long. The use of a larger detector would go some way to improving the precursor ion transmission.

The gate assembly resulted in significant (>90 %) attenuation of precursor signal intensity. The gate must be replaced with a more sophisticated dual interleaved comb mass gate. The manually rotated probe must be automated. This would significantly reduce fragment ion acquisition times and mean that higher laser firing repetition rates could be used.

6.15 References.

[1] B. I. Coopersmith and R. A. Yost, J. Am. Soc. Mass Spectrom., 6 (1995) 976.

[2] X. Tang, W. Ens, K. G. Standing and J. B. Westmore, Anal. Chem., 60 (1988) 1791.

[3] R. Kaufmann, D. Kirsch and B. Spengler, Int. J. Mass Spectrom. Ion Processes, 131 (1994) 355.

[4] Y. Yoshida, 1986 US Patent Number 4,625,112.

[5] A. A. Makarov, E. N. Raptakis and P. J. Derrick, Int. J. Mass Spectrom. Ion Processes, 146/147 (1995) 165.

[6] E. Uggerud and P. J. Derrick, J. Phys. Chem., 95 (1991) 1430.

[7] B. Spengler, D. Kirsch and R. Kaufmann, J. Phys. Chem., 96 (1992) 9678.

[8] R. Kaufmann, B. Spengler and F. Lützenkirchen, Rapid Commun. Mass Spectrom., 7 (1993) 902.

[9] R. Kaufmann, P. Chaurand, D. Kirsch and B. Spengler, Rapid Commun. Mass Spectrom., 10 (1996) 1199.

[10] M. M. Cordero, T. J. Cornish, R. J. Cotter and I. A. Lys, Rapid Commun. Mass Spectrom., 9 (1995) 1356.

[11] U. N. Anderson, A. W. Colburn, A. A. Makarov, E. N. Raptakis, D. J. Reynolds, P. J. Derrick, S. C. Davis, A. D. Hoffman and S. Thompson, Rev. Sci. Instrum., 69 (1998) 1650.

[12] T. L. Selby, C. Wesdemiotis and R. P. Lattimer, J. Am. Soc. Mass Spectrum., 5 (1994) 1081.

[13] A. R. Bottrill, A. E. Giannakopulos, C. Waterson, D. M. Haddleton, K. S. Lee and P. J. Derrick, Anal. Chem., 71 (1999) 3637.

[14] A. R. Bottrill, A. E. Giannakopulos, K. S. Lee and P. J. Derrick, Manuscript in preparation.

[15] R. F. Curl and R. E. Smalley, Scientif. Amer., 32 (1991).